Microstructure and Residual Stress State in the Contact Zone of Rails and Wheels

vorgelegt von
Master of Sciences M. Sc.
Lihong Wang
aus Dalian, P. R. China

Von der Fakultät
- Prozesswissenschaften –
der Technischen Universität Berlin
zur Erlangen des akademischen Grades

Doktor der Ingenieurwissenschaften
-Dr. Ing.-

genehmigte Dissertation

Promotionsausschuss:

Vorsitzender: Prof. Dr.–Ing. M. Möser
1. Berichter: Prof. Dr. rer. nat. W. Reimers
2. Berichter: PD. Dr.–Ing. A. Pyzalla

Tag der wissenschaftlichen Aussprache: 12. September 2002

Berlin 2002
D83

Abstract

Lihong Wang:

Microstructure and Residual Stress State in the Contact Zone of Rails and Wheels

In this thesis, the influences of the loading history of rail-wheel system on the microstructure, texture and residual stress on the superficial surface and also in the near surface area of the rail tracks and wheels have been comprehensively investigated.

For determining the texture evolvement and residual stresses, nondestructive diffraction methods using both conventional X-ray radiation and medium energy synchrotron radiation are employed. For clarifying the formation mechanism of the White Etching Layers, both diffraction analyses and microstructural investigations were performed. The distribution of precipitates has been characterized using ASAXS in DESY, Hasylab, in Hamburg. By means of a profilometer, the surface topography of rails has been well reproduced.

Due to the increasing high axle loading, the surface of rails and wheels inevitably underwent both topographical changes and microstructural alterations. The investigations in this thesis reveal that the combination of plastic deformation and thermal loading in the rail-wheel system induces the formation of WEL and riffle bands that have been known for nearly 100 years. The distribution of the residual stress indicates high local plastic deformations on the surface of rails and wheels, which accounts for the breaking up of the carbide into the nano size and also for the partial dissolution of the carbide lamellas. The simultaneous heating up and the subsequent quick cooling on the surface of rail and wheel lead to thermal microstructural transformations ferrite / perlite – austenite - martensite. A microstructure model for the evolvement of WELs has been established. The appearance of the WELs is supposed to speed up the development of the riffle bands. A <111> fiber texture and a <551> fiber texture were found in the rail-wheel system. Due to the phase transformation, the texture intensity tends to decrease with increasing loading. The maximum of the texture index was found not directly on the superficial surface, but in the interior of the rail and the wheel. The investigations on four rails with different loading history have been compared.

Acknowledgements

This thesis was written beside my work as a research assistant in the department of “Strukturforschung” in Hahn - Meitner - Institut Berlin (HMI) from September 1999 to October 2001 and in the institute of Materials Science and Technologies at Technical University of Berlin from October 2001 to June 2002.

I would like to express my gratitude to Prof. Dr. W. Reimers for giving me this precious chance and giving me valuable suggestions. I also want to thank him sincerely for the review of my thesis.

In particular, I would like to express my most sincere thanks to PD. Dr. A. Pyzalla for her patient instructions. She gave me a lot of valuable advice and her active work attitude is a vivid and practical model and gave me powerful motivation.

Further on, I would like to express my thanks to my dear colleagues, E. Lima, H. Pinto, B. Reetz, J. Wegener, T. Töpfer, Mrs. M. Stempniewicz, C. Bohne, H. Freydank, P. Peter, Mrs. M. Ludwig (HMI) and especially, E. Wild, S. Dieter and T. Poeste. Without their assistance, my work would not have been finished in time. I am also grateful to M. Hill, Mrs. M. Schaube, T. Spreu (HMI), Mrs. H. Malks and B. Lehrer for their sincere help with metallography microscopy and specimen preparations. Special thanks go to Mrs. G. Garke and Mrs. S. Quander for their help with organizational and administrative works. In addition, I would like to acknowledge Dr. T. Wrobleski, G3, Hasylab Hamburg and G. Goerigk, B1, Hasylab Hamburg for their assistance during synchrotron radiation experiments.

I would like to acknowledge the funding of the Deutsche Forschungsgemeinschaft (DFG) in the Sonderforschungsbereich “Elementarreibereignisse”. I also would like to express my thanks to the colleagues in the Sfb, especially to Prof. Dr. Santner, Dr. Spaltmann, Dr. Österle from BAM, Dr. Bucher and Prof. Dr. Knothe from TU Berlin. Further I thank Prof. Dr. E.A. Werner, Dr. W. Stadlbauer from the Technical University of München for the cooperation.

Finally I want to express my special thanks to my husband, Libo Zhou, my parents, Xiaodong Wang and Mrs. Xiumei Zhang, and to my former colleague, Dr. Hans - Michael Meyer and his wife, Mrs. Jin. Without their steady encouragement and without financial support from my parents for my studies, this thesis would never have reached completion.

Content

Abbreviations

1. Introduction 1

2. Literature Review 3

2.1 Rail - Wheel – System 3

2.1.1 Rail - Wheel Contact 3

2.1.2 Contact Stresses and Subsurface Stress Distribution 6

2.2 Microstructure Alterations on Rails and Wheels 8

2.2.1 Riffle Bands 8

2.2.2 White Etching Layers 11

3. Objectives and Methodology 16

3.1 Objectives 16

3.2 Methodology 16

4. Experimental Details 18

4.1 Samples 18

4.1.1 Rail Samples 18

4.1.2 Wheel Sample 18

4.2 Metallography and Microscope 19

4.2.1 Optical Microscope and Scanning Electron Microscope 19

4.2.2 Microhardness Determination 19

4.2.3 WDX Analyses 19

4.3 Anomalous Small Angle X - ray Scattering 20

4.4 Diffraction Methods 21

4.4.1 Phase Analysis 21

4.4.2 Profile Analysis 22

4.4.3 Texture Analysis 23

4.4.4 Residual Stress Analysis 24
4.5 Profilometer Measurements 24
4.6 Corrosion Tests 25
5. Results 26
5.1 Microstructure Changes and Changes in Topograghy 26
5.1.1 Rail Samples 26
5.1.2 Wheel Sample 37
5.2 Texture 39
5.2.1 Rail Samples 39
5.2.2 Wheel Sample 41
5.3 Residual Stresses 42
5.3.1 Rail Samples 42
5.3.2 Wheel Sample 47
5.4 Corrosion Resistance 48
6. Discussion 50
6.1 Formation of the White Etching Layers 50
6.2 Correlation between Changes in Microstructure and Topography 57
6.3 Gradients of Residual Stresses, Texture and Microstructure in the Depth 59
6.4 Comparison between the Rails 62
6.5 Comparison of Microstructure Changes in Rails, Wheels and in Bearings 64
7. Summary and Conclusions 70
8. Zusammenfassung 72
9. Literature 74
10. Resume 86
11. Tables and Figures 87

Abbreviations

ASAXS	Anomalous Small Angle X - ray Scattering	
ASTM	American Society for Testing Materials	
FWHM	Full Width at Half Maximum	
ODF	Orientation Distribution Function	
SEM	Scanning Electron Microscope	
TEM	Transmission Electron Microscope	
WEL	White Etching Layer	
WDX	Wavelength Dispersive X - ray Analyses	
b.c.c.	Body centered cubic	
b.c.t	Body centered tetragonal	
f.c.c	Face centered cubic	
α	Ferrite	
γ	Austenite	
A_1	Transformation temperature: $\alpha <-> \alpha + \gamma$	[°C]
A_3	Transformation temperature: $\gamma <-> \gamma + \alpha$	[°C]
M_s	Martensite start temperature	[°C]
σ_0	Yield strength	[MPa]
$\sigma_{contact}^{max}$	Maximum of the contact stress	[MPa]
K_y	Correlation factor	[MPa(nm)$^{1/2}$]
λ	Wavelength	[Å]
c_m	Lattice distance of martensite	[nm]
a_m	Lattice distance of martensite	[nm]
σ_1	Principal residual stress	[MPa]
σ_2	Principal residual stress	[MPa]

1. Introduction

Since the first iron rail track was developed in 1738, railways have been playing an important role in public transportation. Railway transport during the last years has increased in speed, security and comfort. In comparison to automobiles and planes, railway transport is a more secure and less environmental damaging means of transportation. In order to keep up the competiveness of railroad transportation, increasing requirements on the speed of passenger and freight trains, on the axle load of the trains as well as on the comfort of the passengers have to be met. Further pressure on the development arises from the demand of decreasing the costs of both new trains and new rail tracks as well as the maintenance costs.

Thus, a large number of investigations have focused on an optimization of trains, rail tracks and the rail / wheel system, e.g. optimizing the rail - top profile. The mechanisms of material changes at the rail / wheel interface also have received considerable attention. But, so far the structure changes that occur in the rail and the wheel material during service still have not been completely solved and clarified.

In service the surface of the rail track as well as the surface of the wheel sets are subject to strong changes due to their long - time sustaining load and wear. Among these microstructure changes are the occurrence of riffles as well as the development of so - called White Etching Layers (WEL). These white etching layers emerge on the surface of corrugated rails. Due to their brittleness the white etching layers are starting points for crack propagation and fracture due to spalling. They further are known to increase noise and vibrations of the trains. In order to remove the white etching layers rail surfaces are periodically ground by the railway companies. This grinding process costs several Mio. € per year in Germany.

The aim of this thesis is a study of the surface changes on rails and wheels that result from friction and wear. In particular this thesis is supposed to be a contribution towards a better understanding of the mechanisms leading to the formation of the WEL. Therefore, systematic and quantitative investigation of the microstructure changes, the texture and the residual stress evolution on rail surfaces as well as on the surface of a passenger train wheel are performed. The investigations are

performed mainly by diffraction methods including novel techniques using synchrotron radiation. Additionally small angle X - ray scattering as well as optical and electron microscope are used for microstructure characterization.

2. Literature Review

2.1 Rail – Wheel system

2.1.1 Rail – Wheel Contact

Railways essentially provide transport in self - guided vehicles under conditions of very low tractive resistance by the rolling of flanged steel wheels along steel rails /Dearden 1960/. The rolling of steel wheels on steel rails is a unique feature of rail vehicles distinguishing them from other kinds of machinery.

The contact area of the system encloses only the rail and the wheel track (Fig. 2.1). The wheel has a slightly coned cylindrical shape with a protruded flange that is purposed to ensure the rolling direction and safety. The rail top head owns an arched surface with a certain crown radius. Wheel and rail profiles are envelopes of each other. Now there are dozens of designs for rail profiles and wheel profiles in order to suit the different axle load requirements and conditions. Basic criteria for the design are minimizing the rolling friction and at the same time maximizing the load carrying capacity.

Because of the periodically repeated friction and wear, both, the profiles of rail and wheel change considerably during their lifetime. At any given time, there is a distribution of various wheel profiles running over a rail, each contacting the rail at a different point. The wheel / rail contact zone is a variable, changeable interface at which more than 60 variables or parameters, with complex interrelationships, are at work /Magel 1999/. On a corrugated rail surface, the contact band often even can be seen by eyes. Under different service conditions, the contact positions on the rail track vary. Mathematical methods to simulate the contact area have drawn a lot of attention lately /Andersch 2000/. They revealed that the shape and the size of the contact area plays a very important role in friction processes within the rail – wheel rolling contact.

The wheel and the rail are usually subject to normal, longitudinal and tangential loading. Normal forces are exerted by the mass of the trains. Longitudinal forces

arise from locomotive traction caused by the lateral displacement of a coned wheel. Transverse forces result from the misalignment between wheels and rail track. The transmission of traction forces between wheel and rail is also connected with sliding in the contact area, thus, it is not an ideal rolling contact. The friction coefficient between dry wheels and rails may be as high as 0.6 and frequently exceeds the critical value which causes surface deformation /Bower 1991/. Therefore, the rails almost always suffer from some degree of plastic deformation. The comprehensive examination of rails which have been in service indicates that plastic flow is confined to a thin layer near the surface of the rail head, and that the greatest accumulated strain arises at the surface. The plastic deformation increases linearly with the load exerted /Krause 1979/. /Krause 1979/ also put forward, that the increased thermal stress and thereby the higher temperature gradient should be taken into account during the further loading. The determination of the deformation and rolling resistance in rolling contact has been calculated theoretically by perturbation methods /Marschall 1968/. Calculations of /Marschall 1968/ took into consideration the rolling resistance and permanent surface displacement, and a slip line field is also constructed.

It is already well established that the friction induces a certain amount of frictional heating /Singer 1991/. Since it is difficult to measure the temperature in the wheel - rail contact, theoretical predictions of the temperature rise for various wheel loads, vehicle flow and slip speeds have been formulated. /Jaeger 1943/ has studied these problems in considerable detail, but since a vast range of parameters is involved, any mathematical discussion is limited to the numerical calculations for a particular model. /Blok 1963/ approximated the elliptical pressure distribution in the direction of sliding as a parabolic distribution, obtaining a similar solution as /Jaeger 1943/. Some other work concerning this can be found in /Archard 1959, Ertz 2000, Kuhlmann[1] 1987/. Because of the different assumptions made for the thermal flux distribution along the contact length, there exist some differences between the results. But it is undoubted, that high temperatures can be reached especially in some hot spots /Kuhlmann[1-2] 1987, Quinn 1987/. The temperature caused by frictional heating increases with the train speed. If the train speed would exceed 500 km/h and the friction coefficient is larger than 10%, the temperature in the contact area would reach up to 900°C /Knothe 1995/.

Any pressure fluctuation will increase the contact temperature, while the roughness of the surface has little effect on the temperature rise /Knothe 1995/. In contrast, surface damage may have major influence on contact temperatures. For wheel - rail systems, temperature above 500°C can not be achieved under normal condition /Knothe 1995/. However, when slip between wheel and rail is considered, the contact temperature can reach up to 600°C, even 1000°C /Tanvir 1980/. The heat penetration into the medium is fairly shallow and the thermal gradients are fairly steep, approximately 3000 K/mm. Therefore, thermal stress alone would cause only superficial damage to the rail and the wheel. The thermally induced stresses, which are limited to a small surface layer, strongly influence the tribological behavior /Abdel - Aal 1998, Wieslaw 1980/. The stress induced by a temperature rise of 50 K is of the same magnitude as the stress induced by loading /Knothe 1995/. Repeated normal and shear stresses superimposed with high thermal induced stresses may lead to additional plastic deformation /Knothe 1995/. Thus, the contact surface of the rail track and the wheel undergo the combined effect of periodically varying contact stress and intermittent thermal stress /Lunden 1991/. /Lunden 1991/ compared the plastification under only mechanical load and under combined mechanical and thermal load. It was concluded that the wheel rim surface obtains a drastic increase in plastic cycling amplitude when the thermal load is increased. Below the surface regions of significant plastic amplitude were found even for moderate thermal loads.

In /Baumann 1998/ the requirements for the rail material are listed. One main objective in wheel - rail technology is the avoidance or at least the delay of shape changes of the contact surface as a result of wear. The wear behavior of steel is generally classified into three types: namely oxidative wear, mechanical wear and thermal wear accompanied by melting of contact asperities /Kawamoto 1971/. These three kinds of wear can all be found in the wheel - rail system. The wear behavior can be influenced by the material composition and heat treatments by a surface treatment and by the design parameters, which determine the material stress in the wheel - rail contact area /Krause 1986/. /Aronov 1980/ specialized in analyzing the wear kinetics of rail and wheel steel in dry friction, simulating the rail - wheel contact with two cylinders that had different radii. It was concluded that wear is not directly proportional to the number of load cycles, but increases with time. Wear particle

formation appears to be due to crack generation and propagation in the highly stressed surface layer of the materials.

The contact stress is repeated by the passing of wheels and it creates material fatigue on the running surface /Kashiwaya 1989/.

This material fatigue brought about by thermal and mechanical stresses in the contact region of rails and wheels is a failure mechanism of great practical importance. Although the wear of the surface layer is in general not a direct safety threat, it influences the cost and competitive strength of railway transportation. The current move towards higher speeds and axle loads has created a demand for a deeper knowledge at the rail - wheel contact area.

Literature review, thus, revealed that the rail - wheel contact is a dynamic process. It has implications for the comfort of passengers, for the damage to the track, for the noise generation and for the safety of the railway system.

2.1.2 Contact Stress and Subsurface Stress Distribution

The term contact stresses refers to those stresses produced in the area near the contact point between two bodies with curved surfaces, which are pressed against each other /Wan 1991, Johnson 1985/. Contact stress are among the most important parameters in the design of the geometry of the machinery.

Initially a load is exerted on the railway track at a small number of contact points between the wheel and rail. Then, under pressure, each contact point transforms or spans into a larger contact area. With increasing load and also dependent on both the profile of the wheel and rail, an elliptical contact area will be formed. When the pressure between the surfaces does not act normal to the plane, the surface may sustain a tangential component of the force in longitudinal or transverse direction /Johnson 1958/. Thus, in the system of rail and wheel, due to torsion, sliding of the wheel, the curved surface of the rail and so on, the amplitude of the tangential force exerted on the rail depends on the position within the elliptical contact area. Fig.2.2 illustrates schematically the deformation of the subsurface element. The strongest variation of shear stress may not occur on the axis of symmetry but at some other

point in the principal plane of motion /Fessler 1957/. The shear force in both direction leads to some amount of the friction.

Carter and Fromm are known as the pioneers analyzing the rolling contact stress. /Carter1926/ dealt with the rolling condition of the wheels on the railway. He simulated the railway as an elastic half sphere and the wheel as an elastic cylinder. The rolling contact stress was analyzed in two dimensions /Carter 1926/. /Fromm 1927/ studied the rolling contact problem also in two dimensions, but between two cylinders. Later based on the results of these two pioneers /Johnson 1958/ presented a theoretical calculation analyzing the effect of a tangential contact stress upon the rolling motion of an elastic sphere on a plane. The influence of geometrical surface imperfections on the normal pressure distribution in contact is studied by /Seabra 1987/. A variational formulation based on the principle of complementary virtual work is used to solve the normal contact problem. /Seabra 1987/ draws the following conclusions: the surface waviness and roughness modify the pressure distribution in the contact and induce the existence of several points of maximum pressure and several contact areas instead of only one.

The nominal maximum contact stress particularly in the system rail - wheel system was calculated in several publications. The Hertzian theory was used as a basic theory. The magnitude of the maximum of contact stress $\sigma^{max}_{contact}$ is nearly independent of the individual rail - wheel system. $\sigma^{max}_{contact}$ = - 2000 MPa for rail DB AG when the surface roughness is considered in /Bucher 2001/, $\sigma^{max}_{contact}$ = - 1400 MPa and $\sigma^{max}_{contact}$ = - 1900 MPa for a new AREA rail in two kinds of situations in /Hellier 1986, Hellier 1991/ and $\sigma^{max}_{contact}$ = - 1400 – - 1700 MPa for wheel steel B82 in /Lunden 1991/. It is obviously beyond the tensile strength of the rail steels and wheel steels.

The state of stress below the contact surface is three - axial with gradients in all three directions. These subsurface stresses quickly decrease with increasing distance to the contact surface. Fig. 2.3 shows the theoretical prediction for the in - depth distribution of the subsurface stress in longitudinal direction beneath the center of the contact area.

/Hellier 1986/ used a finite element computation to study the subsurface rail / wheel contact stresses with application to rail fatigue. The results of his calculations

indicate that the depth of plastic deformation should be in the order of 10 mm, which corresponds to the location at which fatigue cracking takes place.

Thus, the various theoretical calculations have shown that the surface and subsurface of the rail heads are subject to considerably high loads, which can give rise to radically changed microstructures and to the marked microstructure gradient in the in - depth direction of the rail.

2.2 Microstructure Alterations on Rails and Wheels

2.2.1 Riffle Bands

The formation of riffle bands on corrugated rail surfaces has been a well - known problem for over one hundred years /Birmann[1] 1958/. It is a damage, that appears directly on the rail surface. It relates to the apparent irregular unevenness on the rolling surface of rail and wheel. Those areas which tower above others on the rail surface are referred to as “riffle hills” and those areas which are well beneath the average surface are named “riffle valleys”. The wavelength of the riffles is between 3 cm and 8 cm /Meywerk 1998, Hempelmann 1994/. Fig. 2.3 gives an overview of a rail surface with a riffle band. Depending on the rail shape, the chemical composition of the rail material, its mechanical properties, the service conditions, surface roughness and so on, the appearances of the riffle band obviously takes on different shapes /Fastenrath 1977/. But, in all cases, the bright shining rising ”hills” and the comparatively dark deepen ”valleys” that lie in - between the ”hills” on the rolling band is clearly recognizable. Riffle bands were found nearly on all kinds of rail segments /Döring 1955, Eisenmann 1977, Walloschek 1988/. They result in undesirable transportation behavior such as excessive vibrations in the rail - wheel system.

From 1895 to 1958 there were several hundreds of publications counted by /Birmann[1-2] 1958/, which show the concern and attention to riffle formation. It is commonly accepted that the riffle formation is a physical - chemical phenomenon occurring during rolling contact. Today, the theory of riffle formation essentially deals with three disciplines: vibration system, tribological analysis and material science.

The existence of riffles leads to direct damage to the rail track and wheel - sets. The damage includes loose of fastening, destruction of sleepers and accompanying effects such as misalignments of track and gauge widening /Helmpelmann 1994, Fastenrath 1977/. The premature deterioration of the track structure leads to high maintenance costs. In addition, it can also lead to a noise more than twice as high as on uncorrugated sites /Stanworth 1986/.

Today the treatment of riffles is grinding them down in - situ in order to remove them. This is done by the Deutsche Bahn AG when the depth of the riffle band reaches about 50µm. Estimated costs for grinding are about 18 Mio. DM for the DB in 1983 /Kaess 1983/, $ 100 Mio. in 1985 in the USA /PR 1985/ and about £ 5 Mio. in UK in 1988 for grinding and maintenance directly related to corrugation /RE 1988/.

Vibration theory of riffle formation

Frequency analyses revealed that the vibration of the railway is over 20 Hz /Steinbeißer 1977/.

/Feller 1991/ analyzed the surface morphology of rails by SEM. He reported that the results of his investigations showed that the vibration of the wheel - tread system leads to the corrugation of the rail. As a consequence there were areas with higher loads, higher deformation, higher hardening and higher wear resistance. This means that the “hills” are distinct and that they carry approximately 90% of the wheel load. Neighboring areas have lower deformation. That means the that “valleys” was deepen due to wear and corrosion.

According to the friction – induced vibration theory it has been proven that corrugations are formed by wear resulting from torsional vibration of the drive wheels and by longitudinal vibration of the rails /Brockley 1988/. Additionally /Schultheiß 1985, Kaess 1983/ have suggested that the plastic deformation induced by the imperfect rolling process with torsion and sliding, the wear between the rail and wheel and the vibrations are the main reasons of the riffle formation. Long - term observations on different railway tracks put forward that a smooth rail and wheel surface tends to delay the formation of riffles and that the formation velocity of the riffle band is dependent on the vibration system of wheel and rail.

Tribological theory of riffle formation

According to /Fink 1953/ the corrugation is due to the formation of an oxidation layer on the surface. During service the oxide layer is broken. The remaining oxide particles then are pressed into the surface. Then corrugation proceeds. /Fink 1953/, thus, contradicted the vibration theory and concluded that not vibration generates the riffles, but that inversely just the formed riffle produces the vibration. Comprehensive observations on different rails /Busse 1908, Vietor 1903/ were summarized by /Fink 1953/.

In addition, /Baumann[1] 1996/ put forward the idea that the riffle band would be strengthened and aggravated with the service time passing by. When it reaches a certain degree of roughness, the riffle band would lead to profile incompatibility between the rail and the wheel. /Baumann 1996/ divided the riffle formation process into three periods regarding the wear process: riffle initiation period (e.g. the first four service years), riffle growing period (e.g. from fourth to seventh service year), saturation period (e.g. after seven service years). After the second period, the white etching layer can already be observed and developed continuously in the subsequent period.

Using a non - linear simulation model /Meywerk 1998/ concluded that the spatial inhomogeneity and the time - dependence of friction coefficients also contribute to the riffle formation. In this hypothesis the influence of metallurgy on the riffle formation is not taken into consideration.

Material theory of riffle formation

/Spieker 1971/ ascertained that not only the production methods but also the mechanical properties of the rail material have a certain effect on riffle formation. The riffle liability will increase with increasing tensile strength of the rail steel. In addition, /Spiekter 1971/ found that a relatively high nitrogen content of the rail steel will promote the riffle formation, but, that alloying the rail steel with manganese and silicon will alleviate or delay riffle formation. But, no results of the quantitative element analyses was given. It is well known that all rail steels used so far showed riffle formation after long – time service. The strongest phenomenon is, that not only the topology of the rail is deformed, but also the microstructure is transformed /Naumann 1961/, and even so - called White Etching Layers are seen on the ”hills”

on the surface /Walf 1991, Baumann[1-2] 1996/. The white etching layer aggravates the working condition and causes fatigue of the rails and wheels. The formation of the WEL is the strongest negative effect that the riffle band induces.

2.2.2 White Etching Layer

White Etching Layer (WEL) is a term referring to hard layers of material which, because of their strong resistance to etching, in comparison to the bulk material, appear white and featureless under optical microscopes /Griffiths1987/. It is one of the strongest side effects of riffle bands in the rail - wheel system. The most remarkable aspect of the white layers is their extremely high hardness. The various investigations referred to report hardness levels at the surface between 700 – 1200 HV0,2.

The occurrence of white layers is neither a new phenomenon nor does it appear only on the surface of corrugated rails. The first reference on WELs can be dated back as far as 1912 /Stead 1912/. At that time /Stead 1912/ identified these WEL on steel wire ropes. He interpreted them as the formation of martensite as a result of frictional heating in service followed by quenching by colder sub - layers. Since then WEL have been continuously observed in a large variety of loading situations and on both ferrous and non - ferrous materials. WEL have not only been detected on the surface of engineering components after they have been removed from their service environments, but also after manufacturing processes, for example, after reaming /Turley 1975/, drilling /Field 1970/, grinding /Field 1970/, impact loading /Glenn 1971/, after strong torsion /Lindholm 1974/, shear loads /Wingrove 1971/ and so on. There have been a series of hypotheses developed to explain the structure of WEL.

In the 1950’s and early 1960’s, quite a lot of work has already been done to study the mechanism of WEL formation and structure of the WEL. /Kuznetsov 1963/ found that the white layer preserves its hardness and is non - etchable when heated up to 700 ~ 800°C on mild steel with 0.09 - 0.18% C, that is subjected to friction at a speed of 10 - 16 m/s using a constant supply of machine oil. Using X - ray diffraction and metallographic analysis /Kuznetsov 1963/ surmised that the structure of the unetchable WEL is a carbide, part of which would be disintegrated with the formation

of graphite. The most probable source of carbon is the oil which decomposed as a result of the heating. /Kuznetsov 1963/ emphasized that all processes which take place in the surface layer under friction promote an increase in the rate of diffusion. This opinion is in accordance with the result that /Rogers 1971/ has present on the scuffing in diesel engines.

However, at the same time /Grozin 1962/ deduced a different theory that the thermal process due to friction or plastic deformation dominates the formation of the white layer. The low susceptibility to etching of white layers of thermal origin is apparently due to the high degree of dispersion of the phases and the lack of homogeneity of the structure, single adjacent micro - crystals differ only slightly from each other in chemical composition and structure and may even have a common crystal lattice. For this reason the etching agent can not form electrochemical micro - cells with large potential difference. And the high degree of dispersion inhibits plastic deformation thereby increasing the hardness of the layer. Additionally he summarized the previous relevant work and found out at that time, that though all kinds of WEL seem to be the same under the optical microscope, the white layers differ markedly, both, in structure and phase composition. The structure of each WEL depends upon how it is formed, on the materials involved and on the environment. /Grozin 1962/ has summarized the previous relevant work and divided the hypotheses about the structure of WEL into seven types as follows:

The white etching layers may contain

1) Martensite or

2) Austenite - martensite, saturated with nitrogen and carbon or

3) Ferrite - martensite or

4) Austenite - martensite with tempered martensite or

5) Ferrite – cementite or

6) Carbides (chromium carbide) or

7) Layers of precipitated non - carburizing elements.

Some of these theories presumed that the structure of the WELs is martensite. It purposely accounts for the extraordinary high hardness, one of the typical and basic features of WEL. This theory coincides well with the current theory that the friction

induces the martensitic transformation given by /Schmidt 1987/. The results of /Newcomb 1984/ also indicate a martensitic structure formed at the wheel - rail contact zone, but, the author excludes high temperatures as the only reason by means of the transmission electron microscope.

Later /Scott 1973/ has observed WEL near the surface in used, hardened and tempered roller bearings. /Scott 1973/ suggested that these structures are the result of temperature flashes and rapid cooling producing a stable martensitic structure of extremely small cell size.

But, /Eyre 1972/ carried out studies on rubbing surfaces and explained that the white layer as a fine dispersion of second phase particles pinning an extremely fine crystallite structure. He emphasized the function of the second phase particles strongly.

Later /Turley1975/ examined the white etching layer on a reamed hole in an ultra - high strength steel. Transmission electron microscope examination of layers revealed that the WEL is produced by intensive plastic deformation. He indicated that the layers had a fine subgrain structure which was body - centered - cubic and that there was a general loss of carbides within the layers owing to the heating effect or the theory of /Wilson 1957/ which says that the carbides in tempered steels dissolve in the plastically deformed area adjacent to hardened indentation.

More recently /Feller 1991/ ascertained by means of TEM investigation that the white layer appears to be not martensite, but instead finely divided cementite.

In order to explain the role of the atmosphere in wear /Kawamoto 1971/ conducted a comparative investigation of wear in vacuum and in air. /Kawamoto 1971/ suggested that the white etching layer appears to be generated through rapid solidification and cooling of the molten region accompanied by severe deformation and that the reaction between atmospheric nitrogen and the sliding surface is not the principal factor causing the formation of the hard layer. It is concluded that the white etching layers are composed of ferrite, austenite, martensite and free cementite. However, the studies of /Kawamoto 1971/ are in complete disagreement with the results of /Torrance 1974/ that nitrogen dissolving has accounted for the formation of the hard white layer.

With respect to the white etching layer on the rail - wheel system, there are only few publications available. /Baumann 1998/ made a systematic study of the structure and the properties of the white layer specifically on rails. Two kinds of samples, which own clearly continuous riffle bands and white etching layers were studied. X - ray diffraction, thermal analyses, REM and TEM were used to determine the structure of the white band. /Baumann 1998/ concluded that the WEL is a nanocrystallite structure with 20 nm grain size. He regarded the nanocrystalline structure as the reason that the WEL seems to be featureless under the optical microscope and as the reason that the WEL has an extraordinary corrosion resistance. Using X - ray diffraction no carbide reflections were visible in the spectrum, so the carbides in the bulk pearlite seemed to be dissolved. This possibility was ascertained by a simulation experiment, which revealed that the Fe_3C disappeared after 70 h grinding of a mixture of Fe_3C and Fe. This was further proven by thermal analysis which showed that in the ground nanocrystalline material carbides precipitated during heat treatment. /Baumann[1] 1996/ suggested that the extremely high deformation and shear stress induced the solution of the cementite and the diffusion of the carbon. Using SEM /Baumann[1] 1996/ found that the WEL consisted of several layers, indicating that the white layer is formed gradually and that the structure of different layers may not be the same. The existence of retained austenite indicated that the formation temperature of the WEL is higher than 800°C. It is the first time that the theory of the formation of a nanocrystalline material was applied to the microstructure changes on the surface of the rail. More recently /Rooch 2000/ supposed that pearlite colonies are dissolved just beneath the surface of the rails as a result of very heavy plastic deformation, forming a nanocrystalline microstructure of ferrite containing small amounts of cementite. It is also stated that partial transformation of the nanocrystalline microstructure to martensite was observed.

In other friction systems it is already a well established phenomenon that sliding of metals can produce a nanocrystalline layer on the surface of one or both of the sliding components. The thickness of this layer depends on the metal system used and on the conditions of sliding. Typically the layer is about 1 µm thick /Ganapathi 1991/. Tensile tests of nanocrystalline metals have shown that they are strong, but, brittle /Agnew 2000/.

Thus, a lot of studies have aimed at trying to discover the composition, structure, essence and mechanism of the WEL and lots of hypotheses were built up, but an unanimous satisfactory explanation of the WEL structure and its formation so far has not been reached.

3. Objectives and Methodology

3.1 Objectives

The aim of this thesis is a study of the microstructure transformations, the texture and the residual stress formation that is induced by rolling contact friction and wear in the rail - wheel tribo - system.

By studying the surface changes on several pieces of rail and wheel samples that underwent different loading while being in service, the relationship between load strength and the induced microstructure changes, residual stress and texture evolution shall be clarified.

3.2 Methodology

Four pieces of rail samples and a piece of an ICE wheel sample were chosen for an analyses of the surface changes in the rail – wheel contact. A multitude of different experiments were carried out in order to analyze the microstructure changes at the surface and the near - surface region of the samples and, thus, to contribute to the understanding of the complex rail – wheel rolling contact system.

Analyses of Structure Changes at Micro Level
Optical Microscope and Scanning Electron Microscope were employed to determine the phase changes and topography of the rolling surface on different resolution levels.

X - ray diffraction methods, using both conventional X - rays and synchrotron radiation were used to analyze the phase composition of the material, its domain size and micro - strain. The volume amount and size of small particles was studied by synchrotron small angle scattering experiments.

The combination of microscope, conventional X - rays and synchrotron radiation was intended for analyzing the sample in different depths and with different spatial resolutions.

Texture and Residual Stress Analyses

The texture and the residual stress were analyzed by X - ray diffraction methods. Analyzes were not only confined to the surface but also performed in different distances below the surface.

Texture analysis provides quantitative information about the orientation distribution of crystallites on the samples. The texture induced by plastic deformation reveals the deformation mechanism during rolling contact. Therefore, texture analyses were performed on both the rail and the wheel samples.

Residual stress analysis shows the residual stress distributions on the sample surfaces and in the near - surface area. This information contributes to the determination of the formation mechanisms of the WEL.

Corrosion Tests

The high corrosion resistance is a typical feature of the White Etching Layer (WEL), that usually appears on the top surface layer of the railway. Here corrosion experiments were performed in order to investigate how the WEL reacts to acid solution trying to analyze the homogeneity of the WEL.

4. Experimental details

4.1 Samples

4.1.1 Rail samples

Four pieces of worn rail samples supplied by different companies and institutes were taken for the present investigations, each of the rails underwent different loading characteristics during service.

The weak loaded rail sample was supplied by Dr. Grohmann of Deutsche Bahn AG. A rail piece is shown in Fig. 4.1. Its service parameters are given in Table 4.1. Here, this rail is denoted as rail DB AG. The center of the rolling surface marked on the rail DB AG in the photo is used as a reference line. Any distance adverted to the rail DB AG is the relative distance to this reference line.

Another weak loaded rail was marked as rail Baumann. Several pieces of this rail are used in this thesis and one exemplary sample of this rail is shown in Fig. 4.2. The service conditions of the rail are supplied in Table 4.2, more details can be found in /Baumann 1998/.

The other two stronger loaded rail samples, provided by the Institute for Mechanics of TU München, were termed respectively as rail sample 2 (Fig. 4.3) and rail sample 3 (Fig. 4.4). The service parameters of these rails are listed in Table 4.3.

The lines indicated on the surface of the rail Baumann, rail sample 2 and 3 in the pictures are used as reference lines. Any distance mentioned in the following is the relative distance to this reference line.

The compositions of the rail DB AG and the rail Baumann listed in Table 4.5 were determined by spectrometry in the Institut für Gießereitechnik GmbH. The compositions of rail sample 2 and 3 shown in Table 4.5 were given by the Institute for Mechanics of TU München.

4.1.2 Wheel sample

One piece of a wheel - set was supplied by Deutsche Bahn AG (Fig. 4.5). It has been in service between Berlin and München. The maximum speed of the train using this wheel was 200 km/h. The wheel - set sample was cut from an ICE wheel using cooling oil and a low cutting velocity. For the sake of convenience of the measurements the flange of the wheel was cut down. The composition of the wheel material is shown in Table 4.4. The wheel material is quite similar to the rail steel in composition, but the wheel steel allows higher limits for the impurity elements phosphor and sulphur.

4.2 Metallography and Microscope

4.2.1 Optical Microscope and Scanning Electron Microscope

The samples were ground on SiC - paper from 100 grit to 1000 grit, after that they were polished carefully with diamond - paper down to a diamond size 1 µm. Afterwards the sample were etched with 3% HNO_3 - alcohol solution for visualizing the different phases.

The microstructures were observed under an optical microscope in the bright field mode. The photos were saved in digital form.

Scanning Electron Microscope served to determine the phase and topological structure with high resolution.

4.2.2 Determination of Microhardness Values

The microhardness tests was performed using an automatic microhardness tester. According to the rail material, medium carbon steel, 200 p (2 N, HV 0,2) and 10 p (98,07 mN, HV 0,01) were chosen to determine Vickers hardness using a holding time up to 15 s. A standard sample was used to define the experiment error.

4.2.3 WDX Analyses

The samples used for Wavelength Dispersive X - ray Analyses (WDX) were polished till 1 µm and cleaned with ethanol. The concentrations of three element C, O, N were measured. The samples were measured from the surface into a depth of 50 µm using 1 µm intervals.

WDX analyses were conducted at the Zentraleinrichtung für Mikroskopie at the TU - Berlin. Electronbeam microprobe Camebax Xmasplus was used to determine the composition changes. The measurement time was 20 seconds for each point. Beam size was 0.2 µm and the irradiated area is 1,5 µm $\times$ 2 µm $\times$ 1,5 µm. The resolution of the apparatus for determining the element concentration is 0.1 ~ 0.2% for 20 s exposure time.

4.3 Anomalous Small Angle Scattering

Small – angle scattering of X - ray is a widely used method for studying the structure of matter /Feigin 1987, Guinier 1955/. Fig. 4.6 shows the principle of the small angle scattering experiment. Monochromatic X – rays are elastic scattered by the structure inhomogeneities of a sample. A scattering curve containing the structure information is exactly measured as a function of the scattering vector $q = k - k'$.

At the diffractometer B1 in HASYLAB microstructure inhomogeneities ranging from 1 nm to 100 nm can be determined /Haubold1987/.

In this thesis, Anomalous Small Angle Scattering is used to analyze the size and distribution of the carbides in the top layer of the railway sample. Using this technique, the scattering data produced by the carbides was separated from those associated with voids or surface roughness by means of varied scattering contrast. An introduction and applications of ASAXS are presented in detail e.g. in /Haubold 1988, Goerigk 1997, Goerigk 1998, Goerigk 2001/.

The samples were taken directly from different areas of the top layer of railway. They were polished from the inside leaving the top layer surface untouched. SiC - paper up to 4000 grit was used in order to get a small surface roughness. The samples were ground to less than 35 µm thickness, which is a thickness favorable for the transmission experiment.

Five energies (6840 eV, 7014 eV, 7074 eV, 7098 eV, 7106 eV) were used. A position - sensitive two - dimensional detector was used to measure the intensity distribution of the scattered synchrotron X - ray in the different positions. Two geometries (935mm and 3635mm) were used to get scattering vector *q* between 10^{-2} nm^{-1} and 1 nm^{-1}.

A menu – oriented software was used for the data processing with the possibility of an optional remote log – in via the telnet network. The data received from the two - dimensional detector was normalized and integrated, then transformed into one dimensional data. After that, the separated scattering curve was simulated assuming a log - normal size distribution of the carbides.

4.4 Diffraction Methods

4.4.1 Phase and Microstructure Analysis

The existing phases in the sample can be determined from the angle and the intensity of the reflection peak in the diffraction diagram. Furthermore, the phase volume can also be determined quantitatively, for example the content of the retained austenite. The crystallite structure can be ascertained by analyzing the reflection pattern.

Determination of Retained Austenite

Synchrotron X - rays were used in order to determine quantitatively the volume of retained austenite. The basic principles of retained austenite determination are presented in detail, e.g. in /Birwirth 1961/ and /Faninger 1972/.

The analysis of retained austenite was conducted at the diffractometer G3, at Hasylab of DESY, Hamburg /Wroblewski 2000/. A radiation with an energy of 6,5 keV ($\lambda \approx 0.1907$ nm) was employed, thus, the penetration depth is roughly 6.1 µm. A small slit collimator of 2×2 mm was used for the location of different positions on the surface of the samples. The diffraction angle 2θ was scanned in the range from 45^0 to 130^0 in order to obtain the X - ray diffraction diagram. A small scanning pace of 0.05^0 with 4000 monitor seconds was used. By determining the

intensity of the peaks of the ferrite / martensite and the austenite, the content of retained austenite was calculated using the equations supplied by /Willbrand 1966/.

Phase Determination by High Resolution X - ray Image Scan

This is an entirely novel technique detecting the local microstructure alterations in a relatively big region of interest by means of synchrotron X - ray diffraction. This technique allows the registration of spectra with a very high local resolution and selects the probed region not in the incoming, but in the diffracted beam /Wroblewski 2000, Wild 2000/. The maximum illuminated area can be up to 10 mm x 10 mm. An array of parallel tubes, a so called micro - channel plate (MCP), is situated in front of a Position Sensitive Detector (PSD). The tubes reduce the crossfire of the radiation scattered from different regions of the specimen (Fig. 4.7). Only the scattered radiation parallel to the micro – channel plane (MCP) can reach the detector, thus, yielding an entire image of the probed sample region. The channels also define the scattering angle 2θ. The arrangement of MCP and PSD is mounted on the 2θ - θ arm of the diffractometer (Fig. 4.8). By means of scanning the reflections of the different phases, the position where the phase is situated within the illuminated region can be defined.

Therefore, this method was used to determine the distribution of martensite and austenite in the white layer of rail samples.

c_m / a_m Ratio and Soluted Carbon Content in Martensite

Martensite has a body centered tetragonal structure. The c_m / a_m ratio denotes the tetragonal distortion of the martensite that is induced by the dissolving of carbon atoms. Here, the 200 reflection of martensite was chosen for obtaining the c_m / a_m ratio. The experiments were carried out at Hasylab, Hamburg, employing synchrotron X - ray radiation. The diffraction angle 2θ was scanned from 71^0 to 81^0 with a scanning interval of 0.05^0.

Since martensite has a tetragonal structure, the 200 reflection profile has an asymmetric shape. The profile can be separated into two reflection curves using Voigt functions. Using the 2θ value of each reflection according to Bragg's law, the

lattice spacings c_m, a_m could be determined. Then, the dissolved carbon content was determined employing the function introduced in /Vöhringer 1977/.

4.4.2 Profile Analysis

By means of analyzing the shape of the reflection profile, the average micro - strain and domain size can be determined. Many different theories and ways to profile analysis were published in the last dozens of years /Williamson 1954, William1963, Groma 1988, Ungar 1989/. A single line method developed by /Delhez 1982/, was used in this thesis. The domain size and strain were determined in terms of integral breadth and full width at half maximum. The broadening of the diffraction profile is attributed not only to the domain size, but also to the microstrain. The profile broadening due to the domain size distribution can be approximated by a Cauchy function, the microstrain induced broadening by a Gauss function.

First the reflection profiles were obtained using synchrontron X - radiation at the diffractometer G3, at Hasylab of DESY, Hamburg. Then they were fitted using a Voigt function and afterwards they were deconvoluted into their Cauchy and their Gauss components. As a result the domain size and strain were determined according to /Delhez 1982/. A profile from a standard sample was used in order to reduce the broadening by the instrument aberration and the wavelength distribution.

In this thesis, the profiles of the 110 and the 200 reflections were measured by means of synchrotron radiation using a θ - 2 θ scan.

4.4.3 Texture Analyses

Texture analyses was performed using a conventional X - ray diffractometer with a position sensitive detector. A tube collimator with 2 mm diameter was utilized to confine the primary beam. Co Kα radiation (Wavelength λ = 1.77892Å) was used in order to reduce the fluorescence.

At least three pole figures were measured. For each reflection, the attached sample was tilted between 0^0 to 75^0 (ψ?angle) and at each tilt it was rotated from 0° up to 360^0 with 10^0 steps (φ?angle). Then from the collected maximum intensity of three reflections at every referred measuring direction, the quantitative information about

the orientation distribution, texture, is statistically discerned /Bunge 1985, Wegener 2001/. In this thesis pole figures of the 111, 211, 200 reflections were measured for marteniste / ferrite texture determination and 110, 100, 311 reflections for austenite texture determination. The orientation distribution function then was calculated using Bunge's methods /Bunge 1985, Bunge 1988/.

Texture analyses were performed on the rail and the wheel samples. By subsequent electrolytic etching and X - ray analyses, the in - depth distribution of the texture was determined.

4.4.4 Residual Stress Analysis

Residual stress determination was conducted on a conventional X - ray diffractometer using CoKα radiation (wavelength λ = 1.78892Å). A position sensitive detector was applied and a tube collimator with 1 mm res. 2 mm diameter were utilized in order to confine the primary beam. For residual stress analyses in the ferrite / marteniste, the 211 reflection was used. For residual stress analyses in the austenite, the 220 reflection was employed. Measurements were performed over a range of several $\pm\psi$ angles usually (63.4^0, 50.78^0, 39.2^0, 26.6^0, 0^0) at the res. φ angles. Thus, the lattice spacing "d" at all nine ψ?angles were determined and the residual stress values were calculated using the $\sin^2\psi$?method /Macherauch 1961, Noyan 1987/. The principal stress tensor and the direction of the principal stress were further determined by analyzing the residual stress in 3 φ ?directions (0^0, 45^0, 90^0).

The residual stress distributions on the rail samples and wheel sample were analyzed both in longitudinal direction and in transverse direction. The in - depth distribution of residual stresses was also studied up to 400 µm below the sample surface by subsequent electrolytic etching and X - ray analyses. The principal stress tensor along the sample surface was also calculated for the rail and wheel samples /Genzel 1999, Wild 2001/.

4.5 Profilometer Measurements

Surface profile determination was conducted at the Institut für Mechanik at the TU - Berlin. An optical interference spectrometer scanner with a white light microscope was used.

The height resolution of the apparatus used is 0,02 µm and the lateral resolution is 0,5 µm. The studied area amounts to 761 x 594 µm² under 10× magnification and 383 x 298 µm² under 20× magnification. 304 x 228 Pixels are measured at one time. For each measurement a new calibration is necessary. The data containing the information about the relative height difference was then transformed into a visual topography picture of the detected area.

Surface profiles were determined in different regions on the surface of rail Baumann.

4.6 Corrosion Tests

The potentiodynamic anodic current density – potential curve /ASTM G5 - 87/ was applied for analyzing the corrosion behavior of the white etching layers on the rail.

A saturated calomel electrode was connected with a test cell by a Luggin capillary using an electrolyte bridge. A closed solution – wet stopper was used in the bridge for the purpose of avoiding siphonage. The current density was normalized to 1cm^2 unit area. Prior to the immersion of the sample, hydrogen was bubbled into the solution for 30 min in order to reduce the oxygen. A 3% H_2SO_4 solution in distilled water (ph = 6) was used for the corrosion analysis.

In order to protect the bulk material and get information only from the interesting region of sample, the rail sample was varnished by vinyles in a solvent mixture containing xylene that can not react with the electrolyte.

5 Results

In the following paragraphs the result of the studies on the rail samples and wheel sample are presented, starting with the changes of the rail microstructure and topography. After that the results of the texture and the residual stress analyses are presented.

5.1 Microstructure Changes and Changes of Topography

5.1.1 Rail Samples

5.1.1.1Rail DB AG

Microstructure Analysis by Microscope and Microhardness Measurement

The rail DB AG (Fig 4.1) is one of two weakly loaded rails investigated in this thesis. On this rail a bright band consisting of white etching layers is present on the rolling surface. This WEL band appears on the bright shining rolling surface within those areas which were subjected to the strongest loading.

Optical microscope on the rail cross - section reveals the white etching layers on the surface (Fig. 5.1.1). At low magnification the white etching layer shows its characteristic homogeneous structure as reported previously by /Grotzin 1962, Pyzalla[1-2] 2000/. It is visible that the white etching layer is not present over the entire upper surface of the rail and that the white etching layers do not have a uniform thickness. Individual white etching layers have the shape of half an ellipse. Several adjacent white etching layers subsequently grow together to form larger WEL areas. Similar WELs were also found on the other rail samples. Beneath the white etching layers the microstructure of the rail steel is the typical microstructure of a medium carbon steel consisting of pearlite (ferrite plus cementite). There is an obvious sharp transition between the white layer and the base metal. Within the upper part of the white etching layer some short cracks are visible. Other cracks transmit the whole WEL and sometimes propagate directly into the bulk material.

Fig. 5.1.2 shows the distribution of the microhardness along line 1, through point 1 and point 4, of the rail DB AG. From the gauge corner towards the field corner of the rail, the microhardness increases gradually. The maximum microhardness values of more than 1000 HV 0,2 are reached on the field corner of the rolling surface. These micro-hardness values are nearly three times as high as those of the bulk material (295 HV 0,2). On the rolling surface the microhardness is not homogeneous which indicates that there are microstructure inhomogeneities present across the rolling surface.

Fig. 5.1.3 shows the microhardness distribution in the in - depth direction at the gauge corner of the rail. There is no white etching layer formed, but a plastically deformed layer can be seen directly under the surface. From the surface to a depth of 500µm below the rail surface, the microhardness varies slightly and randomly between 430 HV 0,2 and 320 HV 0,2.

Fig. 5.1.4 - a and - b reveals the microhardness distribution below the rolling surface in the in - depth direction. The microhardness decreases abruptly in the in - depth direction. On the surface, the maximum of the microhardness is determined to be over 1000 HV 0,2, while in a depth of 70 µm below the rail surface the microhardness has decreased to nearly the same level as the bulk material (295 HV 0,2). This result is different from that at the gauge corner of the rail.

Microstructure Analysis by Diffraction Methods

The microstructure on the rolling surface of the rails was studied using medium energy synchrotron radiation. Fig. 5.1.5 shows the profile of the 200 reflection along line 1 through point 1 and point 4. At the very left and at the very right side of the rail near point 1 and point 4 the profile of the 200 reflection is symmetric and has a very narrow full width at half maximum (FWHM). In contrast to the reflection profiles at point 1 and point 4 the reflection profiles obtained between point 2 and point 3 on the rolling surface are distinctly asymmetric and extraordinarily broad. These reflection profiles contain two individual reflections, which belong to the 200 and 002 reflection of the martensite lattice. The tetragonal distortion of the cubic structure results in a bigger lattice distance c_m than a_m, so that the diffraction angle of the 002 lattice plane is smaller than the reflection angle of the 200 and 020 lattice plane and, thus, an

asymmetry of the reflection profile exists. This means that martensite evolves on the rolling surface of the rail DB AG.

Further, the structure changes in the in - depth direction were studied. Fig. 5.1.6 shows the 200 reflection profile changes in the in - depth direction in the region of the rolling surface of rail DB AG, shown in Fig. 4.1 by a small white square. From the rail surface into a depth of over 12 µm below the rail surface, the profile of the 200 reflection shows an asymmetric shape. But, with increasing distance to the surface the asymmetry of the 200 reflection decreases and below a depth of 12 µm the reflection profile becomes symmetric.

A more detailed study of the 200 / 002 reflection along the rail surface revealed the c_m / a_m ratio distribution along line 1 through point 1 to point 4 (Fig. 5.1.7). It is obvious that the asymmetry of the reflection gradually increases with increasing loading of the rail from its gauge corner towards the field corner. At the field corner of the rail sample, the c_m / a_m ratio of the martensite reaches 1.06. According to the correlation between c_m / a_m ratio and the solute carbon content given in /Vöhringer1977/, the solute carbon content of the martensite was calculated. Fig. 5.1.8 shows the distribution of the solute carbon concentration along line 1 (point 1 to 4) and as well as along line 7 containing point 7 on the rail DB AG. On the rolling surface the solute carbon content tends to increase gradually from the inner towards the field corner of the rail sample. The maximum solute carbon content amounts to 0.2% on the rolling surface near the field corner of the rail. Thus, approximately one - third of the average carbon concentration of the steel is soluted in the martensite.

Besides the ferrite / martensite reflections also austenite reflections appear in the diffraction spectra on part of the rail DB AG. The retained austenite was found in the vicinity of point 7. In the photograph of the rail surface point 7 appears darker than the other areas of the rail. Retained austenite was also found on the field corner of the rolling surface. Fig. 5.1.9 and Fig. 5.1.10 show the retained austenite content present along line 1 and line 7 on the rail DB AG. Along line 7, the maximum of the retained austenite appears at point 7. However, along line 1 through point 1 to point 4, only on the field corner of the rolling surface retained austenite was discovered. The retained austenite content in this area is about $4{,}5 \pm 1\%$.

In addition, the distribution of retained austenite in the in – depth direction below the rolling surface is shown in Fig. 5.1.11. From the surface into a depth of 10 µm, the retained austenite decreases from 4,5 % to 2,9 %. In larger distances to the rail surface, the content of retained austenite is not sufficient to be determined quantitatively, hence it is lower than 2%.

Fig. 5.1.12 and Fig. 5.1.13 are X - ray images which reveal local structure changes on the surface of the rail DB AG even more pronounced than the diffraction spectra obtained at those points of the rail chosen so far.

The eigenbild of the 211 reflection obtained reveals again the martensitic spots in the perlite bulk material on the rolling surface of the rail. The contour shown in the photographs can be identified by the corresponding X - ray images. In Fig. 5.1.12 - d the symmetric profile of 211 reflection denoted with solid symbol originates from the ferrite / pearlite base material and proves that the gray region in the photograph has a ferrite / pearlite structure. The asymmetric profile of the 211 reflection denoted with a hollow symbol indicates a tetragonal distortion of the ferrite lattice and identifies the dark region in the photograph as martensite. In Fig. 5.1.13 - d the reflection profile with solid symbols reveals the dark area as ferrite and martensite and the reflection profile denoted with hollow symbols reveals that the yellow area is retained austenite. The austenite is situated within the region which contains the tetragonal martensite. The slight distortion of the X - ray image relative to the photograph is caused by the detector being not exactly in the $\theta - 2\theta$ geometry, which is caused by the construction of the instrument.

Fig. 5.1.14 reveals the distribution of the domain size on the rolling surface between point 2 and 3 of the rail DB AG. In those areas where the white etching layer is present on the rolling surface of the rail sample, the domain size has its smallest values of 20 nm. In the dark, strongly corroded area, point 4, the domain size is larger than 60 nm.

ASAXS Investigations of Particles Size Distribution

Using Anomalous Small Angle X - ray Scattering (ASAXS), the distribution of the carbide size on the corrugated surface of the rail DB AG were investigated. Fig. 5.1.15 shows one exemplary separated scattering curve after subtracting

fluorescence and background. The dotted lines are fitted by a solid line which was calculated under the assumption that carbides are spherically shaped and have a log - normal size distribution. In area 1, at the very left side of the rail, the size of the carbides is beyond the resolution of the Jusifa spectrometer, thus the carbide size is larger than 100 nm. In area 2 on the left side of the rail there are two kinds of carbide in different size. One of them has a radius of app. 5 nm with a broader distribution range and the other one has a radius of app. 20nm in a small amount (Fig. 5.1.16). While on the rolling surface, in area 3, one carbide size with 2 nm radius with a relative narrow distribution range was found, and the second kind of carbide size with 9nm radius in a small amount was also discovered (Fig. 5.1.16).

5.1.1.2 Rail Baumann

Topography

Especially on rail Baumann (Fig. 4.2), it is clearly visible that separate white etching layer patches are regularly distributed in regular distances. Fig. 5.1.17 to Fig. 5.1.21 show the surface topography profiles obtained on the corrugated surface of rail Baumann.

Fig. 5.1.17 shows the topography profile in the area “riffle hill”, a white layer patch, at x = 0 – 12 mm and y = 20 mm obtained a magnification of x 10. The width of the measurement area transverse to the rolling direction is ?y = 594 µm. Thus, every pixel represents the information from an area ?x = 2.5 µm and ?y = 2.6 µm. In the white etching layer patch it can be seen that the surface consists of many clefts, where even small holes with 0.2 µm diameter are present. A so - called “riffle hill” with a relative altitude of 9 µm in the region of x = 0 ~ 12 mm is also present.

In Fig 5.1.18 in the area of x = 12 ~ 24 mm, a transition from riffle hill to riffle valley is visible. Further a hole with a depth of 0.6 µm in this area is obvious.

The measurement in Fig. 5.1.19 to Fig. 5.1.21 in region of y = 10 mm was performed with a magnification of x 20. The width of the measurement area transverse to the rolling direction is ?y = 298 µm. Thus, every pixel represents the information from an area ?x = 1.26 µm and ?y = 1.31 µm.

With a higher magnification, obviously a hole with a diameter of 0.05 mm can be observed on the sample surface. The hole has a depth of more than 20µm in (Fig. 5.1.20), x = 8.0 – 9.5 mm

Fig. 5.1.19 shows a small riffle hill at y = 10 mm. The profile is horizontal and from x = 5.5 mm a tendency to decline comes into sight. A number of small hills and valleys with an altitude of 2 µm can be identified. Additionally several isolated holes with a diameter of 0.15 mm and depth 4 µm are visible.

As in Fig. 5.1.19, also a lot of small holes are seen in Fig. 5.1.20. In the region between x = 8.0 to 9.5 mm is there a very big hole. The diameter amounts to 1.5 mm with a depth to 20 µm. The further profile altitude goes downhill with an altitude difference of 5 µm.

Fig. 5.1.21 displays the right side of a riffle valley between two riffle hills. There is a inclination of 3 µm in the region of x = 21.35 – 23 mm. The remaining profile is horizontal. Several small holes can be seen.

Fig. 5.1.22 shows the corresponding distributions of the microhardness in this “riffle hill”. In the highest region x = 3 mm, the microhardness reaches its maximum, over 1000 HV 0,2, which indicates the existence of the White Etching Layer under the surface.

Thus, the profiles obtained on the rail surface clearly reveal that the bright area are “riffle hills” with a high altitude while the gray dark corroded areas are the “riffle valleys”. The white etching layers as well as the riffle valleys contain holes. Additionally the white etching layer was usually found in the area with a high altitude.

Microstructure Analysis by Microscope and Microhardness Measurements

Fig. 5.1.23 show optical microscope images of the cross - section of the rail Baumann. The white layers can be clearly identified. As observed on the other rails, the white etching layers do not have a unique thickness and it varies between 5 µm to 60 µm approximately. The elliptical shape of the white layer can again be identified. It is visible that two half elliptical WEL grow together and form a bigger WEL area (Fig. 5.1.23). Again a sharp transition between the white etching layer and the deformed layer beneath it is obvious. Within the white etching layer some spalling is found.

Especially on the rail Baumann, the ferrite boundary was found even within the white etching layer. The remaining ferrite boundary was depicted more clearly in the large magnification (Fig. 5.1.24 a and b). They went through the white etching layer and extended to the top surface. Some of the ferrite boundaries were still connected with the bulk materials and some of them has already been broken up. Using SEM, the breaking - up of the carbide was observed in a sharp transition region from the WEL to the pearlite structure(Fig. 5.1.25).

In a depth of about 0.2 mm beneath the surface the deformed structure seems to have been rolled and a rolling direction is visible in the image obtained by optical microscope. In a depth of more than 1 mm below the rail surface deformation has ceased and the structure of the original material is visible.

Fig. 5.1.27 displays the microhardness distribution on the surface of a piece of rail Baumann shown in Fig. 5.1.26. The coordinate system depicted in Fig. 5.1.27 corresponds to that in Fig. 5.1.26. The microhardness is measured in an interval of ?x = 5 mm and ?y = 2.5 mm. On the surface the average of the microhardness is 315 HV 0,2. In the bright area, the riffle hills, at y = 5 - 20 mm and at x = 0 - 30mm, the microhardness increases and two localized maximum of over 1000 HV 0,2 is present. The martensitic structure revealed by high microhardness stands in corresponding bright patches in Fig. 5.26. The maximum microhardness is nearly twice as high as the microhardness of conventional quenched martensite, similar to the microhardness determined in the WEL on rail DB AG.

Fig. 5.1.28 - a shows the microhardness distribution within the WEL below the rail surface of the rail Baumann. The microhardness in the WEL beneath the surface reaches up to 900 HV 0,2. Below the white etching layer the microhardness decreases to about 340 HV 0,2. But it is higher than the microhardness in the bulk material, in a distance of 3 mm below the surface, 297 HV 0,2. Fig. 5.1.28 – b displays a SEM picture of the region just below WEL. Obviously it was merely weakly deformed.

In contrast, the microhardness below the surface in a region without WEL shown in Fig. 5.1.29 - a has a different distribution. There is no sudden rise or drop of the microhardness in the in - depth direction. The microhardness value varies slightly

from 320 HV 0,2 to 280 HV 0,2. A SEM picture of this region was presented in Fig. 5.1.29 – b.

Microstructure Analysis by Diffraction Methods

In Fig. 5.1.30 - a a photograph of the surface region of rail Baumann is shown. Fig. 5.1.30 - b presents the corresponding X - ray image. Fig. 5.1.30 - c is the sum profile of the 200 reflection of martensite res. ferrite. The differences between these two reflection profiles reveals that martensite is formed in the white layer. The reflection profiles in Fig. 5.1.30 - c show again that the symmetric 200 reflection represents the bulk material which is the dark area in Fig. 5.1.30 - b, and that the asymmetric 200 reflection profile indicating martensite evolves in the bright region. In this spot the martensite does not contain retained austenite.

Fig. 5.1.31 shows another X - ray image obtained for a smaller white layer patch on the rail Baumann. Fig. 5.1.31 - b shows the photograph of this region. Fig. 5.1.31 - a and Fig. 5.1.31 - c show the corresponding X - ray images of ferrite / martensite and austenite. Fig. 5.1.31 - d and Fig. 5.1.31 - e present the sum profiles from the X - ray image of the different phases.

In the X - ray image (Fig. 5.1.31 – a) the region containing the white patch and the other material were separated. The spectrum coming from ferrite, bulk material, is a symmetric reflection. For the white patch the reflection is asymmetric and, thus, clearly it indicates that the structure is martensite. Fig. 5.1.31 - e shows the sum profile of the austenite 220 reflection corresponding to the area studied, the martensite also does not contain retained austenite in this region. That is different from the situation on the surface of rail DB AG.

Fig. 5.1.32 and Fig. 5.1.33 present the distribution of the c_m / a_m ratio and the solute carbon concentration across the surface of the rail Baumann. In the picture the two riffle hills on the rail Baumann surface shown in Fig. 4.2 are present. The maximum of the solute carbon in the WEL reaches up to 0.26%.

Fig. 5.1.34 shows the distribution of the domain size along the surface of rail Baumann. On the “riffle hill” the domain size becomes smaller, 3 nm. Out of this area the domain size reaches up to 100 nm.

Fig. 5.1.35. to Fig. 5.1.36 show the microprobe profile analyses in an area with WEL and in an area without WEL. From the very surface into a depth of 50 µm, the X - ray intensity of nitrogen appears to be nearly the same as background intensity, thus, no nitrogen enrichment was found in this sample both in the area of the WEL and in those areas without WEL. Also no obvious intensity changes in the depth - profile was seen for carbon in two areas investigated. Thus, no decarburization was found at the surface of rail, neither in the regions with WEL nor in the regions without WEL. Further, there are no significant differences in the volume amount of any of the elements between the surface and the bulk of rail. The sudden rise of the element Oxygen and the decrease of the element iron in Fig. 5.3.35 is probably due to the remaining dirty flecks during the sample treatments or due to an oxide particle.

Table 4.5 shows the alterations of 200 reflection profile of samples containing WEL that were annealed at different temperatures and for different annealing times. When the sample was annealed at 100 °C, with prolonging annealing time, the 200 reflection profile that is asymmetric originally becomes symmetric due to the precipitation of the carbide from martensite. With increasing annealing temperature from 100 °C to 700 °C, carbide reflections were found in diffraction diagram. On the other hand the symmetric 200 reflection profile becomes narrow and hence has a very small FWHM. This is due to the structure recovery in higher annealing temperature. Fig. 5.1.37 shows exemplary 200 reflection profiles before and after the annealing.

ASAXS Investigations of Particles Size Distribution

Fig. 5.1.38 shows the distribution of carbide particle size on the riffle hill of the rail Baumann. The carbide distribution was determined by ASAXS. In the area “riffle hill”, the white layer patch marked by a white square box, the average carbide radius is determined to be 1 nm. Within the area “riffle valley”, the carbide size is beyond the resolution of the apparatus JUSIFA in Hasylab, 1 nm – 100 nm, and can not be determined quantitatively, thus in the area of riffle valley the existing of big carbide particles > 100 nm is supposed.

5.1.1.3 Rail Sample 2 and Rail Sample 3

Microstructure Analysis by Microscope

Fig. 4.3 and Fig. 4.4 present photographs of rail sample 2 and rail sample 3. These rails have different head profiles from rail DB AG and rail Baumann. Although the rail surfaces are severely corroded, the trace of the wear process can also be identified on the rail tread of these two rails.

The presence of grooves is obvious on both rails. Additionally, a wear scar in the longitudinal axis of the rail begins to develop at this stage. The WEL are situated on the field corner of the rail sample 3, which is taken from a curved section. On the rail sample 2, that is taken from a straight section, white etching layers were found not only at the field corner but also at the gauge corner. Thus, WELs were found in those positions prone to the larger stress induced by plastic deformation.

Fig. 5.1.39 and Fig. 5.1.40 show typical optical microscope photos of the cross – sections of rail sample 2 and rail sample 3. White layers are observed on the surface of both rail samples. Although the rail sample 2 and the rail sample 3 underwent very heavy loading in the service, the WEL was still found only in some regions, not overall the cross section of the samples. Some white layers are very thick, up to 50 – 60 µm and some of them are very thin, only with a thickness of approximately 10 µm. The structure of the white layer appears to be homogeneous under the optical microscope.

Scanning electron microscope reveals inhomogeneities in the white etching layers (Fig. 5.1.41). The white etching layer can be divided into at least two sub - layers. The top layer is much compacter than the bottom layer. In Fig. 5.1.42 spalling is visible in the top layer. The spalling induced further roughness of the rail surface and cracks are also observed in the white layer. The bottom layer seems to have a coarser structure. Under the bottom layer a sharp transition to the base material is visible. Adjacent to the WEL the deformed ferrite / pearlite in the base material flows in an angle of 45^0 to the surface line. The chemical composition of both rail steels is quite close to the eutectoid composition and, therefore, the bulk microstructure is almost entirely pearlite.

Fig. 5.1.43 and Fig. 5.1.44 shows the microhardness distribution in the in - depth direction for rail sample 2 and rail sample 3. The microhardness in the bulk materials for both rails is 297 HV 0,2. Within the white etching layer the microhardness is significantly higher, the maximum reaches up to 1000 HV 0,2 for the rail sample 2 and 1036 HV 0,2 for rail sample 3. Noticeably even within the white layer the micro-hardness value varies between 1036 HV 0,2 and 835 HV 0,2. Below the white etching layer, the microhardness drops abruptly to about 340 HV 0,2.

Microstructure Analysis by Diffraction Methods

Fig. 5.1.45 shows an X - ray high resolution image of the ferrite / martensite distribution on the surface of rail sample 2. Apparently the crystal lattice of the α - Fe is tetragonal distorted. The 211 reflection profile on the rolling surface is very broad and asymmetric compared to the reflection profile of the bulk material. In Fig.5.1.45 – b the asymmetric 211 reflection profile with the solid symbol representing martensite is shown. The martensite exists in the dark area visible in Fig. 5.1.45 - a. The symmetric 211 reflection profile with open symbol indicates the ferrite – pearlite, which appears as the gray area in Fig. 5.1.44 - a.

The X - ray image reveals that austenite is present in the martensitic region of the rail (Fig. 5.1.46). The sum profile of the austenite 220 reflection (with solid symbols) reveals that the retained austenite corresponds to the gray area in Fig. 5.1.46 - a. This is in good agreement with the results of previous investigations on the rail DB AG.

Fig. 5.1.47 and Fig. 5.1.48 reveal the distribution of the lattice distance c_M, a_M and the ratio c_M / a_M of the martensite at different positions along the marked lines across rail sample 2 and across the marked line on rail sample 3. The solute carbon concentration distributions along both samples have been calculated according to /Vöhringer1977/, and they are shown in Fig. 5.1.49. The carbon distributions reveals that the solute carbon concentration varies across the running surface of the rails. There is a tendency of increasing towards the field corner of the rails. The maximum of the solute carbon concentration reaches up to 0.37% on rail sample 2 and 0.4% on the rail sample 3. Thus, the tetragonal distortion of the martensite is much bigger in sample 2 and sample 3 than in the rail DB AG.

Fig. 5.1.50 shows the retained austenite distribution on the rail sample 2 and rail sample 3 respectively. In the region near the gauge corner of the rails, the weak loaded area, no retained austenite reflections are present in the diffraction spectra. Thus, the austenite content in these regions is definitely below 2%. However, retained austenite is present at the rail treads, on the higher loaded parts of the rolling surface, with a maximum of 12%.

The distribution of the retained austenite in the in – depth direction below the surface of rail 3 is shown in Fig. 5.1.51. In the first 4 µm, the retained austenite tends to slightly increase from 13% to 17%, then in the larger distance to the surface, it decreases very fast. Below a depth of 16 µm, the content of the retained austenite is not sufficient to be detected by X - ray method, thus it is lower than 2%.

Fig. 5.1.52 and Fig. 5.1.53 present the domain size on the rail sample 2 and the rail sample 3. The domain size on the rolling surface of both rails is in the order of some nanometers. Thus, it has its smallest value in those areas where the white etching layers are present.

Fig. 5.1.55 and Fig. 5.1.57 present the microprobe profile analyses in the area of WEL in Fig. 5.1.54 and in the area where no WEL exists on the surface in Fig. 5.1.56 for rail sample 3 separately. Both in the area of the WEL and the area where no WEL is present, at the very surface and also in the in - depth direction (as far as 50 µm) no increased nitrogen content was detected. Further, the carbon concentration is constant in the in - depth direction.

´

5.1.2 Wheel Sample

Microstructure Analysis by Microscope

The wheel sample shown in Fig. 4.5 was taken from an Intercity Express wheel. The tread of the wheel is much broader than the rails. After service, the rolling trace can be observed on the wheel surface, but there is no obvious rolling surface as it can be found on the rail samples. The damage on the wheel is also not as severe as it is on the rails.

Fig. 5.1.58 shows an image of the cross - section of the wheel obtained by optical microscope. A narrow white etching layer is clearly visible at the rail surface. There is

also an obvious sharp transition between the white layer and the bulk material. The thickness of the white etching layer is about 10 µm and, thus, less than that in the rail samples. The white etching layer is found mostly in the area near to the flange. In this region the frequency of contact between the wheel and rail is the highest.

Using scanning electron microscope, the microstructure changes on the wheel surface were analyzed. Fig. 5.1.59 presents an overview of the white layer. It seems that the microstructure changes appear to occur in the semi - elliptical areas of contact. Cracks stretching into the bulk material on the wheel sample are visible. Spalling increases the roughness of the wheel surface. Even with a magnification of 5000, the structure of the WEL appears nearly homogeneous (Fig. 5.1.60). Compared to the white layer on the rails, the layer unraveled on the wheel is much coarser. Beneath the white etching layer the microstructure of the steel is deformed. In the region far away from the flange less white layers were found, but the deformed layer is observed. The strong deformation in the layer just under the surface does not flow parallel to the surface line. A small rolling angle can be seen. The deformation depth amounts to over 50 µm (Fig. 5.1.61).

The bulk material of the wheel is shown in Fig. 5.1.62. The photo is taken in a depth of 1.5 mm beneath the surface. It reveals the typical pearlite structure with fine lamella for a medium carbon steel.

Fig. 5.1.63 shows the microhardness distribution in a particular area on the surface of wheel sample. Due to the warping of the flange area it is not suitable for the determination of the micro - hardness, so the area 40 – 85 mm far away from the reference line is chosen. The maximum of the micro - hardness is 700 HV 0,01. It is slight lower than that of the rail samples. The microhardness in the bulk material of wheel is 322 HV 0,01.

In addition, the microhardness distribution in the in - depth direction of the wheel sample was also analyzed and shown in Fig. 5.1.64. A sudden drop of the microhardness is found again from the WEL to the bulk material in the wheel sample. Just like on the other rail samples, the microhardness within the WEL of wheel sample is also not homogeneous.

Microstructure Analysis by Diffraction Methods

Using synchrotron X - rays, the profile of the 200 reflection along the wheel surface was also analyzed. The lattice distance c_m, a_m and the c_m / a_m ratio distribution along the wheel surface are shown in Fig. 5.1.65. The c_m / a_m ratio in the area near to the flange with a maximum of $c_m / a_m = 1.010$ is much bigger than in the field corner of the wheel. It means that the lattice structure in the area near to the flange is tetragonal distorted strongly due to the frequent contact with the rail. Fig. 5.1.66 shows the distribution of the solute carbon concentration across the wheel tread surface. The solute carbon content reaches up to a maximum of 0.2% in the region adjacent to the flange.

5.2 Texture Analyses

Due to the strong plastic deformation in the rail and the wheel material the crystallites develop preferred orientations (textures) and, thus, also the macroscopic material properties become direction dependent. Therefore, texture analyses were performed on several different loaded rail samples and on the wheel sample.

5.2.1 Rail Samples

Rail DB AG

A texture analysis in the base material, e.g. the material in a depth of 30mm beneath the rail surface, shows a random crystallite orientation distribution. Thus, before the loading by the rail traffic the texture of the rail is nearly isotropic.

Fig. 5.2.1 and Fig. 5.2.2 show the inverse pole figure and the orientation distribution function (ODF) in the strongly loaded area of the rail, at the center of the rolling surface. It is visible that at the center of the rolling surface a combination of a <111> fiber texture and a <551> fiber texture evolves. The <111> fiber texture is a typical compression texture for metals with body centered cubic (b.c.c.) crystal structure. The other fiber texture component in <551> direction is not far away from the <110> crystallite direction and, thus, it might be a texture component induced by shear deformation. Besides on the rolling surface these two fiber texture components are also found in the areas outside of the rolling surface on the rail surface.

On the rolling surface of rail DB AG, the intensity of <111> fiber texture component changes distinctively across the rail surface. Fig. 5.2.3 and Fig. 5.2.4 show the distribution of texture components along a line from point 2 to point 3 and in the area near to point 7 on the rail surface. At the gauge corner of the rolling surface, the intensity of <111> fiber texture component is stronger than on the right side of the rolling surface, which is the field corner of the rail. This change of the texture is visible both in the area between point 2 and point 3 and also in the area near to point 7. In contrast, along both lines across the rail surface investigated here, the <551> fiber texture intensity remains nearly constant.

This implies that the texture development caused by the loading of the rail varies strongly in the transverse direction of the rail. In the longitudinal direction of the rail, a comparison of Fig. 5.2.3 and Fig. 5.2.4 shows only small variations of texture intensity.

Under the surface of the rail, the texture component index is shown in Fig. 5.2.6 and evolvement of the texture is shown using inverse pole figure in Fig. 5.2.5. The same two fiber texture components <111> and <551> as those found on the surface exist in the subsurface of the rail. Only the intensity of texture component varies. They increase to a first maximum in an approximate depth of 16 µm, then they decrease with increasing depth. Below a depth of 100 µm, the texture component <551> and <111> behave further in different way. The fiber texture component <111> increases slowly again and while the <551> component decreases. In a depth of about 200 µm, the <111> texture component reaches a second maximum, then it tends to decrease again, while <551>texture component decreases continually with increasing depth. The <551> texture component almost ceases to exist in a depth of 250 µm

Rail Baumann

Texture analysis in a depth of 50 mm beneath the surface of rail Baumann shows a random orientation distribution. This again reveals that, before the loading by the rail traffic, the texture of the rail is nearly isotropic.

A combination of <111> and <551> fiber textures are found on the rolling surface of rail Baumann. The <111> fiber texture component is a typical compression texture

for b.c.c. crystals. Furthermore, another fiber texture component in <551> direction is revealed on the whole rail surface including the riffle hill and riffle valley. This texture component is supposed to be induced by shear deformation.

Fig. 5.2.7 shows the distribution of the fiber texture components <111> and <551> across the rail surface. The <111> fiber texture index becomes smaller on the “riffle hills”. There are no big changes in <551> texture component between riffle hills and valleys. The texture distribution determined on the rail Baumann, thus, are analogous to those determined on the rail DB AG.

In the subsurface, the distribution of the texture index below the “riffle hill” (area a 1 outlined by a white square in Fig. 4.2) is shown in Fig. 5.2.8 and the detailed evolvement of the texture was shown in Fig. 5.2.10 using inverse pole figures. In the in - depth direction, the <111> texture component decreases firstly, then tends to increase and in a distance of app. 250 µm to the surface the maximum is reached. After that it decreases again. But the <551> texture component changes in another way in the in - depth direction. It increases firstly, then tends to decrease, finally it ceases at a depth of 350 µm. A weak rolling texture was also found at a larger depth.

The distribution of the texture below the “riffle valley” of the rail Baumann (area a 2 outlined by a white square in Fig. 4.2) is present in Fig. 5.2.9 and Fig. 5.2.11. <111> texture component reaches its maximum at the depth of about 200 µm, then tends to decrease with further increasing depth. While <551> texture component decreases continuously with the increasing and ceases at the depth of 650 µm. Here it should be mentioned that a typical (111) [$\bar{2}$11] rolling texture is found at depths of 20 µm, 70 µm below the surface. It is supposed to originate from the production process. In the larger depth, the rolling texture fads off and the fiber texture becomes the dominant texture again.

Rail Sample 2 and Rail Sample 3

Fig. 5.2.12 and Fig. 5.2.13 present the inverse pole figure and the ODF of the ferrite / martensite on the surface of rail 3. Again There is a combination of <111> and <551> fiber textures in the ferrite / martensite on rail 2 and rail 3

Fig. 5.2.14 and Fig. 5.2.15 show the inverse pole figure and the ODF of the austenite phase on rail sample 3. A combination of a relative weak <210> and a <110> fiber

texture was unraveled in the remaining austenite. The volume amount of the retained austenite in this area is about 12% (Fig. 5.1.50). Usually the <110> fiber texture typically develops due to compressive loading of face centered cubic materials. The <210> fiber texture might be attributed to shear deformation induced by the load and wear of rail - wheel system.

5.2.2 Wheel Sample

A combination of the two fiber texture components <111> and <551> was also found in the martensite / ferrite on the surface of wheel sample. Fig. 5.2.16 reveals the inverse pole figure of the wheel sample. Obviously the inserted loading in this region induced a sharp and strong <111> fiber texture.

The texture index distribution below the surface of the wheel is shown in Fig. 5.2.17 and evolvement of the texture is shown in detail by means of inverse pole figure in Fig. 5.2.18. The investigated area is chosen between x = 28 mm to x = 48 mm along line 1 on the surface of wheel. <111> texture component decrease firstly, then tends to increase. The maximum was reached at a depth of 300 µm and then begins to decreases again. However, <551> texture component tends to decrease continuously with the increasing depth. From a depth of 180 µm below the surface on, a new but very weak rolling texture component was found. In larger depths, it increases first, then tends to decrease.

5.3 Residual Stress Analyses

Residual stresses often are crucial to the life time of components /Hauk 1994/. Here, residual stress analyses were conducted on several rail samples and on one wheel sample. The residual stresses were determined both in longitudinal and transverse direction across the sample surface and at certain distances to the sample surface.

5.3.1 Rail Samples

Rail DB AG

The residual stresses of the martensite / ferrite were analyzed along three different lines across rail DB AG (Fig. 4.1.). Line 1 goes through points 1 - 4, line 6 through point 6 and line 7 goes through point 7. The residual stresses studied in all these locations are compressive in longitudinal as well as in transverse direction.

The residual stress distribution along line 1 is shown in Fig. 5.3.1. In the area on the left side of the rail where x = 0 the residual stresses are low tensile residual stresses or low compressive residual stresses. In the region between x = 0 and point 2, the residual stresses show a tendency towards increasing compressive residual stresses of the same magnitude both in transverse and in longitudinal direction. On the rolling surface between point 2 to point 3 (pale area in the center of the rail) the compressive residual stresses increase steeply to a maximum. On the right side of the rolling surface a steep gradient of the residual stresses is visible and the compressive residual stresses relax to values comparable to the residual stress value obtained in the slightly loaded area on the left side of the rail.

The same distribution of residual stresses is obtained by the measurements along line 6 (Fig. 4.1) through point 6 on the rail surface (Fig. 5.3.2). Here also the maximum residual stress, about – 600 MPa, is located on the outside of the rolling surface. With regard to the measurements along line 7 containing point 7 (Fig. 4.1), the distribution of residual stresses reveals nearly the same contour except that the maximum of the residual stress is found near of point 7, that is not exactly on the field corner of the rolling surface (Fig. 5.3.3).

The error bars shown in the figure are due to a splitting of the positive and the negative branches of the d - $\sin^2\psi$ - curve They are especially strong in the areas on the left and the right side of the rolling surface. This indicates the existence of the shear stresses along the rail. Thus, within these positions the principal residual stress state was further analyzed.

Fig. 5.3.4 and Fig. 5.3.5 show the principal residual stress distribution and the direction of principal residual stresses σ_1 and σ_2 along line 1 containing points 1 to 4 on the rail DB AG. It is ascertained that the directions of principal residual stress σ_1 and σ_2 vary along the rail. The direction of the principal residual stresses rotates along the rail cross - section.

The maximum of the principal stress σ_1, approximately - 800 MPa, is reached on the outside of the rolling surface of the rail in a 40^0 angle to the longitudinal direction. However, the principal residual stress σ_2 is relatively constant in transverse direction of the rail. The principal residual stresses tend to decrease in the weakly loaded dark area of the rail.

In the in – depth direction the residual stress distribution was also studied (Fig. 5.3.6). With increasing distance to the rail surface, first the residual stresses decrease with a strong gradient from – 600 MPa on the surface to 100 MPa in a depth of 100 µm. Then the tensile residual stresses tends to increase with increasing depth.

Rail Baumann

Fig. 5.3.7 presents the residual stress distribution along line 1 through two riffle hills and valleys (Fig. 4.2) across the surface of rail Baumann. The residual stresses studied in these locations are compressive in longitudinal and transverse direction.

In the area near to the reference line, the gauge corner of the rail, the residual stresses are low compressive residual stresses ranging from - 150 MPa to - 250 MPa.

In the region of the first white layer patches or so - called riffle hills at a distance between 14 mm and 20 mm to the reference line the residual stresses show a tendency to increase of the same magnitude in transverse and as well as in longitudinal direction. They reach a maximum of more than - 400 MPa. Then the residual stress values suddenly drop to about – 100 MPa within the small valley existing between two riffle hills.

After that in the area of the second small riffle hill near to the strongly corroded area, the residual stresses increase not as significantly as they did on the first riffle hill, but, a small rise in residual stress values is visible. On the field corner of the rail surface

the compressive residual stresses relax to a value that is even smaller than the residual stress value on the gauge corner of the rail.

The principal residual stresses were further determined along line 1. The principal residual stress σ_1 (Fig. 5.3.8) varies in nearly the same way as the principal residual stress σ_2 near the longitudinal direction of the rail (Fig. 5.3.9). The magnitude of the principal residual stress σ_1 is larger than the principal residual stress σ_2. And, because of the existence of the shear stress, the stress tensor rotates along the rail surface. The maximum of σ_1, over – 400 MPa, is situated in the area of the first riffle hill with a small rotation angle of - 6^0.

Due to the inhomogeneity on surface of rail Baumann, the residual stress distribution along line 2 (Fig. 4.2), across the riffle valley, was also determined and is shown in Fig. 5.3.10.

The residual stresses in longitudinal, transverse direction and diagonal direction are all compressive. But, their distribution is completely different from line 1 through the riffle hills in Fig. 4.1

Compared to the residual stresses along line 1, the residual stress minimum, which is smaller than – 100 MPa, is reached in the region between 14 mm to 20 mm along line 2. There is no steep gradient in the residual stress distribution. They vary only slightly across the rail surface from the reference line towards the field corner with the dark corroded area. The residual stresses vary between 0 MPa and – 200 MPa. A comparison of Fig. 5.3.7 and Fig. 5.3.10 shows the variation of the residual stresses in the rolling direction on account of the existence of “riffle hill”s and “riffle valley”s.

The principal residual stresses were additionally determined along line 2. The stress tensor again rotates across the rail surface. The distribution of the principal residual stress σ_1 varies in a different way from the principal residual stress σ_2. Regarding the principal residual stress σ_1 (Fig. 5.3.11), it varies slightly across the rail surface. Regarding the principal residual stress σ_2 (Fig. 5.3.12), it decreases from the reference line towards the field corner of the rail and the maximum, - 300 MPa is reached in the area near to the reference line.

The residual stress distribution in the area at y = 10mm and x = 0 – 24 mm was also investigated and shown in Fig. 5.3.13. The topography of this area was shown from Fig. 5.1.19 and Fig. 5.1.21. In the highest point, x = 3,5 mm, where the highest microhardness was found (Fig. 5.1.22), the residual stresses reach their maximums.

In the subsurface, the residual stress distribution was also studied. Fig. 5.3.14 shows the distribution of residual stresses just below a “riffle hill”. With increasing distance to the rail surface, the residual stresses decrease at first with a strong gradient from – 600 MPa on the surface to more than 0 MPa at a depth of 50 µm. Then in the larger distance to the surface, the tensile residual stresses tends to increase with the increasing distance to the surface.

Fig. 5.3.15 displays the changes of the residual stresses in the subsurface of the “riffle valley” of rail Baumann. A low residual stress, -150 MPa was found on the top surface of the riffle valley. In the in - depth direction, the residual stresses decreases quickly from – 150 MPa to 50 MPa at a depth of 50 µm. Then it tends to increase in the tensile state in the larger distance to the surface.

Rail Sample 2 and Rail Sample 3

The residual stresses of the ferrite and martensite were determined first. Two lines crossing the rolling surface of sample 2 and one line crossing the rolling surface of sample 3 were chosen for residual stress analyses. Then the residual stresses in the retained austenite were analyzed in those positions where the retained austenite content is higher than 9%.

Fig. 5.3.16 and Fig. 5.3.17 present the residual stress distribution in the ferrite and martensite on rail sample 2 and in Fig. 5.3.18 for rail sample 3. Compressive residual stresses are present both in longitudinal and transverse direction on the surface of both rails. This is in accordance with previous investigations on the other rails /Pyzalla 2001, Pyzalla[1-2] 2000/. In those positions corresponding to the highest compressive residual stresses, the white etching layers were observed both by optical and scanning electron microscope. From the reference line towards the field corner of the rail, the residual stresses increase in longitudinal and transverse direction. After a maximum is reached at the field corner of the rolling surface, the residual stresses decrease abruptly in the dark area of the rails.

The maximum compressive residual stress values on rail sample 2 are app. – 700 MPa in transverse as well as in longitudinal direction. The maximum residual stresses on the rolling surface of rail sample 3 with – 600 MPa are slightly lower than on the rolling surface of rail 2.

A splitting of d - $\sin^2\psi$ - curves at the left side of the rail was noticed which indicates that high shear stresses were present. The principal residual stresses and the direction of the principal residual stresses on rail sample 3 were also determined (Fig. 5.3.19 and Fig. 5.3.20). The stress tensor rotates along the rail surface. In those areas, where high compressive residual stress were determined, the rotation angle of the principal stress is much smaller. Near the reference line, the principal residual stress values are very low, beneath 0 MPa. At a distance from the reference line the principal residual stress σ_1 increases slowly and at the field corner of the rail the principal residual stress maximum – 600 MPa is reached. The principal residual stress σ_2 varies in a similar way to the principal residual stress $\sigma_?$ and both residual stress components reach a maximum at the same distance to the reference line.

Fig. 5.3.21 and Fig. 5.3.22 reveal the residual stress distribution of the retained austenite on rail 2 and rail 3 respectively. The residual stresses in the retained austenite are compressive in longitudinal and in transverse direction. They show a tendency to increase towards the field corner of the rail. Since the volume of the material increases at least by 3% during the transformation from austenite to martensite, the compressive stress actually hinders this kind of transformation and instead contributes in a certain degree to the remaining of austenite.

The residual stress development in the in - depth direction of rail sample 3 is shown in Fig. 5.3.23. The residual stresses start to decrease with a very strong gradient. From the surface to a depth of 30 µm the residual stress values decrease from – 600 MPa to 0 MPa. Then, the residual stresses further change towards tensile residual stresses to the larger distance to the surface

5.3.2 Wheel Sample

The residual stresses distributions were determined along two lines on the wheel sample surface from the flange towards the field corner of the sample (Fig. 4.5).

Fig. 5.3.24 shows the residual stresses distribution along line 1 on the wheel sample surface. In longitudinal, in diagonal, as well as in transverse direction, the residual stresses are compressive. In the area near the reference line, which is at the flange of the wheel, high compressive residual stresses were determined.

An increase of the compressive residual stress values towards nearly twice the value at the reference line is found in an area far away from the flange. This indicates that these two areas are in contact with the rail. The maximum of the residual stresses on the wheel surface is – 490 MPa in all three directions. This value is much lower than the maximum residual stress value determined on the rail samples. At the extremely field corner of the wheel, in an area where seldom contact arises, the residual stresses have their lowest value.

The roughly similar residual stresses distribution along line 2 on the wheel ICE surface is shown in Fig. 5.3.27. The residual stresses along line 2 are also compressive. The residual stresses have their lowest value at the field corner of the wheel. But, the maximum of the residual stresses along line 2, - 430 MPa, is slightly smaller than it is along line 1. And unlike the distribution along line 1, there is no sudden decrease of the residual stress in the area near the flange.

A comparison of Fig. 5.3.24 and Fig. 5.3.27 shows the slight variation of the residual stresses in the rolling direction because of the inhomogeneous loading distribution on the wheel sample surface.

Further, a splitting of the d - $\sin^2\psi$ - curves on the wheel samples was noticed, which indicates that shear stresses exist on the wheel surface. Thus, the principal residual stresses and the direction of the principal residual stresses along line 1 were determined, they are shown in Fig. 5.3.25 and Fig. 5.3.26. Similar to the results on the rail sample, the stress tensor rotates along the wheel surface owing to the existence of shear stresses. The principal residual stress σ_1 reaches a maximum of – 580 MPa at the field corner of the wheel with an rotation angle of 12° to the longitudinal direction. The principal residual stress σ_2 changes similar to σ_1. The maximum of σ_2 is about – 550 MPa with rotation angle – 44° to the transverse direction.

Fig. 5.3.28 displays the residual stresses development in the in - depth direction of wheel sample. From the surface to the depth of 60 µm below the surface, the

residual stresses decrease from – 600 MPa to about 0 MPa with a very large gradient. Then, the residual stresses further change towards tensile residual stresses to the larger depth below the surface

5.4 Corrosion Resistance

Potentiodynamic anodic current - density - potential - curves were measured in the area of a white layer patch, a “riffle hill” and in the weak loaded shadily and murky area, a “riffle valley” (Fig. 5.4.1). The current - density - potential - curve for the riffle valley is a typical curve obtained for a normal medium carbon steel. The current density increases quickly at first to a saturation. Then the current density remains constant or increases slightly with further increasing potential.

The current - density - potential - curve of the “riffle hill” is different from the current-density-potential curve of the “riffle valley” of the rail. After the Ruhepotential is reached, the current density increases very slowly in a first stage, afterwards it increases strongly in the same way as the weak loaded murky area. This reveals that the surface roughness conditions on the area of “riffle hill” and “riffle valley” are really different. Moreover, It also reveals that the upper layer structure in the “riffle hill” is different from that in the “riffle valley” that underwent weak loading.

Fig. 5.4.2 shows the potential curves for the different depths below a “riffle hill”, a white layer on the rail Baumann. The surface was ground on the SiC paper with 4000 grits. The first zone including WEL, from the top surface to 1 mm below the rail surface shows the slowest corrosion reaction. In the second zone without WEL, from 1 mm to 2 mm below the surface, the corrosion reaction is faster than in the first zone, but it is still much slower than the reaction of the bulk material, 5 mm to 6 mm far away from the top surface.

6. Discussion

6.1 Formation of the White Etching Layers

Both on the weakly loaded samples and on the heavily loaded samples, distinctive spatial - dependent structures are developed on the rail and wheel surface because of the spatial – dependence of the loading along the rail surfaces respectively the wheel surface during rolling contact. According to residual stress analyses on the rolling surface of the different rail and wheel samples utilizing laboratory X - ray as well as synchrotron X - ray radiation, the white etching layers are always present in those regions where a significant increase in compressive residual stresses is present. Since residual stresses analyses on rail surfaces directly after rail production revealed that tensile residual stresses were formed at the rail head and foot during the processing /Schleinzer 2000, Webster 1993, Hauk 1994/, the residual stress state determined in the investigations performed within this thesis reveals that strong permanent plastic deformation and martensite transformation occurred on the rail surface during service. Together with the phase, profile and X - ray image analyses performed, the residual stress state of the rail surface unravels that the WEL, the immense microstructure alterations, is induced by the cyclic high loading and cyclic wear on the contact area in the rail - wheel system.

Microstructure of the White Etching Layer

Optical and scanning electron microscope reveal that the change from the normal ferrite - pearlite structure of the bulk material of the rail towards the structure of the WEL on the top surface, within all samples investigated is always abrupt. There is no transition layer present. This indicates that plastic deformation must be accompanied by thermal loading during the formation of the WEL /Österle 2001/. If severe plastic deformation would have been the unique mechanism which transforms the ferrite / pearlite microstructure, a gradient deformation substructure should be observed in the topmost surface layer, just like the usually observed deformed surface of the wheel where there are no WELs (Fig. 5.1.61).

Reflection profile analysis shows that there is an asymmetric distortion of the 200 reflection on the samples surface. This proves that the lattice structure in the white etching layer is body centered tetragonal. Along the rolling surface, the crystallite lattice along the rail and wheel surface is distorted gradually changing with increasing loading and wear. According to the theory of /Vöhringer1977/, from the asymmetric distortion, the amount of soluted carbon, which is soluted in the octahedral sites of the martensite, could be quantified (e.g. Fig. 5.1.8). This indicates that massive local structure changes happened at the sample surface due to loading and wear. Within the white etching layers the microstructure does not consist of ferrite with a body centered cubic structure, but, of martensite with body centered tetragonal structure both on the heavily loaded rails, the weakly loaded rails and the wheel sample.

The 200 reflection profile changing from asymmetry to symmetry after annealing unravels the decompose of the martensite into ferrite and carbide. This proves the martensite in the WEL is very unstable.

The extreme high microhardness of 1000 HV 0,2 in the white layer area on the surface of the weakly loaded and the heavily loaded samples unravels further that the WEL does not consist of normal quenched martensite, since a microhardness of only about 500 HV 0,2 is expected for a steel with the same carbon content as the carbon content of the rail steel /Eyre 1972/.

Also, the retained austenite in the strongly deformed region on the rail samples indicates that during the rolling contact in the rail - wheel system, the temperature in the material volumes close to the contact surface rapidly rose because of the generation of heat. Due to this heat generation austenization occurs in the area of contact between rail and wheel. This rapid temperature rise is followed by rapid cooling, which causes martensite formation close to the surface through the usual thermal transformation ferrite / pearlite – austenite - martensite.

It is well known, that a temperature of more than 723°C is necessary for the unalloyed steel to transform into austenite. But, actually 723°C is only a theoretical austenization temperature for an equilibrium thermal transformation at ambient pressure /Smallman 1985/. The heating rate, the pressure, alloy elements and so on, strongly influence this transformation temperature /Baumann1998/.

First, a high heating - up rate will shift the A_1 and A_3 temperatures towards higher temperatures /Smallman 1985, Bever 1986/. A rough estimation gives that for 5s slide, the effective A_1 temperature is shifted about 20 °C while the A_3 temperature is shifted some 30°C /Ahlström 1999/. For less rapid heating or longer - time sliding, the shift in transformation temperature is smaller /Ahlström 1999/.

Further, hydrostatic pressure has been proven to alter the equilibrium lines A_1 and A_3 and the M_s temperature. At high pressure phase many physico - mechanical properties of materials are anomalous /Ortner 1992, Ermolaev 2000/. /Ortner 1992/ indicates a roughly linear decrease of martensite transformation temperatures with increasing hydrostatic pressure, but once the pressure relaxes, the M_s temperature would recover its normal value. It has been found in case of a medium carbon wheel steel SURA B82 that at a hydrostatic pressure of 400 MPa the A_1 temperature was lowered about 4 °C while A_3 decreased from 763 °C to 746 °C. The quantitative value of the almost hydrostatic pressure in the wheel and rail material during sliding contact is not known. A nearly hydrostatic pressure of more than 1400 MPa was estimated res. calculated to be the nominal contact stress on the rail surface by /Bucher 2001, Hellier 1991, Lunden 1991/. This high hydrostatic pressure, thus, may cause a significant decrease in the A_3 temperature in the contact area.

Very high temperatures over 900°C can be attained in the hot spots on dry rolling surfaces /Quinn 1987/. It can be supposed that the austenization starts in the most heavily loaded areas where severe wear occurs at the rail - wheel contact surface. Since the masses involved both regarding rail and wheel are large, the cooling rate is high and therefore, apparently opportune for martensite formation.

While because of the quick heat loss, high temperatures are only present in a very shallow superficial layer, the white layer extends only to some tens of µm. The retained austenite is detected as far as 16 µm into the depth direction of rail sample 3 and as far as 10 µm below the surface of rail DB AG. The asymmetric distortion of reflection profile is also observed to be present in distances to the rail surface up to these depths.

Clearly there is not enough time for dissolution and diffusion during the austenization, thus, the cementite can not be completely dissolved in such a short time and therefore, the carbon content in the austenite is not uniform. This is proven

by the analysis of solute carbon in martensite along the sample surfaces. /Österle 2001, Rooch 2000/ observed the remaining cementite particles under transmission electron microscope.

As it is well established, martensite transformation involves no diffusion of carbon, it inherits the carbon content of the austenite and the carbon atoms do not alter their position /Bain 1924, Bever 1986/.

In martensite transformation, the dissolved carbon induces a lattice distortion in order to produce a body - centered tetragonal structure whose c_m / a_m ratio increases if the carbon content increases. The increasing distortion of the lattice with increasing carbon content that results from the dissolved cementite causes the hardness to increase rapidly /Cridnex 1972, Newcomb 1984, Hoffmann 1997**,** Baumann 1998/. The increasing dissolution of carbon in different stages of rail corrugation is also proven by the c_m / a_m ratio of the martensite determined using synchrotron radiation, that varies considerably across the riffle band of rails.

During martensitic transformation, the deformation would also change the texture a lot /Hatherly1977/. The texture is a tensor not only of the material properties, but also includes the foregoing stress burdening /Bunge 1988/.

A <111> fiber texture is a typical compressive texture for the b.c.c material and the <551> fiber texture is induced by shear stress /Wassermann 1962, Krause 1989/. Therefore, the texture component <111> might evolve through high pressure during the rolling of passing trains. A similar same fiber texture is documented by /Voskamp 1996/ in rolling contact of bearing when the bearing running at a smaller load (maximum contact stress of 3,8 GPa), but at higher operating temperatures (e.g. 90°C).

It is well established that transformation textures have their origin in the orientation relationships between the parent and product phases of the transformation /Harthly 1977/. The <211> in the austenite will change into <111> of the martensite in the shearing structure transformation. So it can be asserted that the martensite fiber texture <111> origins from the <211> fibre texture found in retained austenite. /Bain1924, Kurdjumov 1930/ ever reported the inheritance of the texture during the transformation between austenite and martensite. This gives another powerful support to the conclusion of austenite - martensite transformation

The decrease of the texture index with the loading, and with increasing c / a ratio of martensite reveals the repeated occurrence of the austenite - martensite transformation. Repeated diffusionless martensite transformation is assumed to increase the randomize of the crystallite distribution and thereby takes a negative influence on the texture evolvement.

The texture component distribution together with the analysis of the residual stress of retained austenite, indicates that the austenite undergoes considerable deformation. The predeformed austenite will change the morphology and properties of the transformed martensite. In the following cooling down the subgrain of the austenite would promote the ultra - fine grained martensite transformation and this process has been proved to improve the tensile strength of materials /Sipos 1976/.

Nano-structure and hardening mechanism in the White Etching Layer

In this thesis, the broadness of the reflections obtained in the WEL indicates that the domain size is strongly reduced under the increasing deformation. This is also shown by the presence of cementite particles with a size of only a few nanometers on the rolling surface of the rails using ASAXS. The radius of the remaining carbide particle size is determined to be as small as 2 nm. Two kinds of radius of the particle size, 5nm and 20 nm were also found in the area outside but in the vicinity of the white etching layer. It means that the structure in the white layer consists of nano – structured material.

Therefore, it is assumed that due to the cyclic loading and wear caused by passing trains, a transition from the cementite lamellae of the pearlite in the original material of wheel and rail to coarse broken particles may occur. They later on further break up into the ultra - fine grained particles under the cyclic severe plastic deformation. This process is presented schematically in Fig. 6.1.

It is already established that the sliding of metals can produce a nanocrystalline layer on the surface of one or both of sliding components and the thickness of this layer varies depending on the metal system and the conditions of sliding /Ganapathi 1991/ /Korznikow 1994/ also observed complete cementite solution and grain size reduction till 20 nm in a steel with 1,2% C subjected extremely high torsion deformation. /Ruslan 1997/ even began the fabrication of several pure metals and

alloys with nano - and sub - micrometer grain sizes by severe plastic deformation techniques. /Baumann 1998/ and his co - workers also proposed that the dissolution of the pearlitic microstructure and grain size reduced to nano range on the rail surface are caused by severe plastic deformation of a thin superficial layer at asperities, and he simulated this possibility using mechanical attrition in ball milling. But, they did not see the significance for martensite formation.

A specific parameter for nano - structures is the surface / interface – to – volume ratio. A high percentage of surface atoms introduces many size - dependent phenomena. The mechanical properties of a solid depends strongly on the dislocation density, interface – to - volume ratio and grain size. So the nano - structure contributes partly to the high mirohardness of the WEL and also its strong corrosion resistance. Also it is the reason that homogenous structure is observed under the optical microscope.

The essence of strengthening of grain size is that the grain boundary acts as a barrier to dislocation motion. A dislocation passing into another grain will have to change its direction of motion. On the other hand, the atomic disorder within a grain boundary region will result in discontinuity of slip planes from one grain into the other. A fine grained material is harder and stronger than a coarse grained material, since the fine grained material has a greater total grain boundary area which impedes dislocation motion. For many materials, the yield strength σ_y varies with grain size according to

$$\sigma_y=\sigma_0+K_y d^{-1/2}$$

In this expression, termed Hall - Petch equation, d is the average grain diameter, and σ_0 and K_y are constant for a particular material. Actually this equation is not valid for the extremely fine grain polycrystalline material, but it unravels that the material properties depends significantly on the grain size.

This grain size effect also plays a role in the inhomogeneous properties of the white layer. For the reason of different contact stress in depth, the upper layer of the white layer has a smaller grain size than the lower layer, so the structure seems to be compacter than the lower white layer under the microscope, and the microhardness in the upper layer is also much higher than in the lower white layer. This phenomenon is also adverted in /Bucher 2001/.

The presence of a shear stress necessary in the nanocrystalline material is proven by the splitting of the positive and the negative branches of the d - $\sin^2\psi$ - curve that exist at the edge of the rolling surface. Under the simple hypothesis of Hertzian contact, shear stresses are present outside the center of contact /Johnson 1958, Voskamp 1996/ (Fig. 2.1). Further, the principal residual stress calculation showed that the principal residual stress direction rotates across the rolling surface of the rail and wheel samples.

Dislocation multiplication is another hardening mechanism involved. First, the surface is apt to attract the dislocations in order to reduce the surface energy /FP 1998/. Second, the plastic deformation due to loading and wear induces dislocation multiplication. Third, the martensite hardens by dislocations, then dissolved carbon atom into octaedral site of martensite cause the domain size to become smaller and the mean micro - strain to becomes bigger. /Hoffmann 2001/ has explained the influence of solute carbon in martensite on domain size. Here should be noted that the dislocation density is not directly supplied in this work, but the domain size that is theoretically proportional to the dislocation density that calculated using a single line method. So a smaller domain size means a very high dislocation density.

The extremely high microhardness and strength of the martensite induced by quenching from austenite on the rail - wheel surface can be explained by dislocation strengthening, particle strengthening, work hardening, micro - strain strengthening and grain size strengthening.

Formation of the White Etching Layer

The vibration of the rail - wheel system causes the stress concentrations in regular distance or in certain regions. If the deformation degree in some minute area reaches a critical value, the cementite lamellae in these area on the surface layer are broken first into coarse particles. Then, during cyclic loading the cementite lamellae break further into smaller particles, finally into very fine grain particle of a few nanometer size. In these areas the dislocation density is very high.

Within these minute areas on the rail - wheel surface the contact temperature is high enough for austenization. During the short time interval of contact the cementite can not be completely dissolved. But, the austenite is strongly deformed under the

loading. During the following cooling the austenite transforms into ultra - fine grained martensite in these areas. Accordingly the White Etching Layer with ultra - fine grained martensite, nanocrystalline cementite and the austenite is formed.

The white etching layers are found not only on the worn railway rails but also on the other components such as piston rings, gear wheels and in various machining processes (e.g. cutting, grinding), and also under various operating conditions(e.g. friction). It has been the subject of a number of experimental as well as numerical studies. However, the micro - mechanisms leading to the different sorts of layers seem to be quite different. Thus, the result obtained in the investigations described here are only comparable and also valid for other white etching layer formed in similar materials and under similar loading conditions.

6.2 Correlation between Changes in Microstructure and Topography

Due to the accommodation of inhomogeneous, micro - plastic deformation during the service, the state of surface would be altered and the formation of surface topography involves imperatively the changes of the microstructure /Bucher 2001/.

The wear and the roughness formed during the manufacture in rail - wheel system would lead to the unevenness of the surface even before and during service /Bucher 2001/. The profilometer measurements in this thesis show a jagged rail surface topography after service. There are some small holes with a diameter 0.2 mm and a depth to 2 µm. They are distributed irregularly on the rail surface. The altitude difference between the riffle hills and riffle valleys amounts to 6 µm – 9 µm in this thesis. Actually altitude differences as high as 100 µm was ever reported in /Walf 1981/. The towering area on the rail surface is of course more often impacted by the wheel during the rolling than the low area. Thus, the severe structure transformation takes place in these regions. On the other hand, the contained spatial frequencies in the roughness profiles influence the shape of the distribution of those normal traction in the way, that with higher frequencies it get more and more clefted and the real contact area of contact decreases and the damage would arise sooner /Bucher 2000/.

The vibration and contact of rail - wheel system result in local stress concentration in some regions. The protruding points on the surface was broken up or rubbed down and, thus, the roughness in these areas become smaller. But, the plastic deformation accumulates day by day. After long – time cyclic loading and wear, the carbides in the near – surface area was broken into small particles, then further into nano - particles as related in chapter 6.1. The simultaneous heating - up process induced by friction gives rise to the austenite/martensite transformation in these area. Therefore, some small white etching layers evolve under the towering areas on the surface, then with cyclic loading, the white etching layers increase in thickness and connect with other adjacent white etching layers. Finally long - ribbon white etching layers can be observed under the surface.

Mainly because of the different corrosion resistance of “riffle hill” and “riffle valley” that was obviously reflected in the potential curve (Fig. 5.4.1), the “riffle hill” and “riffle valley” on the rail show the different visual effect. The “riffle hill” which has the high corrosion resistance shines bright, but the lower area, “riffle valley” that was seldom contacted by the wheel was seriously corroded by the environment, thus, they shine black and murky.

The structure alterations can be proven by the big contrast of the microhardness between the bright area, “riffle hills” and dark area, “riffle valleys”. And the X - ray image analyses in these areas gives additional powerful support to this structure transformation. /Baumann 1996[1]/ reported that after enough long service time, the structure alteration would take place even in the “riffle valleys” on the rail surface.

The study in this thesis shows that the properties of riffle hills bears not only resemblance, but also difference to each other. Even within one bright patch, riffle hill, inhomogeneous properties are uncovered, e.g. microhardness and residual stresses. It might be explained by the surface corrugation and complicated coordinated action in rail - wheel system. The contact between the rail and wheel is accompanied by twisting, shear, torsion and rolling /Wild 2001/. That brings the alternating and localized different loading and wear on the rail surface.

By shear deformation during the contact between the rail and wheel, the grains are rolled and stretched. This effect could be seen clearly not only in the area within the bright patch without white etching layer, but also in the dark, weakly loaded area (e.g.

Fig. 5.1.61). It builds a strong contrast to the bulk material, uniformly lamellae pearlite structure.

In conclusion it is clear that by external vibrations and developments of riffle waves within a rail track, the rail surface would be corrugated. Due to material modifications and transformation, the hardness and wear resistance in some region are increased and that leads to a self - sustaining surface modulation, then a considerable noise level is caused and the most severe outcome is the damage and fatigue of the materials.

6.3 Gradients of Residual Stresses, Texture and Microstructure in the Depth

The rail and wheel samples experience local changes in the microstructure when exposed to high rolling contact stresses and high contact temperatures. These alterations are a result of the accumulated plastic deformation occurring during over - rolling. These strong plastic deformations are not only present at the surface of rails and wheels, but, they extend into a depth of some hundreds of µms into the bulk material.

/Grotzin 1962, Birmann[1-2] 1958/ brought about the question that besides the plastic deformation also chemical gradients are present in the near - surface region of the rails and wheel, e.g. that a decarburization occurs at the surface. In the rail samples investigated here, according to the results of the microprobe analyses into a depth of 50µm, the carbon concentration is constant within this region of the sample. This means that decarburization does not take place at the rail surface. Further, microprobe analyses revealed that there are no significant gradients of nitrogen and oxygen near the rolling surface. Thus, the martensite formed in the top surface layer can not be a nitrogen martensite as assumed by /Torrance 1974/.

The findings of retained austenite with a volume of about 3%, even in the depth of 10 µm below the rail DB AG surface and with a volume of approximately 4% in the depth of 16µm below the surface of rail sample 3, uncover that the high contact temperatures extend into a certain depth below the sample surface. In a depth of about 12 µm below the rail DB AG the 200 reflection profile becomes approximately symmetric again which means that not tetragonal martensite, but, possibly cubic martensite res. ferrite / pearlite are present in a depth of about 12 µm.

The microhardness varies also in the depth below the surface. There is a considerable drop at 10 ~ 14µm below the surface. From the surface to this depth, the microhardness decreases steeply from 1100 HV 0,2 to 400 ~ 600 HV 0,2 that is just expected or even lower than the micro - hardness for normal martensite. With the depth increasing, the solute carbon concentration decreasing and the grain size increasing contributes to this changes in microhardness.

The potential curves for the different depths below the surface of rail Baumann indicate that the structures even in different large depths of the subsurface are still different from each other due to the production process and the service process.

The accumulation of the plastic deformation during cyclic stressing under rolling contact loading condition results in a complex state of residual stress in the subsurface volume of rail sample.

Sample surface changes arise from the accommodation of inhomogeneous, micro-plastic deformation. It develops from the occurrence of many contact events between rail and wheel. The main sources are sliding, slip, vibration, the presence of small, solid particles and so on. That induces a stress concentration in the surface that yields a local state of stress far above the shakedown or yield limit. The hard rail or wheel steel immediately undergoes small amounts of local plastic deformation. This occurs at any locations randomly distributed over the contact surface and leads to a very inhomogeneous state of deformation over a thin surface layer.

It is well known that the transformation of austenite into martensite is associated with a volume expansion of the order of 3% of the decomposed volume. The observed phase transformation will, thus, generate internal stresses, which cause extra compressive stress in this region.

Thus, the residual stress on the surface is influenced by the manufacturing, the alternating contact stress and the microstructure change. Therefore, the higher compressive residual stresses was always found on the surface of the rail samples and wheel sample. Below a depth of about 100 µm, the plastic deformation decreases and thereby the residual stresses go down to 0 MPa or even change towards lower tensile residual stresses originating supposedly from the production.

Compared to the analyses of the residual stress, the texture development in the subsurface of rail DB AG, rail Baumann and wheel sample shows a different evolution.

As it has been described in part 6.1, the martensitic transformation, especially a repeated austenite - martensite transformation, weakens the texture. In fact texture varies in a rather complicated way within the first tens of µm below the rail surface.

Beneath the surface of rail DB AG into a depth of about 4 µm the <111> texture component shows only a slight inhomogeneity between 3,9 mrd and 3,4 mrd and then increases again to nearly 4,2 mrd in a depth of 16 µm. The <551> texture component reveals a similar distribution with increasing distance to the rail surface. The fiber texture index increases with the depth in the first 16 µm below the surface.

The variation of the texture index with depth might be attributed to competing mechanisms. At the surface of sample the white etching layer contains martensite that undergoes the martensite – austenite – martensite transformation several times. In a depth of 16 µm the high temperatures necessary for the austenization occur less often and the cooling rates are not as high as they are at the surface. Thus, less martensite is present and texture is slightly less randomized by the austenite – martensite - austenite deformation.

In a depth of more than a 100 µm beneath the surface, the texture components <551> and <111> further vary in a different way. The fiber texture component <111> increases slowly to the second maximum of 3.9 at a depth of about 200 µm, then it decreases in larger distances to the surface. In contrast to the <111> texture component the <551> texture component decreases continuously with increasing depth. This can be explained by the fading off of the shear stresses in these depths.

/Johnson 1958/ has calculated that the maximum of the contact stress is reached in a certain depth under the loaded surface using a simple model. This theory has been confirmed and further developed by /Seabra 1987, Hellier 1991, Bijak 1997/. Based on this theory, it can be concluded that the rise of the texture index in a depth 200 µm is evoked by the big contact stress in this depth during service.

Comparison of the texture analyses in the subsurface of the “riffle hill” and the “riffle valley” on the rail Baumann reveals that on the surface, the “riffle valley” has a stronger fiber texture index than the riffle hill due to the martensite transformation on

the rail surface. And it is also unraveled that the maximum of the texture was situated not on the surface, but in the subsurface of the rail whatever for the strongly loaded area and the weakly loaded area. In addition, at a depth of 200 µm below the “riffle hill”, a relative weak rolling texture component was found, which supposedly originates from the manufacturing process. On the surface, a <111> fiber texture component was preferred since it decreases the surface energy. The <111> fiber texture component is a typical compressive texture for a b.c.c. material. However, inside the sample, the combination of a weak rolling texture and a <111> texture component is found. This is due to the deformation during the manufacturing and the contact loading during service. For the sample DB AG, a weak rolling texture component was also found at a larger depth of about 600 µm below the surface.

Nearly same texture distribution was found in the depth below the surface of riffle valley and also a weak rolling texture was revealed at a deep depth below the riffle valley. It should be mentioned that a typical (111) $[\bar{2}11]$ rolling texture was found obviously even at a shallow depth of between 20 µm and 70 µm below the riffle valley, which indicates that the weak loading in this area is not enough to completely destroy the rolling texture originating from the production process.

During the service, a wheel and a rail have to bear any movement together at their contact area. Therefore the investigations of wheel sample unravel a nearly same texture evolvement in the subsurface as the rail samples. The maximum of the texture was also situated in the subsurface of the sample and a weak rolling texture was also found at a certain depth below the surface.

6.4 Comparison of the Rails investigated

The four rail samples investigated in this thesis have roughly the same composition (Table 4.4) and also have nearly the same microstructure in the bulk materials, pearlite. The tensile strength of them is also in the same range. In addition, the white etching layers were invariably found on all four kinds of corrugated rail samples. Nevertheless, due to the different loading and different working conditions, the microstructure alterations, texture evolvement and the residual stress state on the rail sample surface are still different from each other.

According to Table 4.1, the rail DB AG has been in service as the outside rail segment in a left turn. Certainly, most loading was exerted at the field corner of the rail, therefore an obvious bright rolling band was in sight just at the field corner of the rail surface (Fig. 4.1). In contrast, on the rail Baumann that was at work in a straight section, the separated bright white patches were observed not only at the field corner of the rail but also at the gauge corner of the rail due to the unstable contact between the rail and wheel (Fig. 4.2). Thus, the different service conditions cause the different contact and loading pattern on the rail surface.

In those frequently contact areas, the plastic deformation accumulates with an increasing load cycles. Then, the high compressive residual stresses arise in these regions. Thus, different contact and loading patterns induced further different residual stress distributions on rail surfaces. On the surface of rail DB AG, the residual stresses showed a tendency to increase from the gauge corner of the rail towards the field corner of the rail and the maximum of residual stress was found at the field corner of the rail (Fig. 5.3.1). However on the surface of the rail Baumann, the residual stress was apt to increase in the white patches and the maximum was situated within a white patch (Fig. 5.3.7). The analogous residual stress distributions were also found on the other two strongly loaded rail samples, rail sample 2 and rail sample 3.

Further comparison between the weakly loaded rails (rail DB AG and rail Baumann) and strongly loaded rails (rail sample 2 and rail sample 3) reveals that a higher loading magnitude causes a more severely corrugated surface (Fig. 4.3 and Fig. 4.4). And higher maximum compressive residual stresses was also induced. But, the magnitude of residual stresses is not simply proportional to the loading magnitude, it is influenced also by other factors, e.g. working conditions and the rail profile.

On the surface of these four rail samples, the same fiber texture components <111> and <551> were found. The detailed texture analyses on the rail DB AG and the rail Baumann showed a same tendency that the fiber texture decreased with the increasing loading.

Although the hard and homogeneous White Etching Layers were observed on these four rails under the optical microscope, the difference of the structure is obvious. On the rail Baumann, the most weakly loaded rail, there is obvious ferrite boundary

existing even within the white etching layer. It indicates that the contact temperature on the surface of rail Baumann is not high enough for the ferrite to transform into the austenite and then the ferrite remains in the WEL. However no such white etching layer intermixed with ferrite boundary was found again on the surface of rail sample 2 and rail sample3, even also not on the surface of rail DB AG. Thus, it can be deduced that the contact temperature is influenced strongly by the loading during the service. Of course the roles of rail head profile and working condition playing in the microstructure changes also should not be overseen.

As for the microhardness of the WELs, there is no big difference found on these four rail samples. The microhardness of the WEL on the rail sample 2 and rail sample 3 is a little bit higher than that on the rail Baumann, but the difference is not very much, only 100 HV 0,2. The inhomogeneous microhardness distribution within the WEL was invariable found in all of these four investigated rail samples.

In addition, the different loading and different service parameters did not induce very different distributions of residual stresses and texture in the sample subsurface. The in - depth responses to the cyclic loading in these four rail samples were roughly in the same way. The higher compressive residual stresses was always found on the top surface of the rail samples. Without exception among these four rail samples, the residual stresses change quickly from compressive state to the tensile state with increasing distance to the surface. The texture in the in - depth direction was investigated only on two weakly loaded rails. It distributes also in the nearly same way in the subsurface of two rail samples. The maximum of the texture index was determined not on the superficial surface, but in the interior of the rail samples.

6.5 Differences between Microstructure Changes in the System Rail – Wheel and in Bearings

Although the geometry and lubricant requirement in the bearings and rail - wheel system build a big contrast to each other, both are categorized as rolling contact and even the same simple simulation model, a cylinder rolling on a plane, could be applied to both systems /Voskamp 1996, Johnson 1958/. Also, owing to the requirement to the ever - increasing loading requirements, the bearings face the same challenge as the rail - wheel system and, thus, receive a lot of scientific and

technological interest. For the purpose of a better understanding of the material responses to the rolling contact a comparison between the rail – wheel system and bearings is given in the following paragraph.

Materials

The material used in bearing and rail - wheel system is steel, but with different carbon content and different alloying elements, and, therefore, with different microstructures. Medium carbon steel with 0,9% ~ 1,5% manganese is usually used as rail and wheel steels, while through - hardened and partially tempered chromium steel is mostly used in bearings /Wan 1991/. Since there are various kind of bearings for different working conditions, a 6309 type deep grooved ball bearing with hardened and tempered steel SAE 52100 with 0,97% carbon, 1,43% Chromium, 0.31% Manganese that was studied in detail by /Martin 1966, Swahn 1976, Voskamp 1996/ is chosen here for comparisons to the rail and wheel samples studied in this thesis.

As already stated, the rail - wheel steel studied here is ferrite / pearlite with a micro - hardness of about 300 HV 0,2, while the hardened and tempered bearing with SAE 52100 is composed of martensite and the dispersed retained austenite intermixed with globular cementite particles and a microhardness of 820 HV 0,2.

Microstructure changes

In both the rail - wheel system and the bearings, distinct microstructure changes occur due to cyclic stressing in the rolling contact /Bush 1961, Pyzalla[1 - 2] 2000/.

The formation of White Etching Layers is a well - known problem in the rail - wheel system. No method is found to avoid the occurrence of the WEL and only its developing time can be supposedly delayed.

As for the ball bearing inner ring, a Dark Etching Region that is usually first observed in the rolling contact process is followed by the development of a White Etching Band in the dark etching regions /Jones 1946, Voskamp 1997/. They occurred beneath the raceway along the whole circumference of the bearing ring, which characterizes the massive microstructure changes within the ball bearing.

The white etching layer that looks like to be inhomogeneous in the rail and wheel under the SEM is observed extended to the surface with the half elliptical contact contour, and it can be divided into at least two layers under the SEM in virtue of the different grain size.

While the dark etching region and white etching band in the bearing inner ring do not extend till the surface, but also with the shape of contours resembling the contact load induced subsurface stress field /Voskamp 1998/. The white etching bands in the bearings occurs with two different morphologies and orientations, namely low angle bands and high angle bands, according to the angle of the band that inclined to the raceway surface in the rolling direction /Voskamp 1996/. This phenomenon is also reported by /Martin 1966, Swahn 1976/. But the mechanism of the formation of the band angle can not be clearly explained yet.

That indicates the close association of the massive microstructure alteration with the contact stress in both rolling contact system. On the other hand it reveals that the different working condition cause the massive deformations to form in the different position. The lubricant supplies very good protection to the surface of bearing, so the structure changes happen not on the surface, but in a certain depth of the maximum contact stress. However the severe dry rolling contact rise the temperature very much on the surface of rail and wheel samples so that the transformation happens directly at the surface.

As it has been demonstrated here, the white etching layers in wheel and rail samples are composed of the ultra - fine grained martensite and retained austenite intermixed with well dispersed globular nano - sized carbides that bring about extremely high micro - hardness of up to 1000 HV 0,2 (compared to 300 HV 0,2 in the bulk material). The ultra – fine martensite is induced by a phase transformation under severe plastic deformation on the rough rolling surface. The nano - sized carbides originate from the continually broken of remaining carbide that do not dissolve during the austenization under the strong mechanical stress.

/Swahn 1976, Voskamp 1996/ supposed that a martensite decay into ferrite and carbides is the reason for the formation of dark etching region in ball bearing system. It happens in the incipient period of the rolling contact service. The decay is

attributed to a localized stress - induced phase transformation under the cyclic loading. With prolonging service time, the dark etching layers become dense.

Gradually the white etching bands in the bearing inner ring evolve with increasing service time. A long ribbon of a ferrite and carbide rich region or globular cementite particles are found in low angle bands. An equi - axed ferrite region with a small fraction of tiny cementite particles is present in high angle bands. A significant reduction in hardness to about 670 HV 0,2 has been found for the microstructure in the high – angle bands. This hardness decrease in the high angle bands is understood from an increase of the amount of ferrite during cycling stressing. A strong local reduction of carbon is proven within the high angle bands and the carbides in these areas are supposed to be removed into the low angle band area. During this process, the stress - induced carbon diffusion is possible over sufficiently long range. Similar to the rail - wheel system, the stress - induced breakup of the large primary carbides is frequently observed in bearing system.

Although the bearing works in a well lubricant condition, a significant rise of temperature is also expected. An estimation of temperatures exceeding 200 °C is reported by /Johnes 1946/. The internal deformation that is associated with energy dissipation is supposed to be the reason. The local rise in temperature is the cardinal effect leading to material softening. Thus, the carbon diffusion induced can lead to the activation of potential slip systems. As a result an increasing number of dislocation can move, and over increasing distance. It promotes martensite softening and carbon diffusion. Due to the difficulty in measuring the temperature rise, the magnitude of the temperatures in the service has stayed an arguable point in these two rolling contact systems.

Texture development and residual stresses

The inserted plastic deformation will bring the formation of the texture in these two rolling systems.

A combination of <111> and <551> fiber texture is found in the rail - wheel system. They are supposed to be provoked by the axle loading and the shear stress on the rail – wheel system. (111) $[\bar{2}11]$ rolling texture that supposedly originated from the

production process was found only at a specific depth below the surface of rail Baumann.

However in the bearing system the rolling textures of {111} <211> and {100} <110> are found /Voskamp 1996/. These two common rolling textures might be considered as the result of deformation and dynamic recrystallization. Clearly in these two system the dominant force is different, axle loading control the texture development in the rail - wheel system while in the bearing system does the rolling action governs the texture evolvement. The maximum of the texture is found in a certain depth below the surface in both system. Another point that should be alluded is that the fiber texture is also observed when the bearing running at a smaller load (maximum contact stress of 3,8 GPa), but at higher operating temperatures (e.g. 90°C), resulting primarily in an onset of a same <111> fiber texture, as in rail - wheel system /Voskamp 1996/

Compressive stresses are found both in the rail - wheel system in longitudinal, transverse and diagonal direction and in the bearing system in circumferential and axial direction.

A continuous increase of residual stress with the number of inner ring revolution is found, just as the residual stress distribution with the loading along the rail surface. In bearing system, the local plastic deformation involves material flow in direction parallel to the surface. This lateral flow, in the axial and circumferential direction, resulting in the building up of the compressive stress in these two directions. The same mechanism contributes to the compressive residual stresses developed in the longitudinal direction, equivalent to the circumferential direction of the bearing, and in the transverse direction, equivalent to the axial direction of bearing.

The residual stresses are the result of plastic deformation on highly localized scale. The residual stresses reach the maximum in a depth below the bearing inner ring surface that the maximum of texture happens. However the maximum of the residual stresses are found on the surface of the rail since only two dimensional residual stresses were analyzed in the interior of the rail sample. The rolling contact under the load would bring the unavoidable plastic deformation to the rail - wheel system and bearing system. But for the different working requirements, the reaction of the materials is different and thus the subsurface response is also not the same.

7. Summary and Conclusions

Under the cyclic loading and wear, obviously microstructure alterations and the corrugation on the rail and wheel surface are induced.

Distinctive spatial - dependent structures are developed on the rails and wheel surface because of the spatial – dependence of the loading along the rail surfaces and the wheel surface during rolling contact both on the weakly loaded samples and on the heavily loaded samples.

The local plastic deformation induced on the rail and wheel surface brings about the compressive residual stresses in longitudinal and transverse directions. The compressive residual stresses increase with the loading on the surface. The maximum of the residual stress was situated on the sample surface.

A strong loading causes more severely corrugated surface and induces higher maximum of the residual stresses. But the magnitude of residual stresses is not simply proportional to the loading magnitude.

The different loading exerted on the samples does not induce a very big difference in the microhardness of the WEL and the subsurface response.

The contact surface of rail - wheel system undergoes not only mechanical stress but also thermal stress.

White Etching Layer are formed in the region showing the increasing compressive residual stresses. In these regions high temperature is reached and even extends to a certain depth below the surface. The thermal structure transformation of ferrite into austenite and austenite into martensite during cooling is imperative for the formation of White Etching Layer.

Martensite comes into being by repeated thermal phase transformation through ferrite / pearlite – austenite – martensite. The severe predeformed austenite would bring about the ultra - fine grained martensite during the quick cooling.

The carbide cannot be completely dissolved for the reason of the time shortage of the austenization happened in the contact zone of rail - wheel system. The remaining

undissolved carbide is broken under the strong loading and wear and finally exists as nano – sized particles.

The White Etching Layer consists of ultra - fine grained marteniste, the remaining austenite and ferrite / pearlite intermixed with well – dispersed nano - sized carbide.

No decarburization happens in the top layer of rails. The possibility of the formation of Nitrogen martensite can also be excluded for the samples in this thesis.

The formation of nano - structured martensite and carbide on the rail and wheel surface causes the extremely high microhardness and the strong corrosion resistance of the White Etching Layer.

A combination of a <111> and <551> fiber texture is formed on the rail and wheel surface under the loading and the rolling contact. The texture component <111> might evolve through high pressure during the rolling of passing trains and the <551> fiber texture is induced by shear stress.

The texture components of the martensite is inherited from austenite. The martensitic transformation, especially a repeated austenite - martensite transformation, weakens the texture. The texture component decreases with the loading increasing on the sample surface.

The maximum of the texture is found not on the sample surface, but in a certain depth below the surface. In the subsurface, a weak rolling texture was found below the surface of rail Baumann. (111) $[\bar{2}11]$ rolling texture was also found in the depth between 20 µm and 70 µm below the weakly loaded area of the rail Baumann.

8. Zusammenfassung

In der vorliegenden Arbeit wurde der Einfluss der Betriebsbeanspruchung auf die Mikrostruktur, Textur und Eigenspannungen an der Schienenoberflächen und im oberflächennahen Bereich von Eisenbahnschienen untersucht. Die hohen mechanischen und thermischen Belastungen an der Schienenoberfläche, die beim Überrollen durch Schienenfahrzeuge vorhanden sind, führen zur Entstehung sog. Weißer Schichten und Riffelbänder. Obwohl die weißen Schichten bereits seit längerem bekannt sind, ist deren Entstehung und Struktur weiterhin strittig.

In der vorliegenden Arbeit wird ein Mechanismus für die Entstehung der weißen Schichten formuliert, der auf den Ergebnissen der Röntgenanalysen sowie mikroskopischen Untersuchungen basiert. Dazu wurden zerstörungsfreie Textur – und Eigenspannungsanalysen mittels Röntgen- und mittelenergetischer Synchrotronstrahlung durchgeführt. Der Ausscheidungszustand wurde mittels ASAXS im DESY, Hasylab, in Hamburg charakterisiert. Die Darstellung des Gefüges erfolgte am Lichtmikroskop sowie im Rasterelektronenmikroskop. Weiterhin wurden in unterschiedlichen Abständen zur Schienenoberfläche Mikrohärteverläufe und mittels Mikrosonde durch chemische Elementanalysen aufgenommen. Mit einem Profilometer wurde die Schienentopographie abgebildet.

Die weißen Schichten und Riffelbänder lassen aufgrund der lokalen Verteilung an der Schienenoberfläche, die im Lichtmikroskop sichtbar ist, darauf schließen, dass die Schiene im Betrieb lokal an einzelnen Stellen stark beansprucht wurde.

Im Bereich von weißen Schichten sind hohe Druckeigenspannungen vorhanden, wobei sich das Maximum der Eigenspannungen direkt an der Schienenoberfläche befindet. Demzufolge liegt der Schluss nahe, dass die weißen Schichten durch plastische Verformung entstehen.

Auf der Schienenoberfläche wurde in den weißen Schichten Restaustenit festgestellt. Da im Herstellungszustand kein Restaustenit vorhanden ist, muss während der Betriebsbeanspruchung zeitweise die GS – Linie im Eisen – Kohlenstoff – Diagramm überschritten worden sein. Bei der Abkühlung nach der blitzartigen Temperaturerhöhung entsteht der Restaustenit sowie Martensit in den weißen

Schichten. Der Martensit ist gegenüber dem Ferrit tetragonal verzerrt, was sich im c_m / a_m – Verhältnis des Martensites äußert. Außerdem ist die Mikrohärte in den weißen Schichten im Vergleich zum Grundwerkstoff, aber auch relativ zu den Werten für herkömmlichen Martensit, besonders groß. Eine solch große Härte ist typisch für nanokristalline Werkstoffe. Im Zusammenhang mit den Halbwertsbreiten der Reflexe, die mit Röntgen – und – Synchrotronstrahlung aufgenommen wurden, sowie den Ergebnisse von ASAXS, wird deshalb geschlossen, dass der Martensit in den weißen Schichten eine nanokristalline Struktur besitzt.

Die starke Verformung an der Schienenoberfläche erfolgt zum Teil im Austenitgebiet. Dies ist zugleich die Ursache bei anschliessender Abkühlung zur Bildung des sehr feinen Martensit. Die stetige Verformung indes führt zu einer Verringerung der Domänengröße.

Der Zementit wird während der thermischen Belastung durch Schubspannungen gebrochen und teilweise aufgelöst. Der mittlere Radius der Zementitteilchen in den weißen Schichten beträgt 2nm.

Eine <111>-Fasertextur auf der Oberfläche der Schiene weist darauf hin, dass diese Fasertextur durch die hohen Druckspannungen beim Überfahren der Schiene entsteht. Eine weitere Texturkomponente <551> wird von der Scherspannung hervorgerufen. Im Inneren dieser Schiene wird außerdem eine schwache Waltztextur gefunden.

In dieser Arbeit wird die bekannte Texturvererbung zwischen den Phasenumwandlung von Austenit zu Martensit bestätigt. Ein Effekt der Phasentransformation ist die Schwächung der Texturkomponenten wobei die Ursache eine mehrmalige Transformation über die Schienenlauffläche ist, im Detail Ferrit/Perlit – Austenit – Martensit. Der Texturverlauf über die Schienenlauffläche, der durch eine Verringerung der Textur mit steigender Belastung, d.h. steigendem c/a – Verhältnis des Martensits gekennzeichnet ist, deutet darauf hin, dass im Austenitgebiet erhebliche Deformation stattgefunden hat.

Das Maximum der Texturkomponente befindet sich nicht an der Oberfläche der Schienen, sondern innerhalb der Schiene. In der Schiene Baumann wurde in der Tiefe zwischen 20 µm und 70 µm eine $(111)\,[\bar{2}11]$ Walztextur ermittelt.

9. Literatures

/Abdel - Aal1998/ Abdel-Aal, H.A.; Smith, S.T.: On Friction - induced Temperatures of Rubbing Metallic Pairs with Temperature - dependent Thermal Properties, Wear 216 (1998), S. 41 – 59

/Agnew 2000/ Agnew, S.R.; Elliott, B.R.; Youngdahl, C.J.; Hemker, K., J.A. and Weertman, J.R.: Microstructure and Mechanical Behavior of Nanocrystalline Metals, Materials Science and Engineering A285 (2000), S. 391 - 396

/Ahlström 1999/ Ahlström, J.; Karlsson, B.: Microstructural Evaluation and Interpretation of the Mechanically and Thermal Affected Zone under Railway Wheel Flats, Wear 232 (1999), S. 1 – 14

/Andersch 2000/ Andersch, L.: Entwicklung eines FE - Modells mittels einer speziellen Substrukturtechnik zur Ermittleung von Vorgängen im Rad – Schiene - Kontakt, Diplomarbeit, Technische Universität Berlin Institut für Luft - und Raumfahrt, Sept. (2000)

/Archard 1959/ Archard, J.F.: The Temperature of Rubbing Surface, Wear 2 (1958 / 1959), S. 438 - 455

/Aronov 1980/ Aronov, V. and Kalpakjian, S.: Wear Kinetics of Rail and Wheel Steels in the Dry Friction Condition, Wear 61 (1980), S. 101 - 110

/ASTM G5 - 87/ ASTM - Norm G5-87, Annual book of ASTM standards, Vol. 03.02 (1991)

/Bain 1924/ Bain, E.: The Nature of Martensite, Trans. American Institute of Mining and Metallurgical Engineerings 52 (1924), S. 25 - 46

/Baumann[1] 1996/ Baumann, G., Grohmann, H.D. und Knothe, K.: Wirkungsketten bei der Ausbildung kurzwelliger Riffeln auf Schienenlaufflächen, ETR 45 (1996), H12, Dezember, S.792

/Baumann[2] 1996/ Baumann, G., Fecht, H.J. and Liebelt, S.: Formation of White - Etching Layers on Rail Treads, Wear 191 (1991), S.133 - 140

/Baumann 1998/ Baumann, G.: Untersuchungen zu Gefügestrukturen und Eigenschaften der “Weißen Schichten” auf verriffelten Schienenlaufflächen, Dissertation, TU - Berlin, 1998

/Bever 1986/ Bever, B.M.: Encyclopedia of Materials Science and Engineering 6 (1986), R - S.

/Bijak 1997/ Bijak - Zochowski, M. and Marek P. : Residual Stress in some elasto - plastic Problems of Rolling Contact with Friction, Int. J. Mech. Sci. 39 (1997), S. 15 - 32

/Birmann 1958[1]/ Birmann, F. und Minden, I.W.: Schienenriffeln, ihre Erforschung und Verhütung Teil 1: Schwingungsuntersuchungen, VDI - Z. 100 (1958) Nr. 26, 11 September, S. 1253 - 1262

/Birmann 1958[2]/ Birmann, F. und Minden, I.W.: Schienenriffeln, ihre Erforschung und Verhütung Teil 2: Werkstoff - Untersuchungen und Abhilfemaßnahmen, VDI - Z. 100 (1958) Nr. 26, 11 September, S. 1253 - 1262

/Birwirth 1961/ Bierwith, G.: Die röntgengraphische Bestimmung des Restaustenits in einsatzgehärteten Stählen, Materialprüf. 3 (1961) Nr. 6

/Blok 1963/ Blok, H.: The Flash Temperature Concept, Wear 6 (1963), S. 483 - 494

/Bower 1991/ Bower, A.F.: Plastic Flow and Shakedown of the Rail Surface in repeated Wheel - Rail Contact, Wear 144 (1991), S. 1 – 18

/Brockley 1988/ Brockley, C.A.: An Investigation of Rail Corrugation Using Friction - Induced vibration Theory, Wear 128 (1988), S. 99 - 106

/Bucher 2000/ Bucher, F.; Knothe, K. und Theiler, A.: Normal and Tangential Contact Problem of Surfaces with Measured Roughness, 5th International Conference of Contact Mechanics and Wear of Rail / Wheel System, Tokyo, Japan, 25 - 28 July 2000

/Bucher 2001/ Bucher, F.; Goltsch, M.; Österle, W.; Pyzalla, A.; Reimers, W.; Santner, E.; Spaltmann, D.; Theiler, A.; Urban, I.; Wang, L.; Wild, E.: Untersuchungen an der Oberflächen - Randschicht einer unverriffelten UIC60 - Schiene, Schriftenreihe des

Sfb605, Sfb - Bericht 2001/1, Technische Universität Berlin, Sonderforschungsbereich 605, S. 6

/Bunge 1985/ Bunge, H.J.: Technological Applications of Texture Analysis, Z. Metallkunde 76 (1985), S. 457 - 470

/Bunge 1988/ Bunge, H.J.: Directional Properties of Materials, DGM, Oberursel (1988)

/Bush 1961/ Bush, J.J.; Grube, W.L. and Robinson, G.H.: Microstructural and Residual Stress Changes in Hardened Steel Due to Rolling Contact, Transactions of the ASM 54 (1961), S. 391 - 413

/Busse 1908/ Busse, H.: Riffelbildung auf den Schienenfahrflächen der Bahnen, Internationaler Straße - und Kleinbahnkongress München 7. bis 10. Sept, 1908

/Carter 1926/ Carter, F.W.: On the Action of Locomotive Driving Wheel. Proc. Roy. Soc., Ser. A., Vol.112 (1926), S. 151

/Cridney 1972/ Cridnev, V.N.: Investigation of Carbide Phase in strained Steel by Method of Nuclear Gamma Resonance, Phys. Stat. Sol.(a) 14 (1972)

/Dearden1960/ Dearden, J.: The Wear of Steel Rails and Tires in Railway Service, Wear 3 (1960), S. 43 - 59

/Delhez 1982/ Delhez, R.; Keijser, Th.H.De and Mittemeijer, E.J.: Determination of Crystallite Size and Lattice Distortions through X - ray Diffraction Line Profile Analysis, Fresenius Z. Anal. Chem. 312 (1982), S. 1 - 16

/Döring 1955/ Döring, J.: Untersuchungen von Riffelschienen, DB-Versuchsamt für mech. Stoffprüfung Nr. 46294 (1995)

/Eisenmann 1977/ Eisenmann, J.: Riffelbildung bei Schienen, Mittelungen des Prüfamtes für den Bau von Landverkehrswegen der TU München 29 (1977)

/Ermolaev 2000/ Ermolaev, G.N.: Mechanical Properties of Materials in the Range of Martensitic Transformations at High Pressures, The Physics of Metals and Metallography Vol. 89, 4 (2000), S. 86 - 90

/Ertz 2000/ Ertz, M. and Knothe. K.: Die Temperaturentwicklung im Rad-Schiene - Kontakt und ihre Auswirkungen auf Kraftschluss und Materialbeansprung, BahnBau Sept. (2000)

/Eyre 1972/ Eyre, T.S. and Baxter: The Formation of White Layers at Rubbing Surfaces, Tribology, December (1972), S. 256 - 261

/Faninger 1972/ Faninger, G. und Hartmann, U.: Physikalische Grundlagen der quantitativen röntgenographischen Phasenanalyse (RPA), HTM 27 (1972), S. 233 - 244

/Fastenrath 1977/ Fastenrath, F.: Die Eisenbahnschiene, Verlag von Wilhelm Ernst & Sohn (1977)

/Feigin 1987/ Feigin, L.A. and Svergun, D.I.: Structure Analysis by Small - Angle Neutron Scattering, 1. Edition, Plenum Press, New York and London (1987)

/Feller 1991/ Feller. H.G. and Walf. K.: Surface Analysis of Corrugated Rail Treads, Wear 144 (1991), S. 153 - 161

/Fessler 1957/ Fessler, H. and Ollerton, E.: Contact Stresses in Toroids under radial Loads, British Journal of Applied Physics, 8 (1957), S. 387 - 393

/Field 1970/ Field, M.; Koster, W.P.; Kohls, J.B.; Snider, R.E. and Maranchik, J.: Machining of High Strength Steels with Emphasis on Surface Integrity, Air Force Machinability Data Center Report No. AFMDC – 70 - 1, (1970)

/Fink 1953/ Fink, M.: Die Entstehung der Schienenriffel, Stand der Riffelforschung nach rund 60 Jahren, Glasers Annalen 77 (1953), S. 342 - 373

/FP 1998/ Friction Theory, Published in Marine University of Dalian, China, (1998)

/Fromm 1927/ Fromm, H.: Berechnung des Schlupfes beim Rollen deformierbarer Schienen, Zeitschrift für Angewandte Mathematik und Mechanik 7 (1927), S. 27

/Ganapathi 1991/ Ganaphathi, K.S.; Aindow, M.; Fraser, H.L.; and Rigney, D.A.: A Comparative Study of the Nanocrystalline Material Produced by Sliding Wear and Inert Gas Condensation, Mat. Res. Soc. Symp. Proc. 206 (1991), S. 593 - 598

/Genzel 1999 / Genzel, C.: Entwicklung eines Mess- und Auswerteverfahrens zur röntgengraphischen Analyse des Eigenspannungszustandes im Oberflächenbereich vierkristalliner Werkstoffe, Habilitation, Humboldt Universität Berlin (1999)

/Glenn 1971/ Glenn, R.C., and Leslie, W.C.: The Nature of White Streaks in Impacted Steel Armour Plate, Met. Trans. 2 (1971), Oct. S. 2945 - 1947

/Goerigk 1997/ Goerigk, G.; Haubold, H.G. and Schilling, W.: Kinetics of Decomposition in Copper – Cobalt: A Time – Resolved ASAXS Study, J. Appl. Cryst 30 (1997), S. 1041 - 1047

/Goerigk 1998/ Goerigk, G. and Williamson, D.L.: Nanostructured Ge Distribution in α - SiGe: H Alloys From anomalous Small - Angle X - ray Scattering Studies, Solid State Commuciations, Vol. 108, 7 (1998), S. 419 - 424

/Goerigk 2001/ Goerigk, G.; Williamson, D.L.: Quantitative ASAXS of Germanium Inhomogeneities in amorphous Silicon - Germanium Alloys, Journal of Non – Crystalline Solids 281 (2001), S. 181 - 188

/Griffiths 1987/ Griffiths B.J.: Mechanisms of White Layer Generation With Reference to Machining and Deformation Processes, Journal of Tribology 109 / 525 (1987)

/Groma 1988/ Groma I. and Ungar, T.: Asymmetric X - ray Line Broadening of Plastically Deformed Crystals I. Theory, J. Appl. Cryst. 21 (1988), S. 47-53

/Grotzin 1962/ Grotzin, B.D., and Iankevich, V.F.: The Structure of White Layers, Friction and Wear in Machinery 15 (1962) 143

/Guinier 1955/ Guinier, A. and Fournet, G.: Small - Angle Scattering of X - rays, New York, Wiley (1955)

/Hartherly 1977/ Hartherly, M.; Hutchinson, W.B.: An Introduction to Textures in Metals, The Institute of Metallurgists (1977)

/Haubold 1988/ Haubold, H.G.: Jusifa – Ein nutzerfreundliches Instrument für die Röntgenkleinwinkelstreuung, Sonderdruck aus:

Jahesrbericht 1987 / 1988 der Kernforschungsanlage Jülich GmbH

/Hauk 1994/ Hauk, V.; Kockelmann, H.: Eigenspannungszustand auf der Lauffläche einer Eisenbahnschiene, HTM 49 (1994), S. 340 - 351

/Hellier 1986/ Hellier, A.K.: A Study of Subsurface Rail / Wheel Contact Stresses with Application to Modelling Rail Fatigue, Contact Mechanic and Wear of Rail - Wheel Systems 2 (1986), S. 421 - 434

/Hellier 1991/ Hellier, A.K.: A Finite Element and Fatigue Threshold Study of Shelling in Heavy Haul Rails, Wear 144 (1991), S. 289 - 306

/Hempelmann 1994/ Hempelmann, K.: Short Pitch Corrugation on Railway Rails, VDI Reihe 12, Nr. 231, VDI - Verlag, Düsseldorf (1994)

/Hoffmann 2001/ Hoffmann, B.; Vöhringer O. and Macherauch, E.: Effect of Compressive Plastic Deformation on Mean Lattice Strains, Dislocation Density and Flow Stresses of Martensitically Hardened Steels, Materials Science and Engineering A 319 - 321 (2001) S. 299 - 303

/Hoffmann 1997/ Hoffmann, B.; Vöhringer O. and Macherauch, E.: Effect of Tempering on the Microstructure and Strength of Martensitically Hardened Plain Carbon Steels, Materials Science and Engineering A 234 - 236 (1997), S. 707 - 710

/Jaeger 1943/ Jaeger, J.C.: Moving Sources of Heat and Temperature at Sliding Contacts, Proc. R. Soc. NSW 76 (1943), S. 203 - 210

/Johnes 1946/ Johnes, A.B.: Metallographic Observations of Ball Bearing Fatigue Phenomena, Proceedings American Society Testing Materials 46 (1946), S. 1

/Johnson 1958/ Johnson, K.L.: The Effect of a Tangential Contact Force upon the Rolling Motion of an elastic Sphere on a Plane, September (1958), England, Cambridge University Press

/Johnson 1985/ Johnson K. L.: Contact Mechanics, Cambridge University Press (1985)

/Kaess1983/ Kaess, G.: Ergebnisse von Riffelversuchsstrecken der Deutschen Bundesbahn, ETR 32 (1983) 10, S. 701 - 707

/Kashiwaya 1989/ Kashiwaya, Kenji; Inoue, Yasuo and Satoh Yukio: Study of Rolling Contact Fatigue in Rails Using X - ray, QR of RTRI Vol. 30, 3 (1989) Aug., S. 162 - 169

/Kawamoto 1971/ Kawamoto, M. and Okabayashi, K.: Wear of Cast Iron in Vacuum and the Frictional Hardened Layer, Wear 17 (1971), S. 123 - 138

/Knothe 1995/ Knothe, K., Liebelt, S.: Determination of Temperature for Sliding Contact with Application for Wheel - Rail Systems, Wear 189 (1995), S. 91 - 99

/Krause 1979/ Krause, H. and Demiric, A.H.: Plastische Verformungen hervorgerufen durch Reibungsbeanspruchung im Kontaktflächenbereich eines Wälzsystems, Z. Metallkde, 70 (1979), S. 496 - 499

/Krause 1989/ Krause, H. and Demiric, A.H : Texture Changes in the Running Surfaces of Face - centered Cubic Metals as the Result of Frictional Stress, Wear 61 (1980) S. 325 - 332

/Krause 1986/ Krause, H. and Poll, G.: Wear 113 (1986), S. 103 - 122

/Kuhlmann – W^1 1987/ Kuhlmann – Wilsdorf: Demystifying Flash Temperatures, 2. First – Order Approximation for Plastic Contact Spots. Materials Science and Engineering 93 (1987), S. 119 - 133

/Kuhlmann -W^2 1987/ Kuhlmann – Wilsdorf: Demystifying Flash Temperatures, 1. Analytical Expressions Based on simple Model, Materials Science and Engineering 93 (1987), S. 107 - 117

/Kurdjumov 1930/ Kurdjumov, G. and Sachs, G.: Walz und Rekristallisationstextur von Eisenblech, Mitteilung aus dem Kaiser – Wihelm - Institut für Metallforschung, Berlin-Dahlem (1930), S. 592 - 599

/Kuznetsov 1963/ Kuznetsov, V.D.: Some Features of the Structure of White Layers, Fiz. Metal. Metallurgy. 15 (1963), S. 145

/Lindholm 1974/ Lidholm, U.S.: Review of Dynamic Testing Techniques and Material Behavior, Proceedings of the Conference on Mechanical Properties of Materials at High Rates of Strain, held in Oxford, England, 2 - 4 April 1974, published by Institute of Physics, Conference Series No. 21, S. 18

/Lunden 1991/ Lunden, R.: Contact Region Fatigue of Railway Wheels under Combined Mechanical Rolling Pressure and Thermal Brake Loading, Wear 144 (1991), S. 57 - 70

/Macherauch 1961/ Macherauch, E. und Müller, P.: Das $\sin^2\psi$ - Verfahren der röngenographischen Spannungsmessung, Zeitschrift für Angewandte Physik 13 (1961), Heft 7, S. 305 - 372

/Magel 1999/ Magel, E.: Optimizing Wheel, Rail Profiles, Railway Track and Structures, July (1999)

/Marschall 1968/ Marschall, E.A.: Rolling Contact with Plastic Deformation, J. Mech. Phys. Solids 16 (1968), S. 243 - 254

/Martin 1966/ Martin, J. A.; Borgese, S. F.; Eberhardt, A.D.: Microstructural Alterations of Rolling - Bearing Steel Undergoing Cyclic Stressing, Journal of Basic Engineering Sep. (1966), S. 555 - 567

/Meywerk 1998/ Meywerk, M.: Riffelbildung auf Schienen mit Orts - und Zeitabhangigen Verschleißkoeffizienten, Technische Mechanik 18 (1998) 2, S. 95

/Naumann 1961/ Naumann, F.K.: Gefügeuntersuchungen an verriffelten Schiene, Arch. f. d. Eisenhüttenwesen, 32 (1961), S. 617 - 626

/Newcomb 1984/ Newcomb, S.B.: A Transmission Electron Microscope Study of the White Etching Layer on a Rail Head, Materials Science and Engineering 66 (1984), S.195 - 204

/Noyan 1987/ Noyan, J.; Ismail, C. and Cohen, B.: Residual Stress Measurement by Diffraction and Interpretation, Springer – Verlag, New York (1987)

/Österle 2001/ Österle, W.; Rooch, H.; Pyzalla, A.; Wang, L.: Investigation of White Etching Layers on Rails by Optical Microscope, Electron Microscope, X - ray and Synchrotron X - ray Diffraction, Materials Science and Engineering A 303 (2001), S. 150 - 157

/PR 1985/ Focus on Corrugations. Progressive Railroading 12 (1985), S. 42 - 46

/Pyzalla[1] 2000/ Pyzalla, A.; Wild, E.; Wang, L.; Wroblewski, T.: Investigation of the Microstructure and the Residual Stress State of a Worn Railway Rail, Proc. ICRS6, Vol. 2, Oxford, 10 - 12 July 2000, IOM Communications Ltd., London, GB (2000), S. 889 - 896

/Pyzalla[2] 2000/ Pyzalla, A.; Wild, E.; Wang, L.; Wroblewski, T.: Einfluss des Verschleisses auf die Mikrostuktur und Eigenspannungszustand von Schiene, Mat. - Wiss. Wekstofftechnik 31 (2000), S. 776 - 779

/Pyzalla 2001/ Pyzalla, A.; Wang, L.; Wild, E.; Wroblewski, T.: Changes in Microstructure, Texture and Residual Stresses on the Surface of a Rail resulting from Friction and Wear, Wear 251 (2001), S. 901 - 907

/Quinn 1987/ Quinn, T.F.J. and Winer, W.O.: An Experimental Study of ”Hot Spots” Occurring During the Oxidation Wear of Tool Steel on Sapphire, Journal of Tribology Vol.109, April (1987), S. 315 - 328

/Ortner 1992/ Ortner, B.; Kühlein, W.; Stüwe, H.P.: Martensite Formation by Relaxation of Hydrostatic Pressure, Z. Metallkunde 83 (1992), S. 405 - 408

/RE 1988/ Roaring rails explained? Railway Engineer 2 (1988), S. 28 - 29

/Rogers 1971/ Rogers, M.D.: The Mechanism of Scuffing in Diesel Engines, Wear 15 (1971), S123 - 138.

/Rooch 2000/ Rooch, H., Li, Pengxi and Österle, W.: Metallographical Investigation of White Etching Layers on Railway Lines, Prakt. Metallgr. 38 (2001) 1

/Ruslan 1997/ Ruslan, Z.: Structure and Mechanical Properties of Ultrafine-grained Metals, Materials Science and Engineering A 234 - 236 (1997) S. 59 - 66

/Schmidt 1987/ Schmidt, I. and Wilhelm, M.: Friction-induced Martensitic Transformation of Hot - Rolled Austenitic Mn - Steels, Z. Metallkde 78 (1987) H. 2, S. 127

/Schultheiß 1985/ Schultheiß, H.: Riffelbildung auf Schiene, Stahl u. Eisen, 105 (1985), Nr. 25 - 26, S. 1457 - 1462

/Schleinzer 2000/ Schleinzer, G.: Residual stress Formation During the Roller Straightening of Rails, Fortschritt - Berichte VDI, Reihe 18, Nr. 251, Düsseldorf; VDI - Verlag (2000).

/Scott 1973/ Scott, D. and Mills, G.H.: Wear 24 (1973), S. 235 - 242

/Seabra 1987/ Seabra, J. and Berthe, D.: Influence of Surface Waviness and Roughness on the Normal Pressure Distribution in the Hertzin Contact, Transactions of the ASME, 109 (1987), July, S. 462 - 470

/Singer 1991/ Singer I.L., and Pollock H.M.: Fundamentals of Friction: Macroscopic and Microscopic Processes, Kluwer Academic Publisher, Dordrecht / Boston / London (1991), S. 3

/Sipos 1976/ Sipos, K.; Remy, L. and Pineau, A.: Influence of Austenite Predeforamtion on Mechanical Properties and Strain – induced Martensitic Transformations of a High Manganese Steel, Metallurgical Transactions A 7a (1976) June, S. 857 - 864

/Smallman 1985/ Smallman R.E.: Modern Phasical Metallurgy, Butterworth – Heinemann, Oxford, UK (1985)

/Spieker 1971/ Spieker, W.; Köhler, H.; Kühlmeyer, M.: Untersuchungen über die Riffelbildung auf Schienen in Versuchsstrecken unter üblichen Bedingungen des Fahrbetriebes, Stahl u. Eisen 91 (1971), Nr. 26

/Stanworth 1986/ Stanworth, C.G.: Wheel - Rail Noise Generation, Wear 113 (1986), S. 143 - 150

/Stead 1912/ Stead, J.W.: Micro - Metallography and its Practical Application, J. West. Scot. Iron and Steel Inst. 19 (1912), S. 169 - 204.

/Steinbeißer 1977/ Steinbeißer, L.: Schallmessungen in Zürich und München, VDJ – Berichte (1977) Nr. 217, S. 37 - 42

/Swahn 1976/ Swahn, H.; Becker, P.C. and Vingsbo, O.: Martensite Decay During Rolling Contact Fatigue in Ball Bearings, Metallurgical Transctions A, 7A (1976) August, S. 1099 - 1109

/Tanvir 1980/ Tanvir, M.A.: Temperature Rise due to Slip Between Wheel and Rail - An Analytical Solution for Hertzian Contact, Wear 61 (1980), S. 295 – 308

/Torrance 1974/ Torrance, A.A. and Cameron, A.: Surface Transformations in Scuffing, Wear 28 (1974), S. 299 - 311

/Turley 1975/ Turley, D.M.: The Nature of White – Etching Surface Layers Produced during Reaming Ultra-high Strength Steels, Materials Science and Engineering 19 (1975), S. 79 - 86.

/Ungar 1989/ Ungar, T. and Groma, I.: Asymmetric X-ray Line Broadening of Plastically Deformed Crystals. II, Evaluation Procedure and application to [001] - Cu Crystals, J. Appl. Cryst. 22 (1989), S. 26 - 34

/Vietor 1903/ Vietor, H.: Zum Kapitel Schienenabnutzung bei elektrischen Bahnen, Mittlg. Str. u. Kl. Bahnverwaltungen (1903), S. 265

/Voskamp 1996/ Voskamp, A.: Microstructural Changes during Rolling Contact Fatigue, Dissertation, TU Delft, Niederland

/Voskamp 1997/ Voskamp, A.; Nierlich, W. and Hengerer, F.: X - ray Diffraction Provides Answers to Bearing Failures, Evolution 4 (1997), S. 25 - 31

/Voskamp 1998/ Voskamp A.P.: Ermüdung und Werkstoffverhalten im Wälzkontakt, HTM 53 (1998), S. 25 - 30

/Vöhringer 1977/ Vöhringer, O. and Macherauch E.: Struktur und Mechanische Eigenschaften von Martensit, HTM 32 (1977), S.153 - 202

/Walloschek 1988/ Walloschek, Peter - Ulrich,.: Beitrag zur Ermittlung der Ursachen der Riffelbildung beim Rad / Schiene – System, VDI - Verlag GMBH Düsseldorf (1988)

/Walf 1981/ Walf, K.: Zur Bildung von Riffeln auf Schienenlaufflächen, Dissertation TU - Berlin (1981), D 83

/Wan 1991/ Wan Changsen: Analysis of Rolling Element Bearings, Mechanical Engineering Publication LTD London (1991), ISBN 0 85298 745 5

/Wassermann 1962/ Wassermann, G.; Grewen, J.: Texturen metallischer Werkstoffe, Springer - Verlag, Berlin (1962)

/Webster 1993/ Webster, P.J.; Mills. G.; Wang, X.; Xang, W.P.: Residual Stress Measurements in Rails by Neutron Diffraction, In Rail Quality and Maintenance for Modern Railway Operation, Kluwer Academic Publishers, Dordrecht, the Netherlands (1993), S. 307 - 314

/Wegener 2001/ Wegener, J.: Mikrostruktur, Textur und Eigenspannungen von stranggepressten und reibrührgeschweißten aushärtbaren Aluminiumlegierung, Dissertation, TU – Berlin 2001.

/Wieslaw 1980/ Wielsaw, A.R.: The Surface Layer of Friction Plastics, Wear 65 (1980), S. 21 - 27

/Wild 2000/ Wild, E.; Wang, L.; Wroblewski, T.; Pyzalla, A.: Investigation of the Microstructure and the Residual Stress of a Worn Railway Rail, the Sixth International Conference on Residual Stresses, July, 2000, Oxford, UK

/Wild 2001/ Wild, E.: Untersuchung weisser Schichten auf Schienenlaufflächen, Diplomarbeit 2001, Technische Universität Berlin

/William 1963/ William M.M.; Gavin R.M. and Marie J.F.: Advances in X - ray Analysis, Proceeding of the Twelfth Annual Conference on Applications of X - ray Analysis 7 (1963), S. 46 - 65

/Williamson 1954/ Willianson, G.K.: The use of Fourier Analysis in the Interpretation of X - ray Line Broadening from Cold - Worked Iron and Molybdenum, Acta. Cryst. 7 (1954), S. 574 - 581

/Willbrand 1966/ Willbrand, J. und Hillnhagen, E.: Beitrag zur röntgenographischen Bestimmung des Restaustenits, Techn. Mitt. Krupp. Forsch – Ber. 21 (1966), H. 4

/Wilson 1957/ Wilson, D., Acta Met. 5 (1957), S. 293

/Wingrove 1971/ Wingrove, A.L.: A Note on the Structure of Adiabatic Shear Bands in Steel, J. Aust. Inst. Metals 16 (1971), S. 67 - 70,

/Wroblewski 2000/ Wroblewski, T.; Wild, E.; Poeste, T.; Pyzalla, A.: Processing of X - ray Diffraction Image Data Using Remote Sensing Techniques, Mat. Sci. Letters 19 (2000), S. 975 – 978

10. Resume

Lihong Wang

First name: Lihong *Last name: Wang*

Birth date: Nov. 3, 1973 *Birth place: Jilin, China*

Family status: Married

- **September, 1980 ~ July, 1985**
  No. 1 Primary School in Hunjiang, Jilin Province, China
- **September, 1985 ~ July, 1988**
  No. 21 Middle School in Hunjiang, Jilin Province, China
- **September, 1988 ~ July, 1991**
  No. 2 Senior School in Hunjiang, Jilin Province, China
- **September, 1991 ~ July, 1995**
  Studies of Materials Science and Engineering, Dalian University of Technology, China
  Degree: Bachelor of Engineering (B. Sc.)
- **September,1995 ~ July, 1999**
  Studies of Materials Science and Engineering ,
  Graduate School of Dalian University of Technology, China
  Degree: Master of Engineering (M. Sc.)
- **June ~ August, 1998**
  Practice in Gemeinschaftlabor für Elektronenmikroskopie (GFE), RWTH, Aachen, Germany
- **September, 1999 ~ Current**
  Researcher at Hahn - Meitner - Institut, Strukturforschung, Germany
  Researcher at Institute of Materials Science and Technologies, Technical University of Berlin, Germany

11. Tables and Figures

Table 4.1 Service Parameters of Rail DB AG

Axle load: Passenger transportation: Freight transportation:	36500 t/d 12800 t/d 23700 t/d
Rail radius:	6002,35 m
Track gauge:	1435 mm
Superelevation:	75 mm
Maximum Speed:	280 km/h (Intercity Express ICE)
Montage date:	1988
Demontage date:	August 1997
Location:	Downhill, left turn
Position:	Outer side

Table 4.2 Service Parameter of Rail Baumann

Profile type	material	Max. axle loading per year [Mio. Lt]	Max. speed [km/h]	source	producer	Location
S54	900 A	4,9	120	Ingolstadt/ Donauwörth	Maxhütte 1984	Straight line

Table 4.3 Service Parameters of Rail Sample 2 and Rail Sample 3

	Rail Sample 2	Rail Sample 3
Traffic	45000 t/day	85000 t/day
Speed Maximum	130 km/h	140 km/h
Location	straight	curved, R = 1050 m
Profile / Grade	UIC 60 / 900A	UIC 60 / 900B

Table 4.4 Composition of Rail Samples and Wheel Sample

	C	Si	Mn	Al	P	S	Fe
Rail DB AG	0,63	0,26	0,99		0,029	0,043	balance
Rail Baumann	0,63	0,24	0,95		0,029	0,038	balance
Rail Sample 2	0,75	0,27	0,93	< 0,005	0,012	0,016	balance
Rail Sample 3	0,64	0,23	1,51	0,012	0,014	0,030	balance
Wheel ICE	0,80	0,176	0,0747		0,009	0,019	balance

Table 4.5 200 reflection profile after annealing

Anneal temperature and time	200 reflection of martensite / ferrite	Carbide reflection
100°C, 1h	asymmetric	No
100°C, 5h	asymmetric	No
100°C, 10h	symmetric, FWHM (0,2356)	No
400°C, 1h	symmetric, FWHM (0,15258)	yes
400°C, 5h	symmetric, FWHM (0,18307217)	yes
400°C, 10h	symmetric, FWHM (0,03829141)	yes
600°C, 1h	symmetric, FWHM (0,05486)	yes
600°C, 5h	symmetric, FWHM (0,055048)	yes
700°C, 1h	symmetric, FWHM (0,0566)	yes
700°C, 5h	symmetric, FWHM (0,0564)	yes

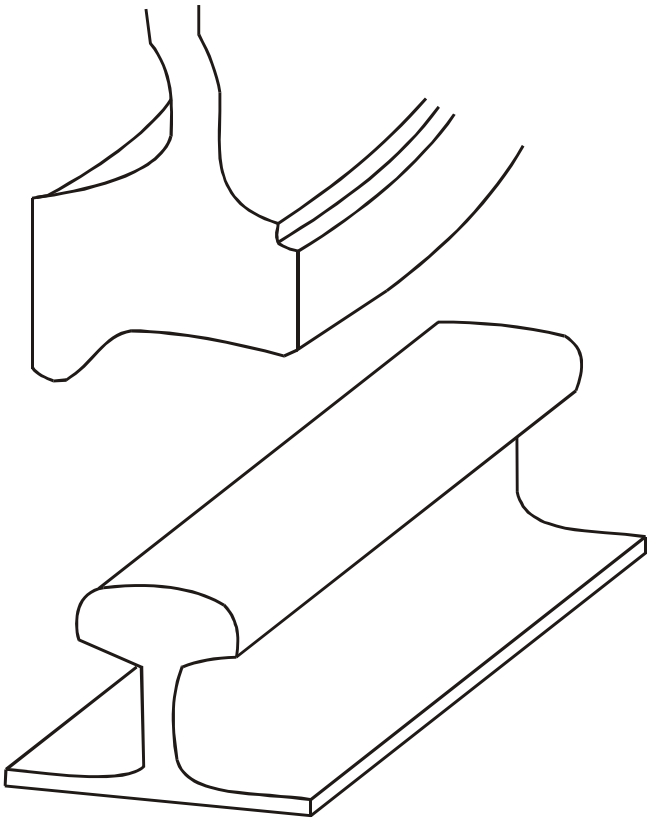

Fig.1.1 Geometry of the rail - wheel rolling system

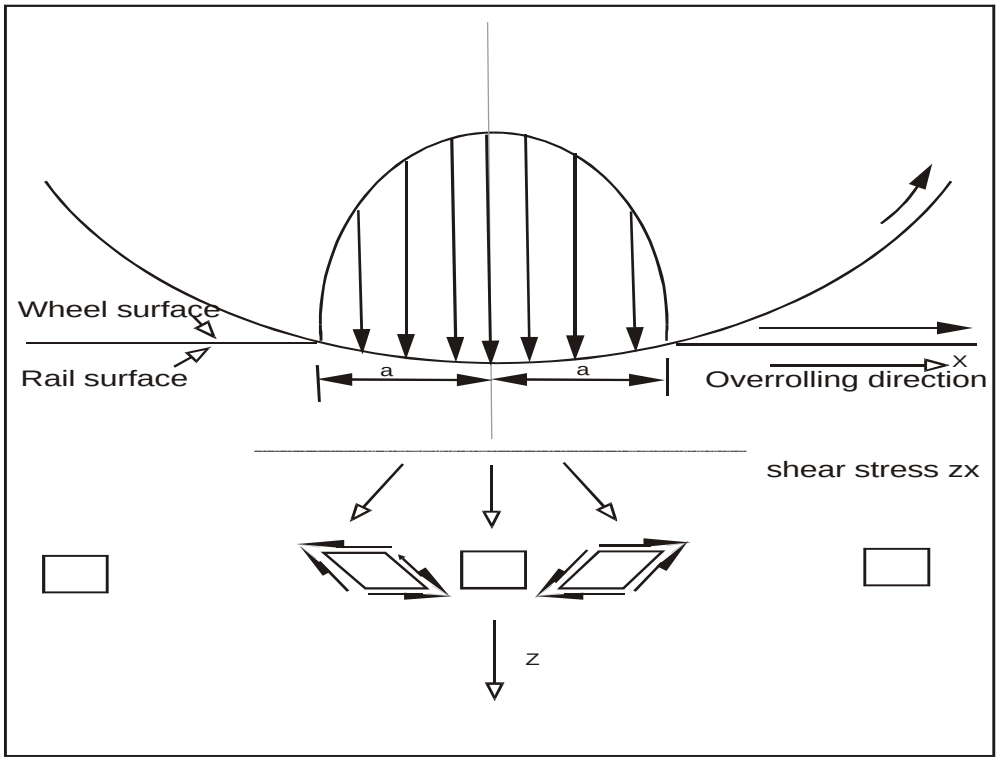

Fig. 2.1 Subsurface element

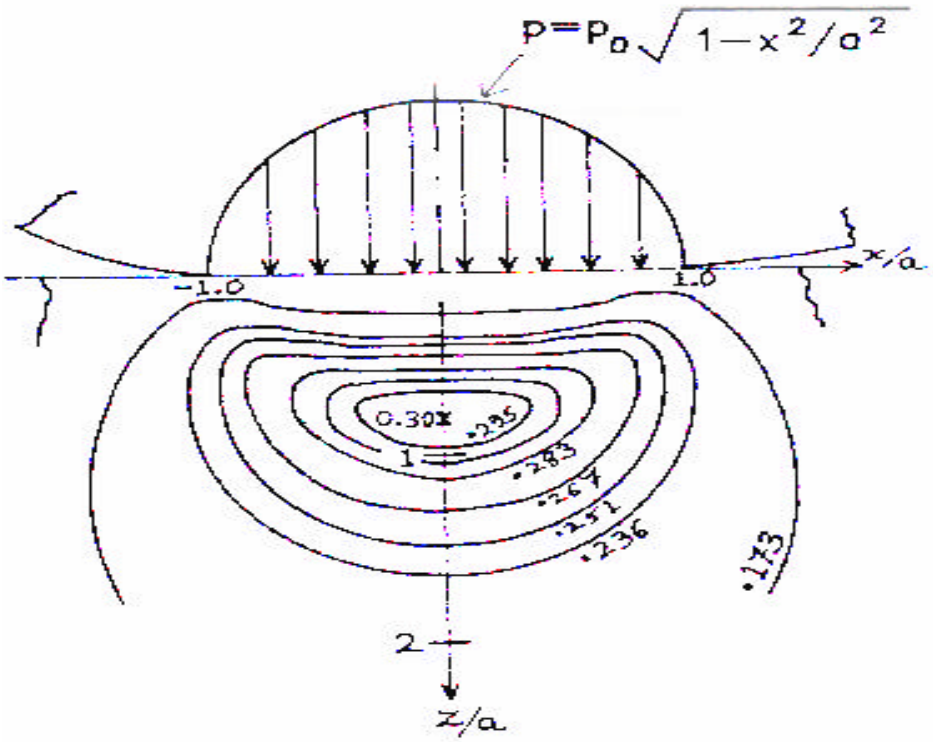

Fig. 2.2 In - depth distribution of contact stress /Singer 1991/

Fig. 2.3 Riffles on an exemplary rail (supplied by Mr. Peter F.J. Wild)

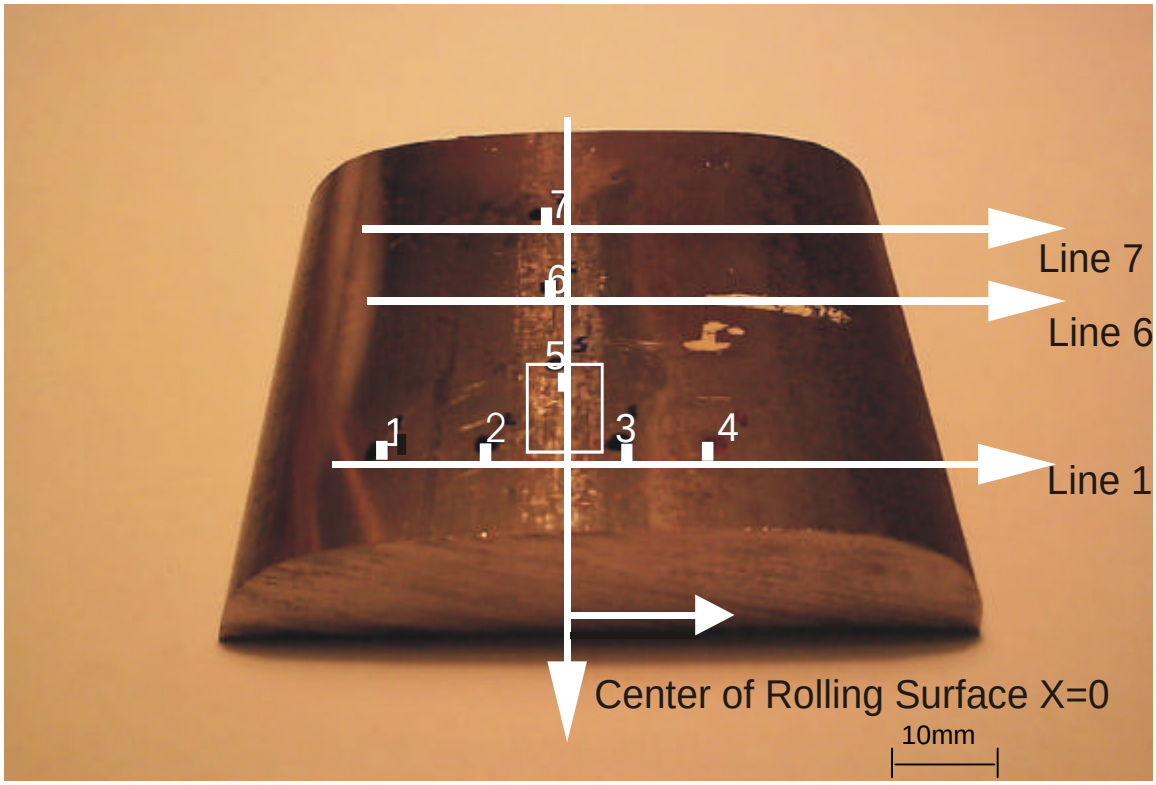

Fig. 4.1 Photo of rail DB AG

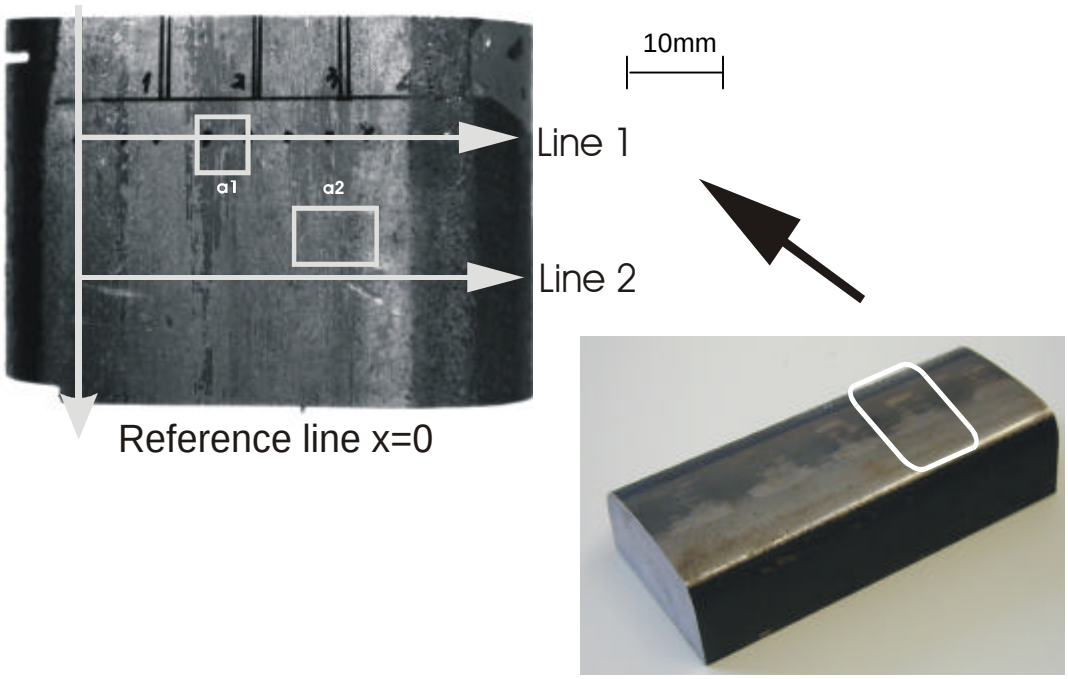

Fig. 4.2 Photo of rail Baumann

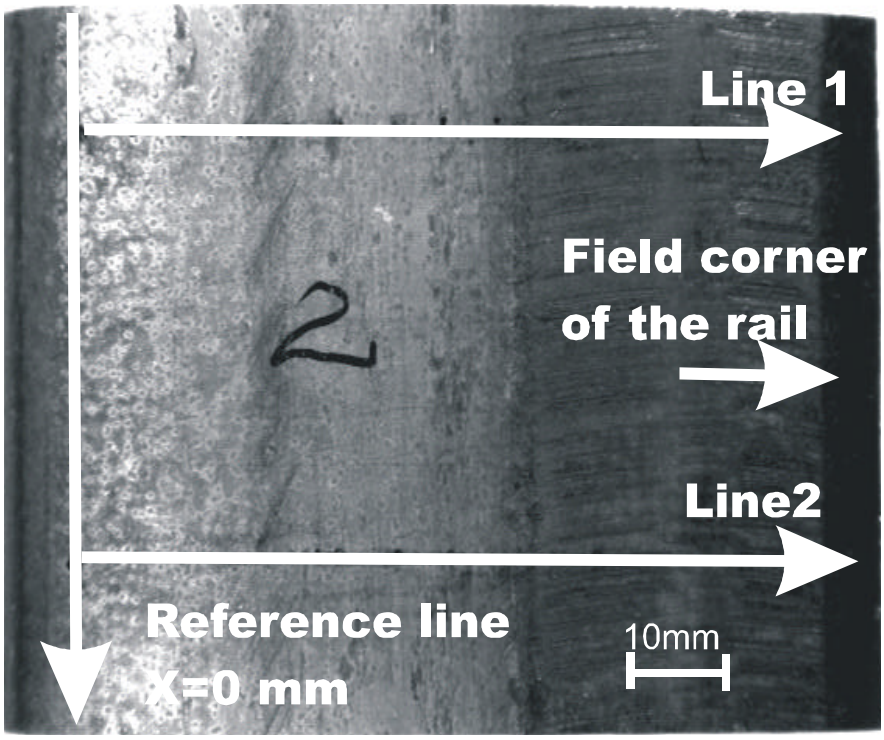

Fig. 4.3 Photo of rail sample 2

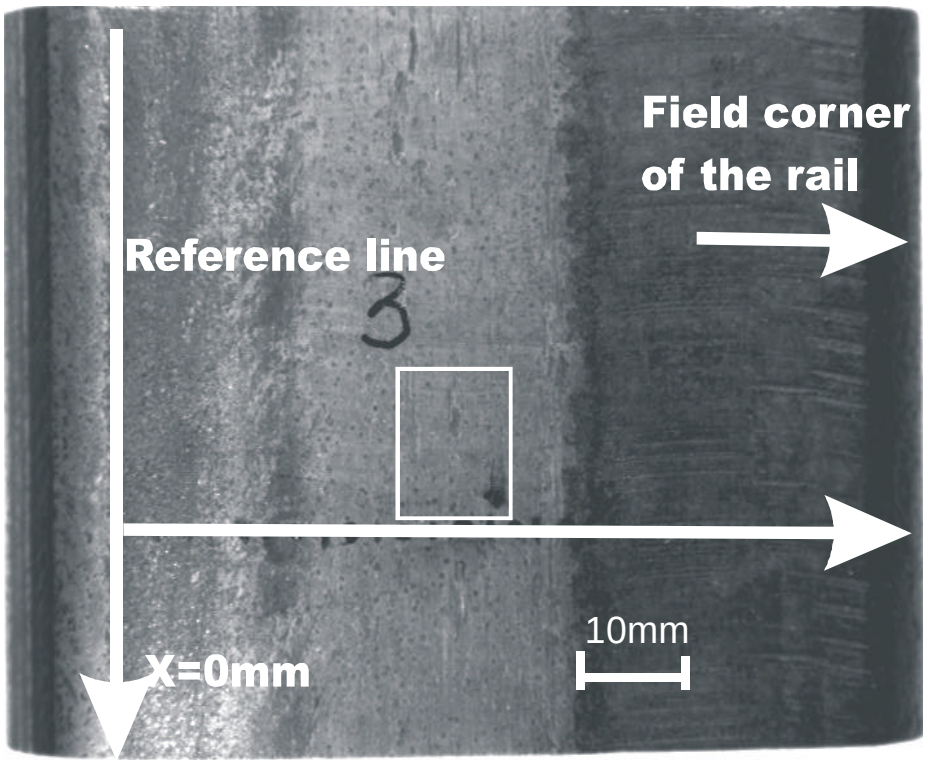

Fig. 4.4 Photo of rail sample 3

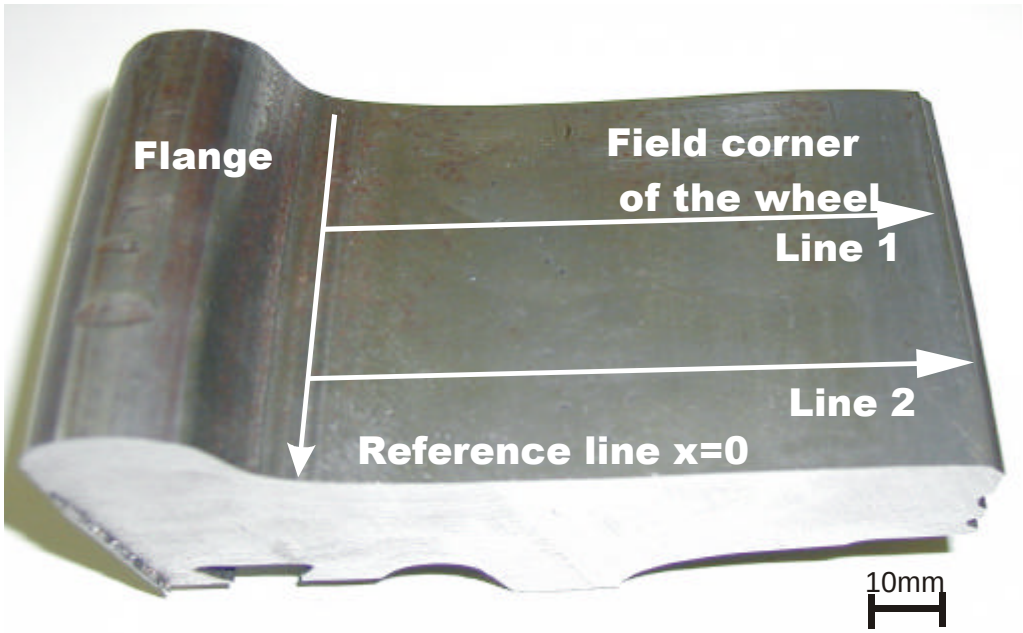

Fig. 4.5 Photo of wheel sample

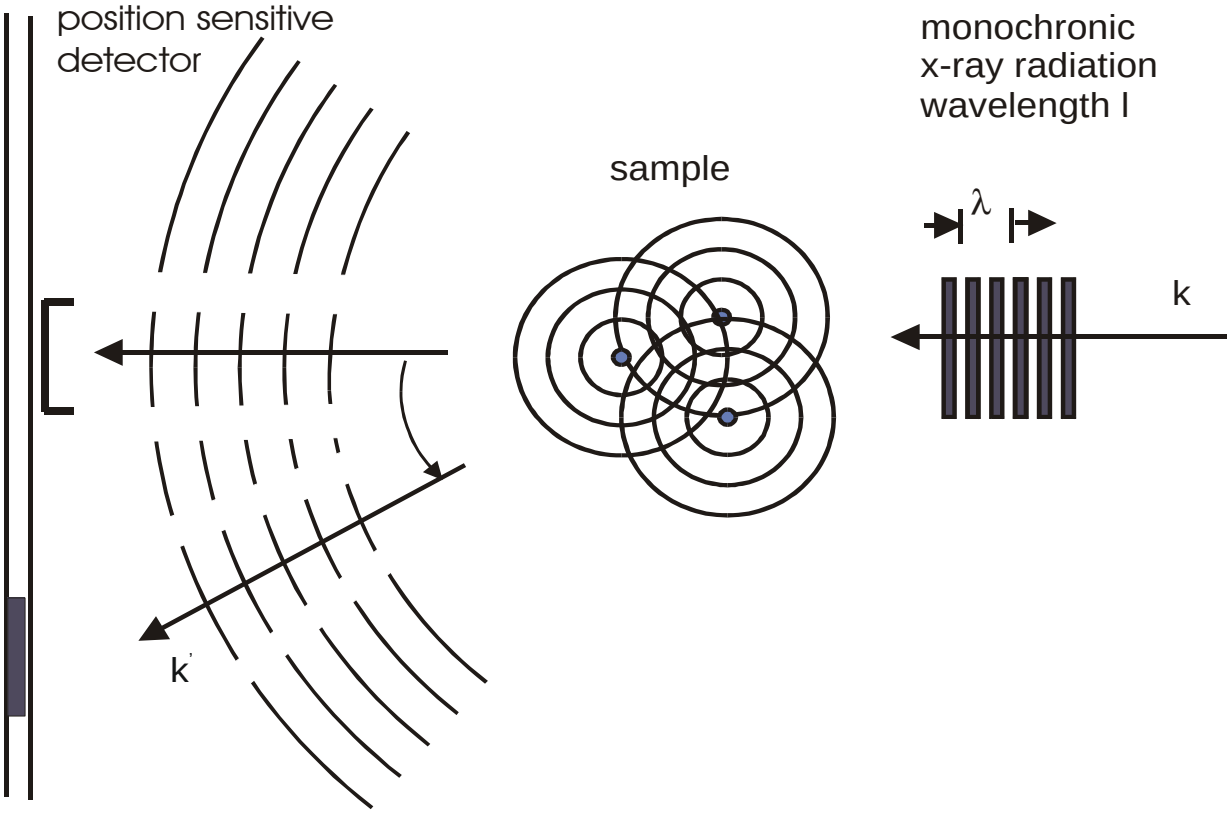

Fig.4.6 Principle of small angle x – ray scattering at beamline B1, Jusifa in Hasylab

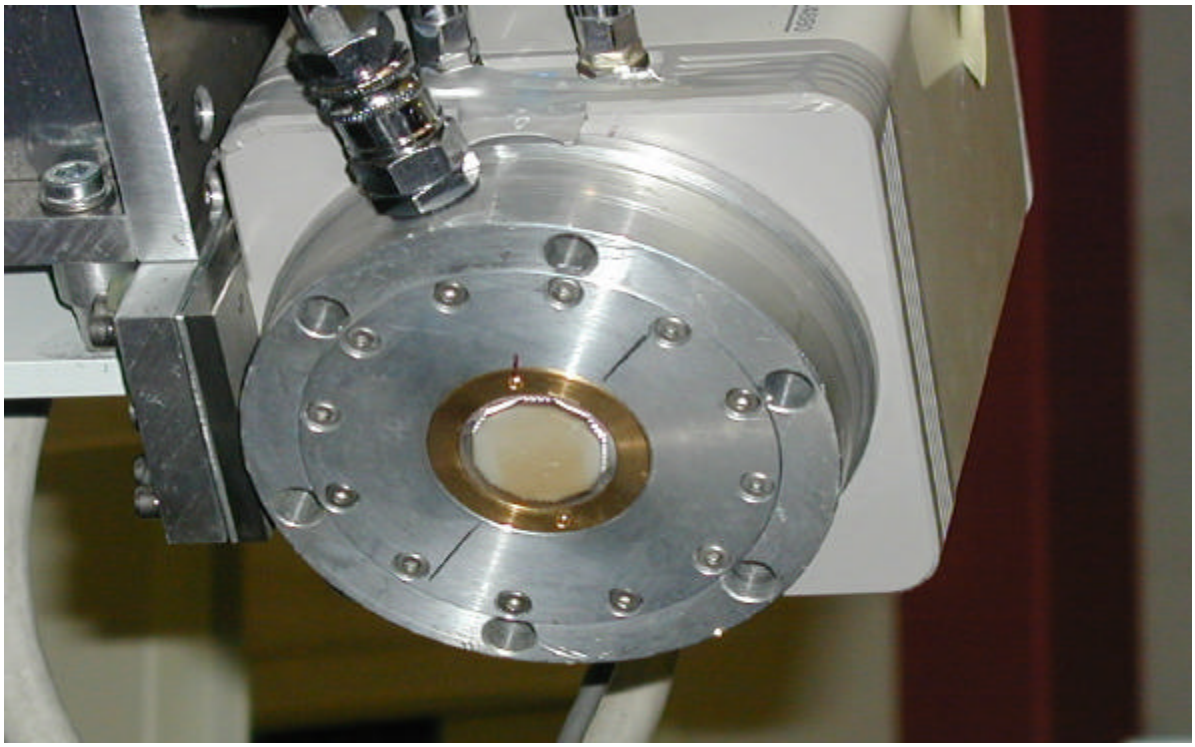

Fig. 4.7 CCD - camera and microchannel plate at the instrument G3, Hasylab

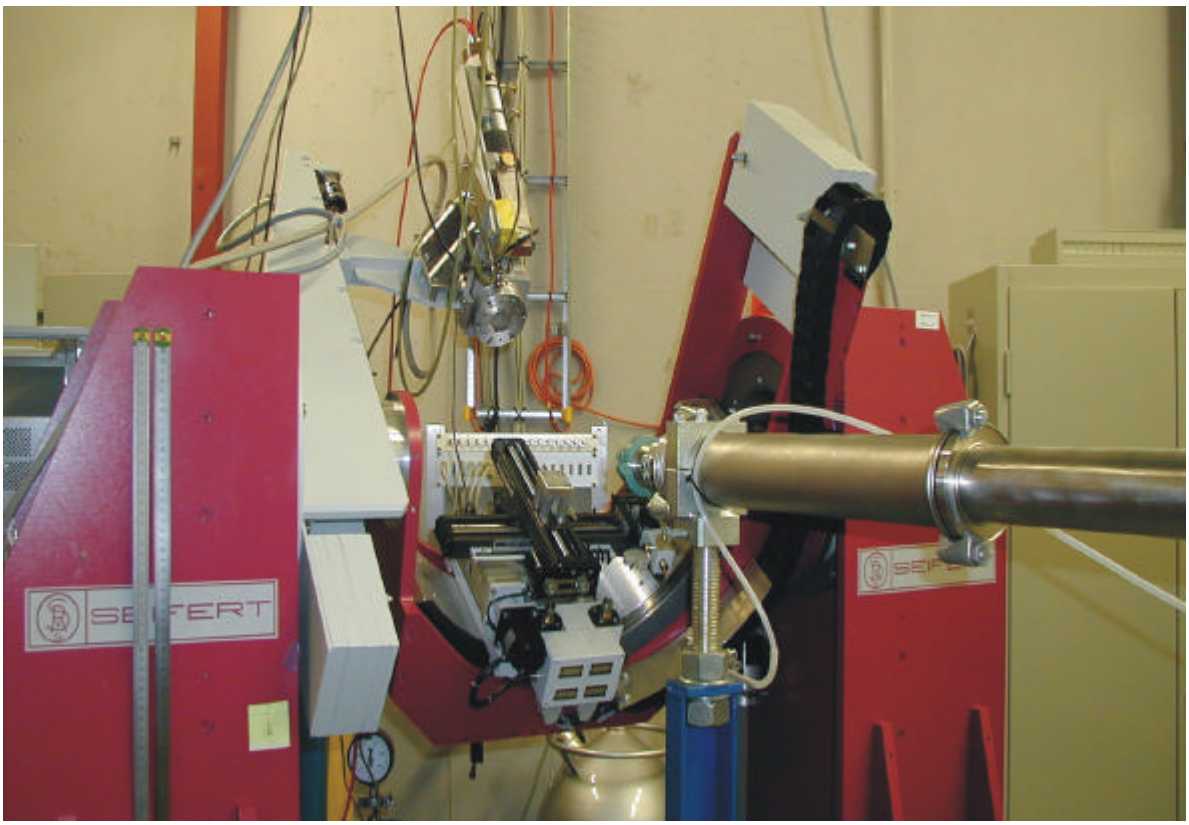

Fig. 4.8 Instrument G3 Hasylab

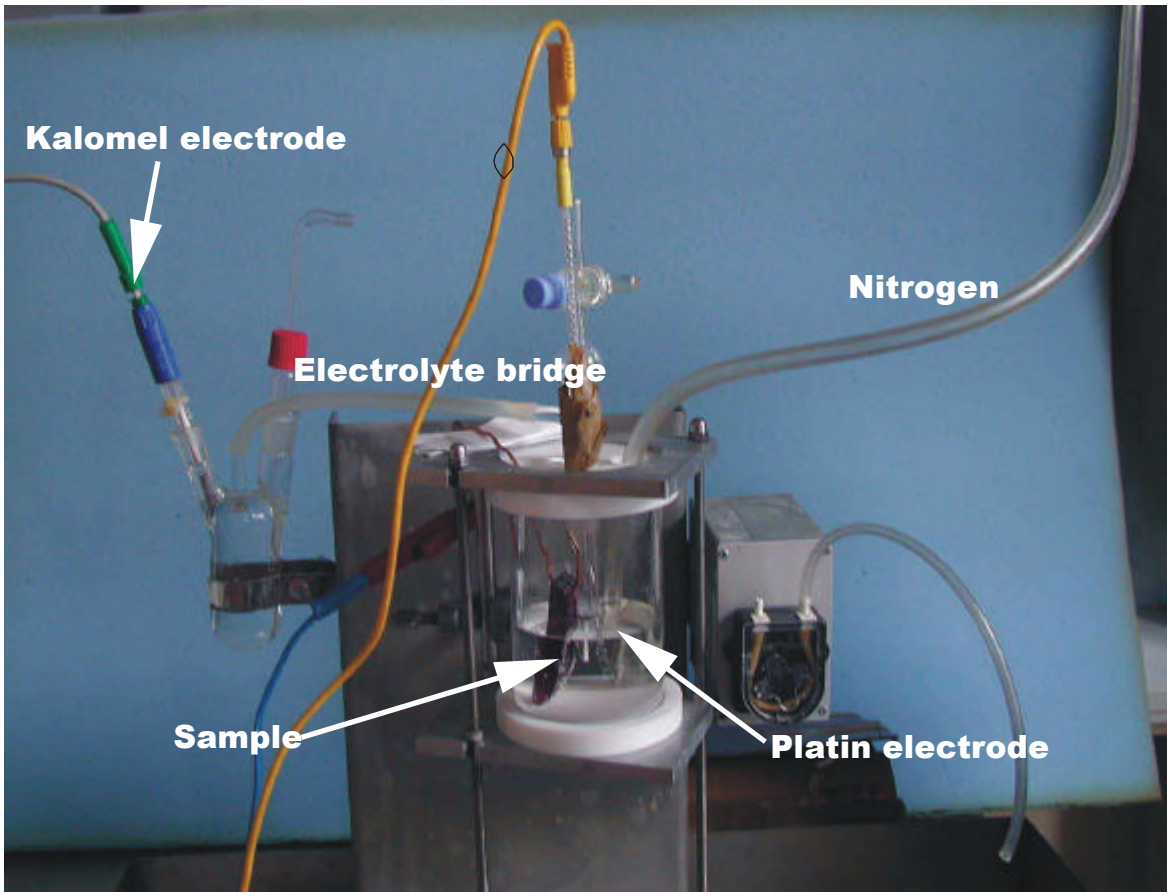

Fig. 4.9 Corrosion cell

Fig. 5.1.1 Optical micrograph of White Etching Layer in cross section of rail DB AG /BAM Berlin, Dr. Spaltmann, Prof. Dr. Santner/

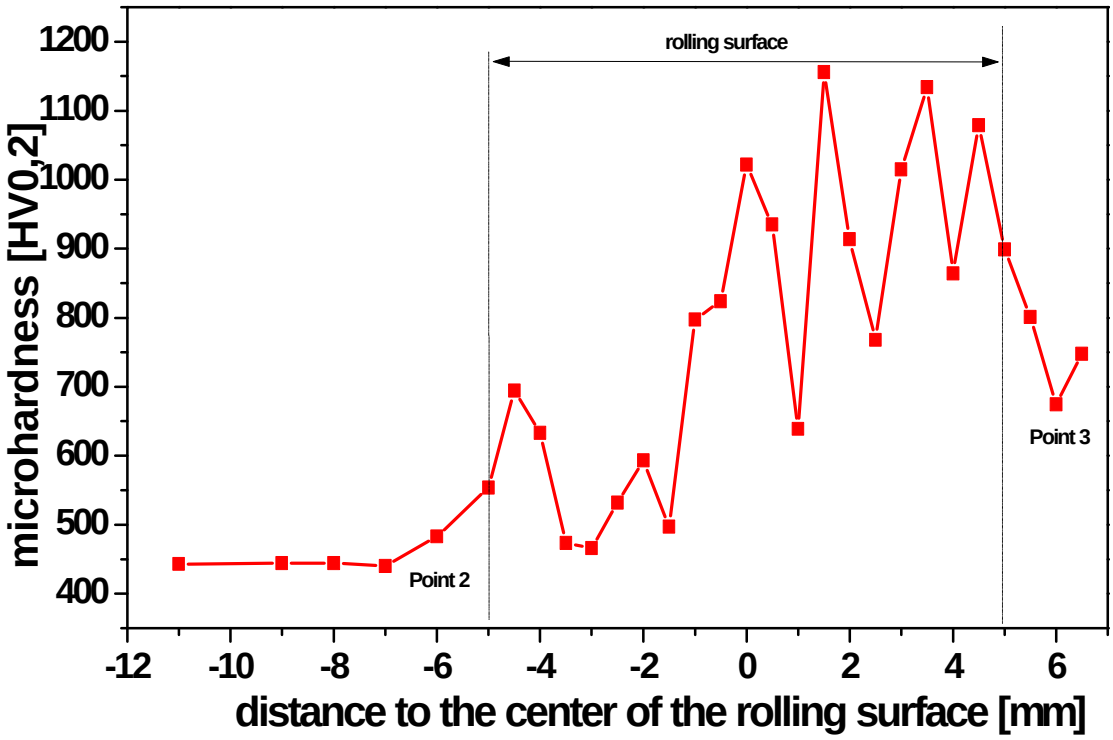

Fig. 5.1.2 Microhardness distribution across the surface of rail DB AG

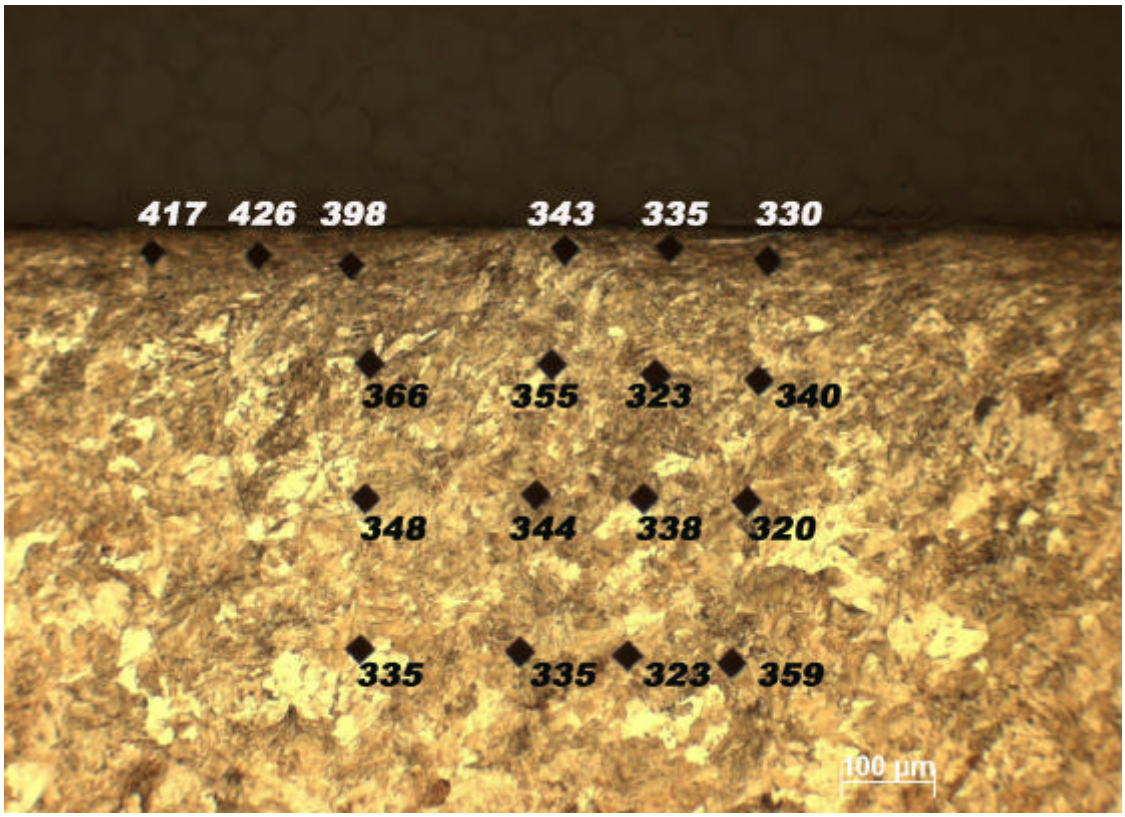

Fig. 5.1.3 Microhardness distribution below the surface of rail DB AG in the region without WEL

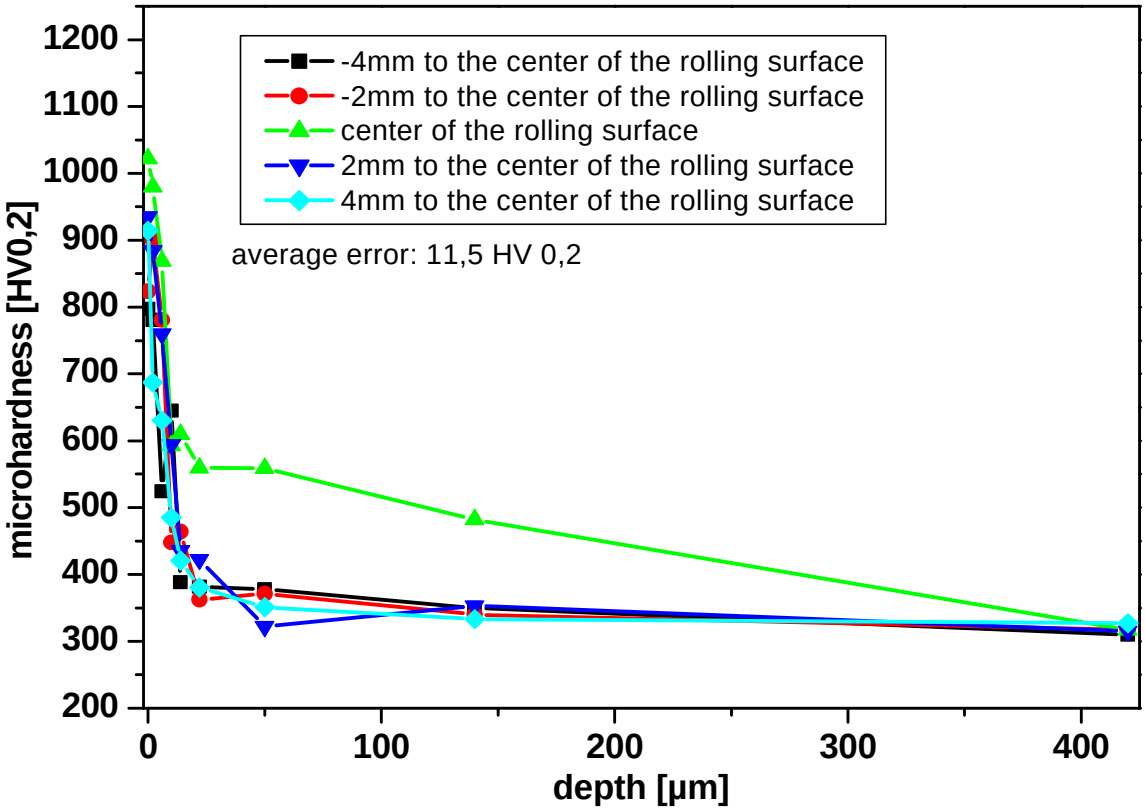

(a)

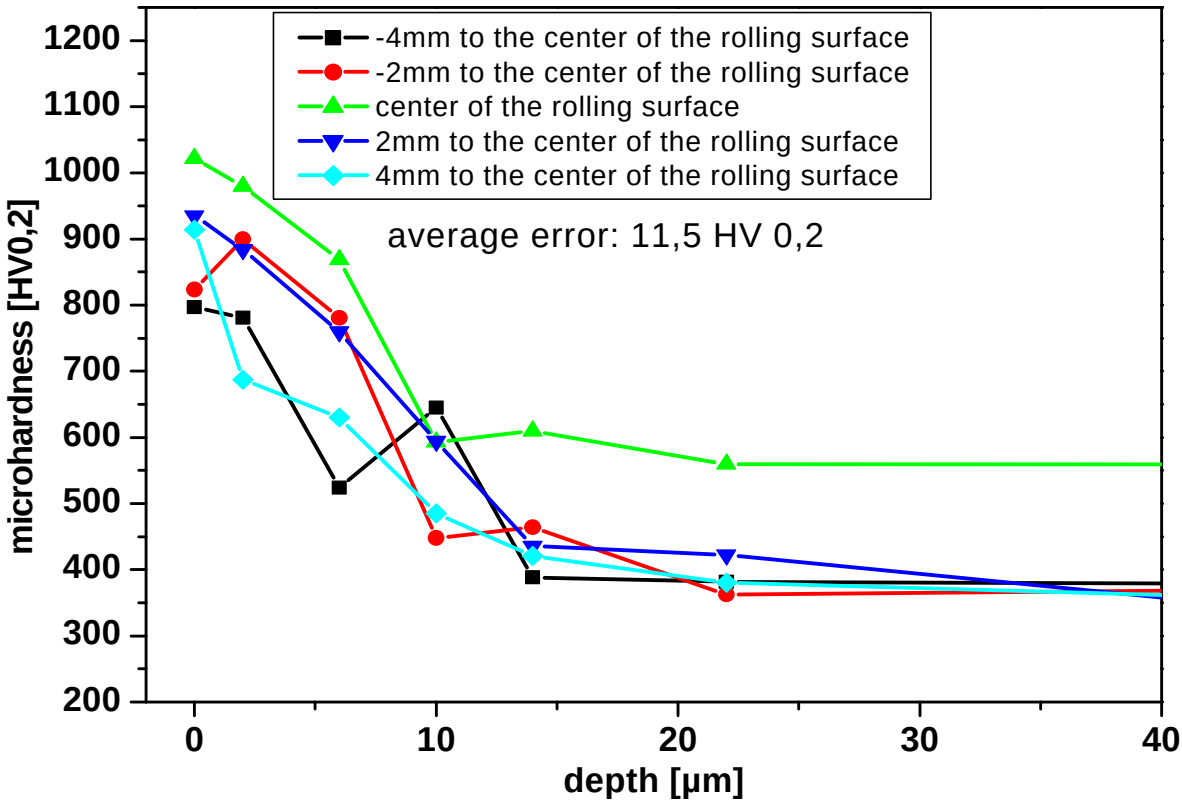

(b)

Fig. 5.1.4 Microhardness distribution below the rolling surface of rail DB AG
(a) from surface to 400µm, (b) from surface to 40µm

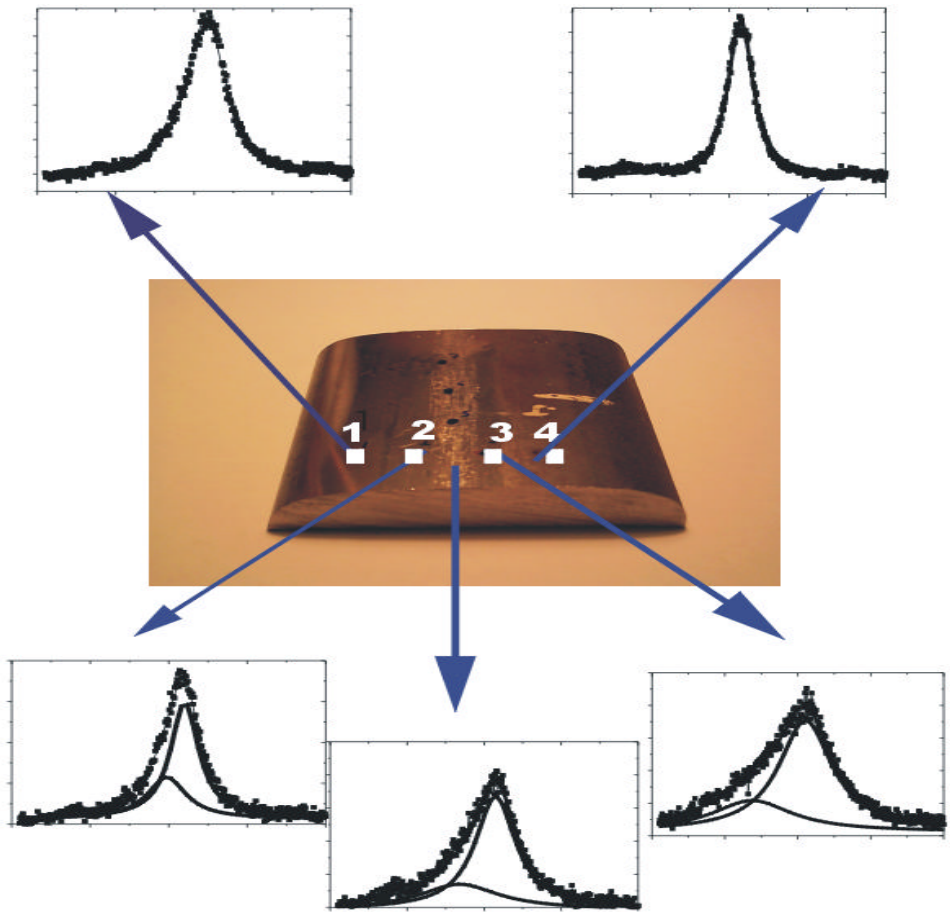

Fig. 5.1.5 200 reflection profile along line 1 on the surface of rail DB AG

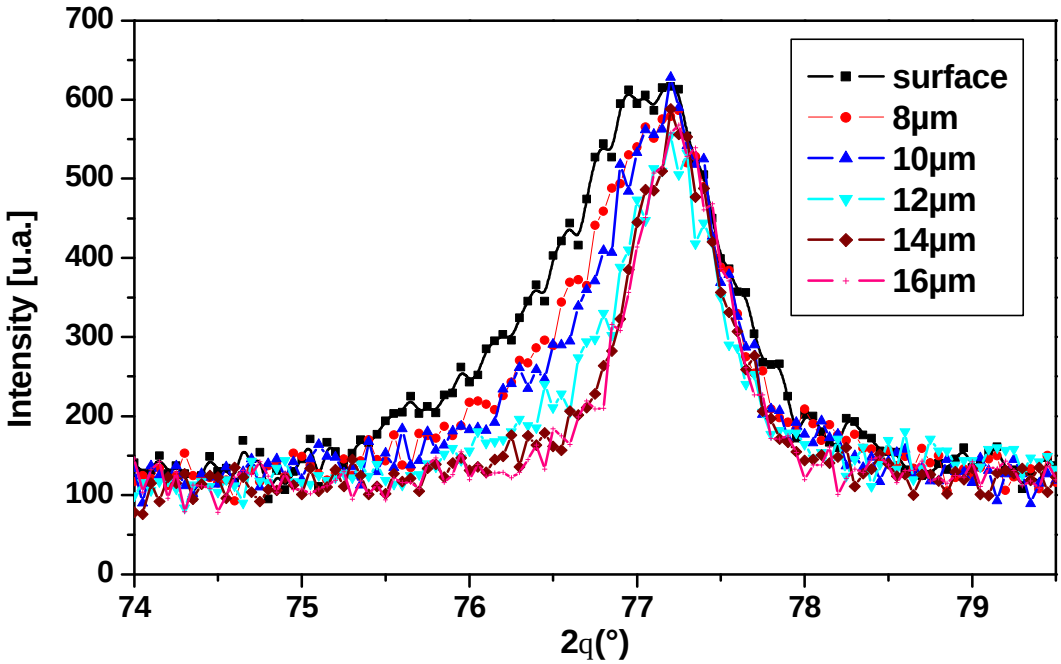

Fig. 5.1.6 200 reflection profile in the in - depth direction below the surface of rail DB AG

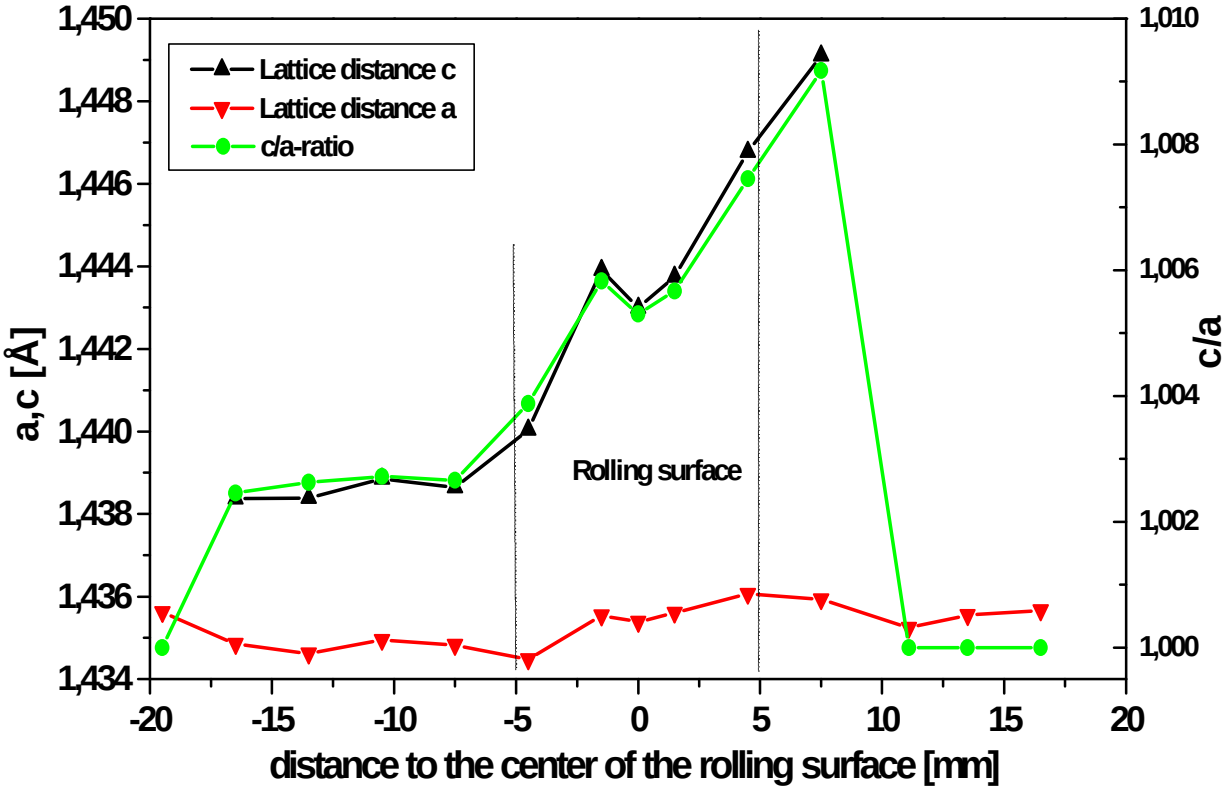

Fig. 5.1.7 Lattice distance and c / a ratio distribution across the surface of rail DB AG

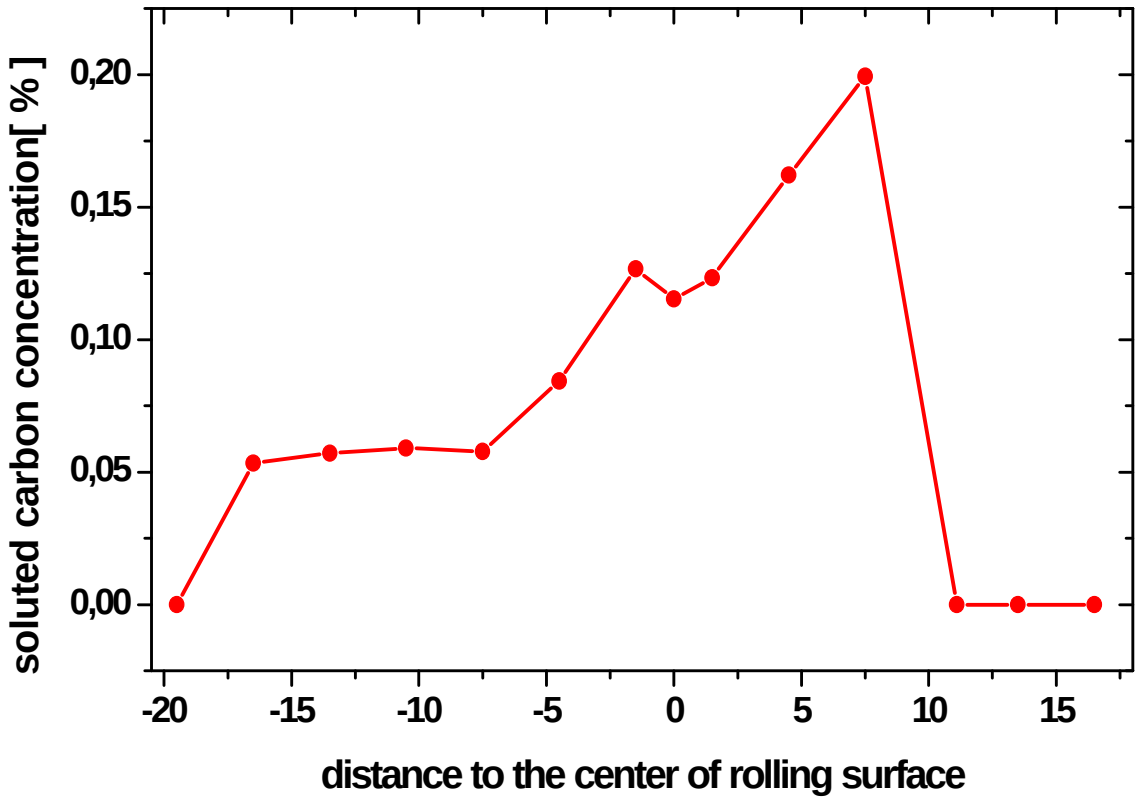

Fig. 5.1.8 Solute carbon concentration across the surface of rail DB AG

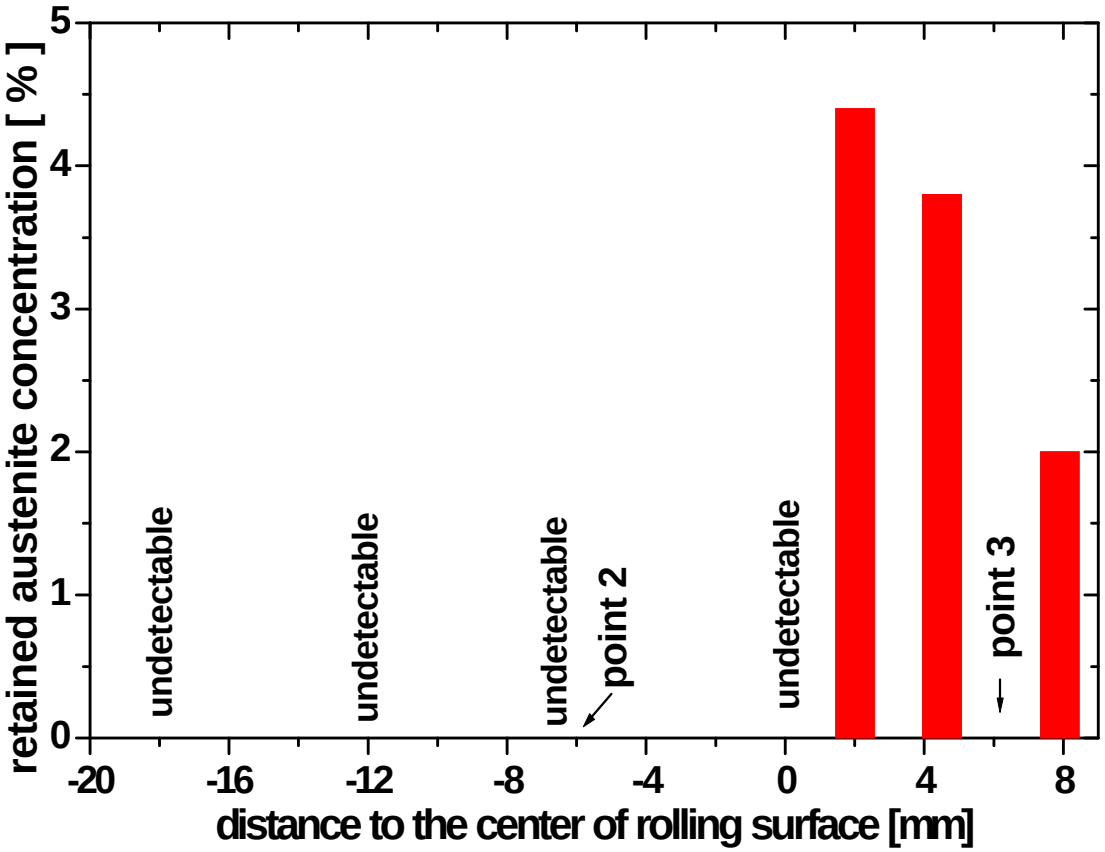

Fig. 5.1.9 Retained austenite content along line 1 on rail DB AG

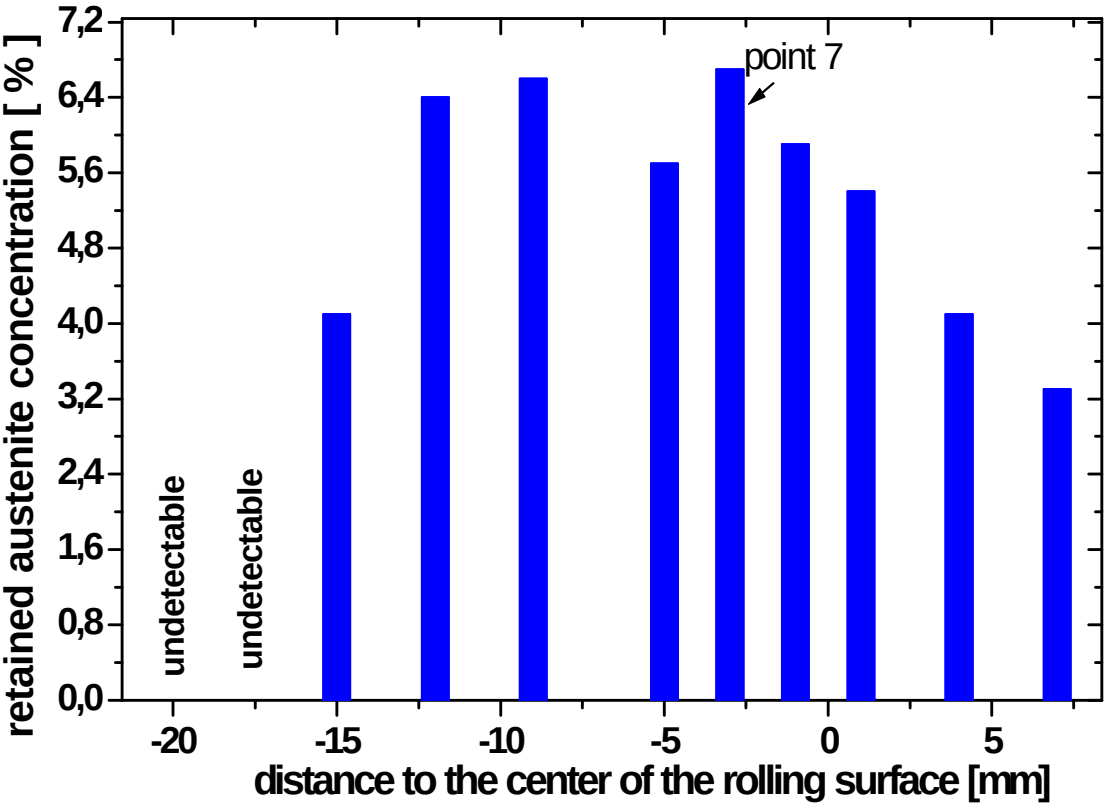

Fig. 5.1.10 Retained austenite content along line 7 on rail DB AG

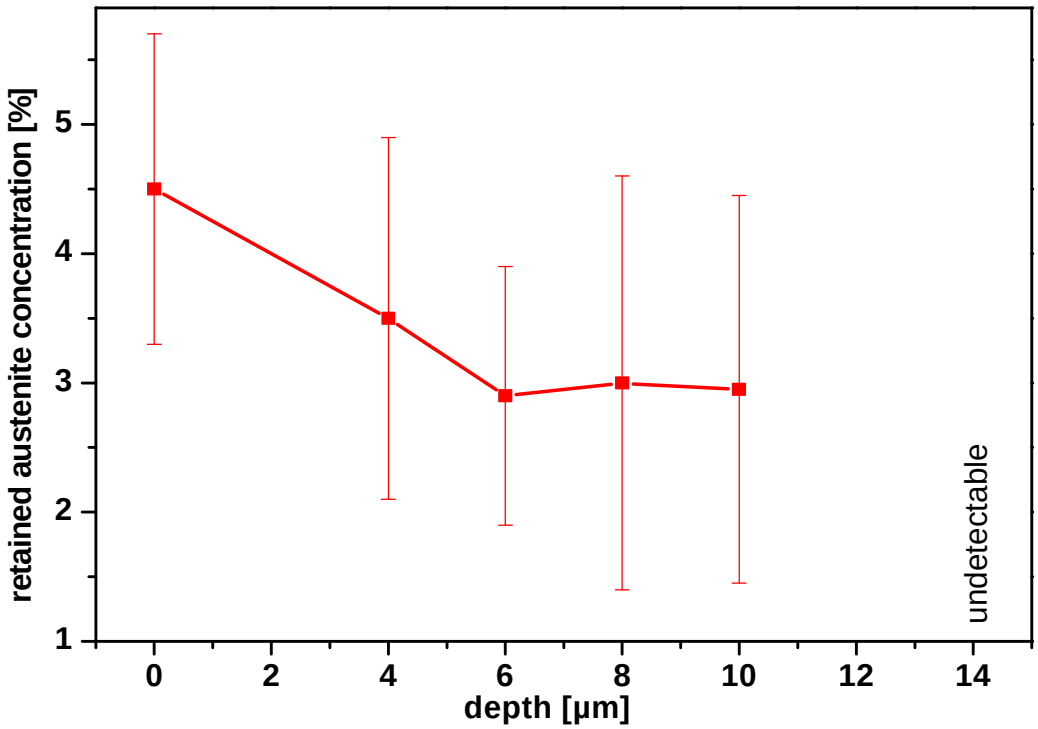

Fig. 5.1.11 Retained austenite distribution in the in - depth direction below the rolling surface of rail DB AG

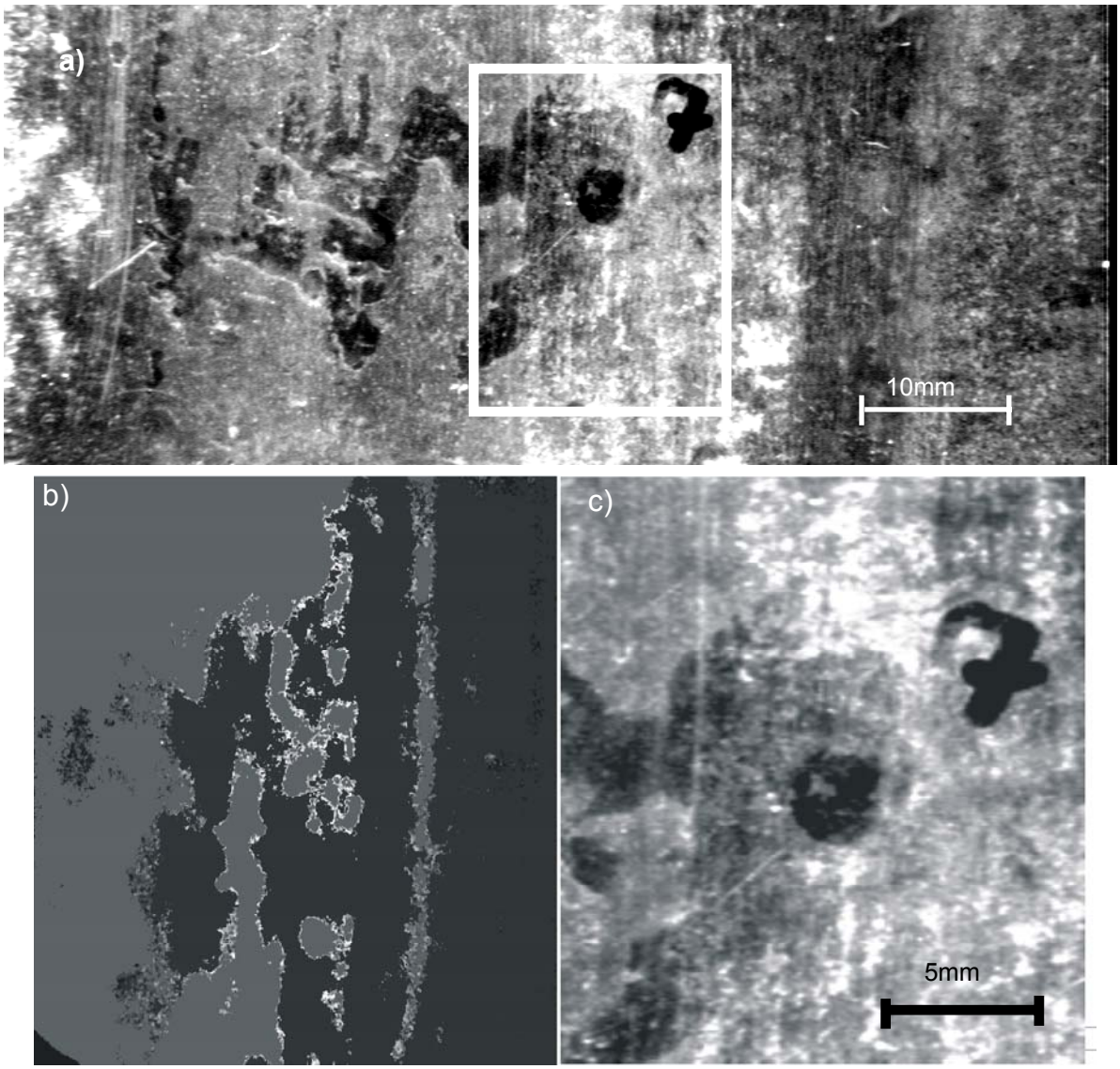

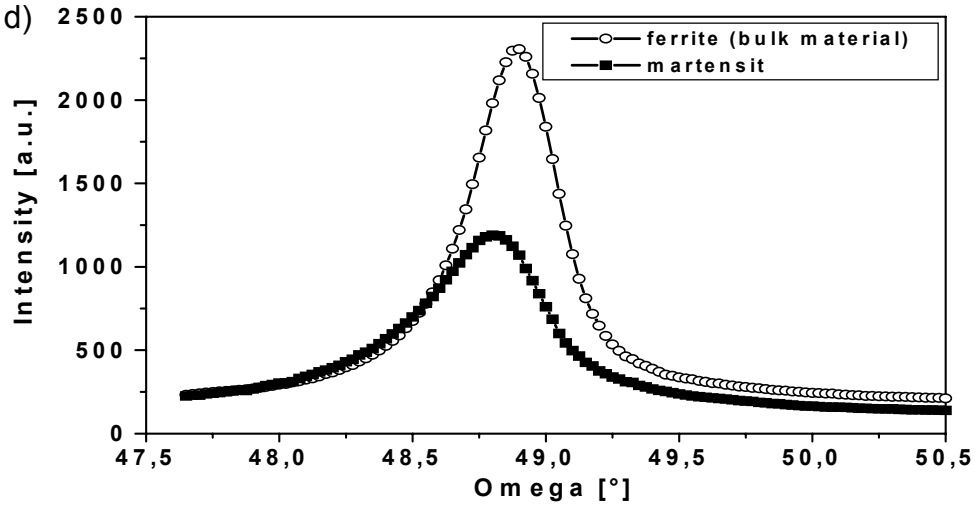

Fig. 5.1.12 a) Photo of the rail DB AG surface
b) X - ray image of α - Fe – 211 reflection
c) Photo of the rail surface with high magnification
d) Sum profile of the α - Fe – 211 reflection

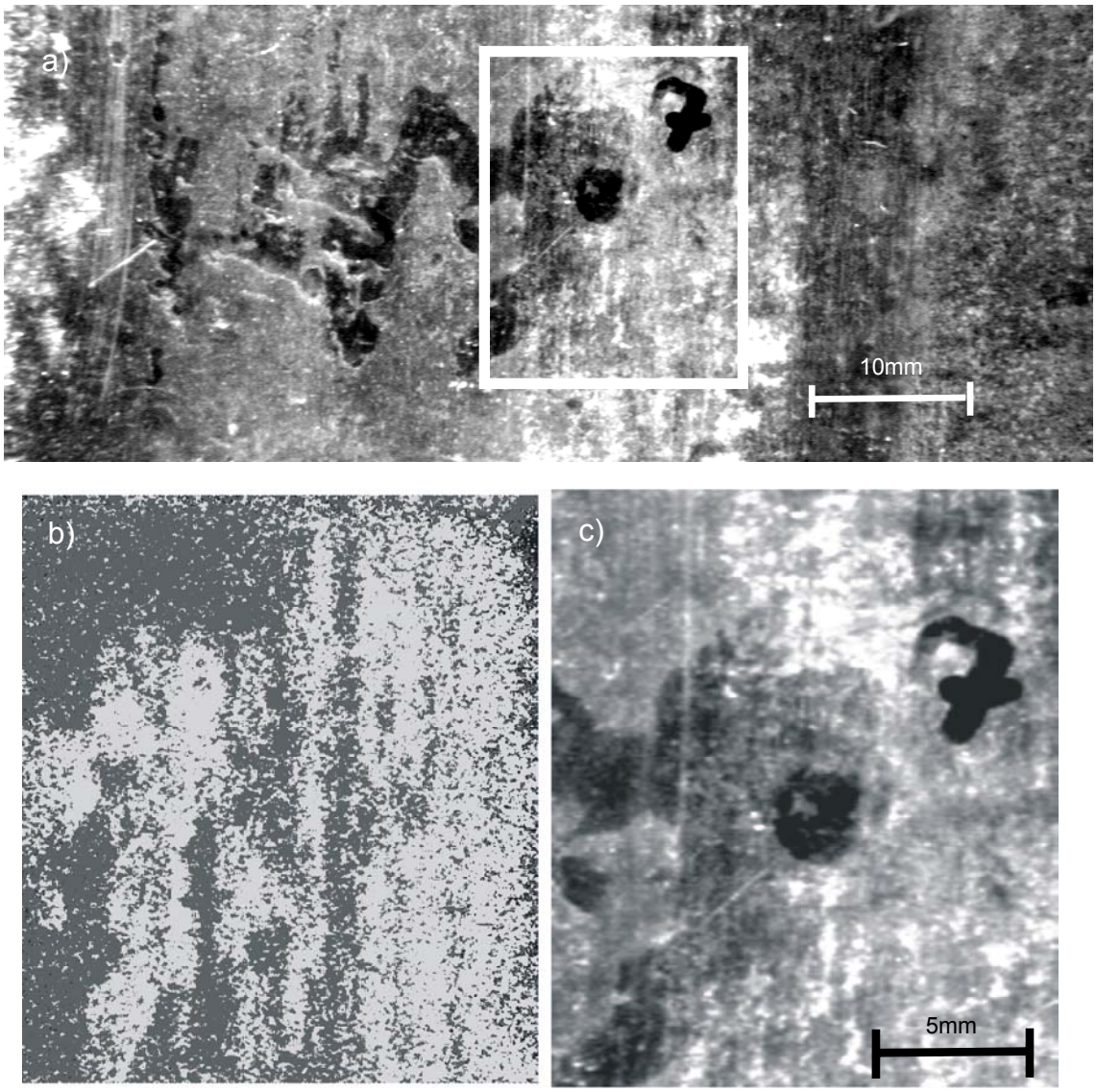

Fig. 5.1.13 a) Photo of rail DB AG surface
b) X - ray image of γ - Fe - 200 reflection
c) Photo of rail DB AG with high magnification
d) Sum profile of γ - Fe - 200 reflection

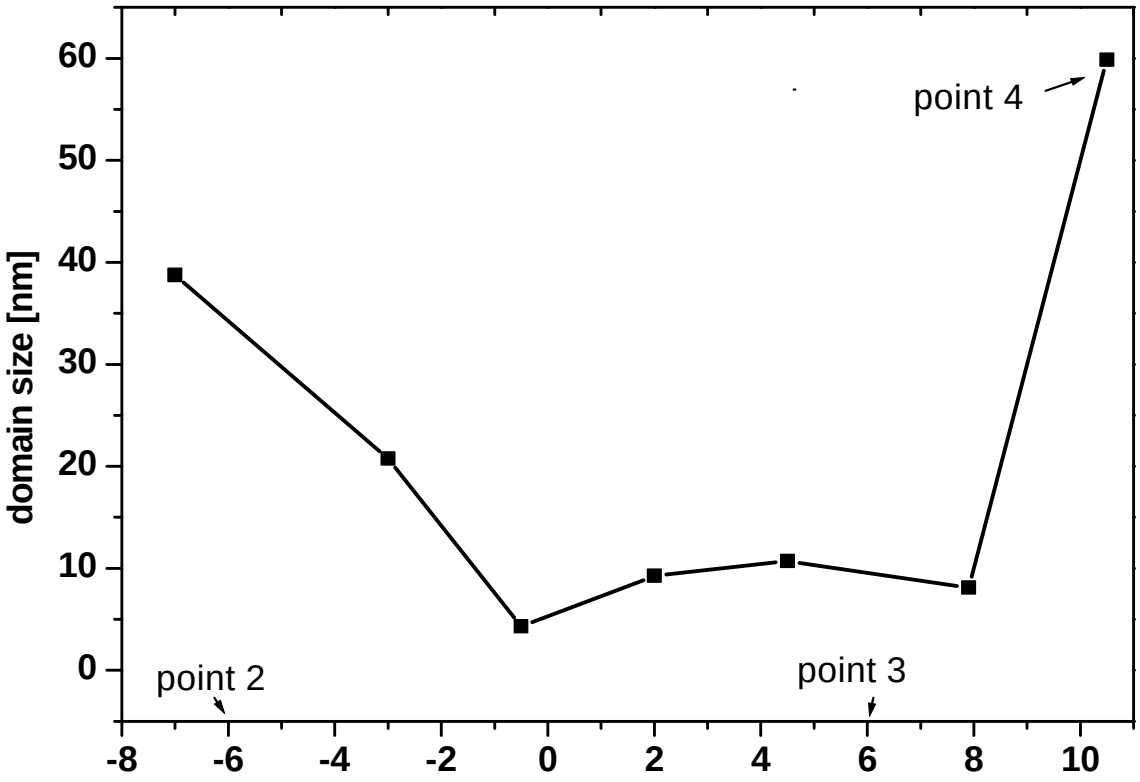

Fig.5.1.14 Domain size distribution across the surface of rail DB AG

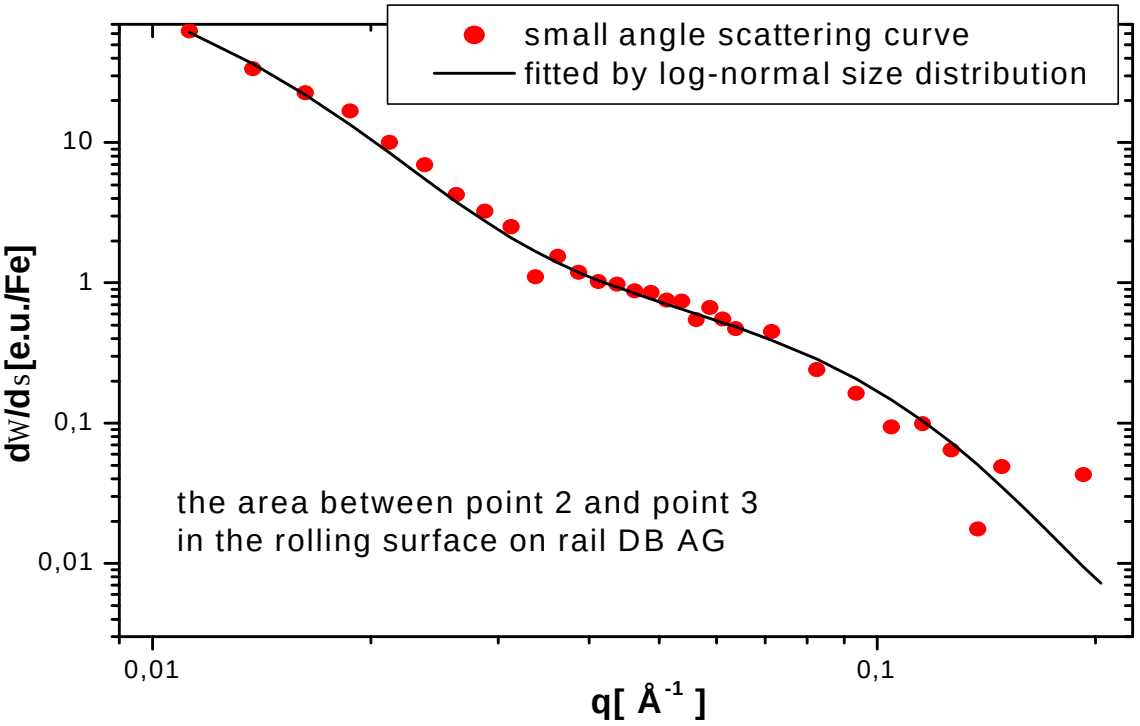

Fig.5.1.15 Small angle scattering curve in the area within the rolling surface on rail DB AG

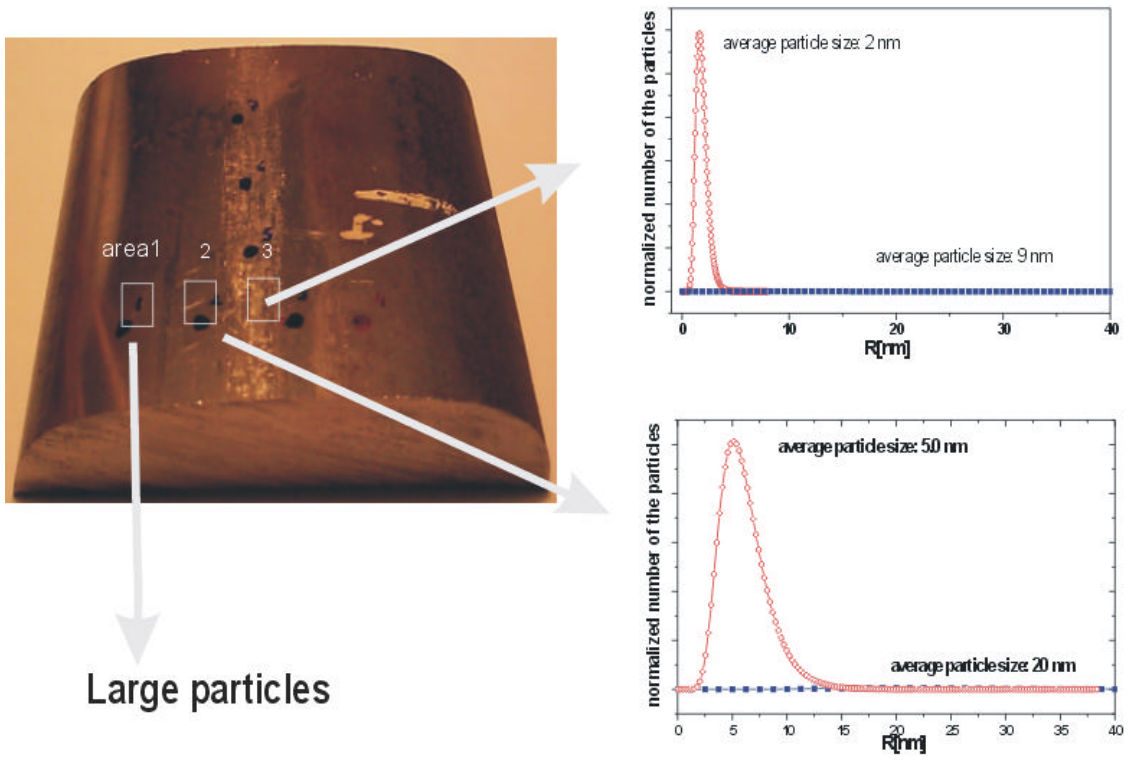

Fig. 5.1.16 Distribution of carbide size on the surface of rail DB AG

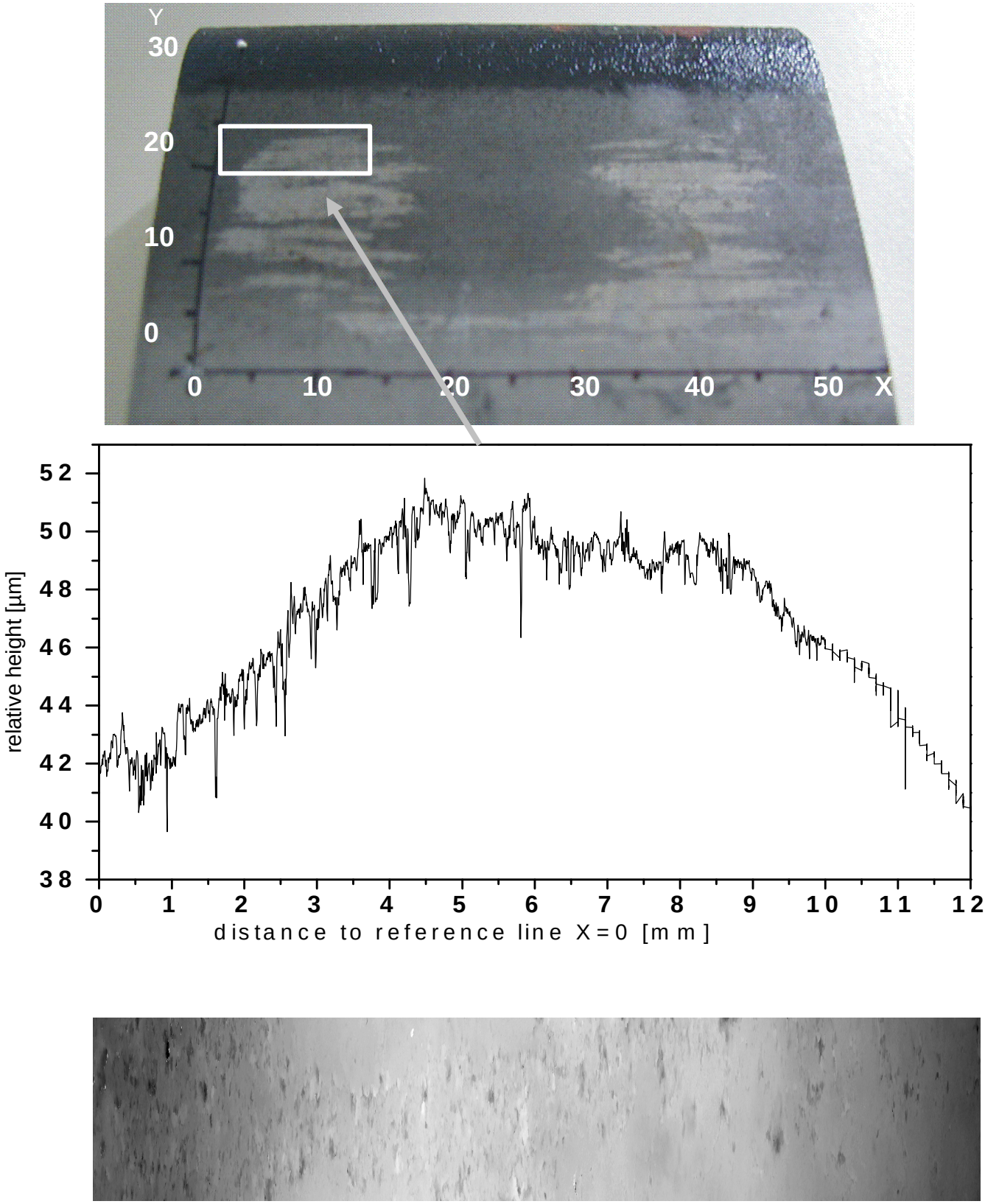

Fig. 5.1.17 Profile over a segment of rail at y = 20mm and x = 0-12 mm with the corresponding interference spectroscopic picture

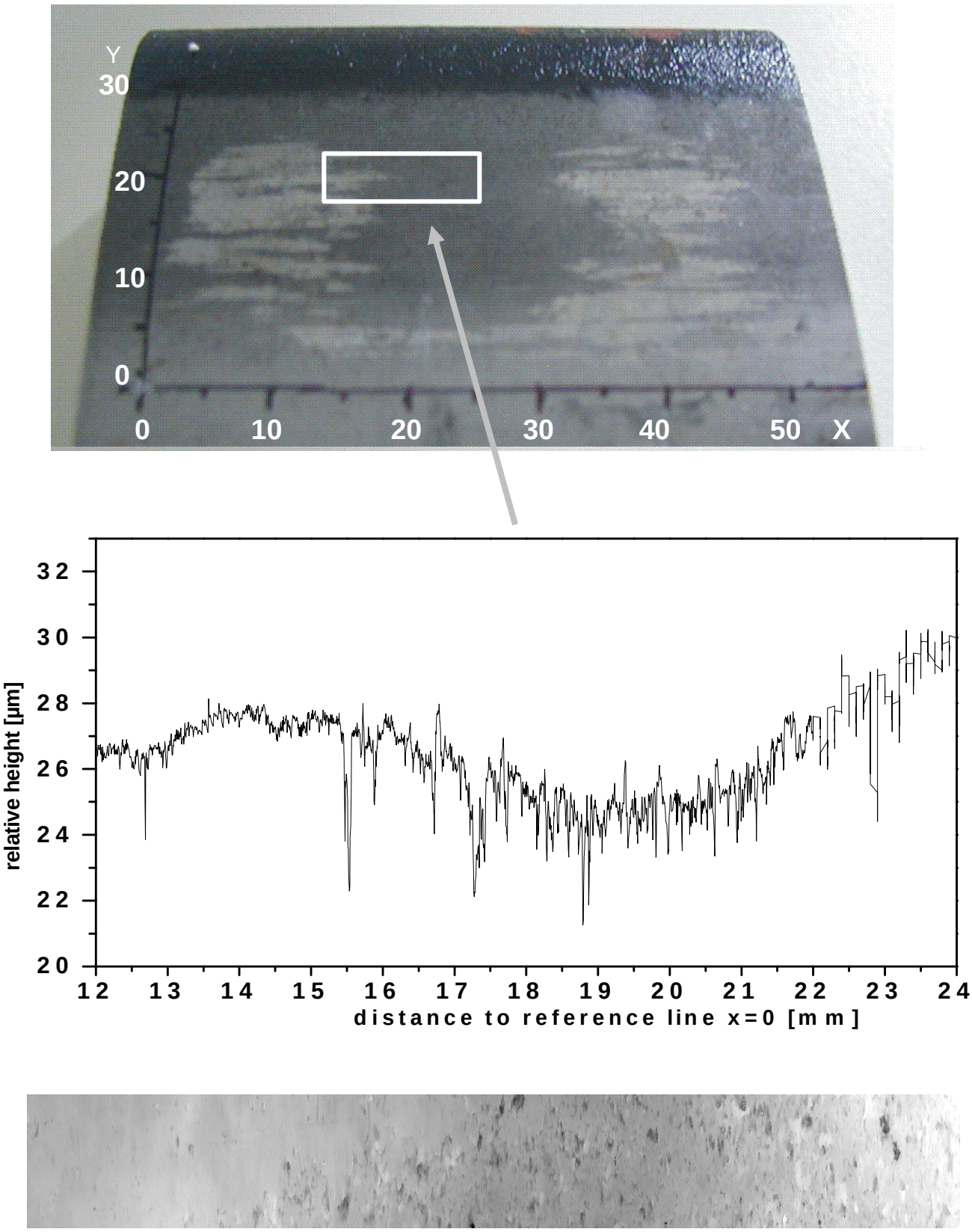

Fig. 5.1.18 Profile over a segment of rail at y =20mm and x =12 – 24mm and corresponding interference spectroscopic picture

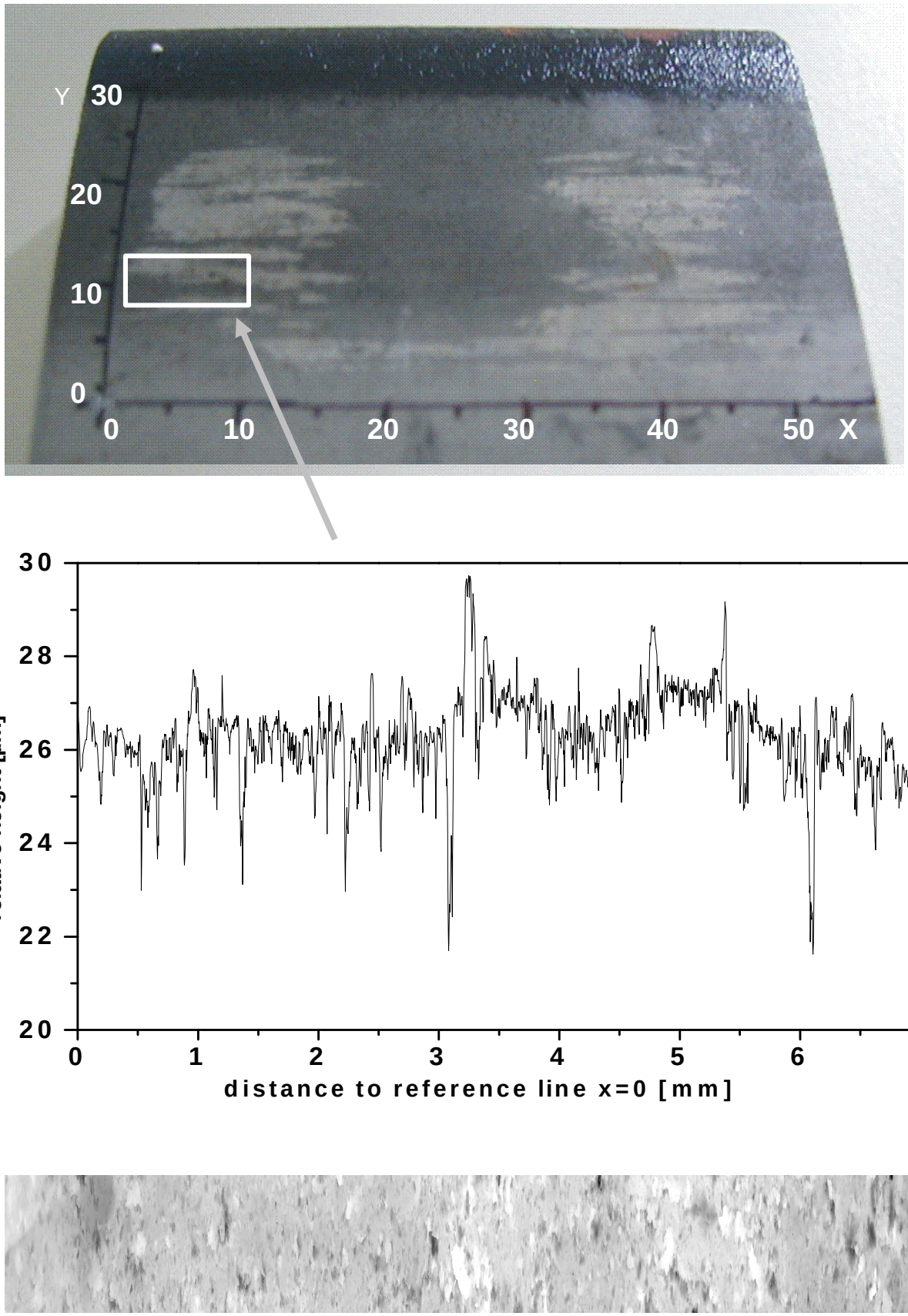

Fig. 5.1.19 Profile over a segment of rail at y = 10mm and x = 0-7.1 mm with the corresponding interference spectroscopic picture

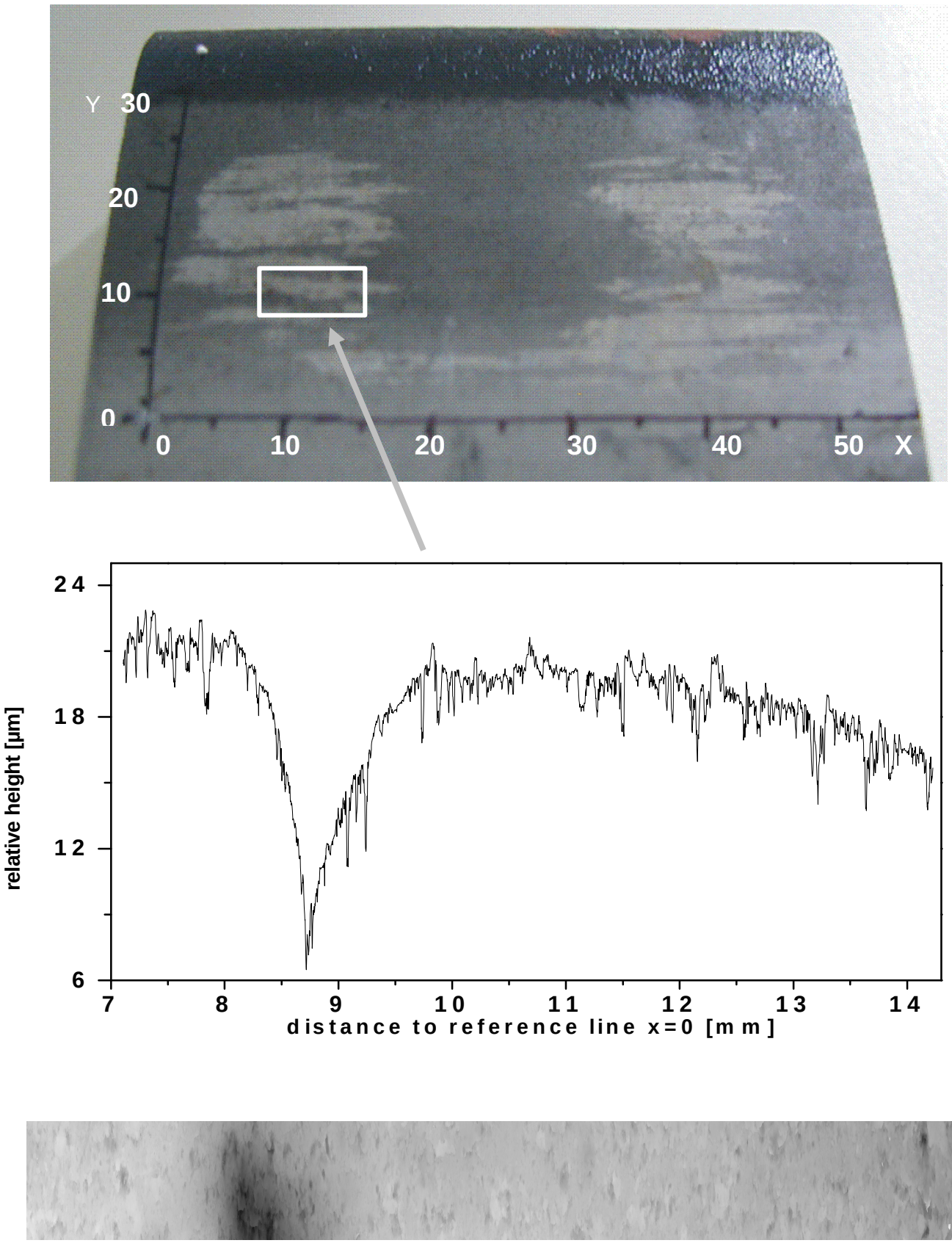

Fig. 5.1.20 Profile over a segment of rail at y = 10mm and x = 7.1-14.2 mm with the corresponding interference spectroscopic picture

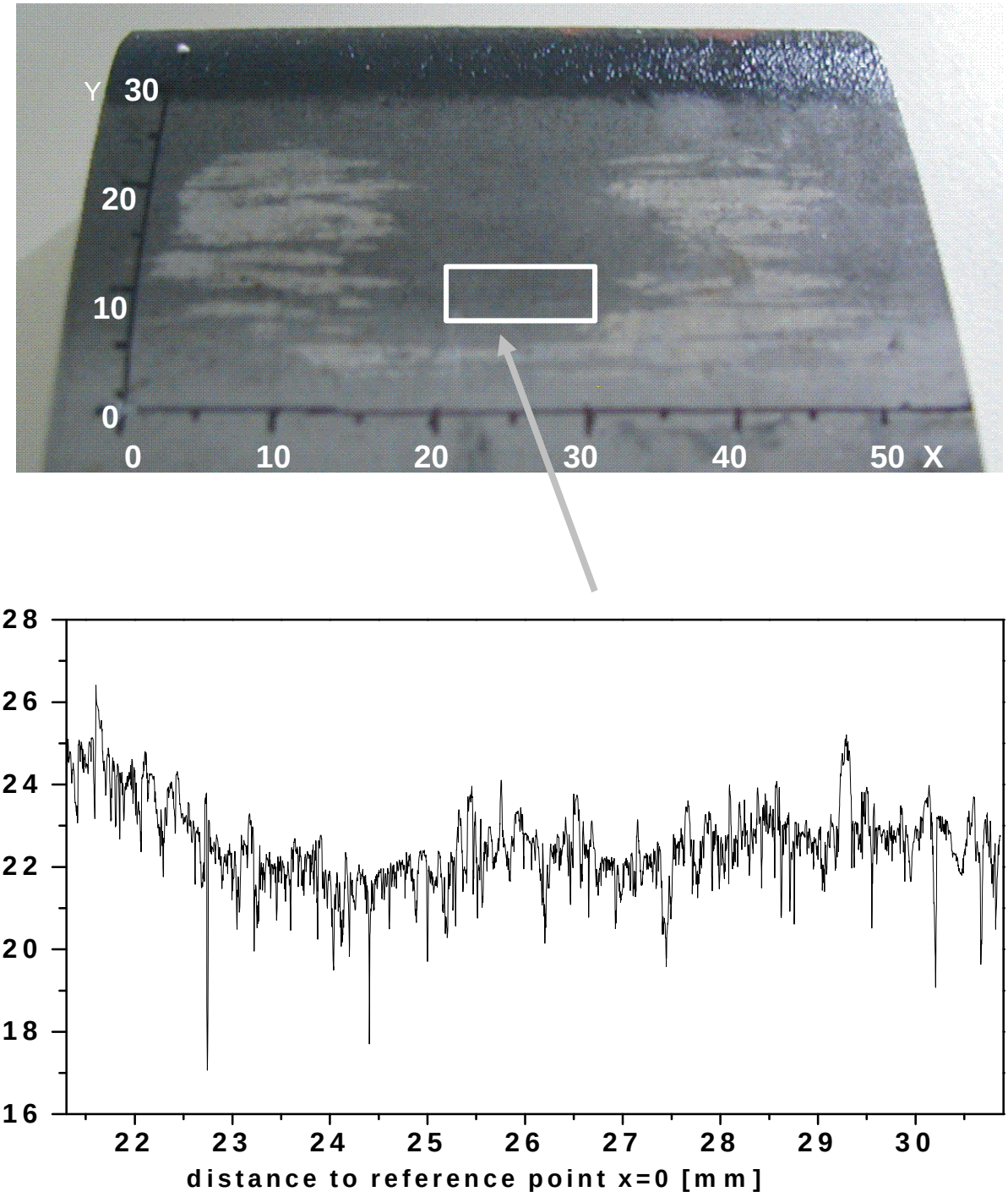

Fig. 5.1.21 Profile over a segment of rail at y = 10mm and x = 21.8-30.8 mm with the corresponding interference spectroscopic picture

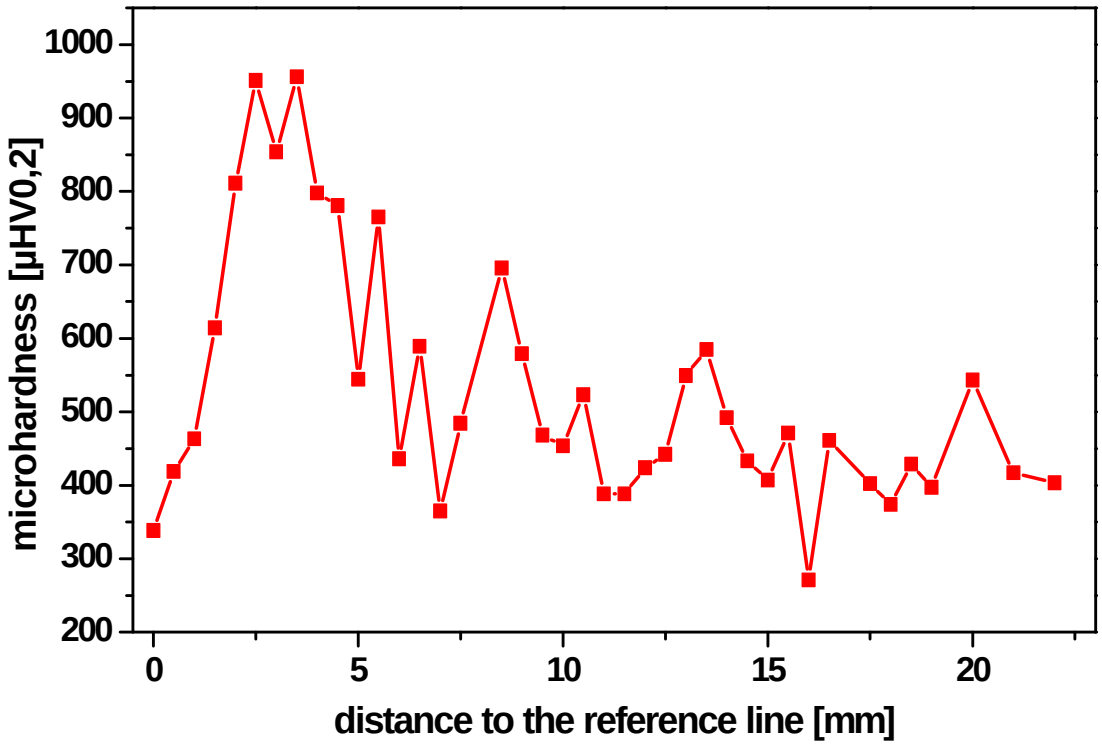

Fig. 5.1.22 Microhardness distribution on the segment of rail at y = 10mm and from x = 0mm to x = 24 mm

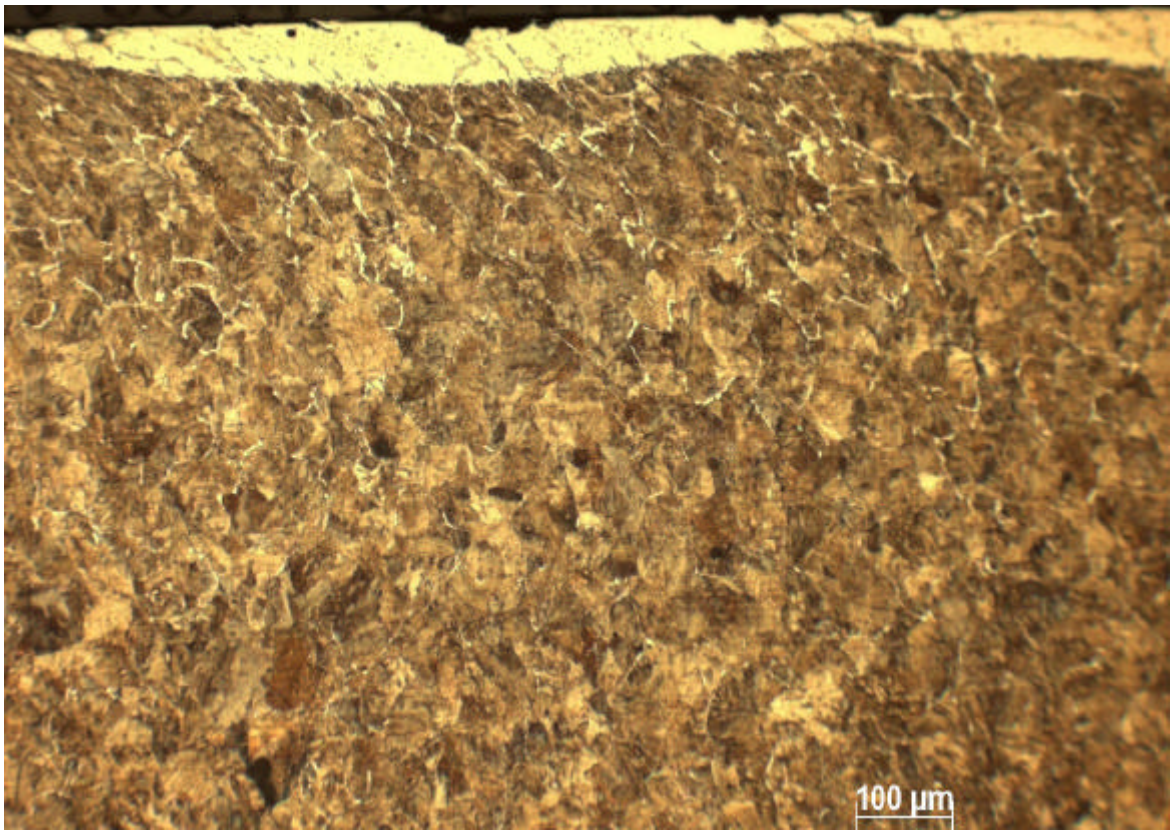

Fig. 5.1.23 Optical microscopy picture of rail Baumann in cross section

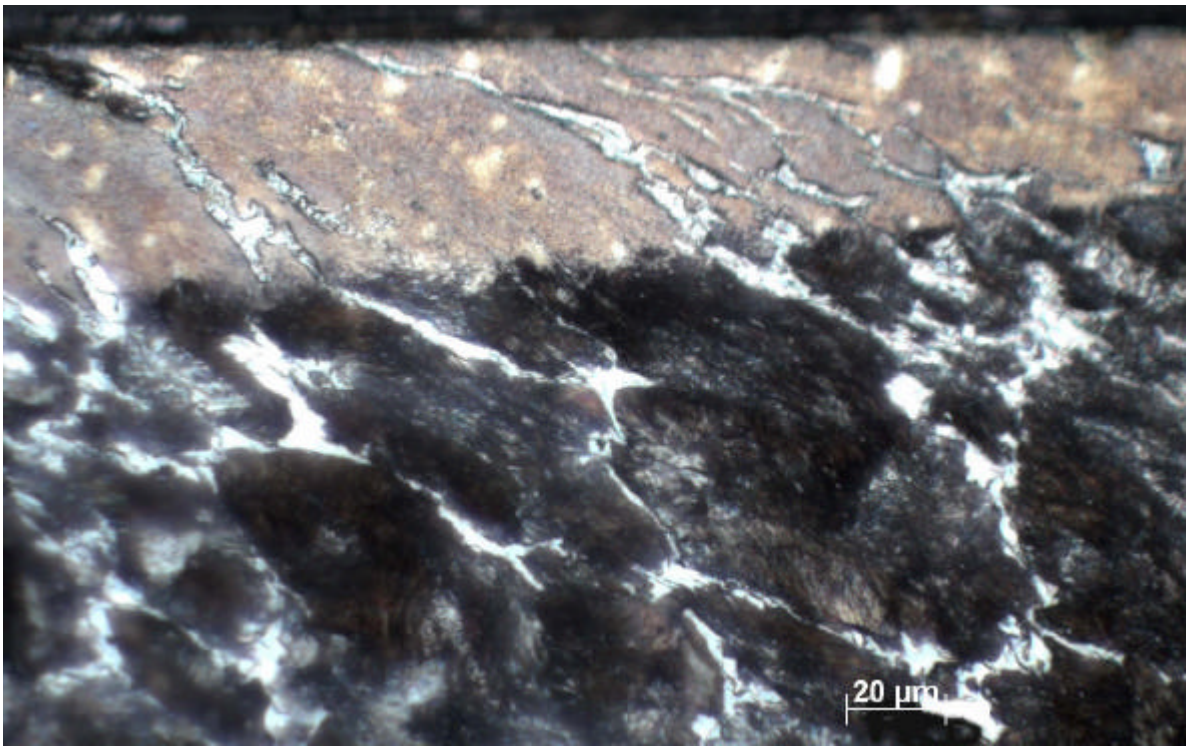

(a)

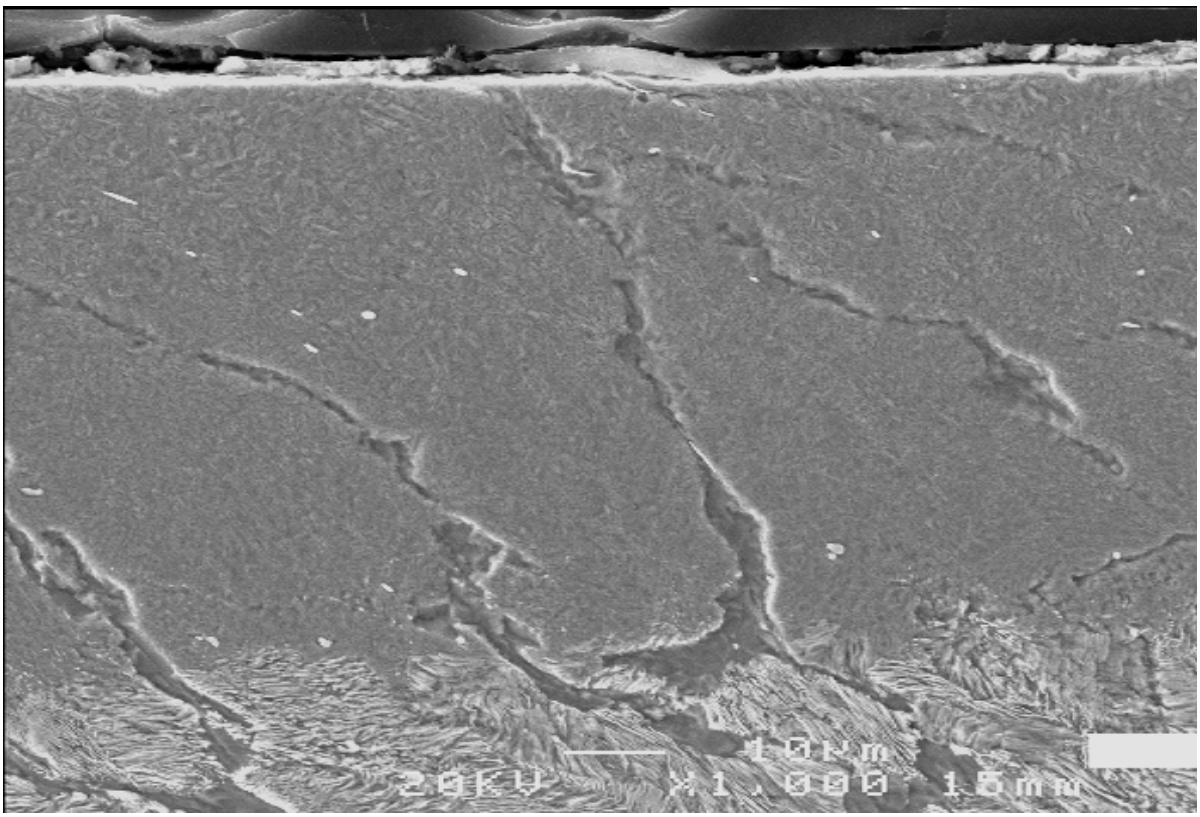

(b)

Fig. 5.1.24 Pictures of ferrite boundary in White Etching Layer in cross section
(a) Optical microscopy
(b) SEM

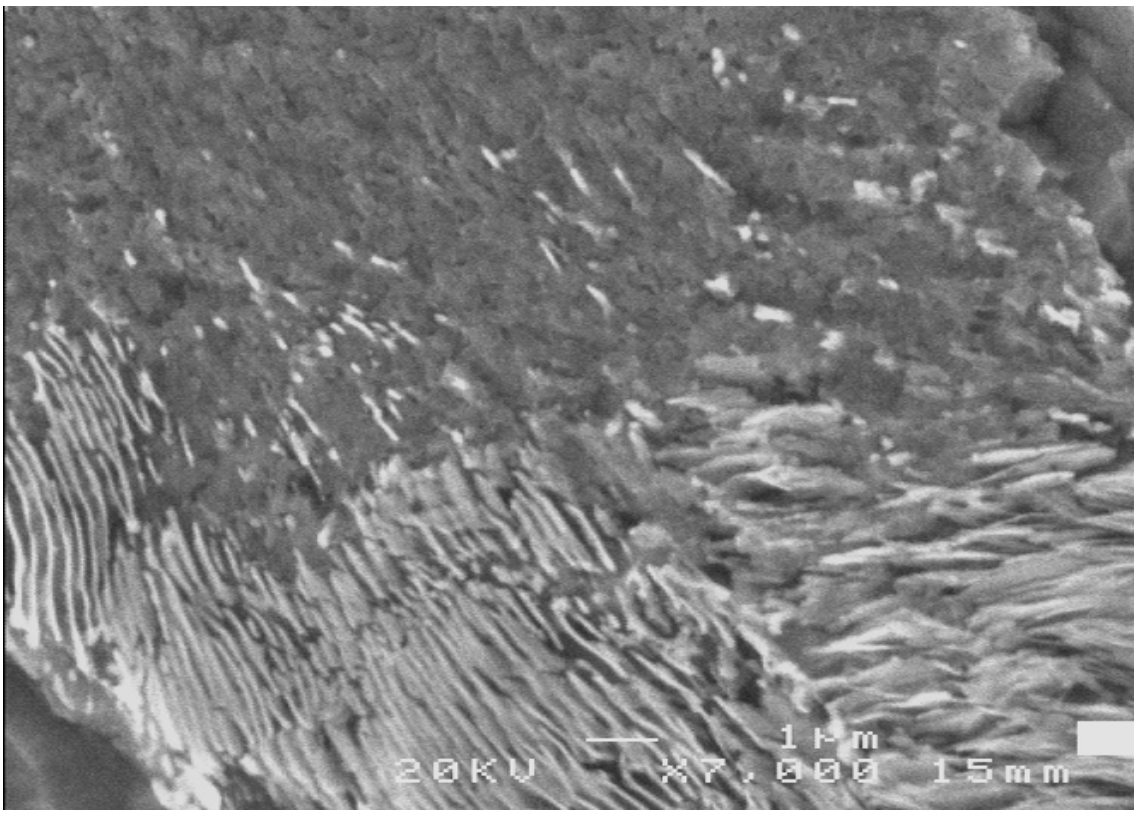

Fig. 5.1.25 SEM picture of carbide breaking up

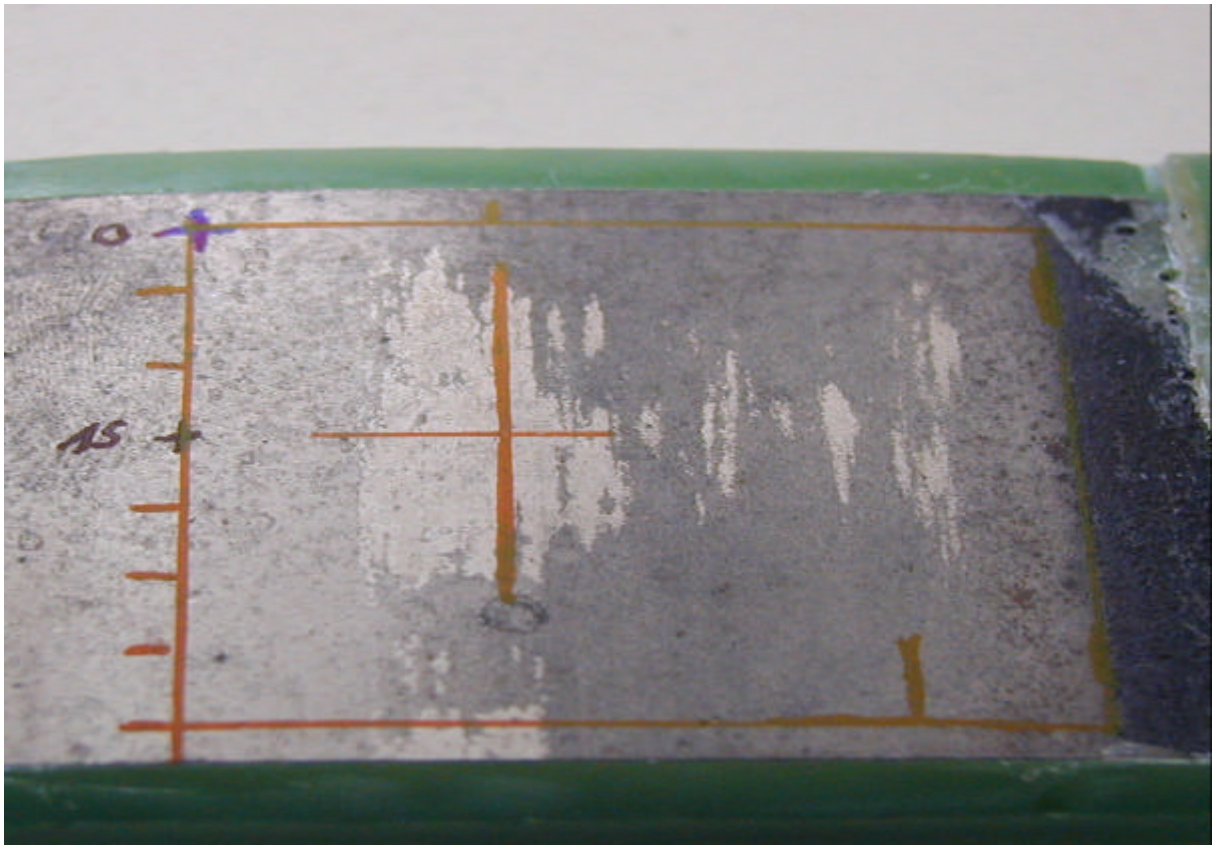

Fig. 5.1.26 Photo of the sample of rail Baumann for the determination of the microhardness

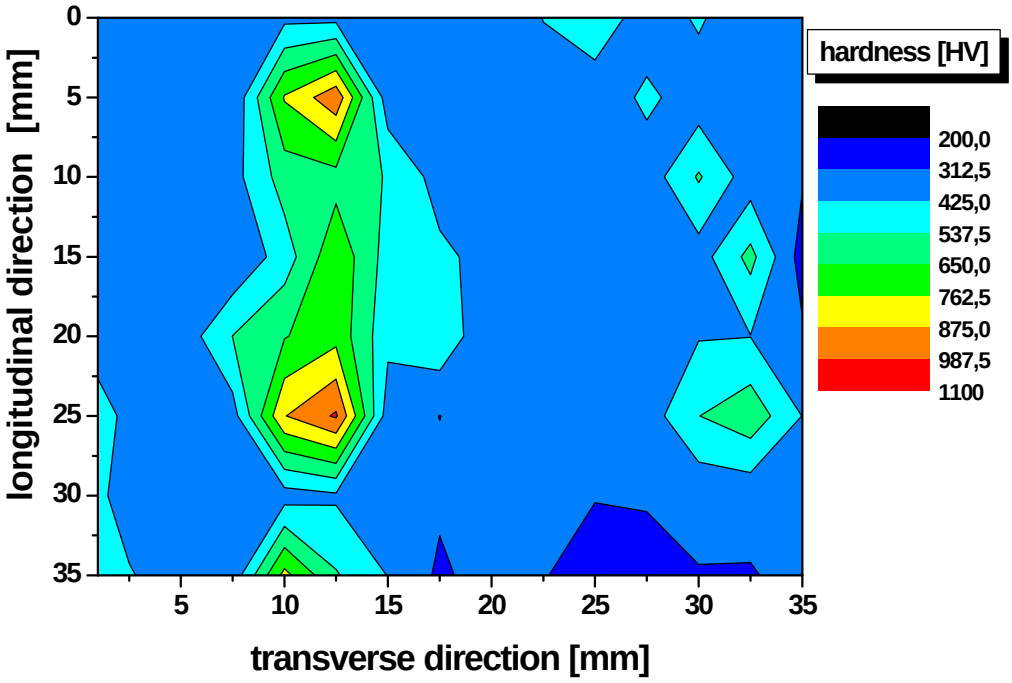

Fig. 5.1.27 Microhardness distribution across the rail Baumann

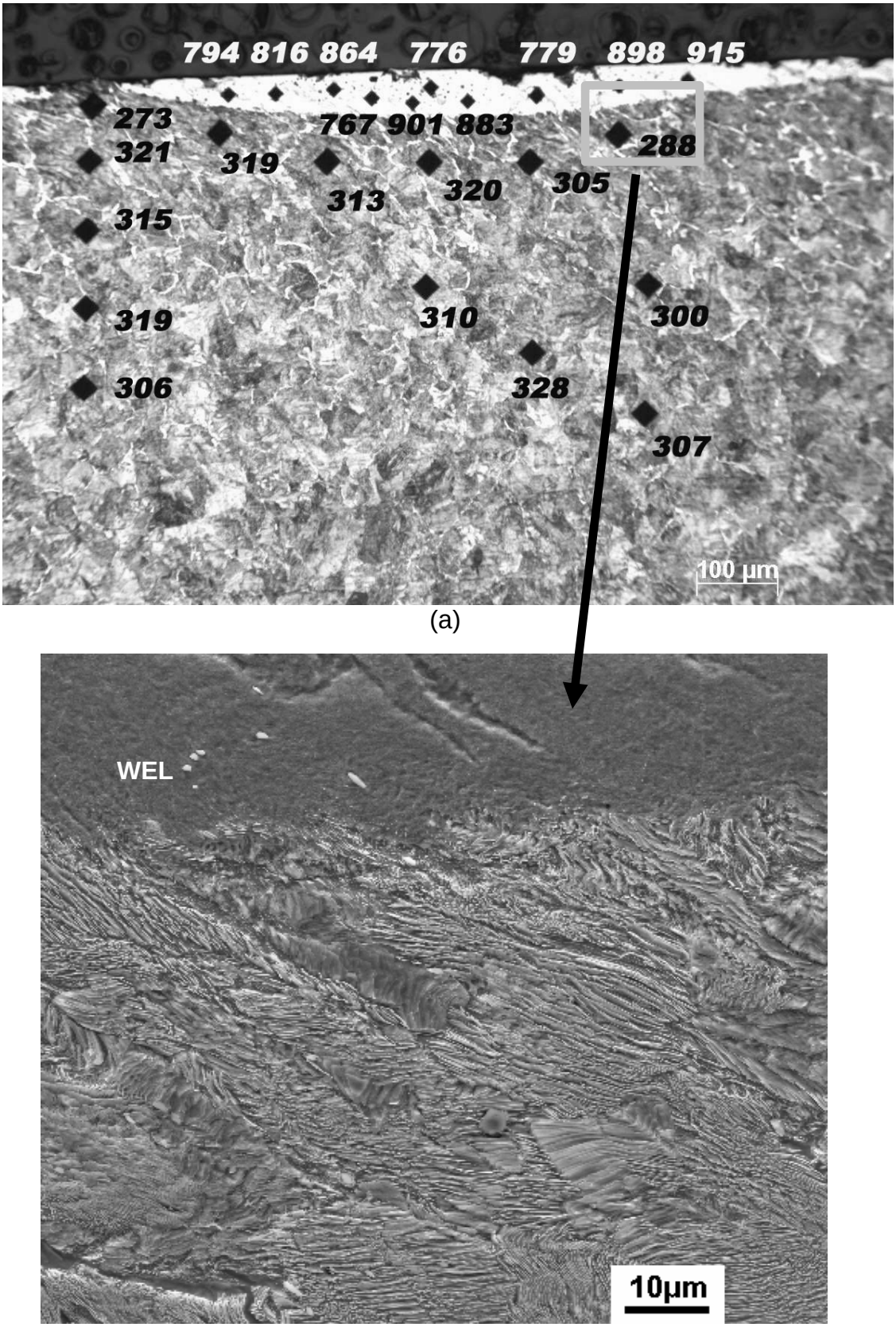

(a)

(b)

Fig. 5.1.28 (a) Microhardness distribution in the subsurface region of rail Baumann (with WEL)
(b) SEM picture of the region just below WEL

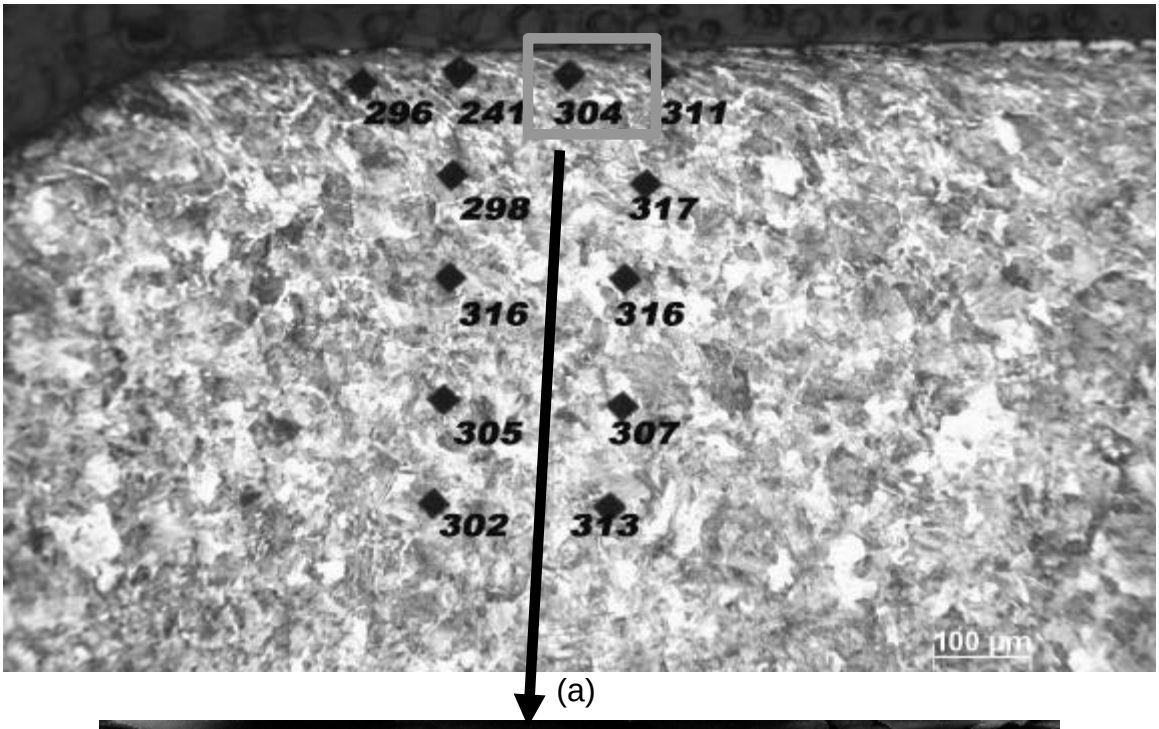

(a)

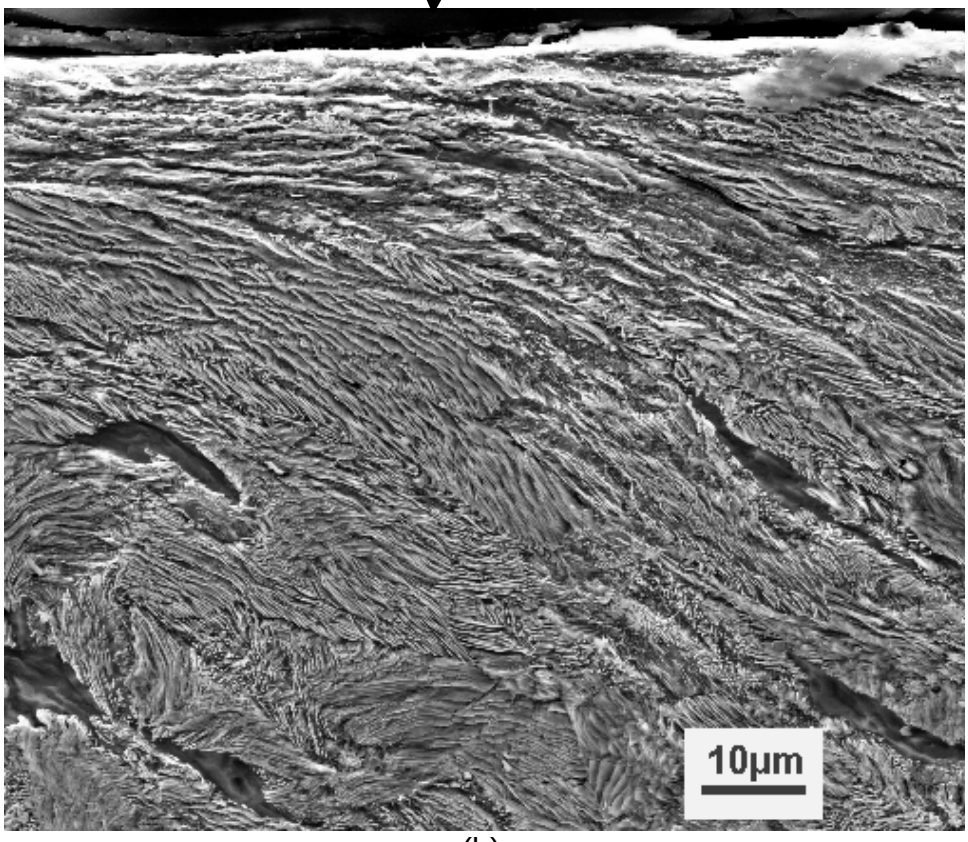

(b)

Fig. 5.1.29 (a) Microhardness distribution in the subsurface region of rail baumann (without WEL)
(b) SEM picture of the deformed layer

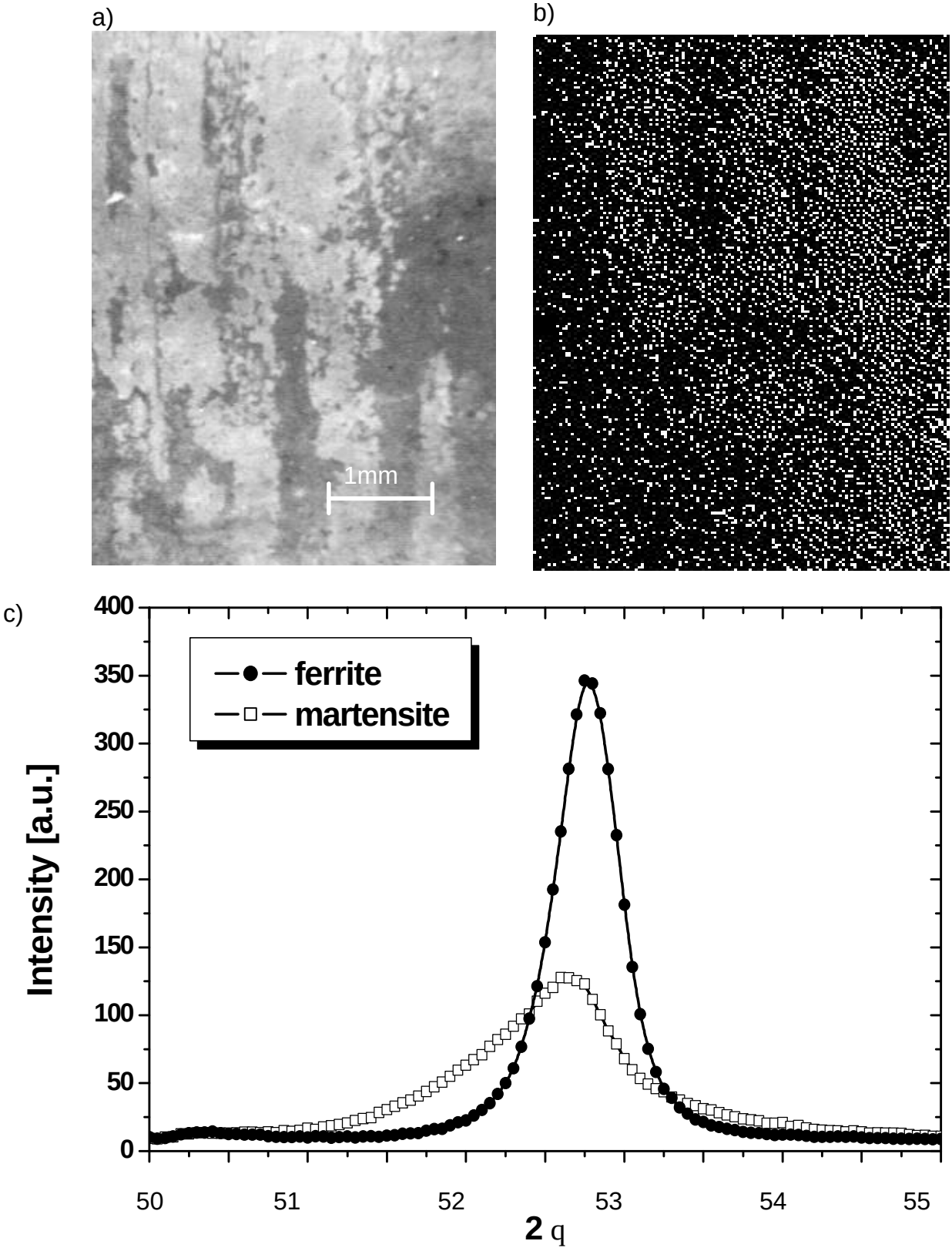

Fig. 5.1.30 a) Photo of rail Baumann
b) X-ray image of α -Fe 110 reflection
c) Sum profile of α -Fe 110 reflection

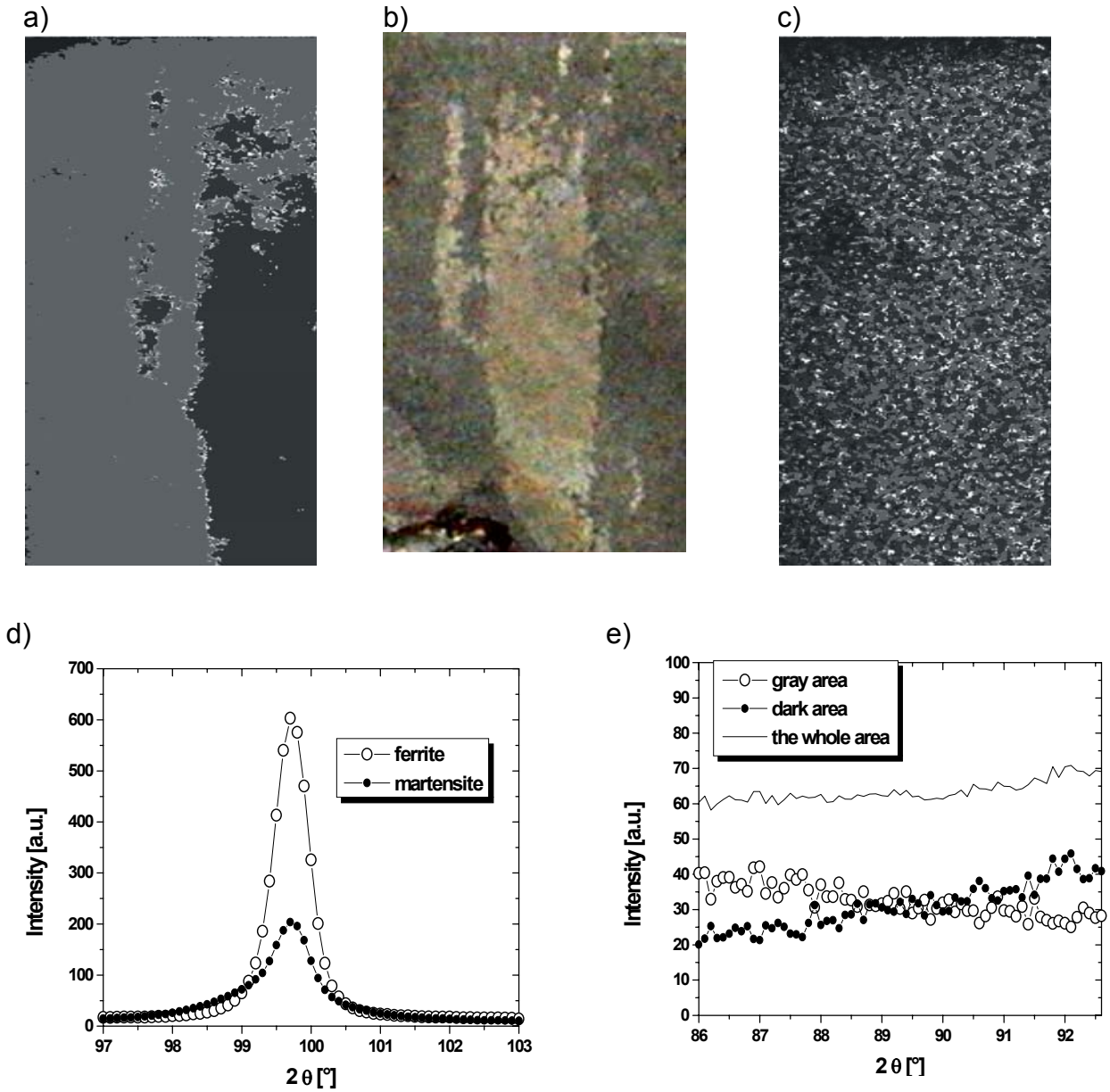

Fig.5.1.31 a) X - ray image scan of α–Fe 211 reflection
b) Photo of rail Baumann surface
c) X - ray image scan of γ–Fe 220 reflection
d) Sum profile of α–Fe 211 reflection
e) Sum profile of γ–Fe 220 reflection

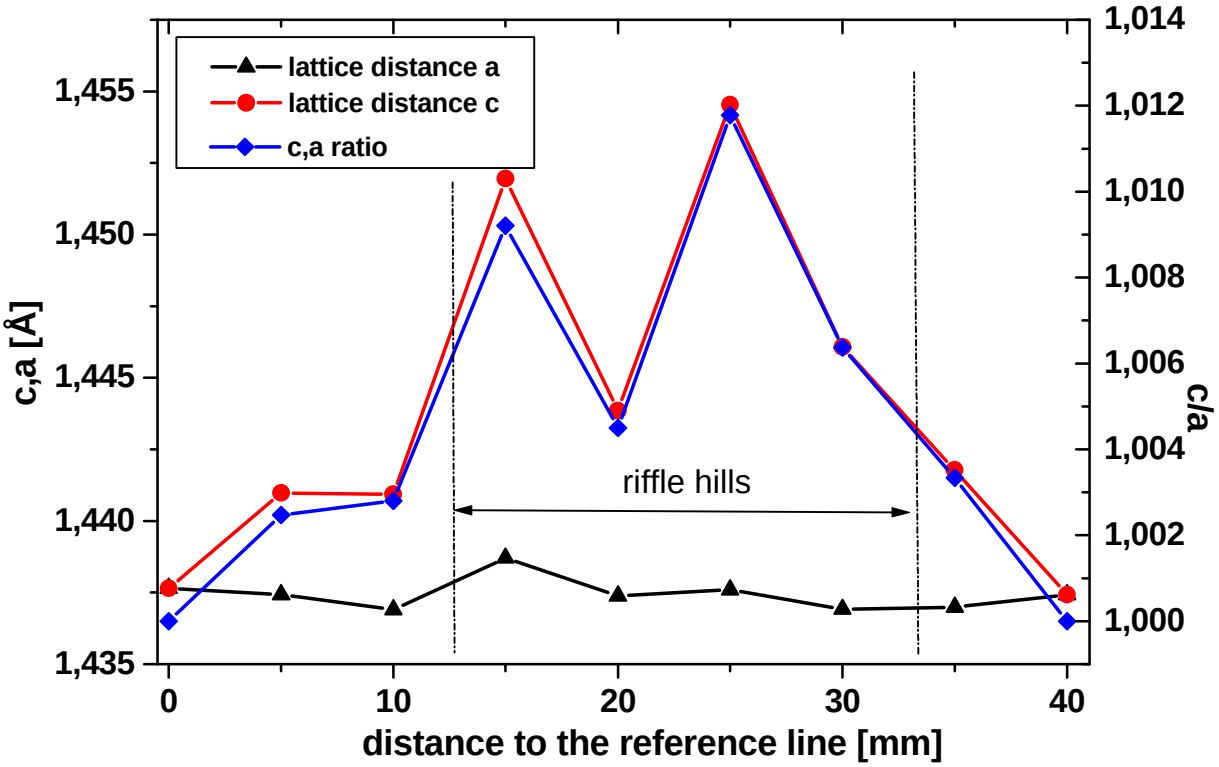

Fig. 5.1.32 Lattice distance c, a and c/a ratio across the rail Baumann surface

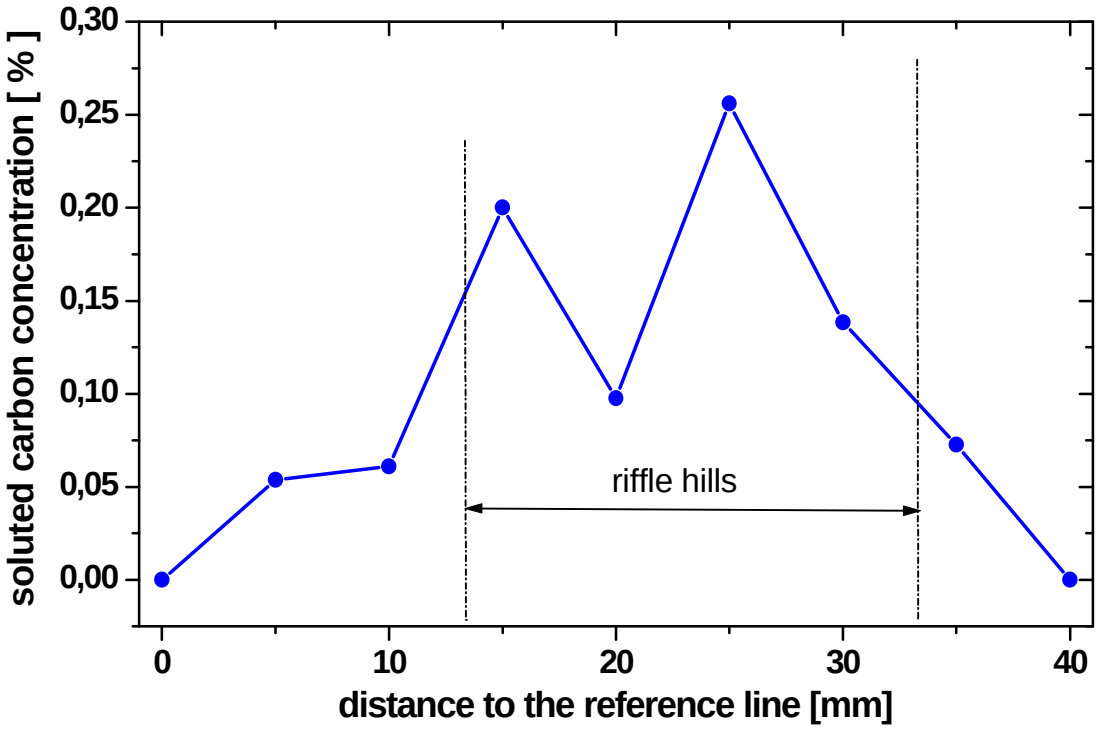

Fig. 5.1.33 Solute carbon concentration distribution across the rail Baumann

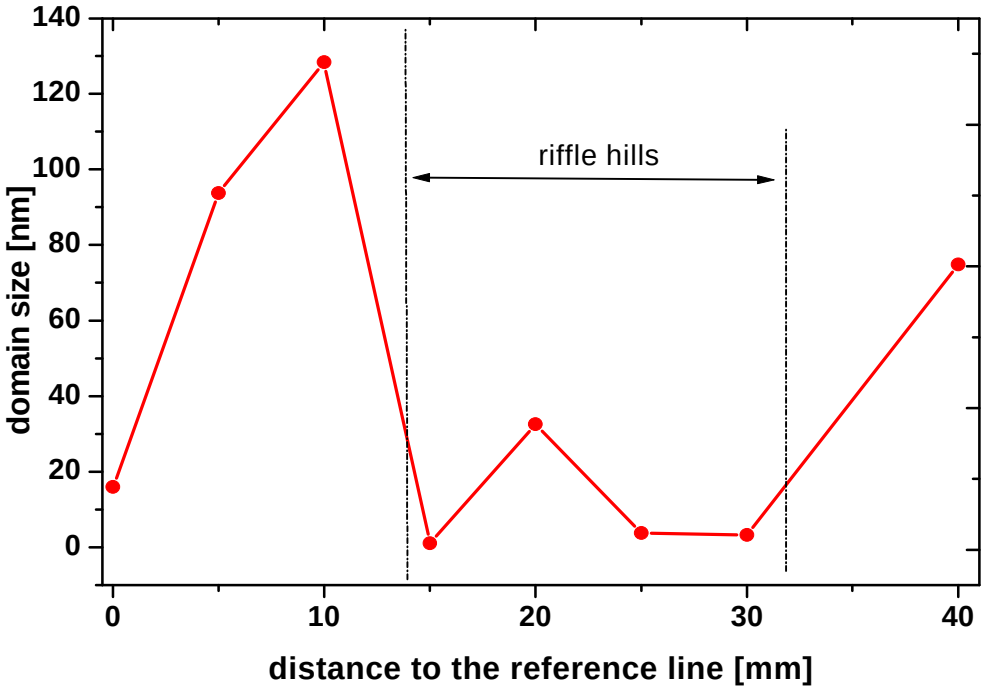

Fig. 5.1.34 Domain size distribution across the rail Baumann

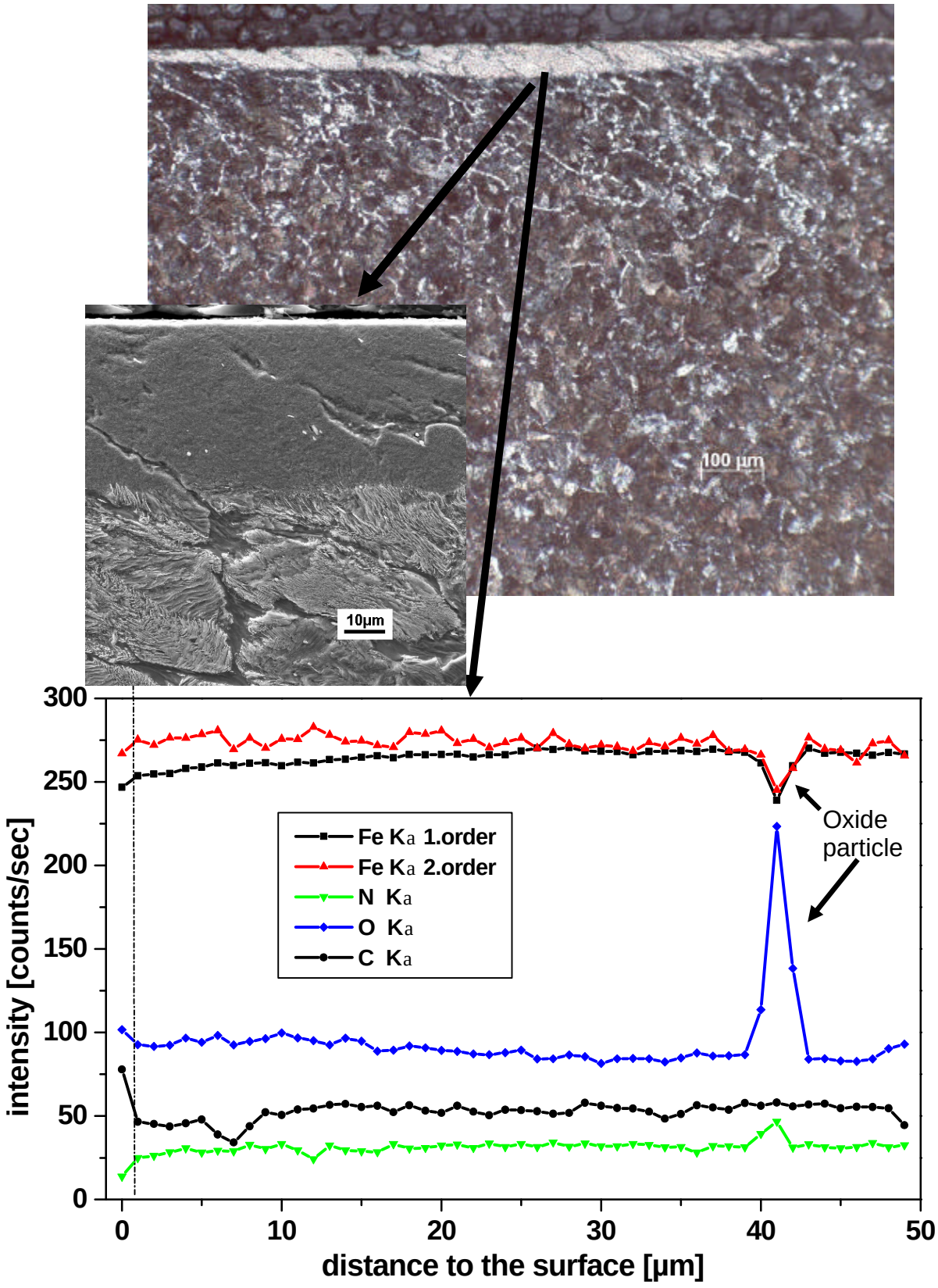

Fig. 5.1.35 Microprobe analyses in the area of the WEL on rail Baumann

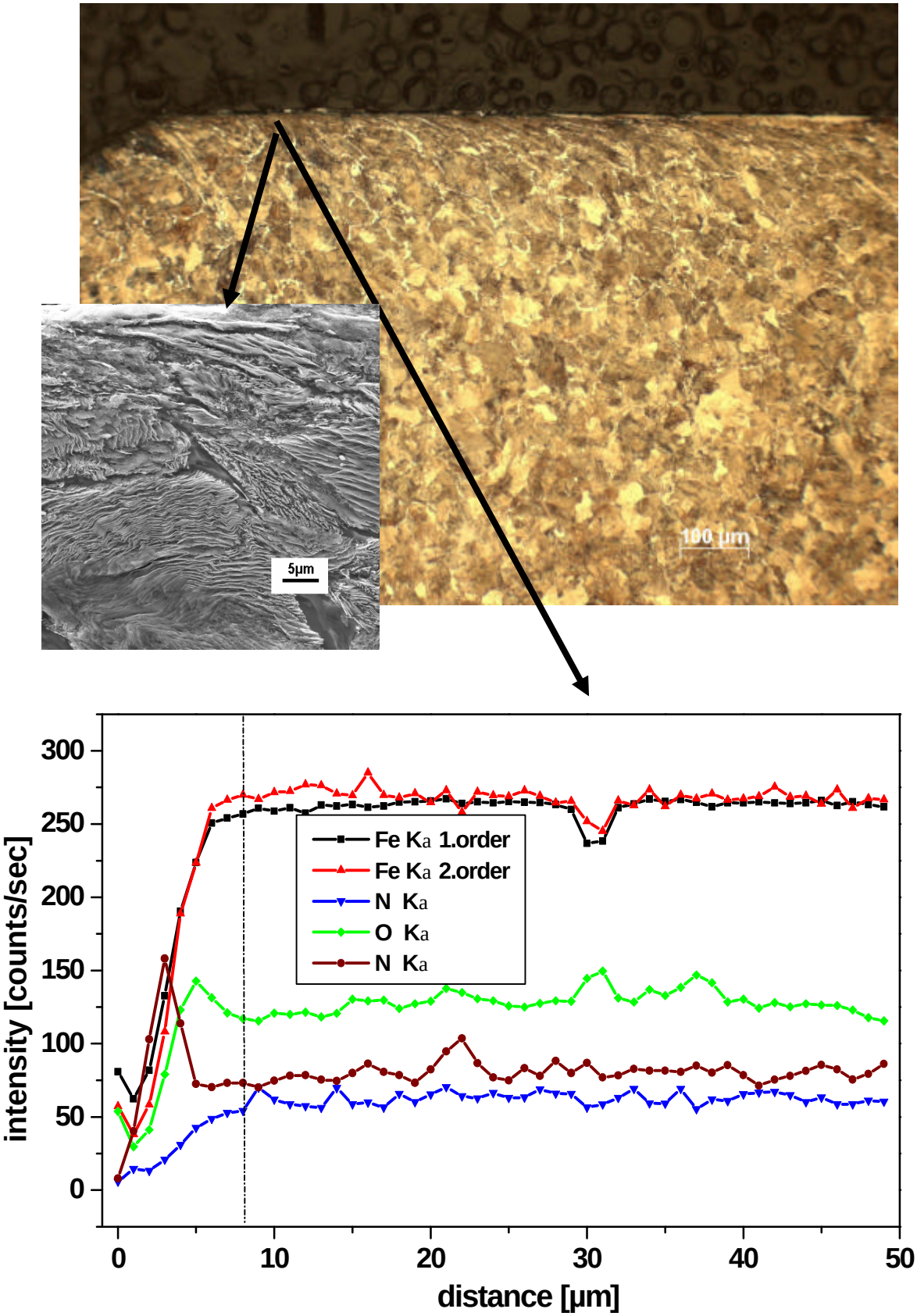

Fig. 5.1.36 Microprobe analyses in the area of non - WEL on rail Baumann

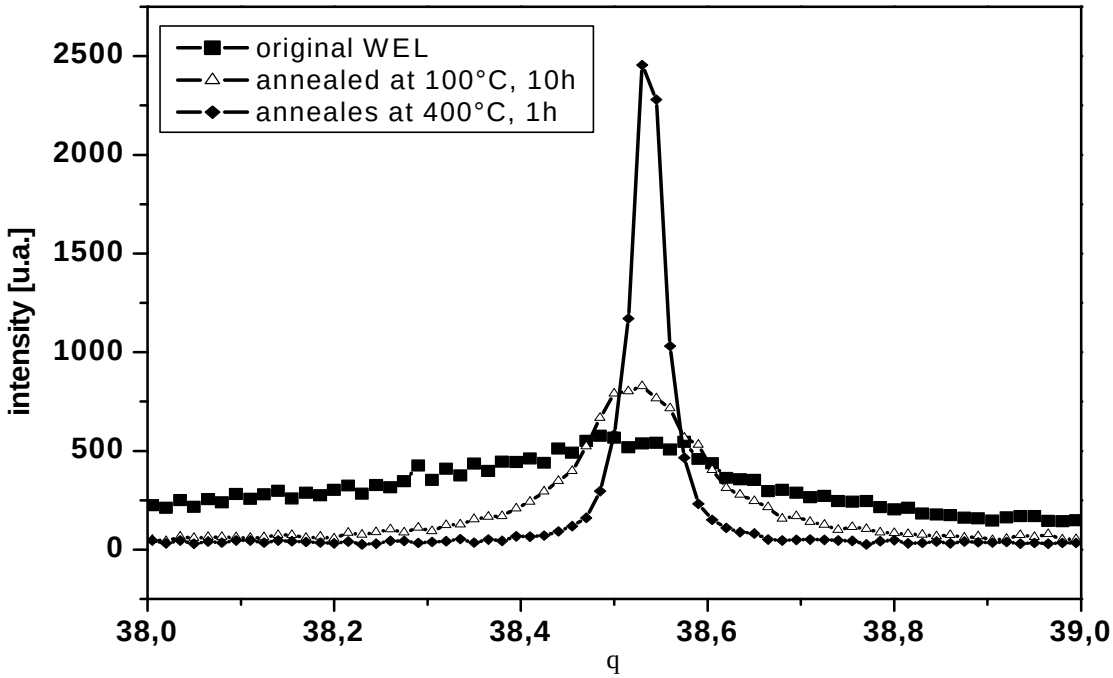

Fig. 5.1.37 A exemplary 200 reflection profile before and after annealing

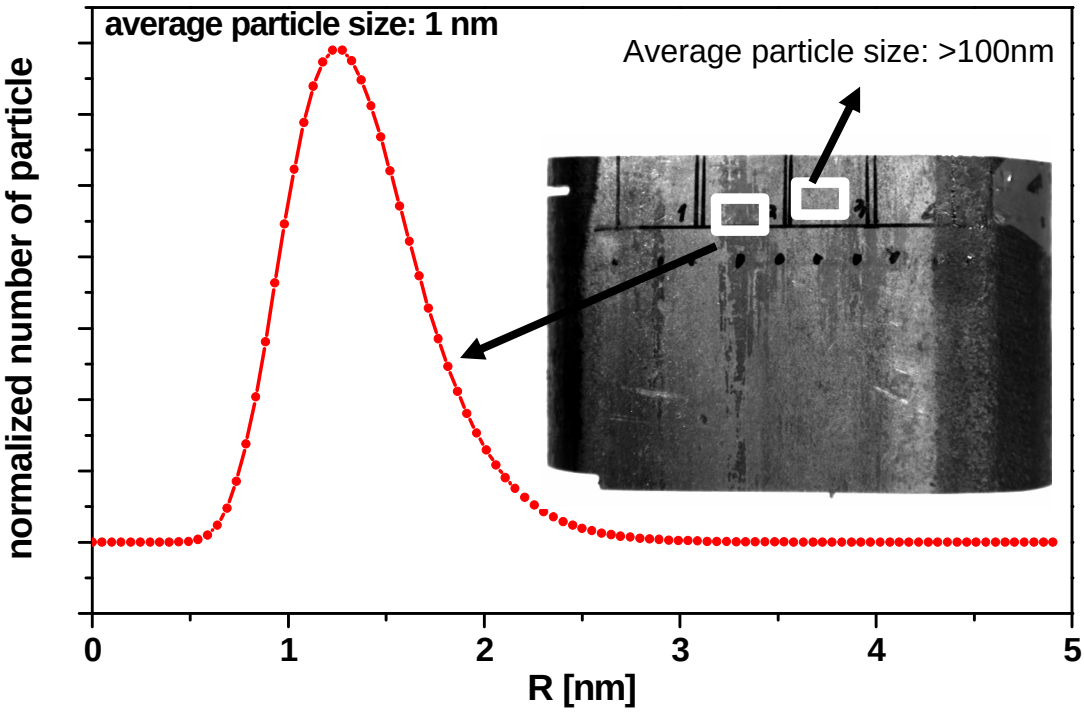

Fig. 5.1.38 Average carbide size using small angle scattering

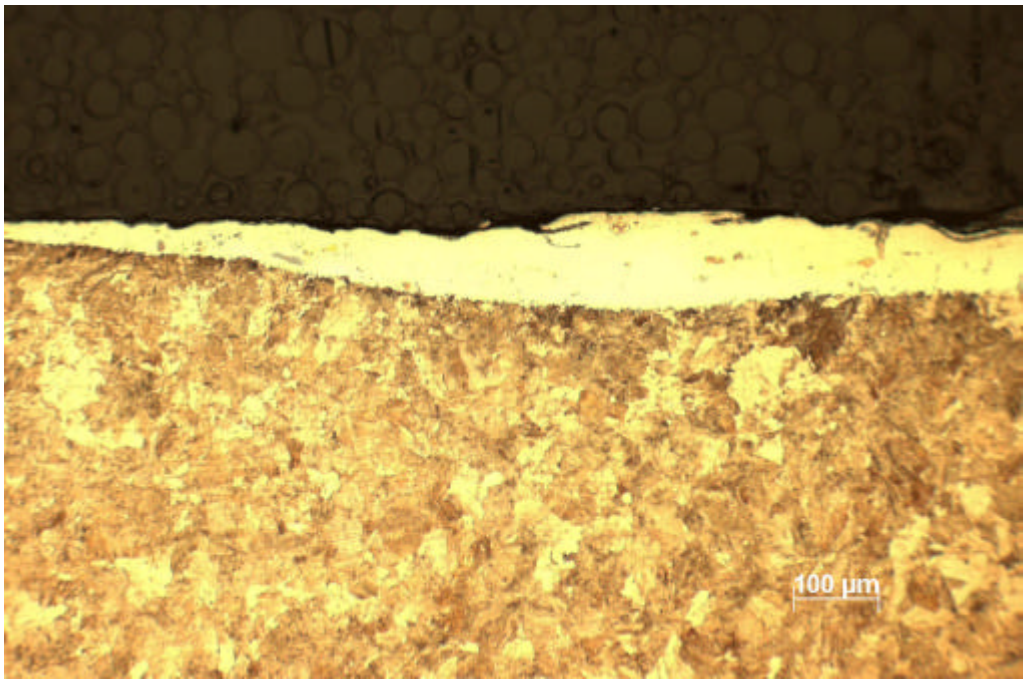

Fig. 5.1.39 Optical picture of WEL on rail sample 2

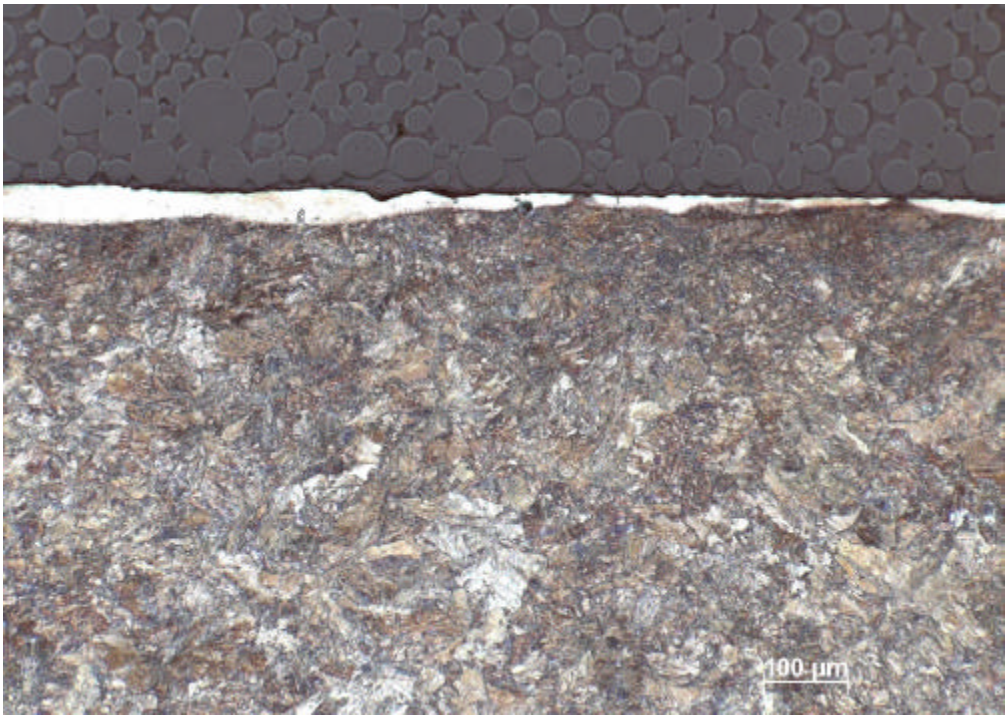

Fig. 5.1.40 Optical picture of WEL on rail sample 3

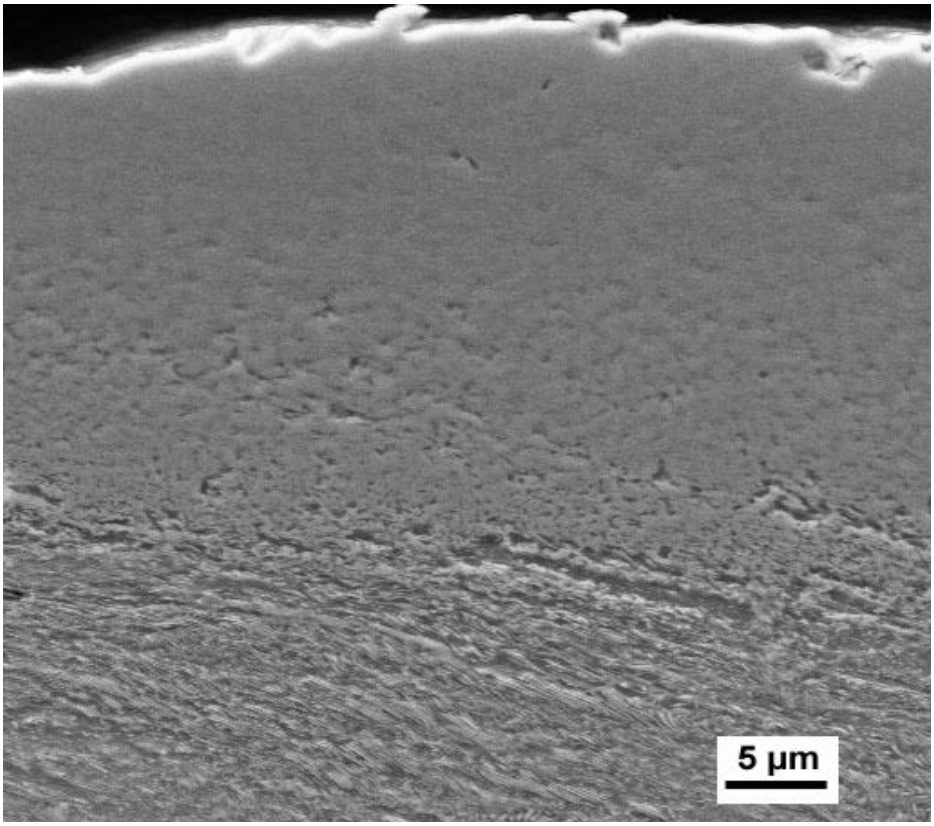

Fig. 5.1.41 White Etching Layer under Scanning Electron Microscopy

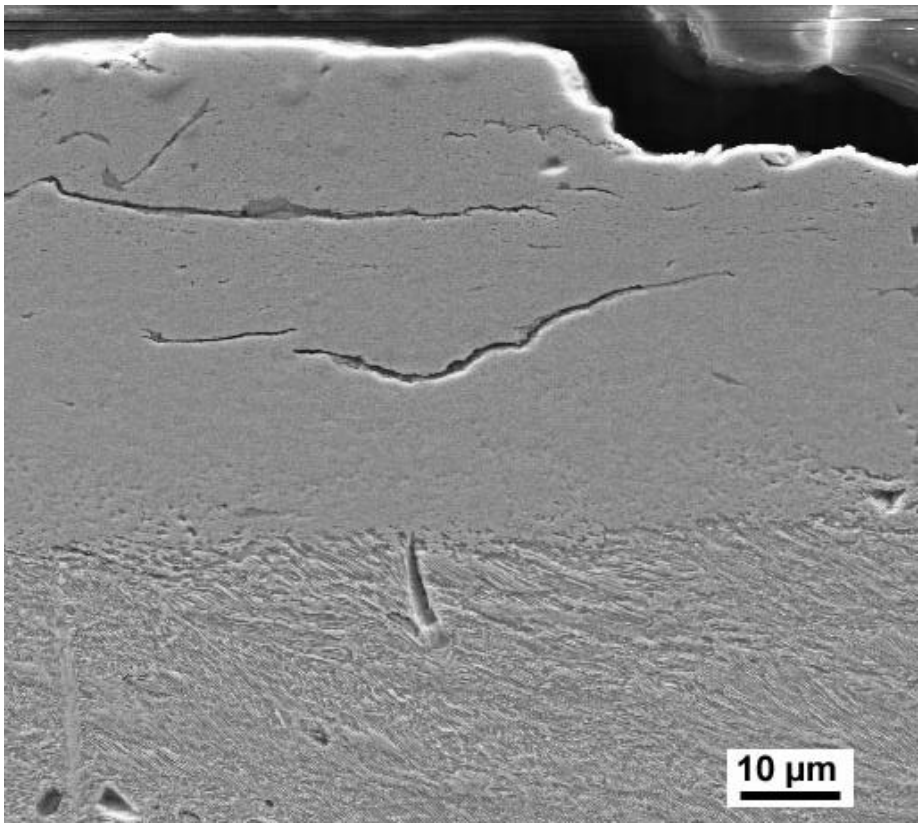

Fig. 5.1.42 Spalling and cracks in WEL under Scanning Electron Microscopy

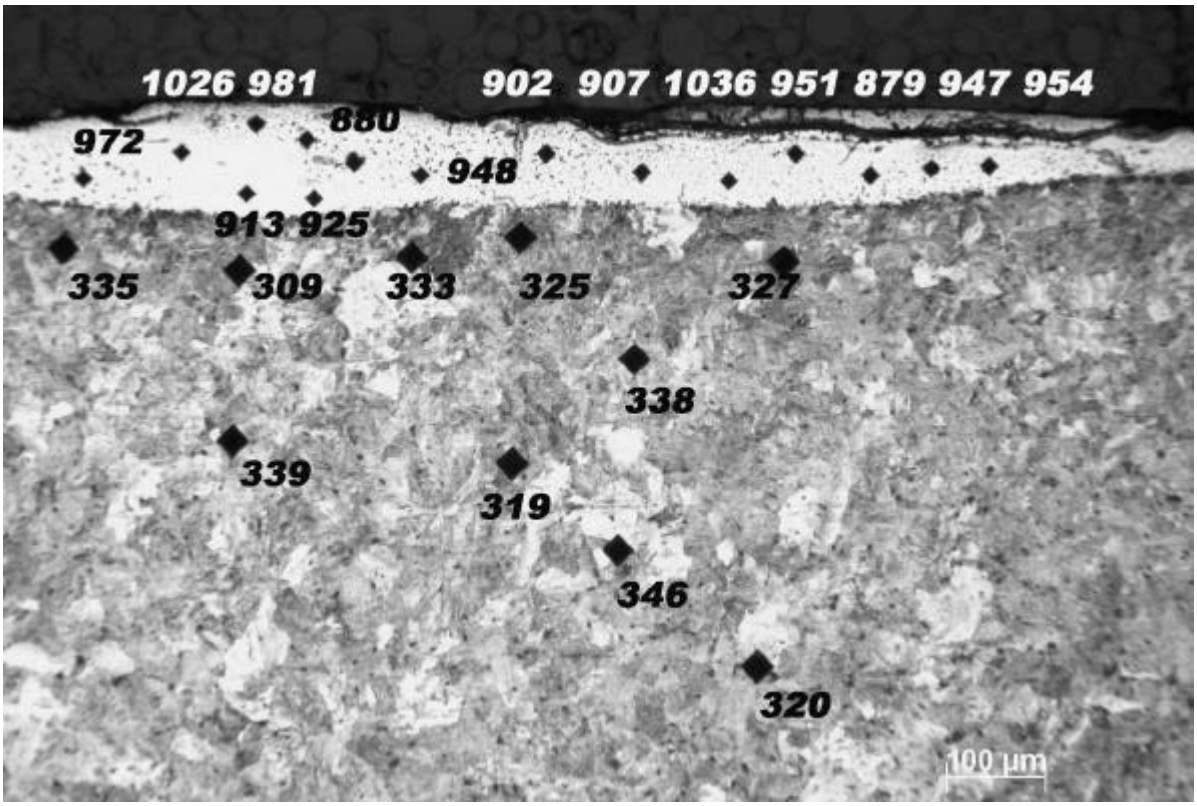

Fig. 5.1.43 Microhardness distribution in-depth of rail sample 2

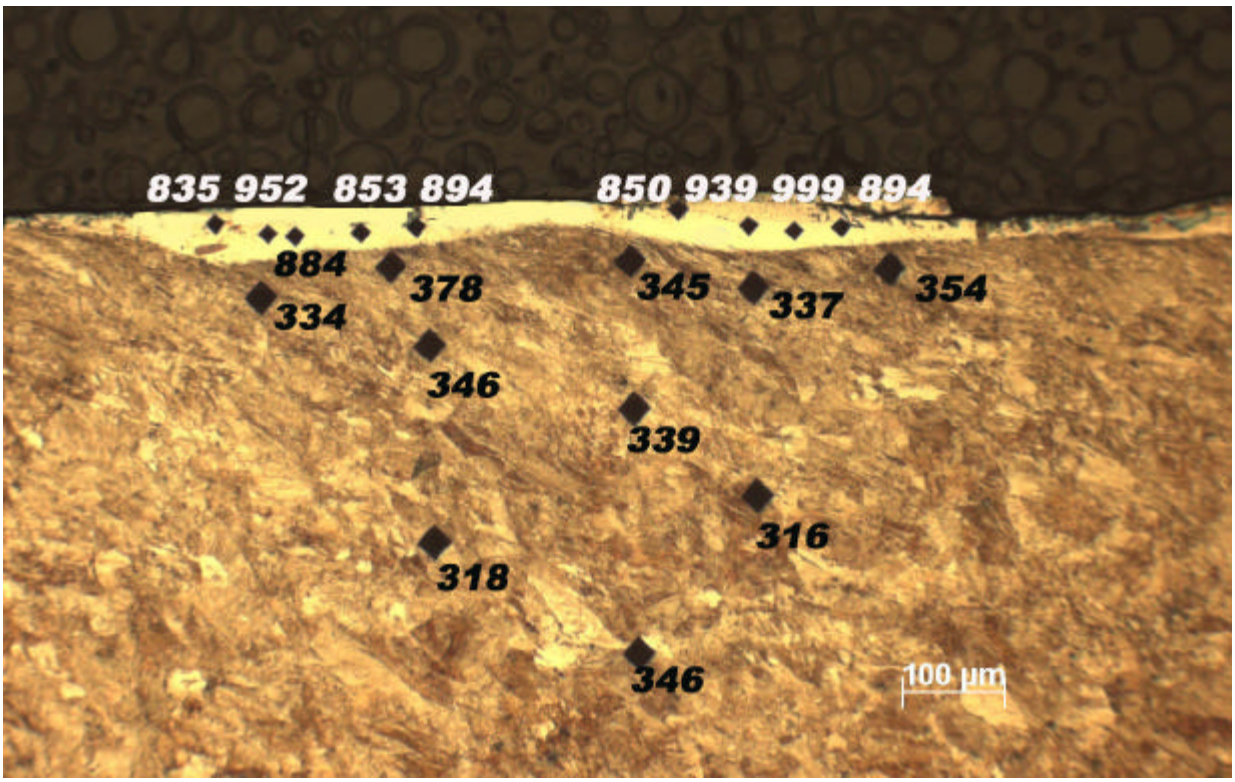

Fig. 5.1.44 Microhardness disribution in-depth of rail sample 3

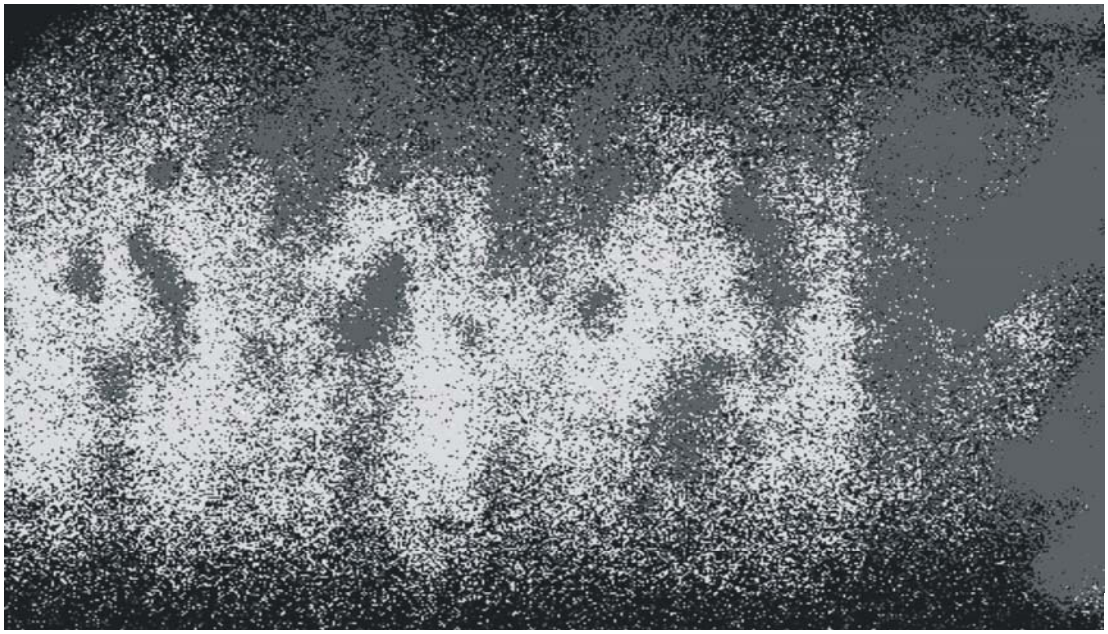

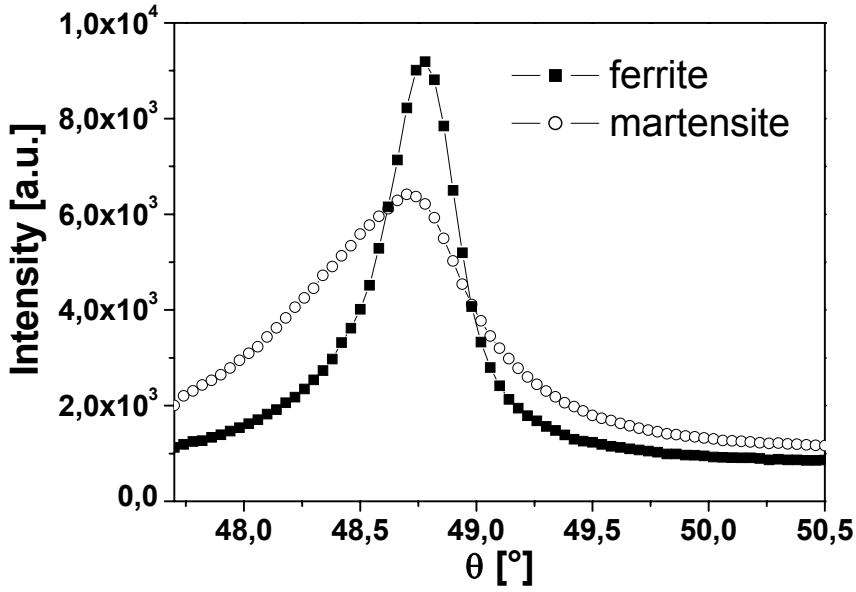

Fig. 5.1.45: Ferrite and martensite distribution on the surface of rail sample 2

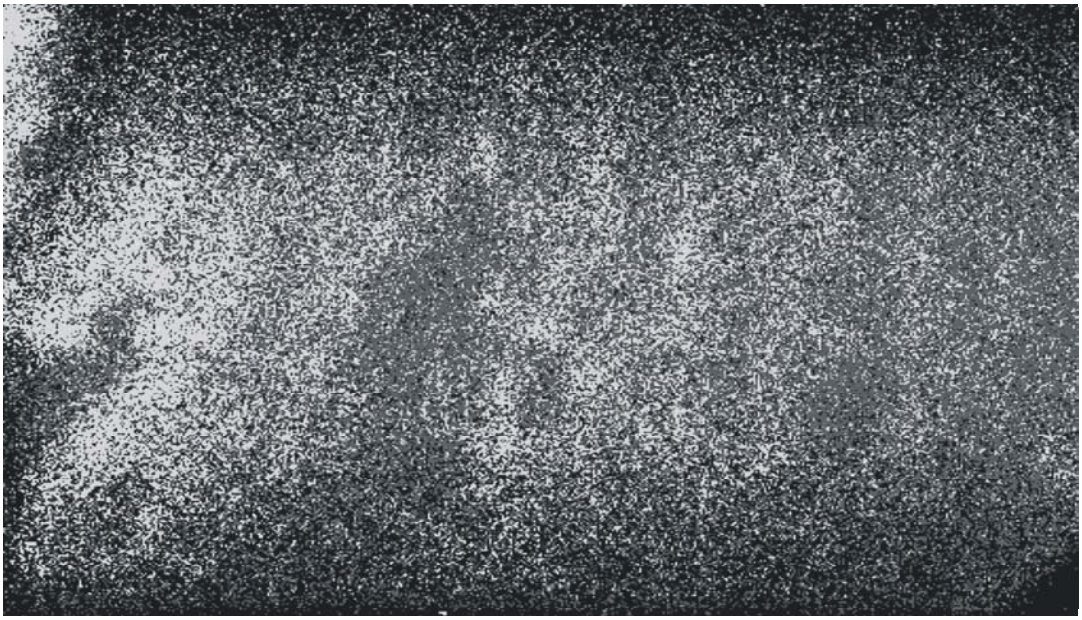

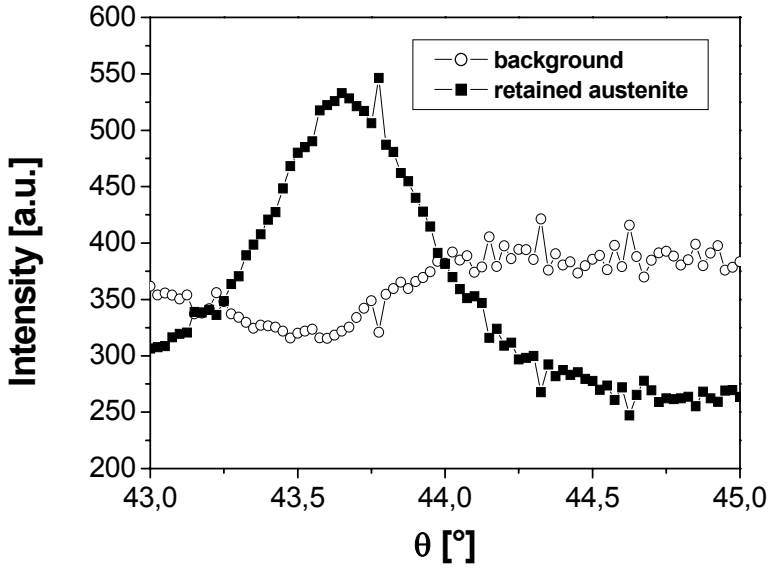

Fig. 5.1.46 Retained austenite distribution on the surface of rail sample 2

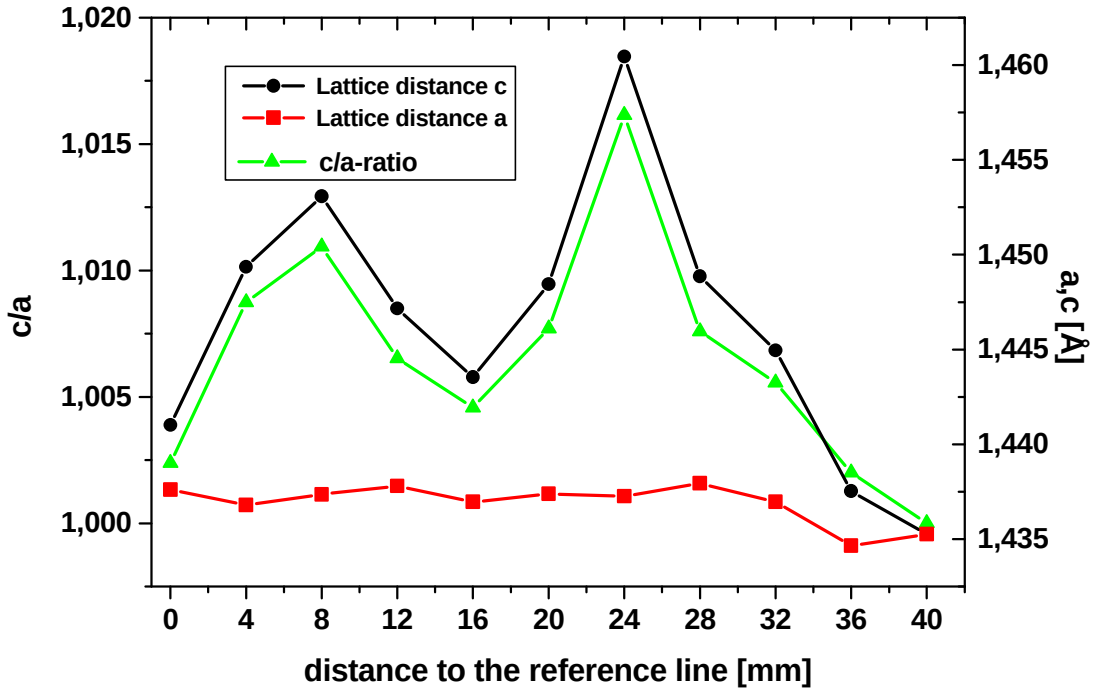

Fig. 5.1.47 Lattice distance and c,a ratio distribution cross the surface of rail sample 2

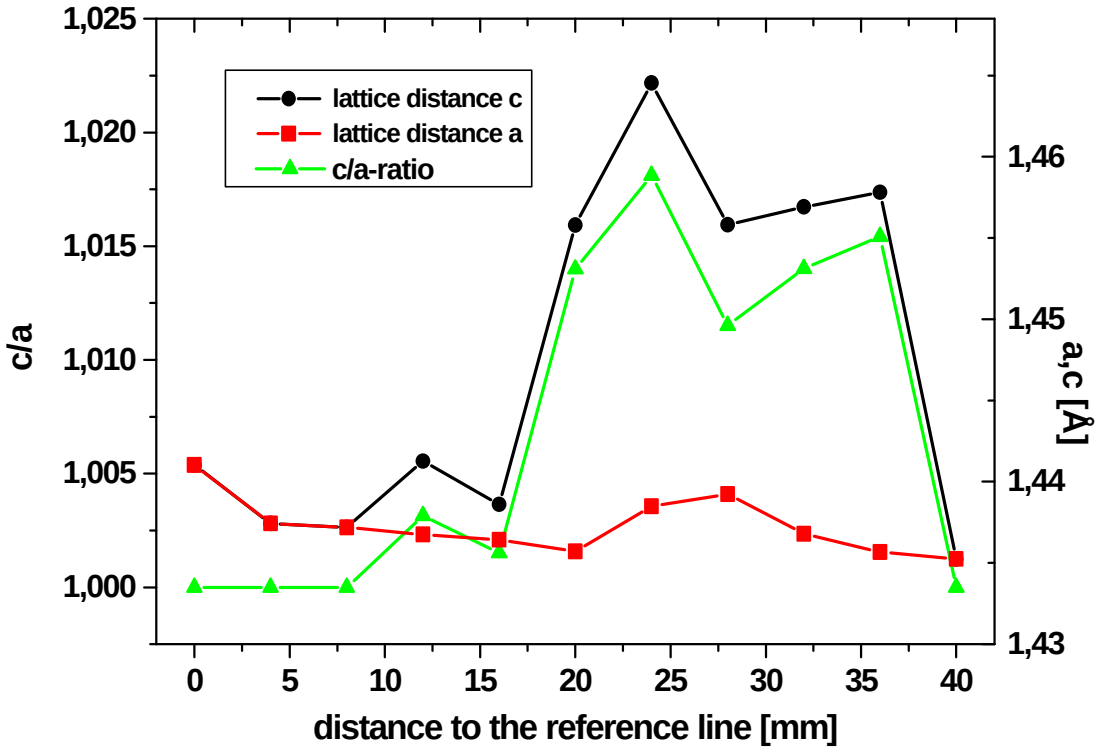

Fig. 5.1.48 Lattice distance and c,a ratio distribution on the surface of sample 3

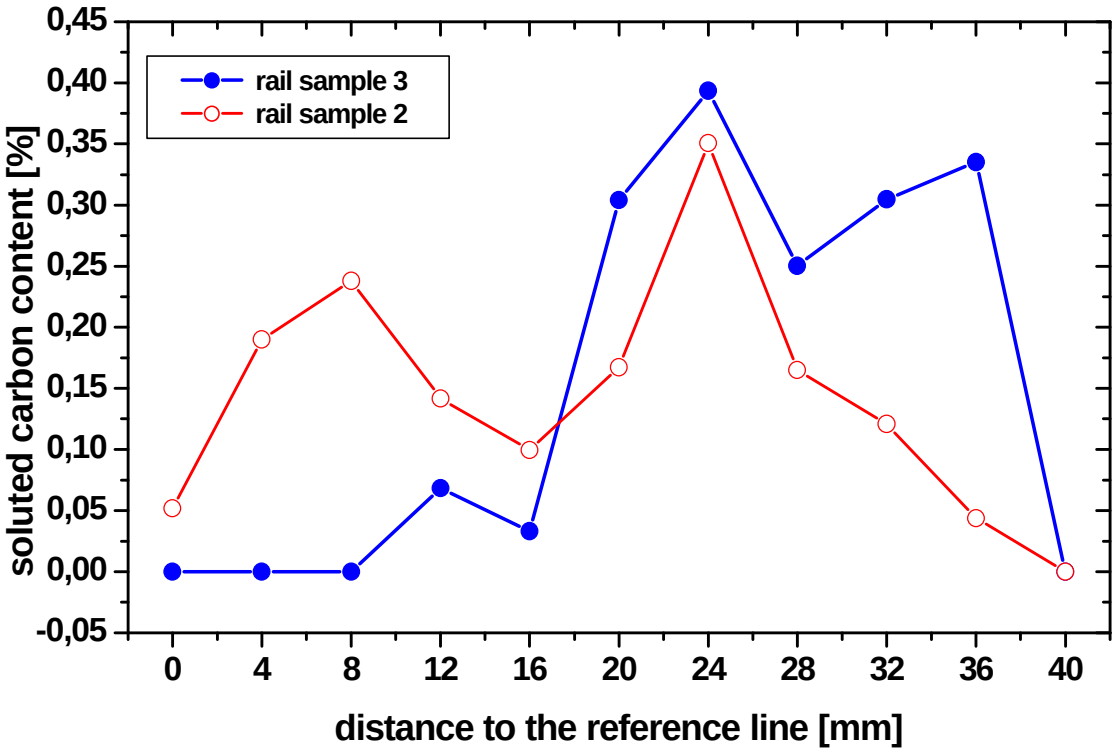

Fig. 5.1.49 Solute carbon concentration on rail sample 2 and rail sample 3

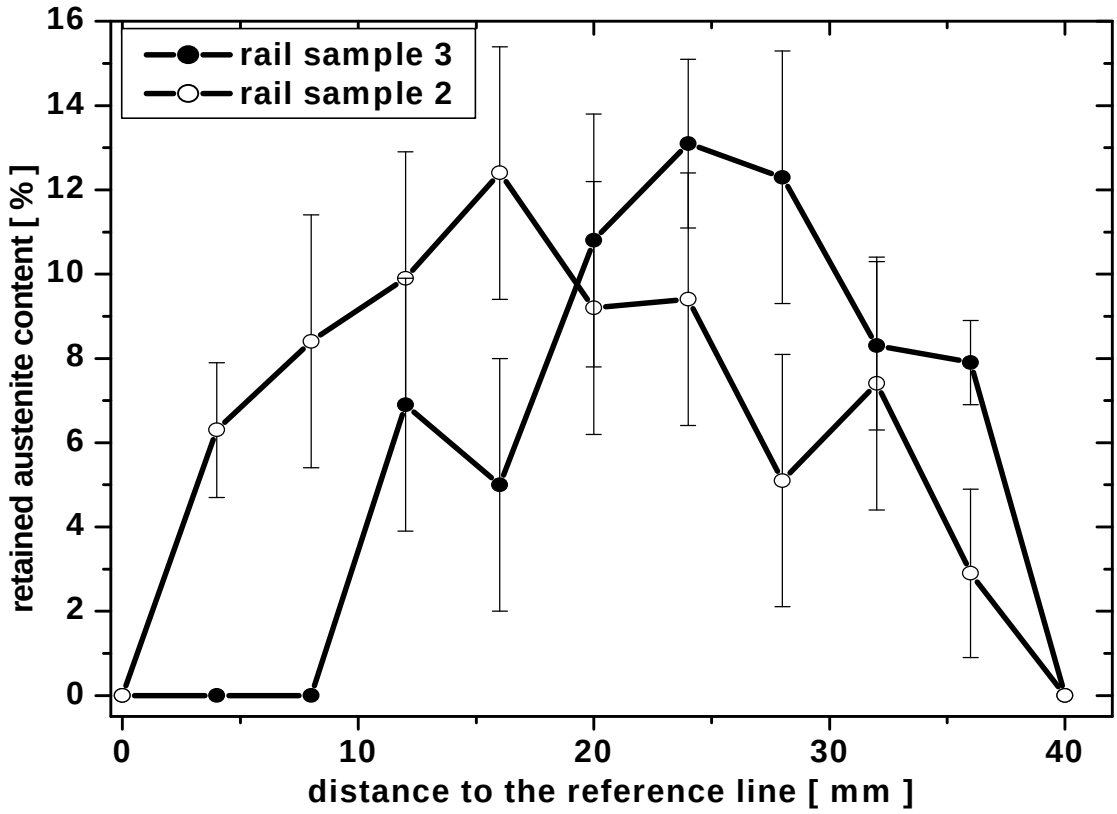

Fig. 5.1.50 Retained austenite content across the surface of rail sample 2 and rail sample 3

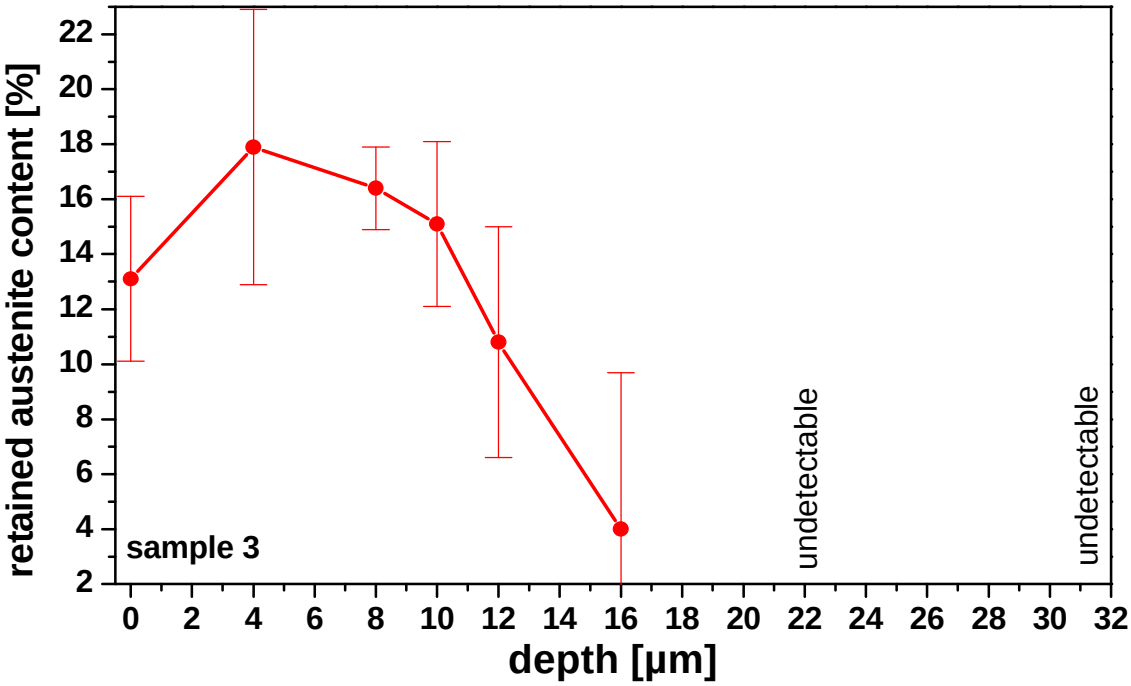

Fig. 5.1.51 Retained austenite content in - depth below the rolling surface of rail sample 3

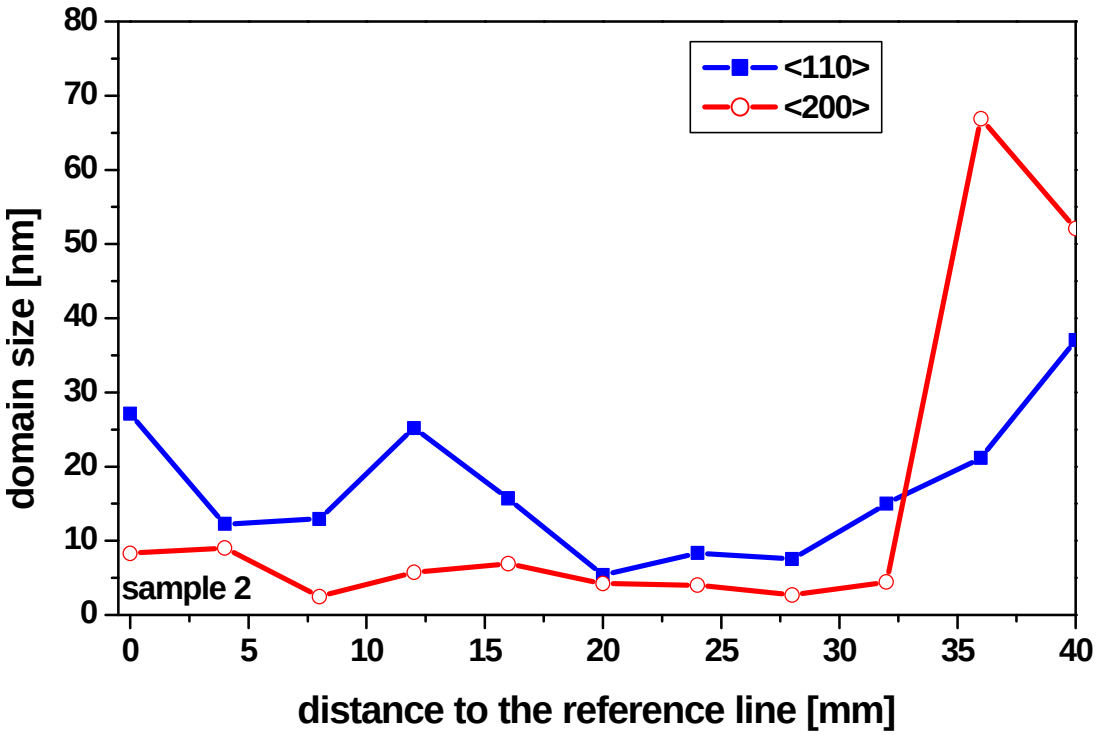

Fig. 5.1.52 Domain size distribution across the surface of rail sample 2

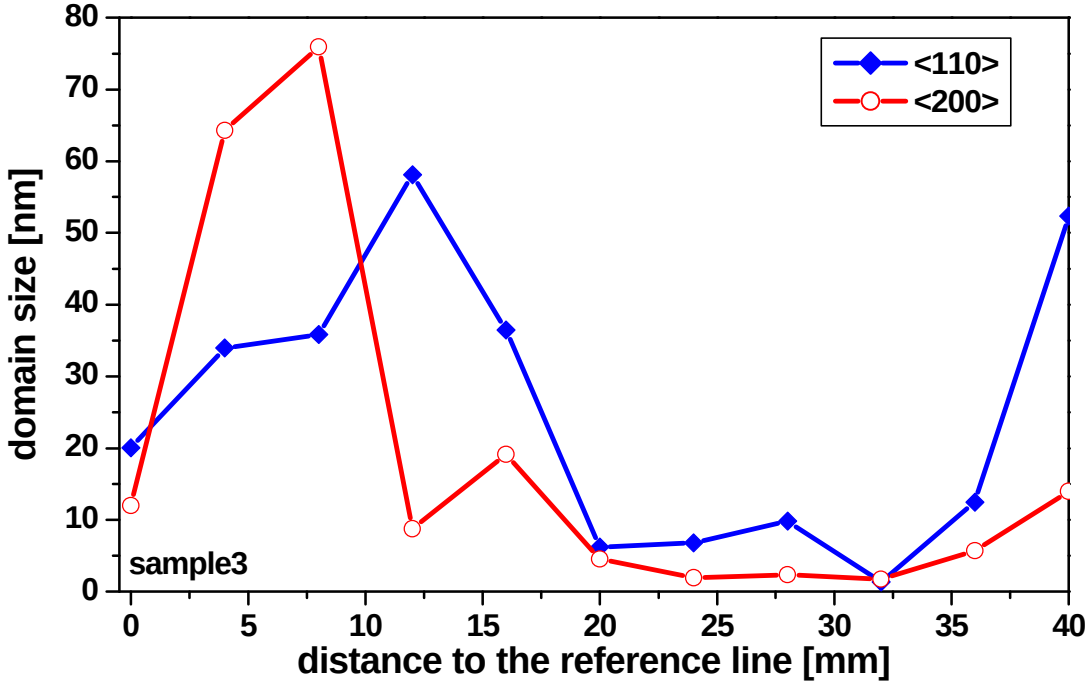

Fig. 5.1.53 Domain size distribution across the surface of rail sample 3

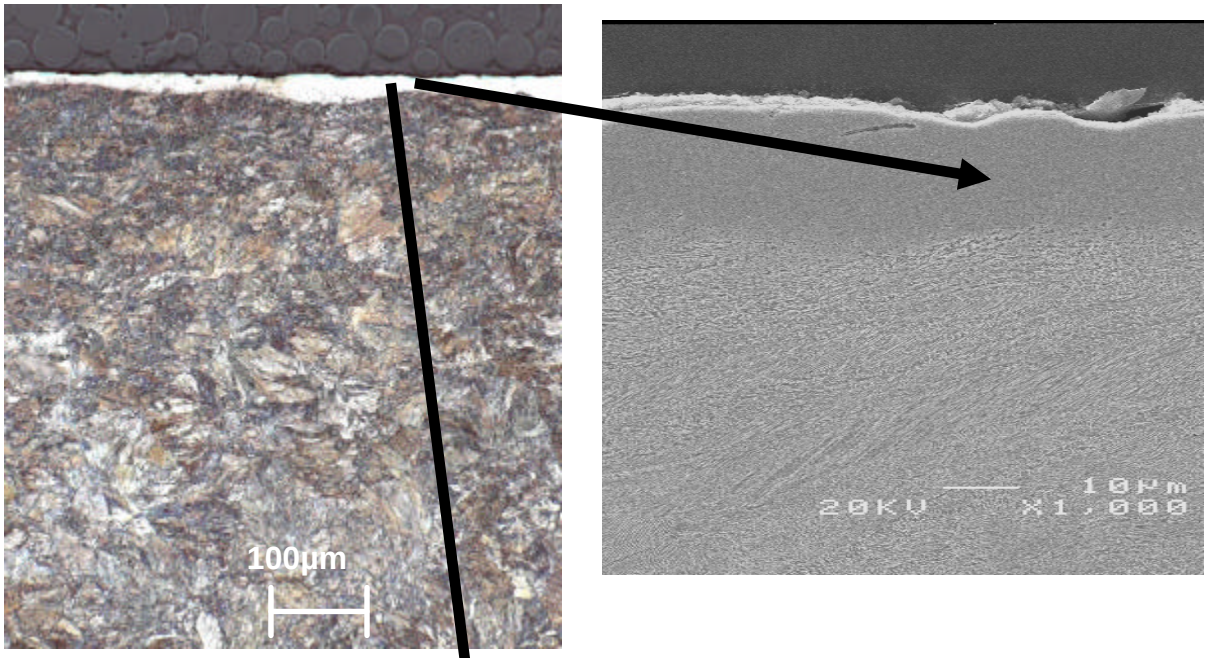

Fig. 5.1.54 Area of WEL of rail sample 3 for the microprobe analyses

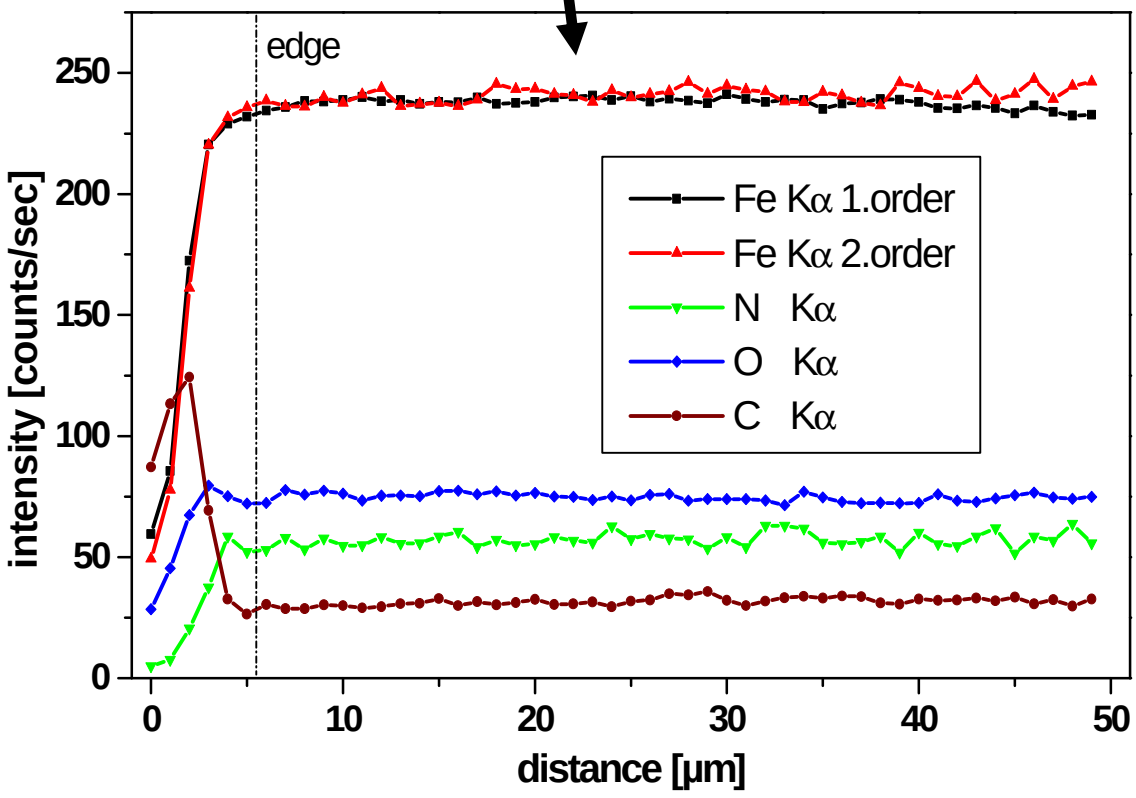

Fig. 5.1.55 Microprobe analyses in the area of WEL in rail sample 3

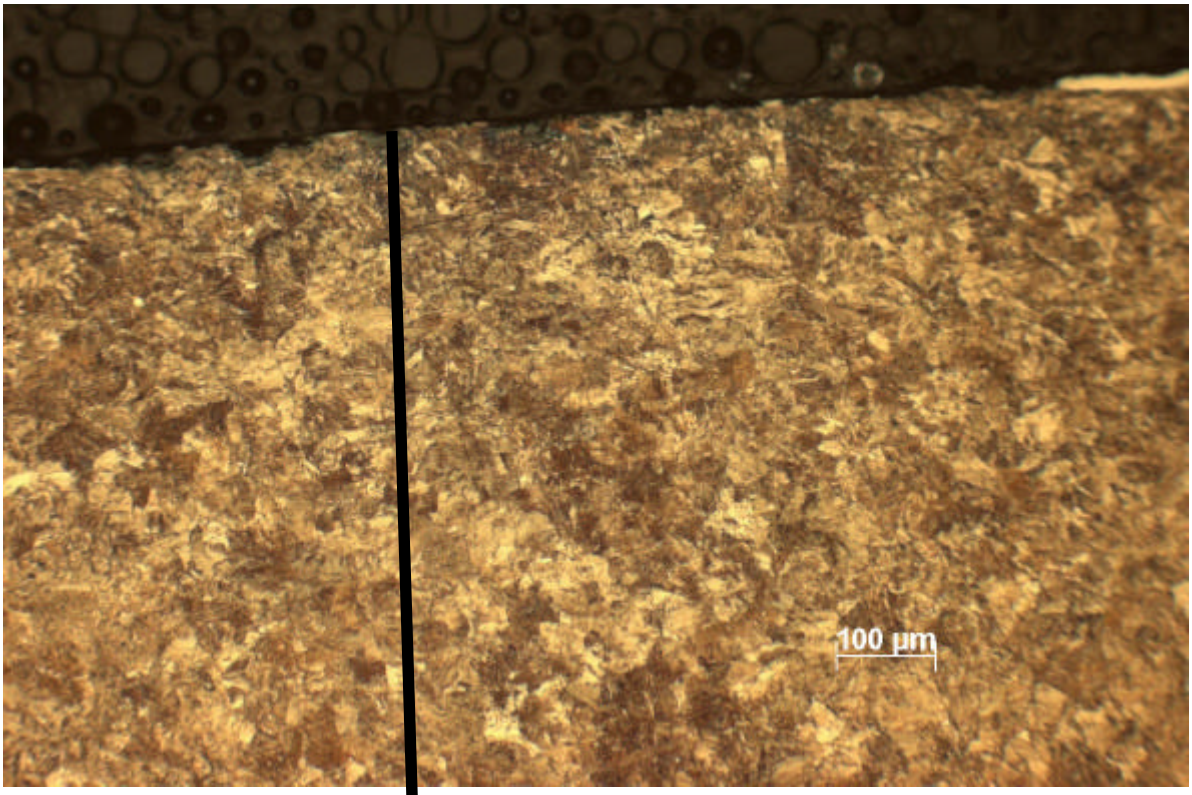

Fig. 5.1.56 Area of non-WEL for the microprobe analyse in rail sample 3

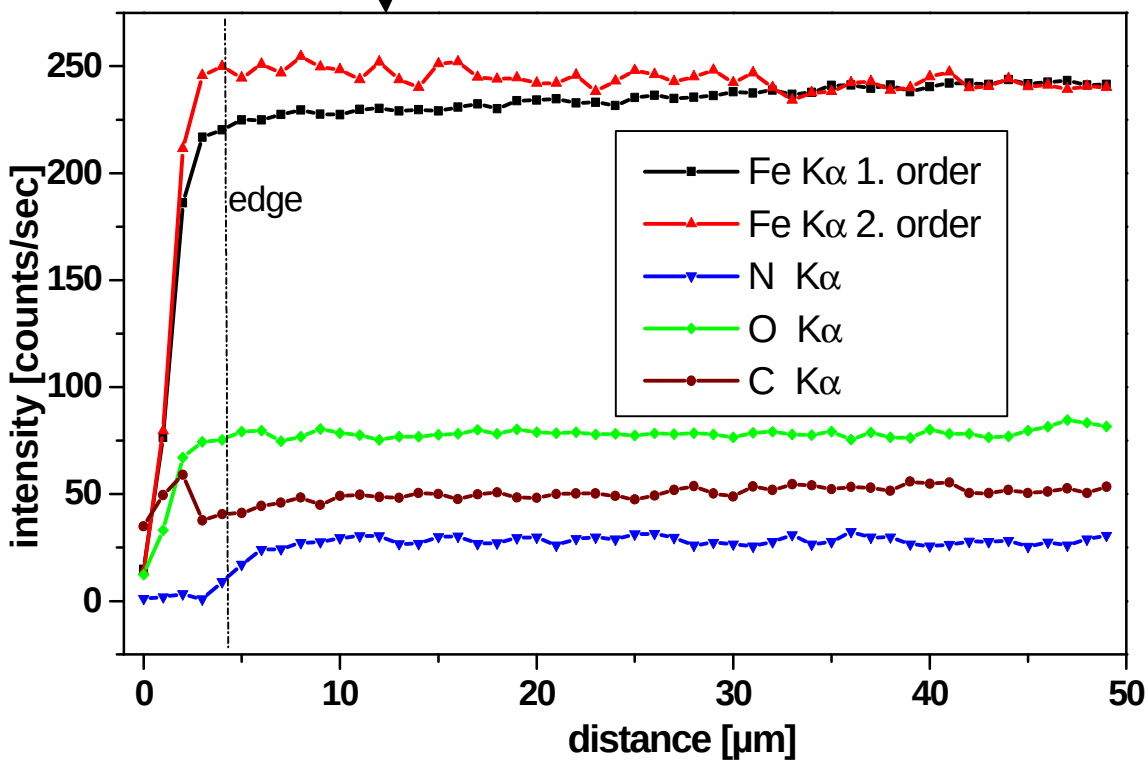

Fig. 5.1.57 Microprobe analyses in the area of non - WEL in rail sample 3

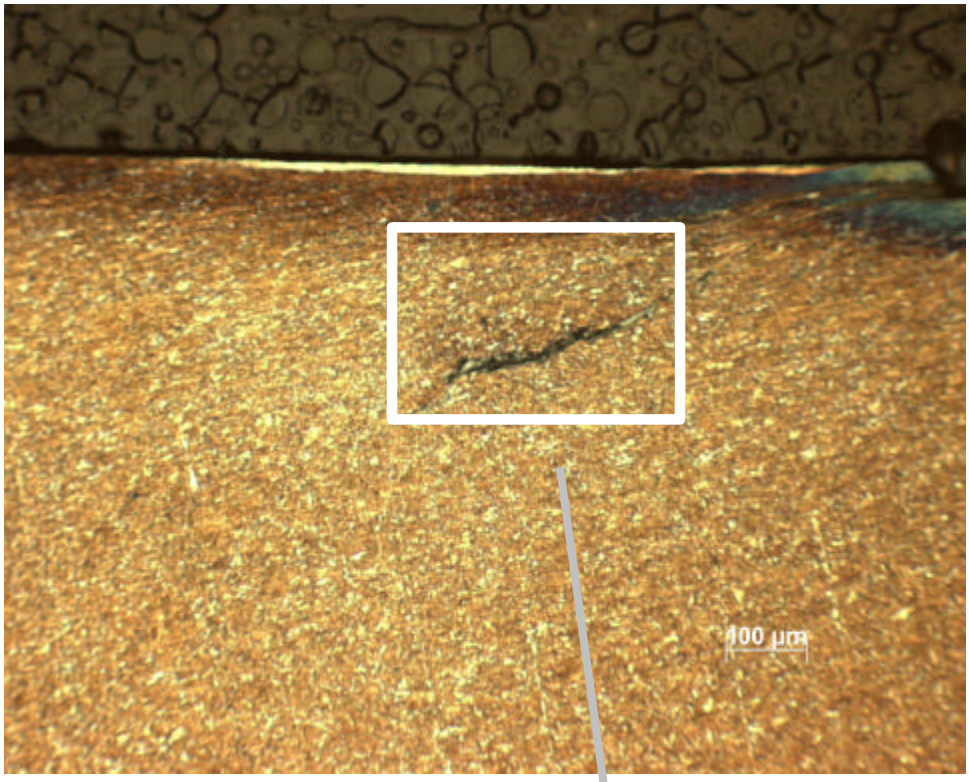

Fig. 5.1.58 Micrograph of wheel sample in cross section

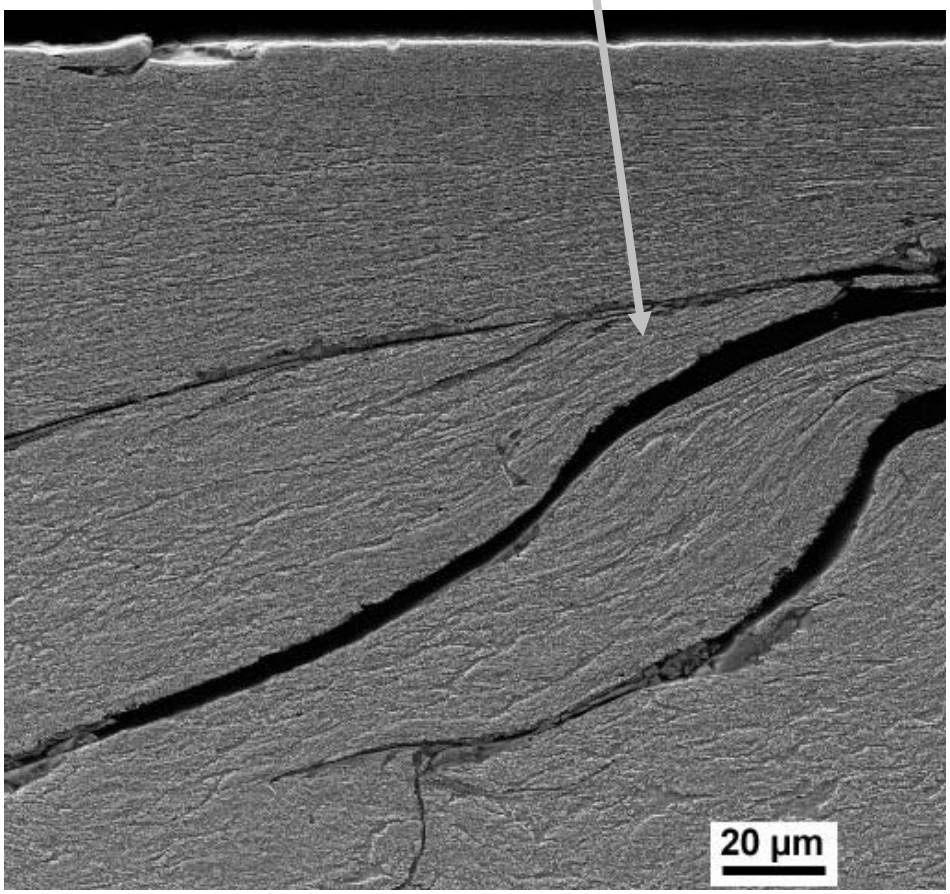

Fig. 5.1.59 Overview picture of WEL in wheel sample under SEM

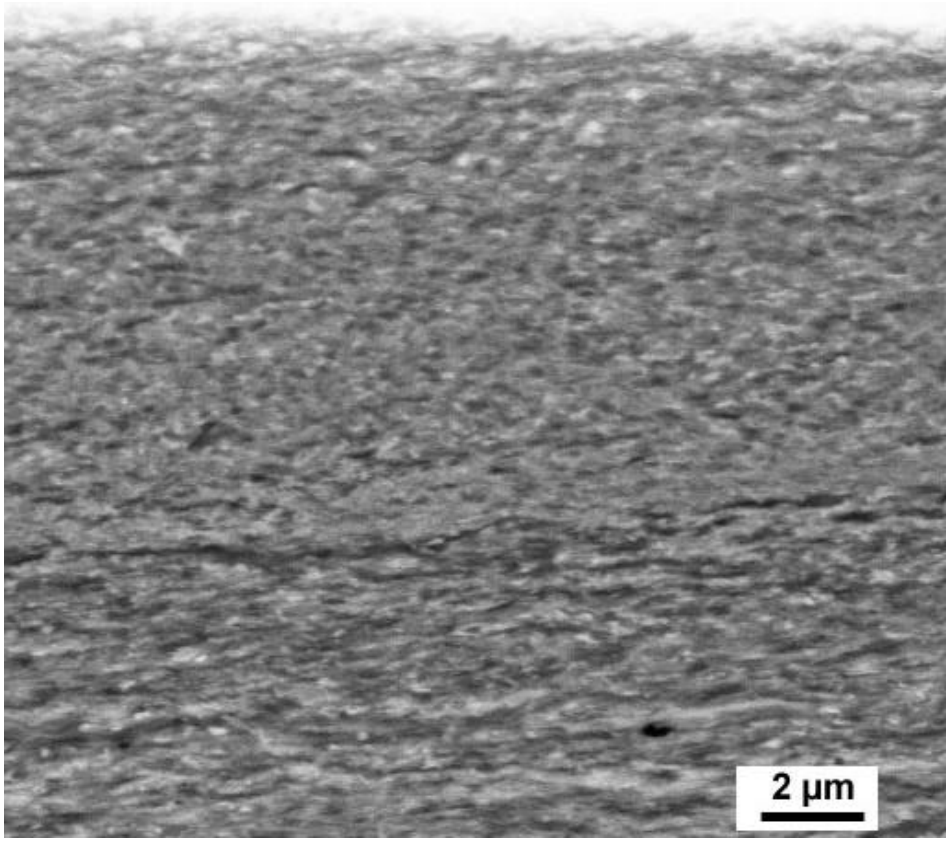

Fig. 5.1.60 Picture of WEL in wheel sample under SEM in cross section

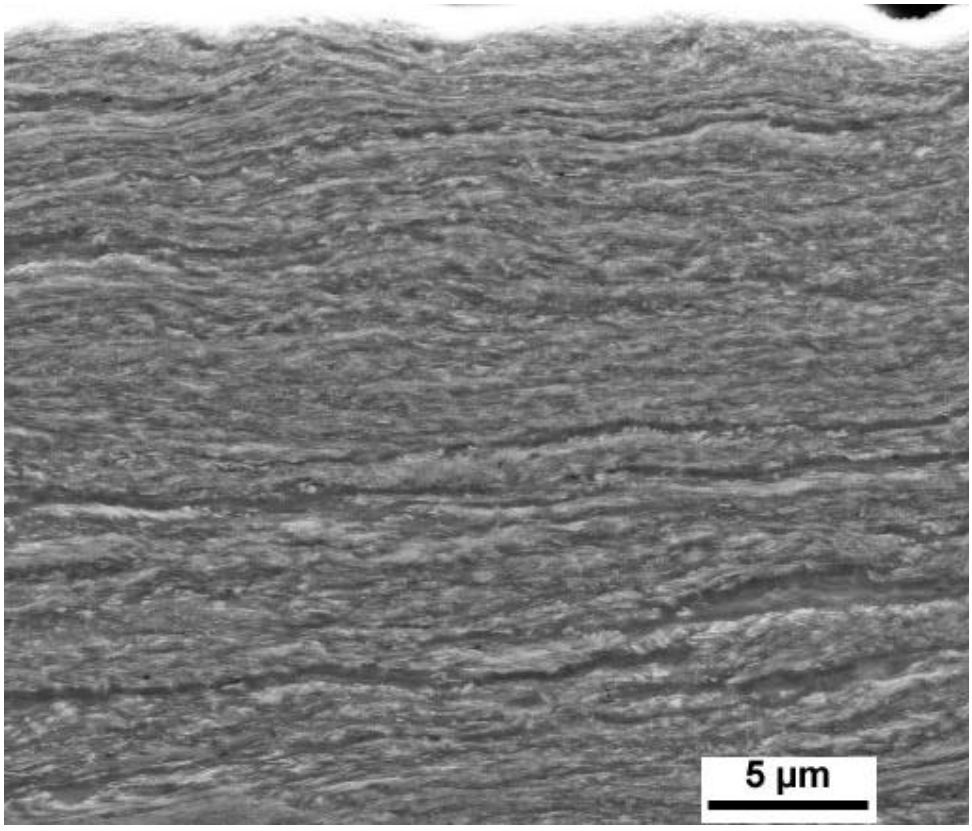

Fig. 5.1.61 Deformed area of non-WEL in wheel sample under SEM

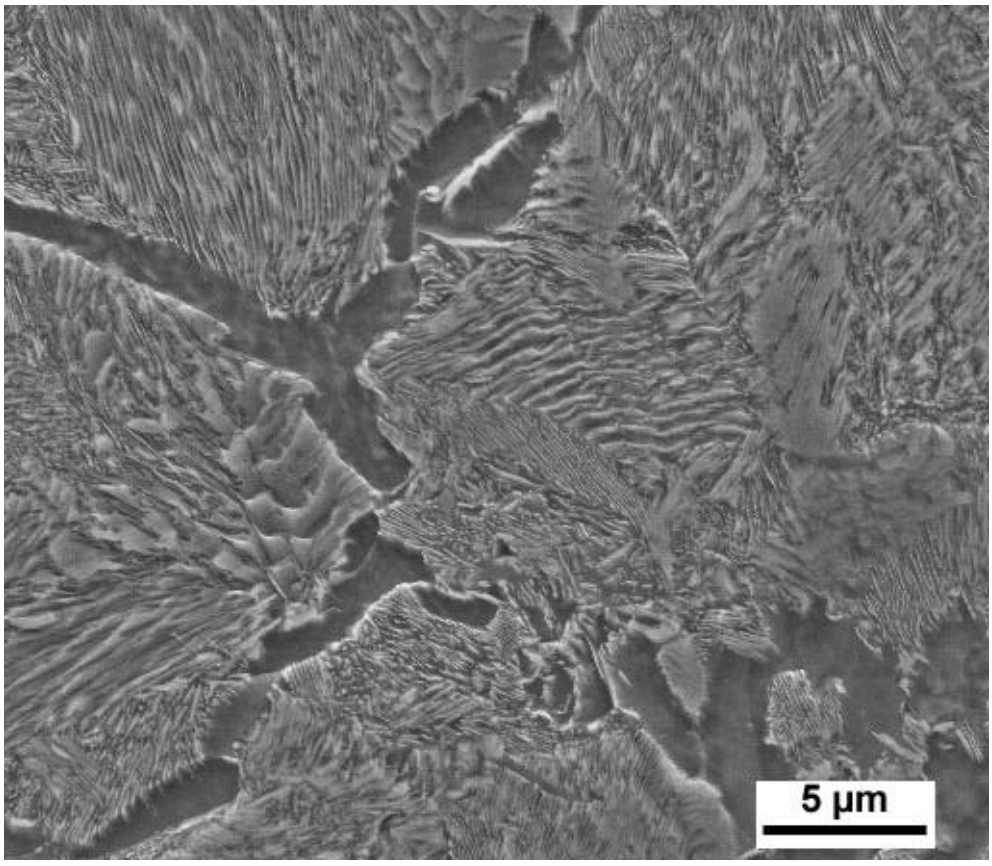

Fig. 5.1.62 Pearlite structure of bulk material in wheel sample under SEM

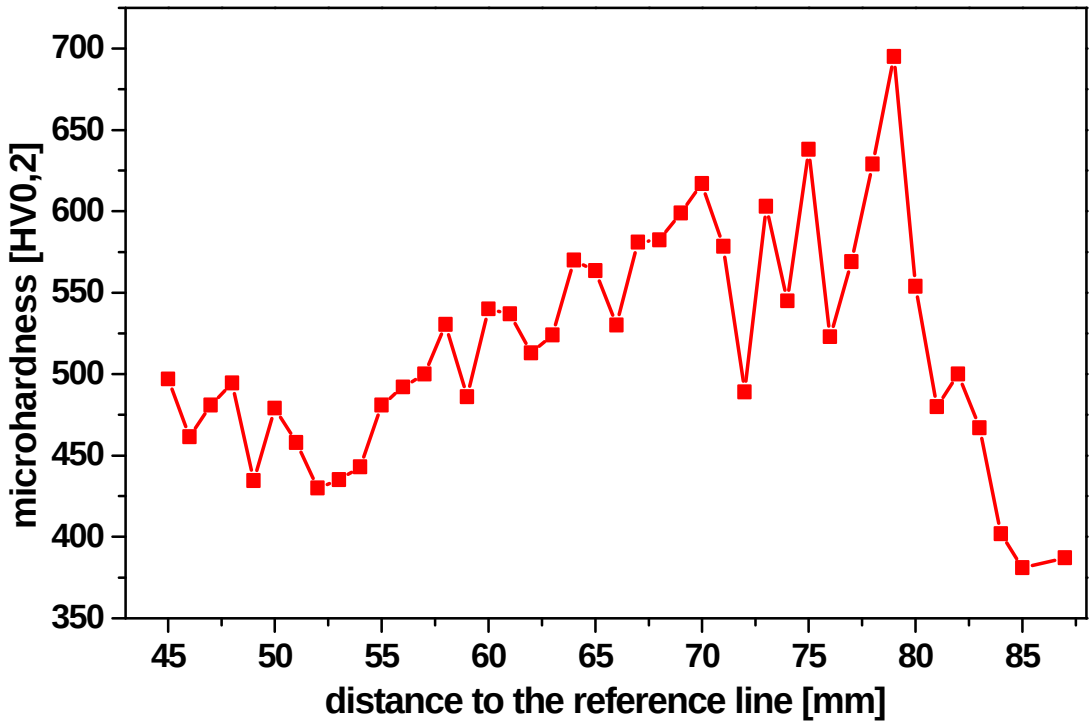

Fig. 5.1.63 Microhardness distribution on the surface of wheel sample

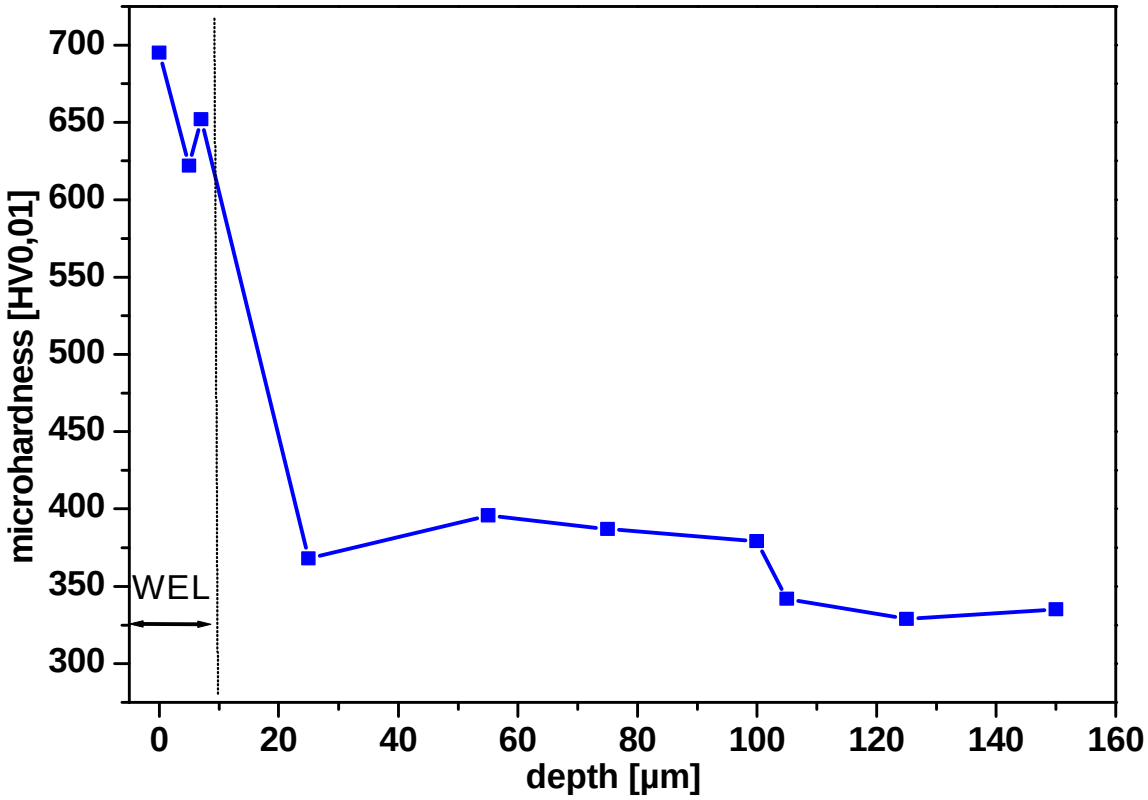

Fig. 5.1.64 Microhardness distribution in the subsurface region of wheel sample

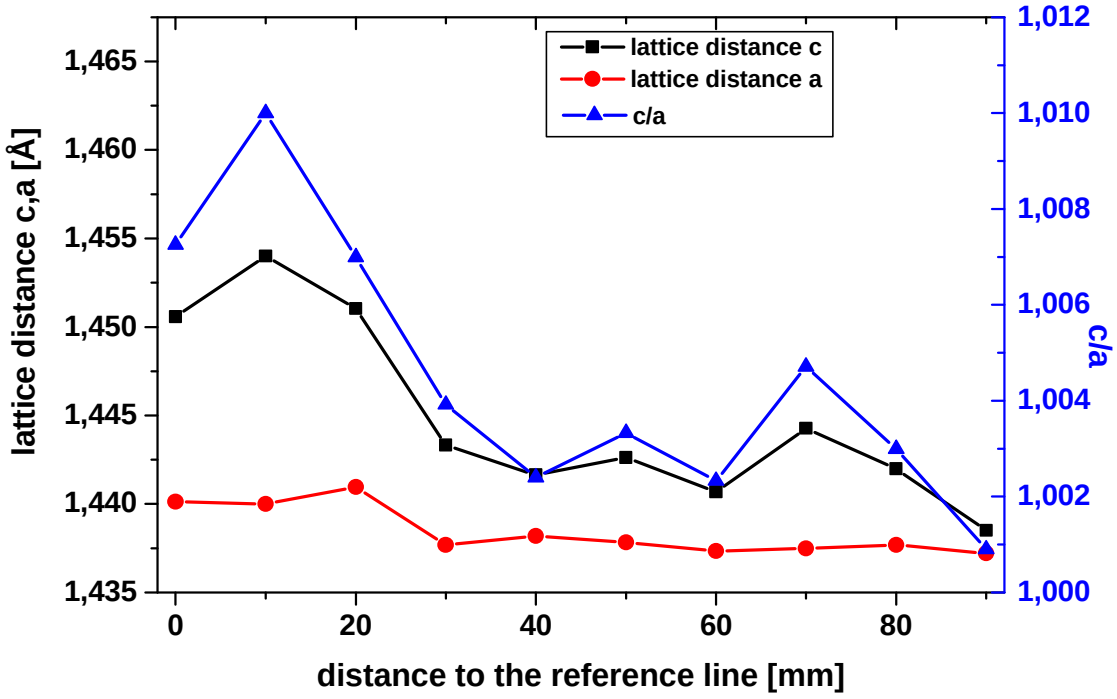

Fig. 5.1.65 Lattice distance c_m and a_m and c, a ratio distribution along the surface of Wheel sample

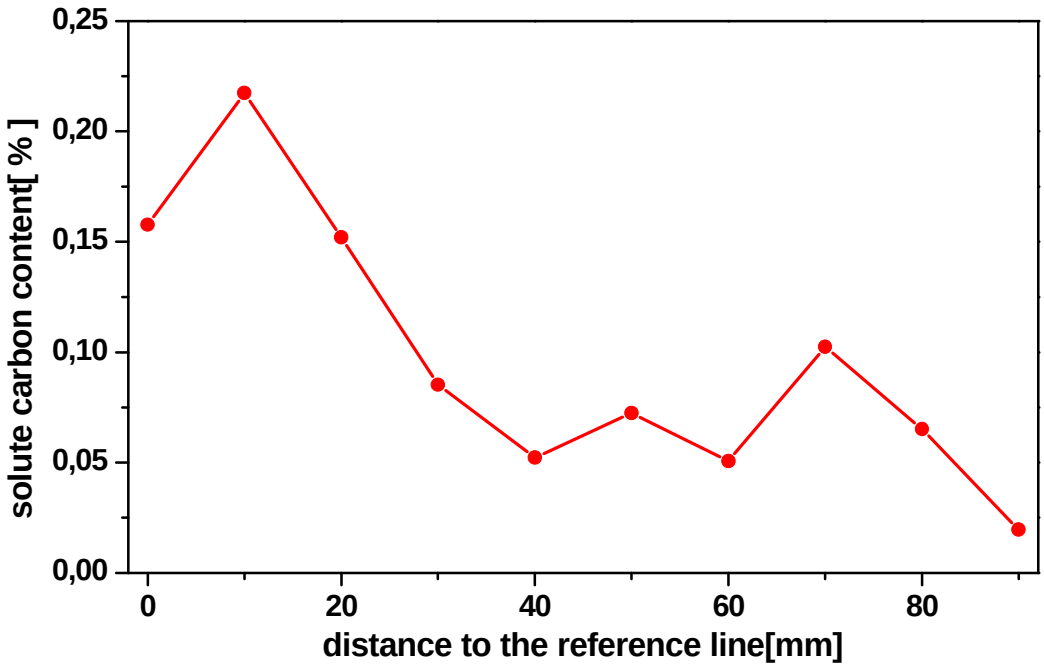

Fig. 5.1.66 Solute carbon content distribution along the surface of wheel sample

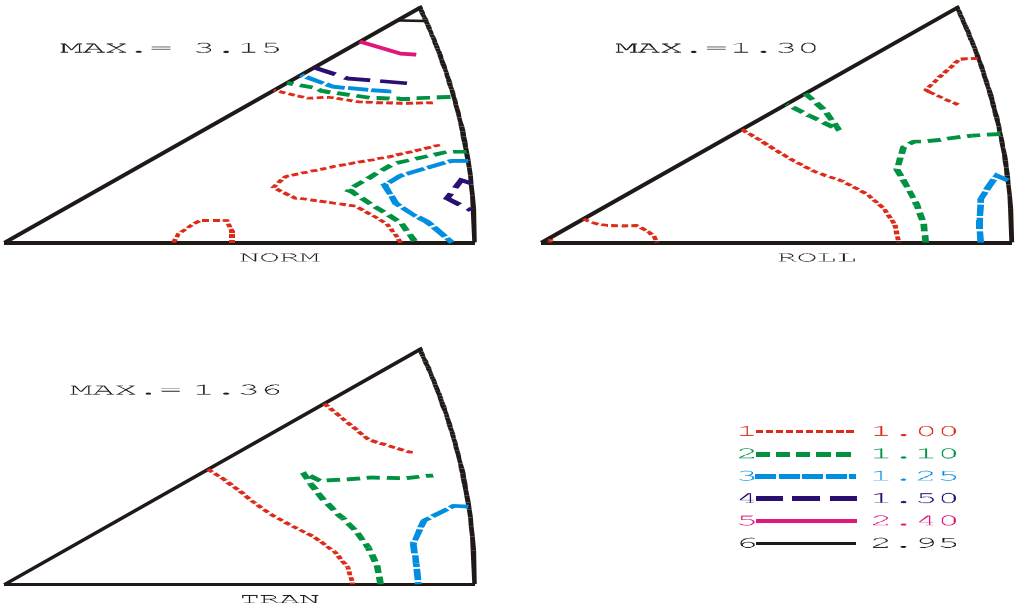

Fig. 5.2.1 Inverse pole figure in the center of the rolling surface on rail DB AG

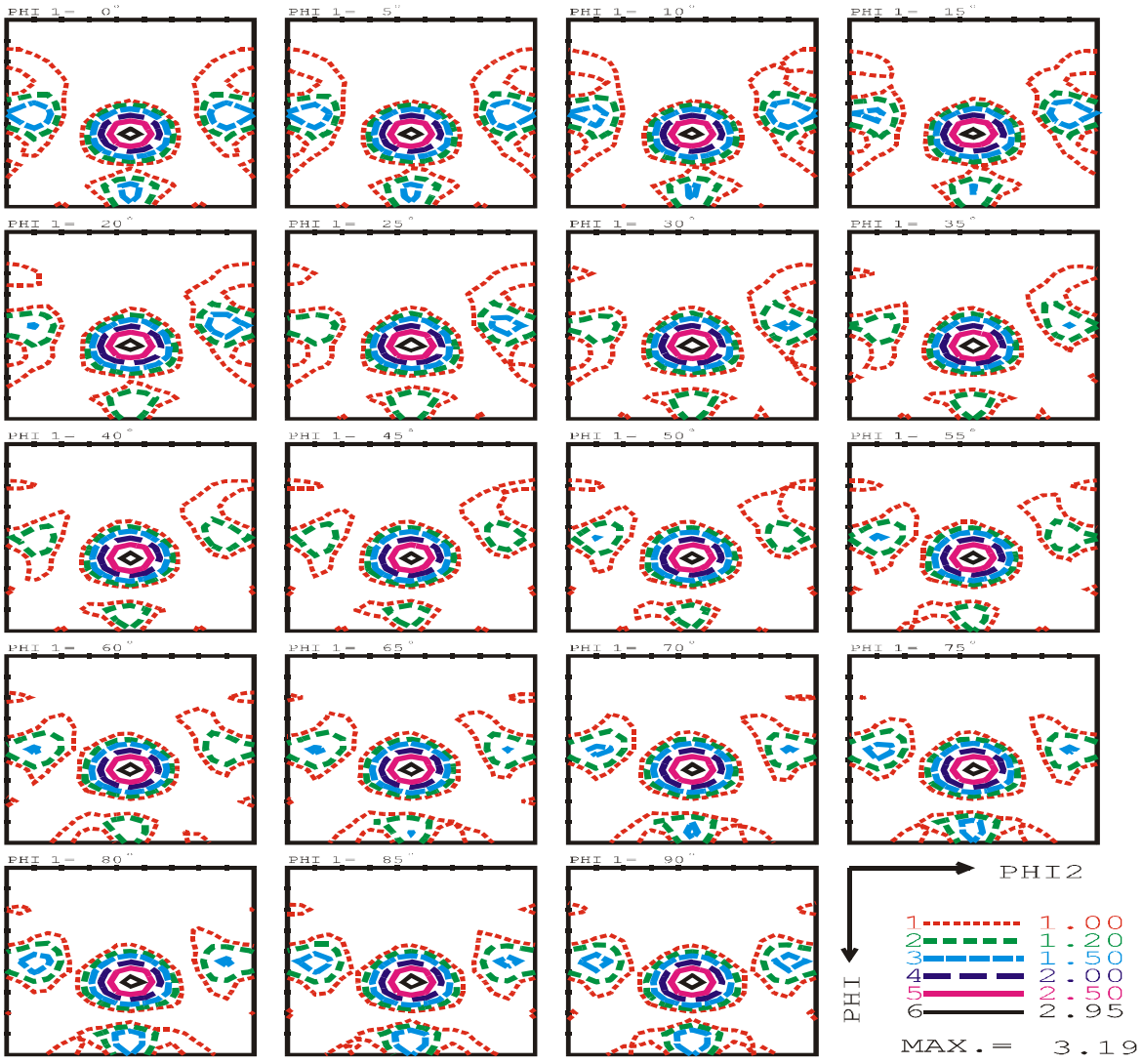

Fig. 5.2.2 ODF in the center of the rolling surface on rail DB AG

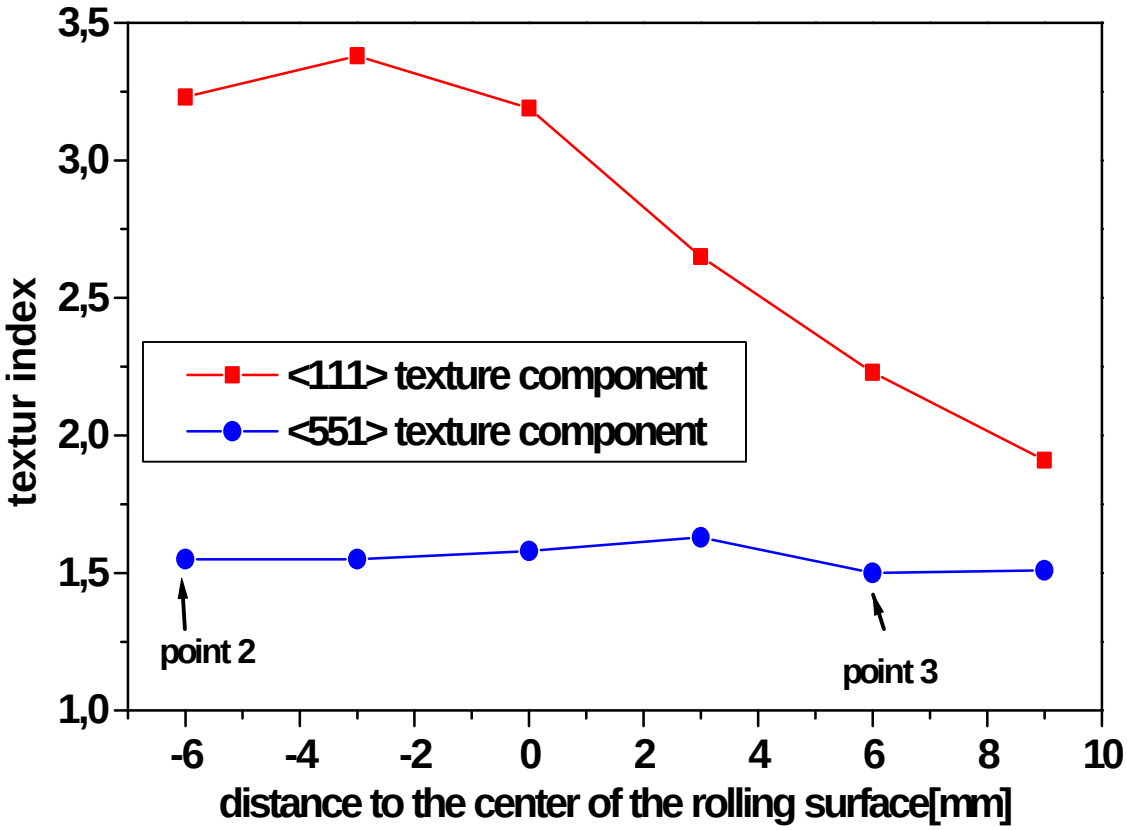

Fig. 5.2.3 Texture distribution from point 2 to point 3 on rail DB AG

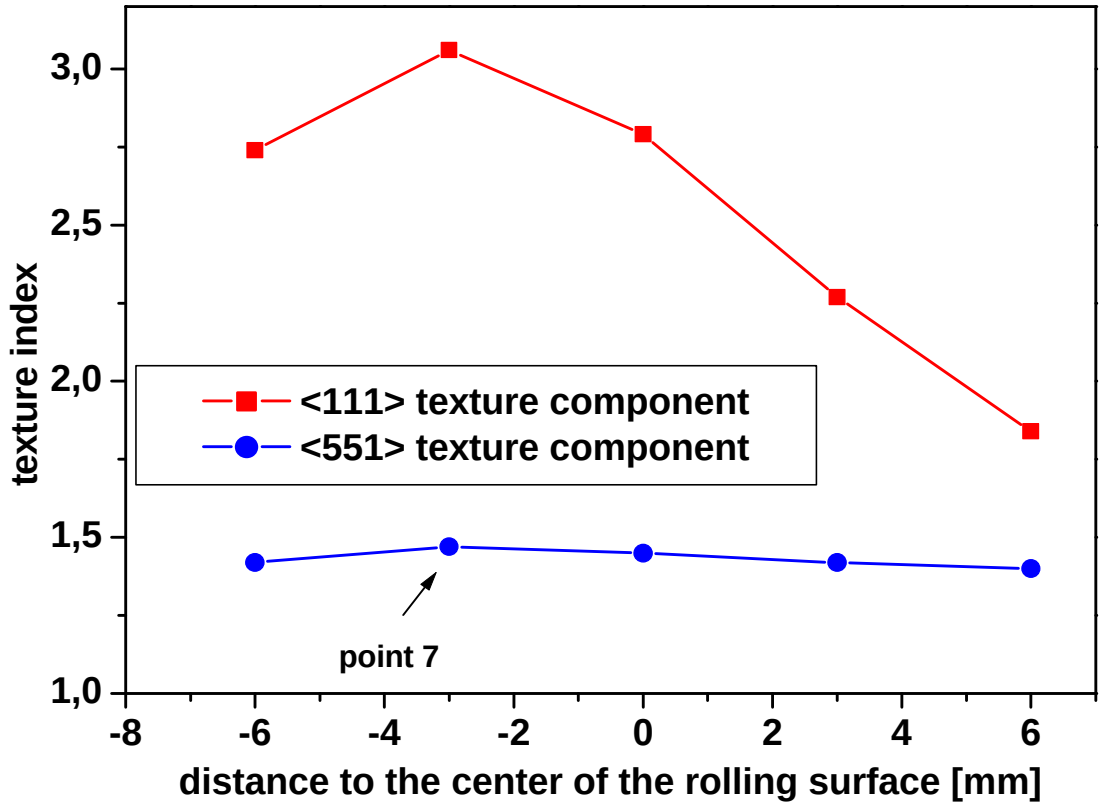

Fig. 5.2.4 Texture distribution in vicinity of point 7 on rail DB AG

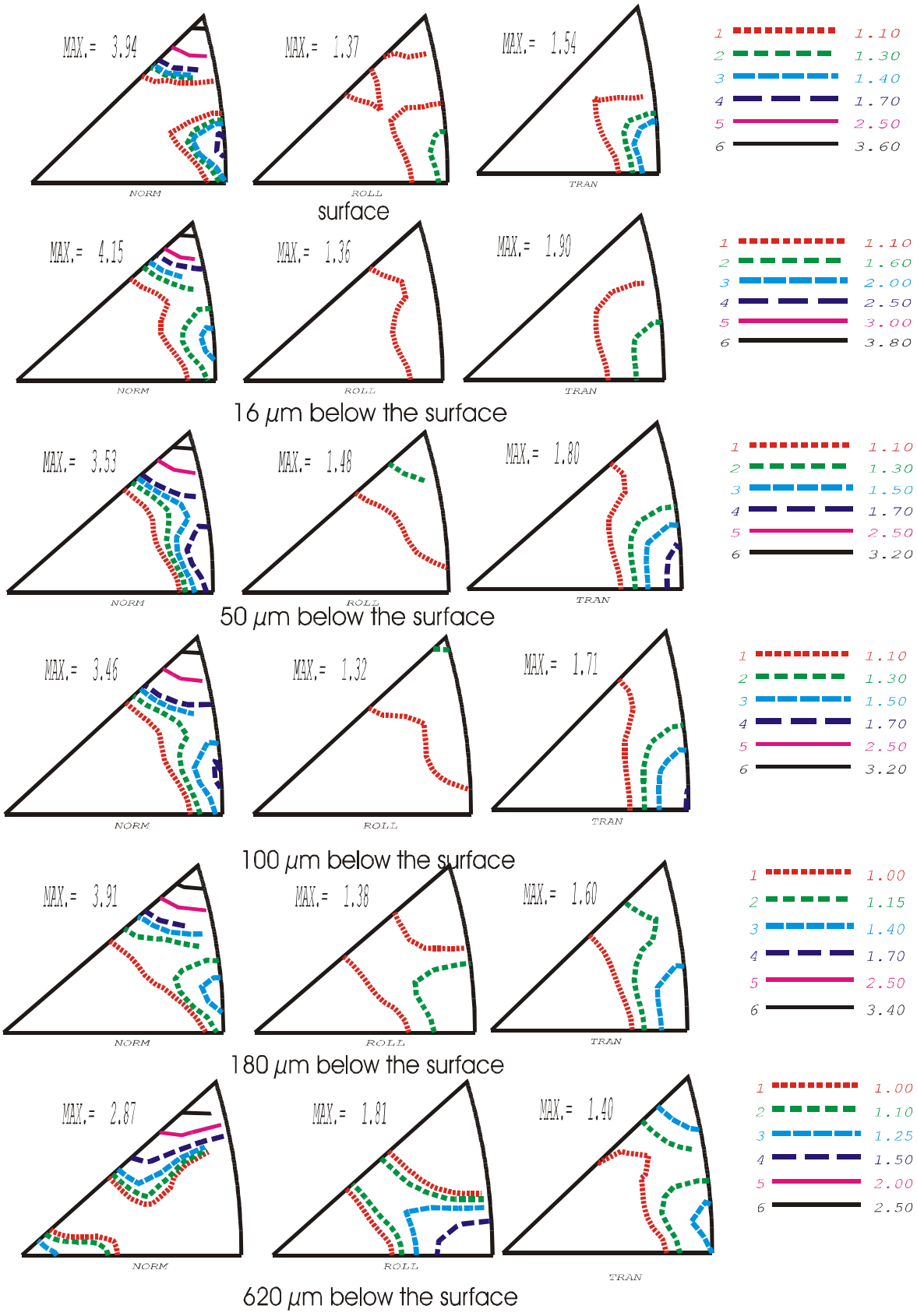

Fig. 5.2.5 Inverse pole figure in the subsurface region of rail DB AG

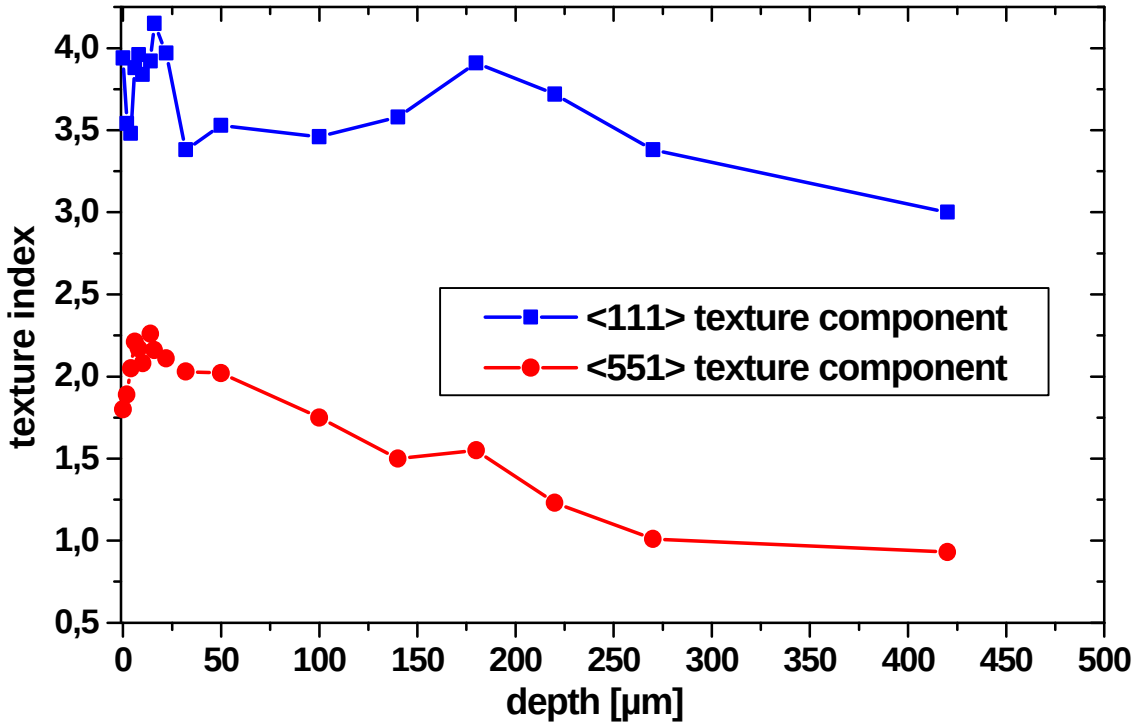

Fig. 5.2.6 Texture distribution in the subsurface region of rail DB AG

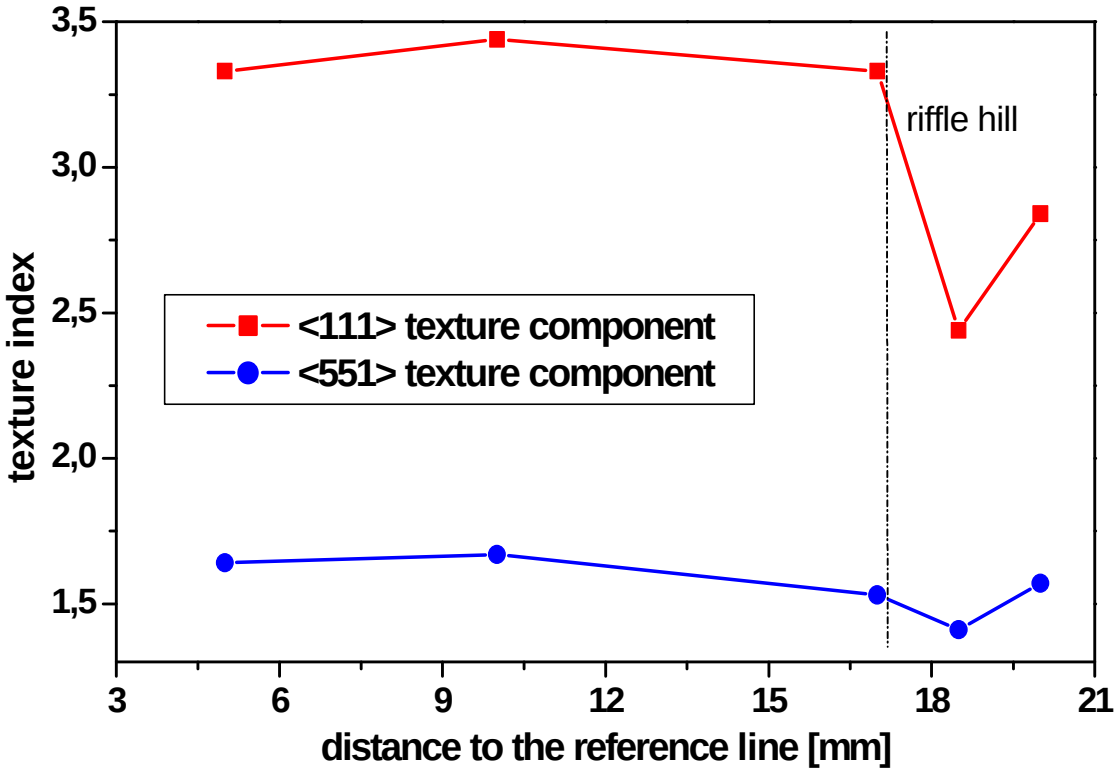

Fig. 5.2.7 Texture distribution on the surface of rail Baumann

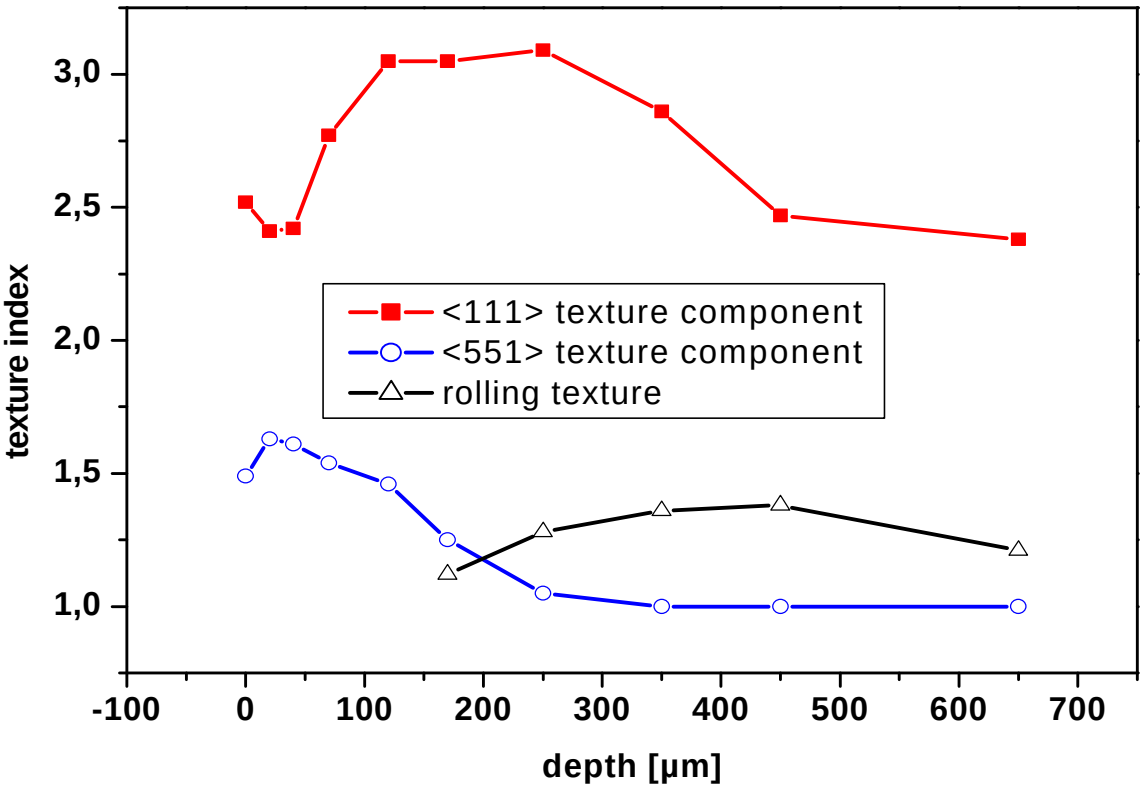

Fig. 5.2.8 Texture distribution below the “riffle hill” of rail Baumann

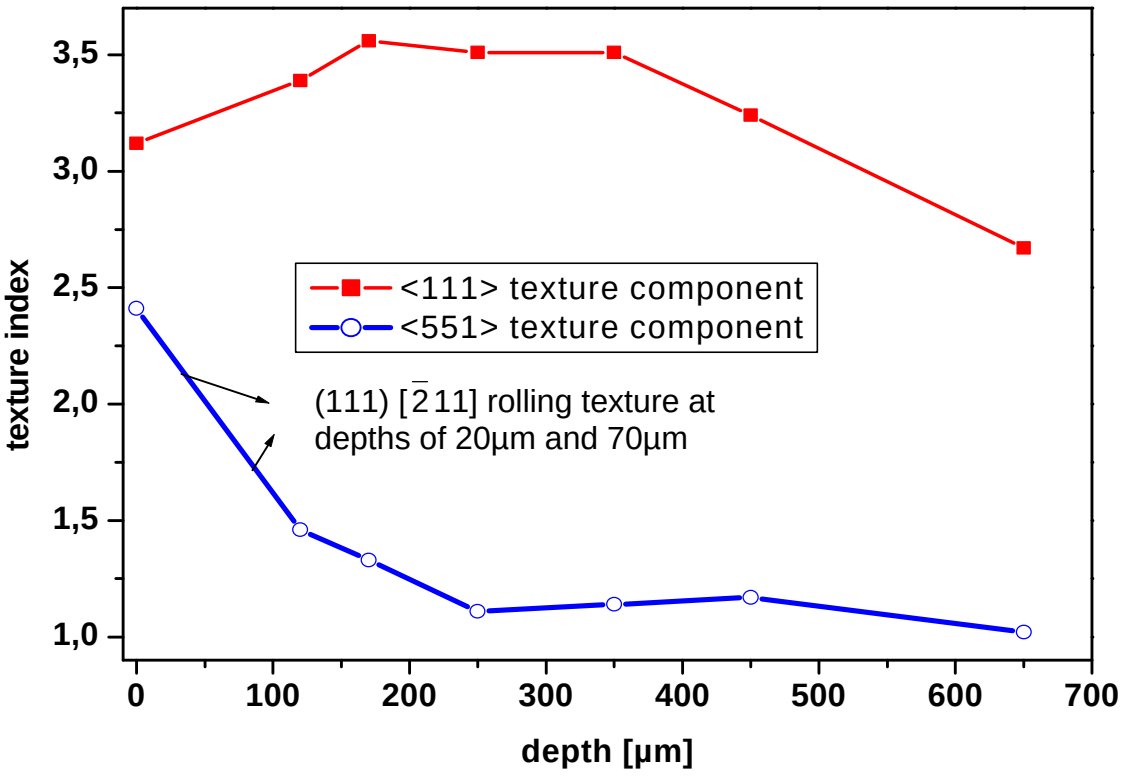

Fig. 5.2.9 Texture distribution below the “riffle valley” of rail Baumann

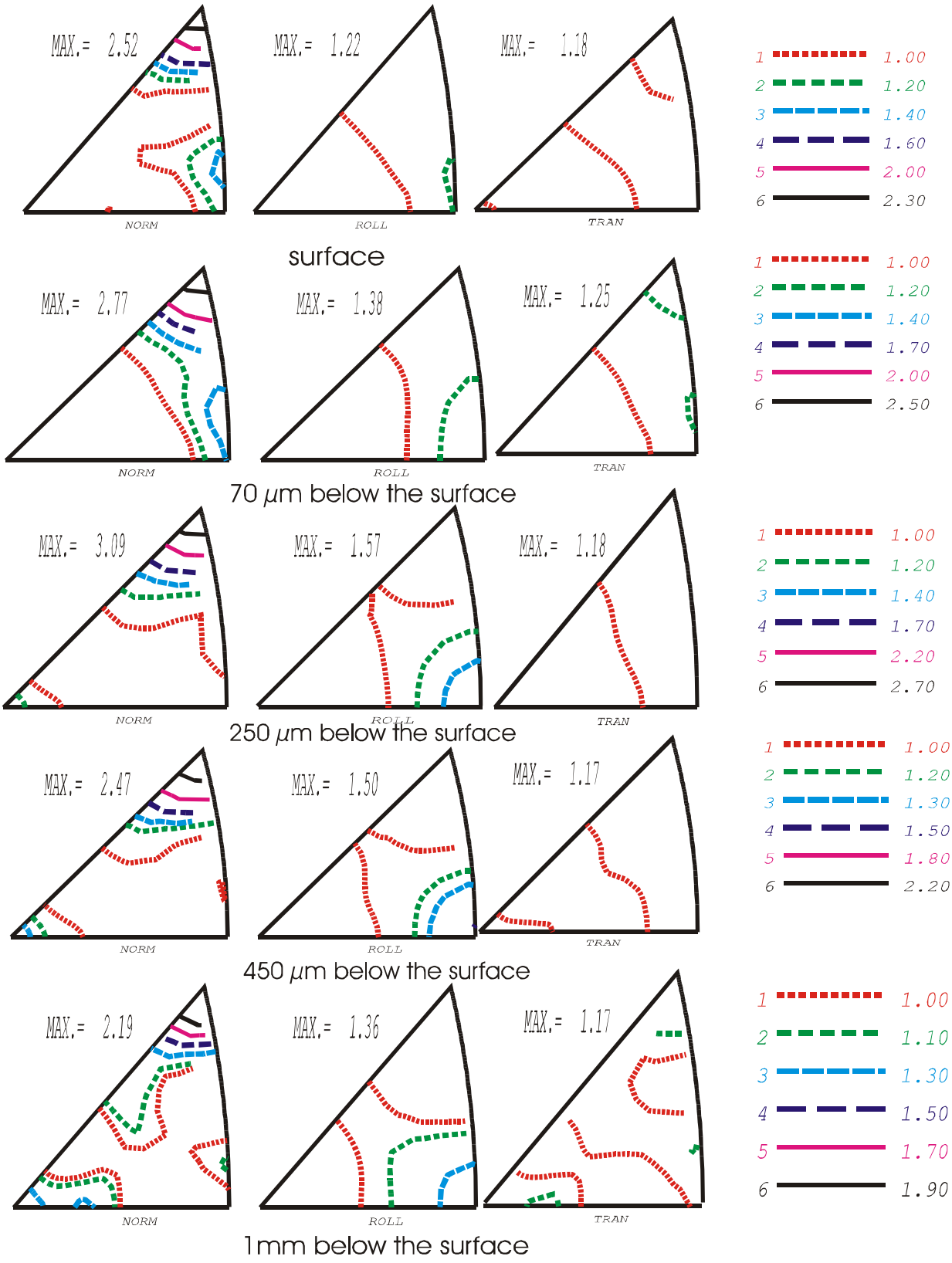

Fig. 5.2.10 Inverse pole figure below the “riffle hill” of rail Baumann

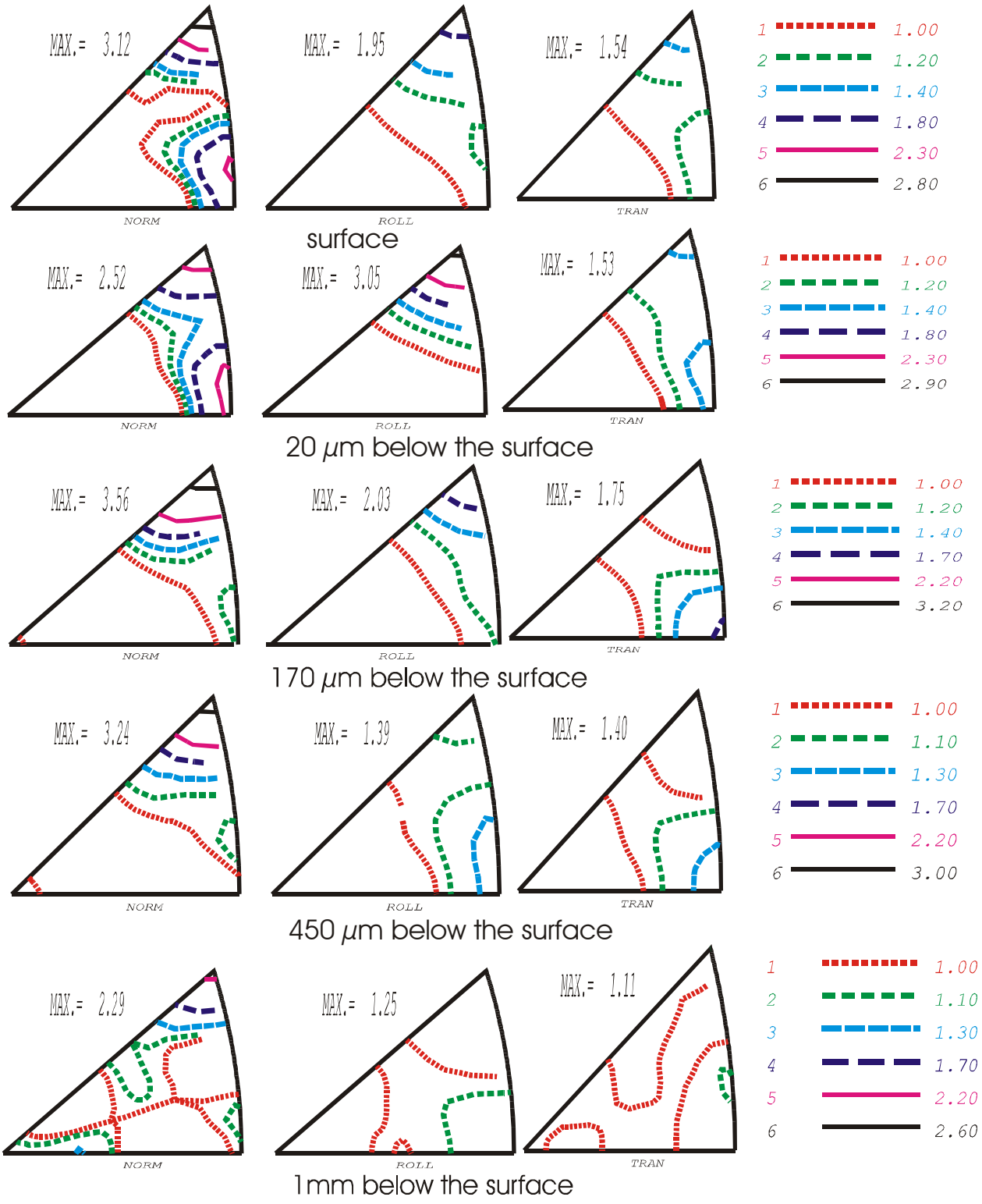

Fig. 5.2.11 Inverse pole figure below the “riffle valley” of rail Baumann

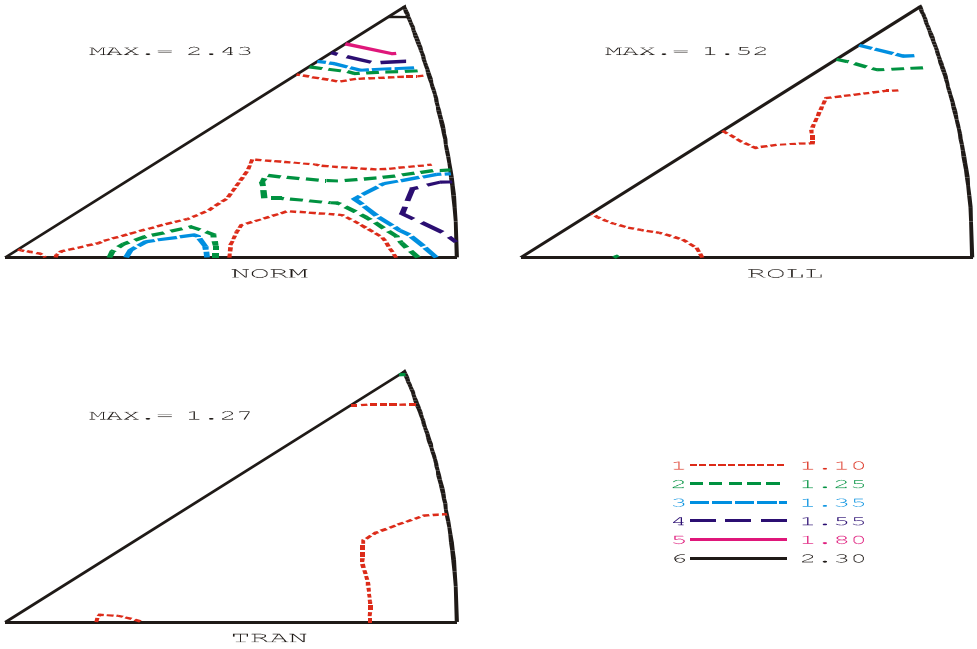

Fig. 5.2.12 Inverse pole figure of martensite/ferrite on rail sample 3

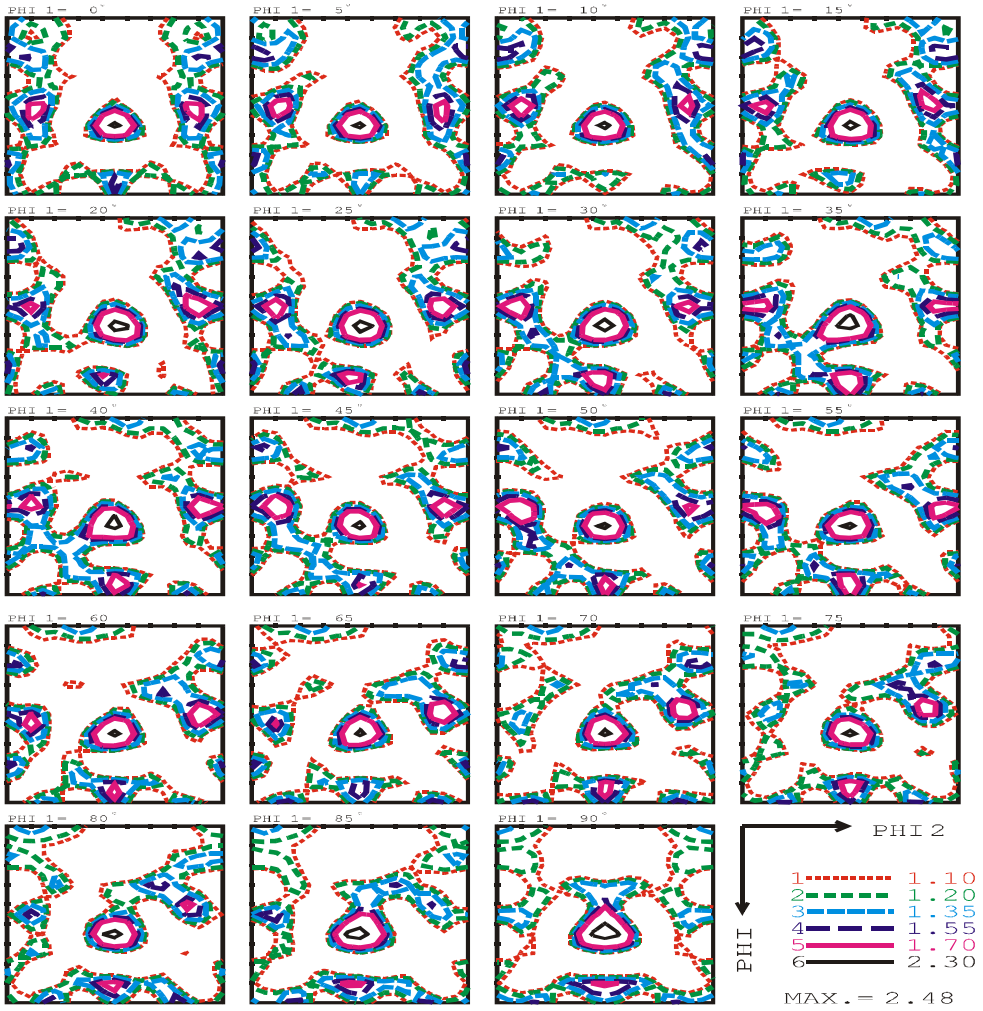

Fig. 5.2.13 ODF of martensite/ferrite on rail sample 3

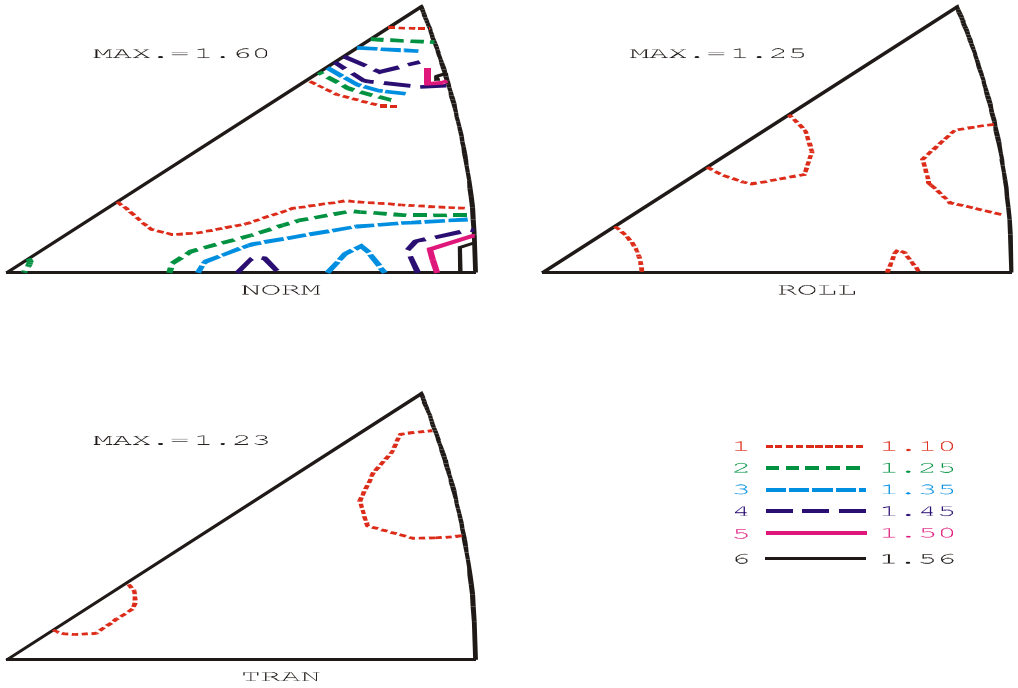

Fig.5.2.14 Inverse pole figure of austenite on rail sample 3

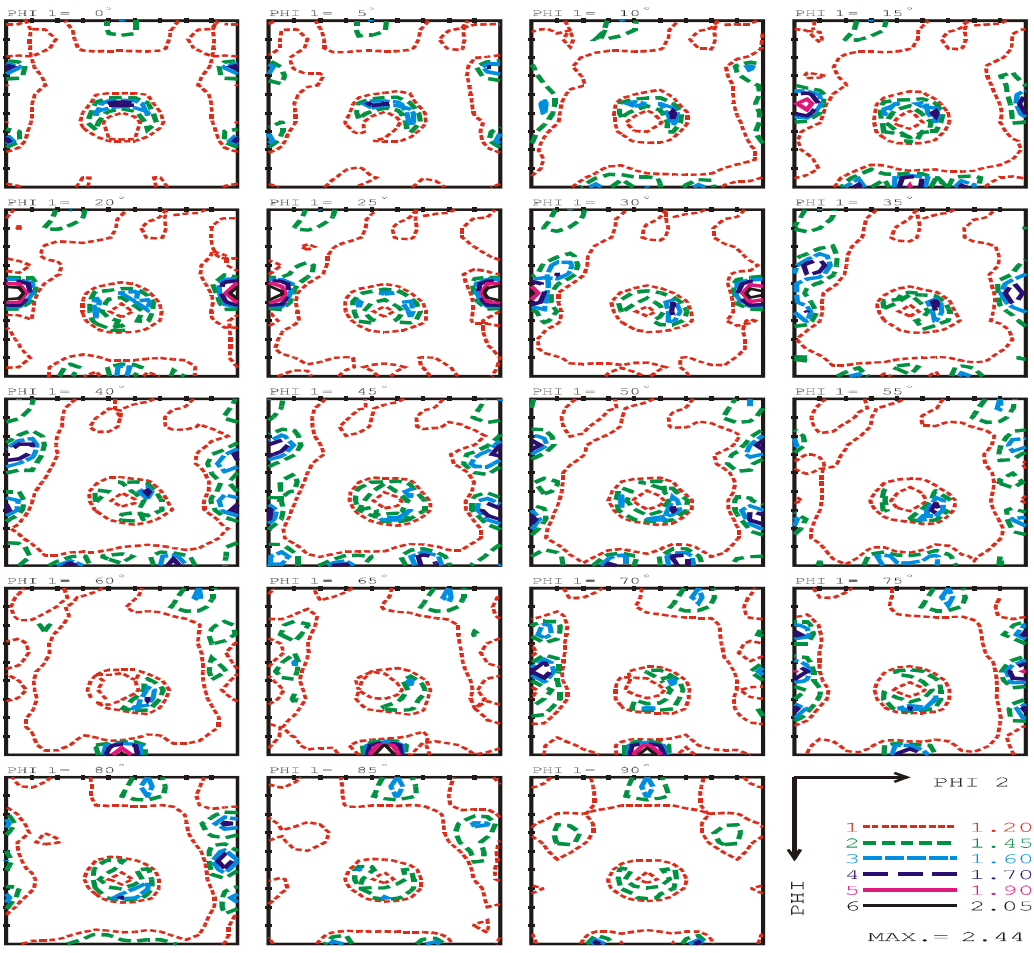

Fig. 5.2.15 ODF of austenite on rail sample 3

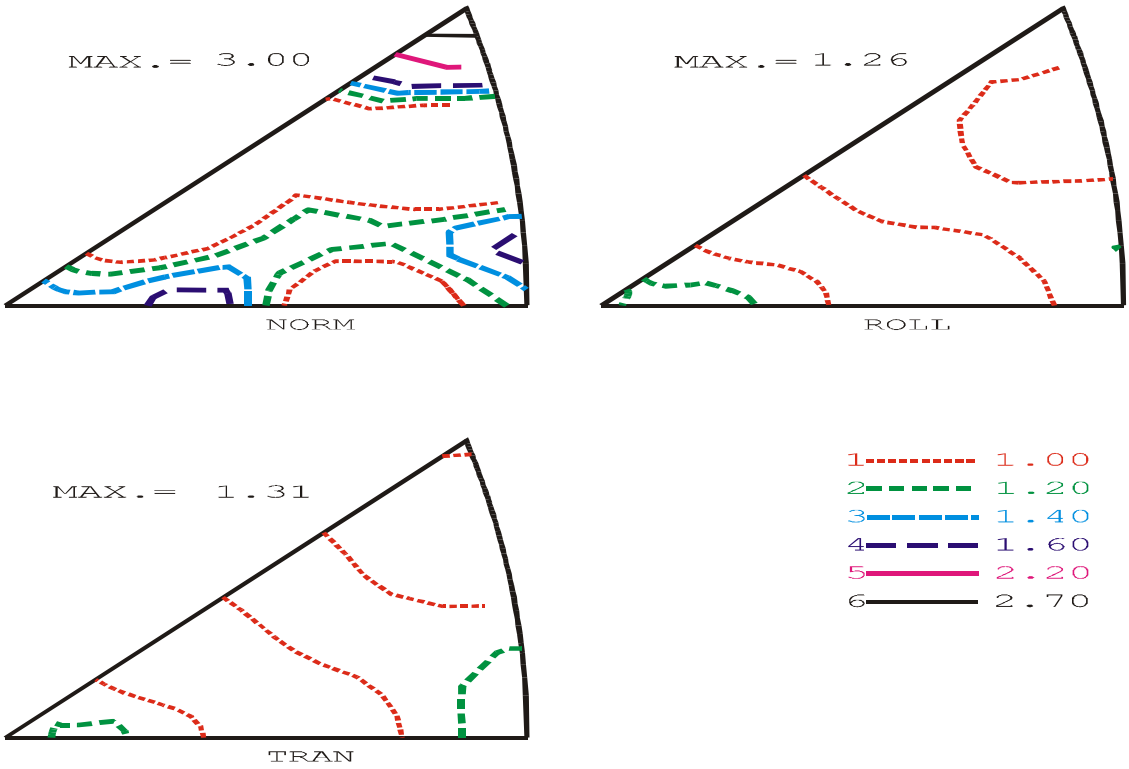

Fig. 5.2.16 Inverse pole figure of wheel sample

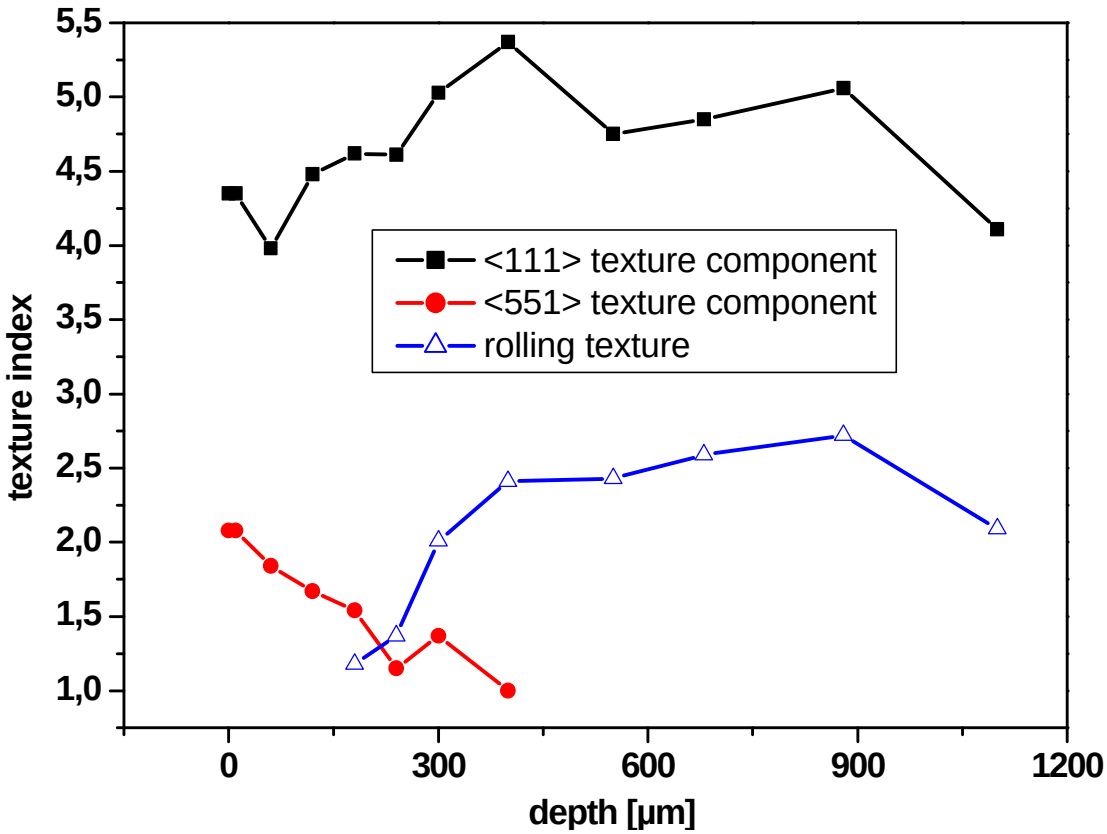

Fig.5.2.17 Texture distribution below the surface of wheel sample

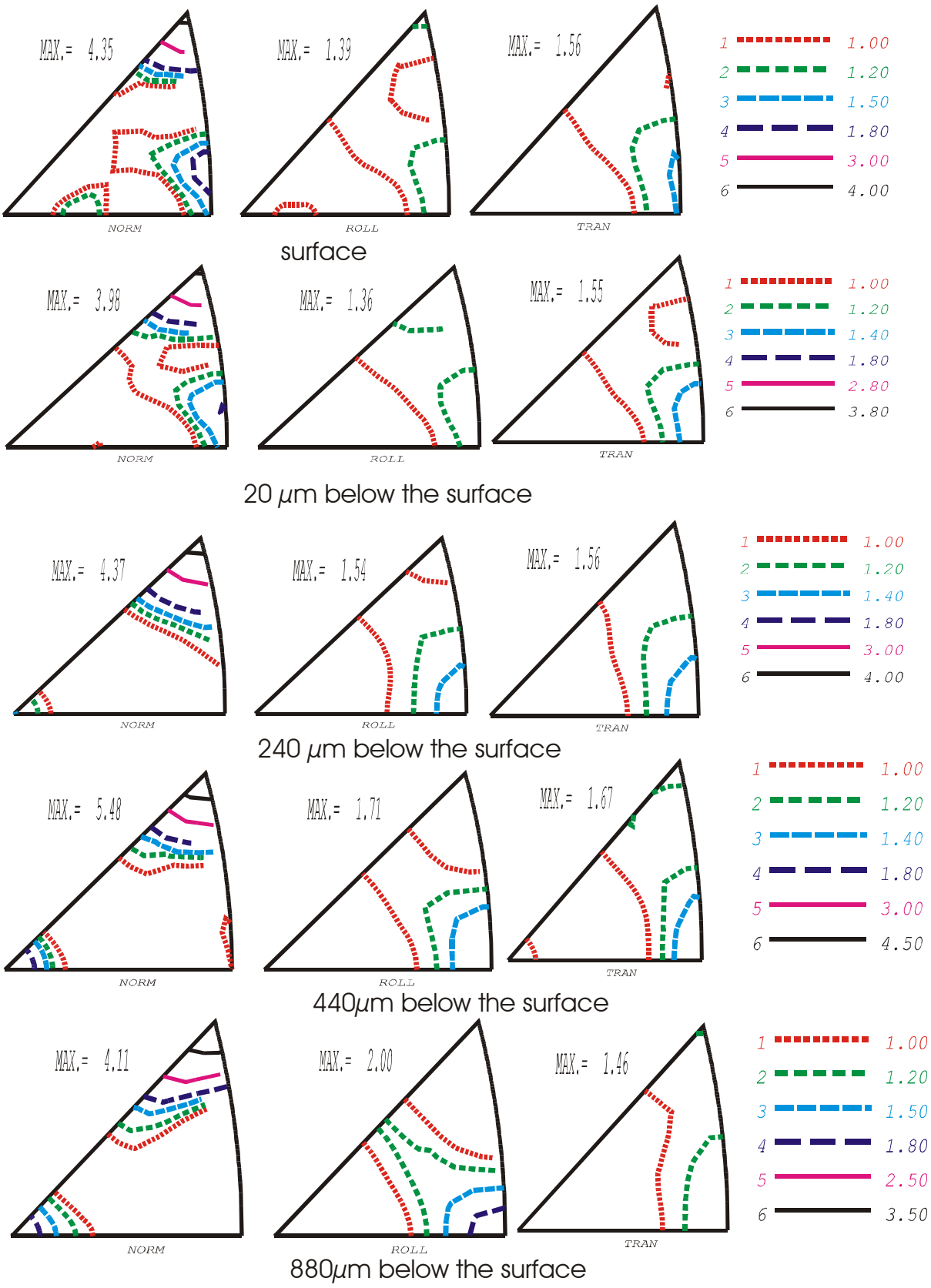

Fig. 5.2.18 Inverse pole figure in the subsurface region of wheel sample

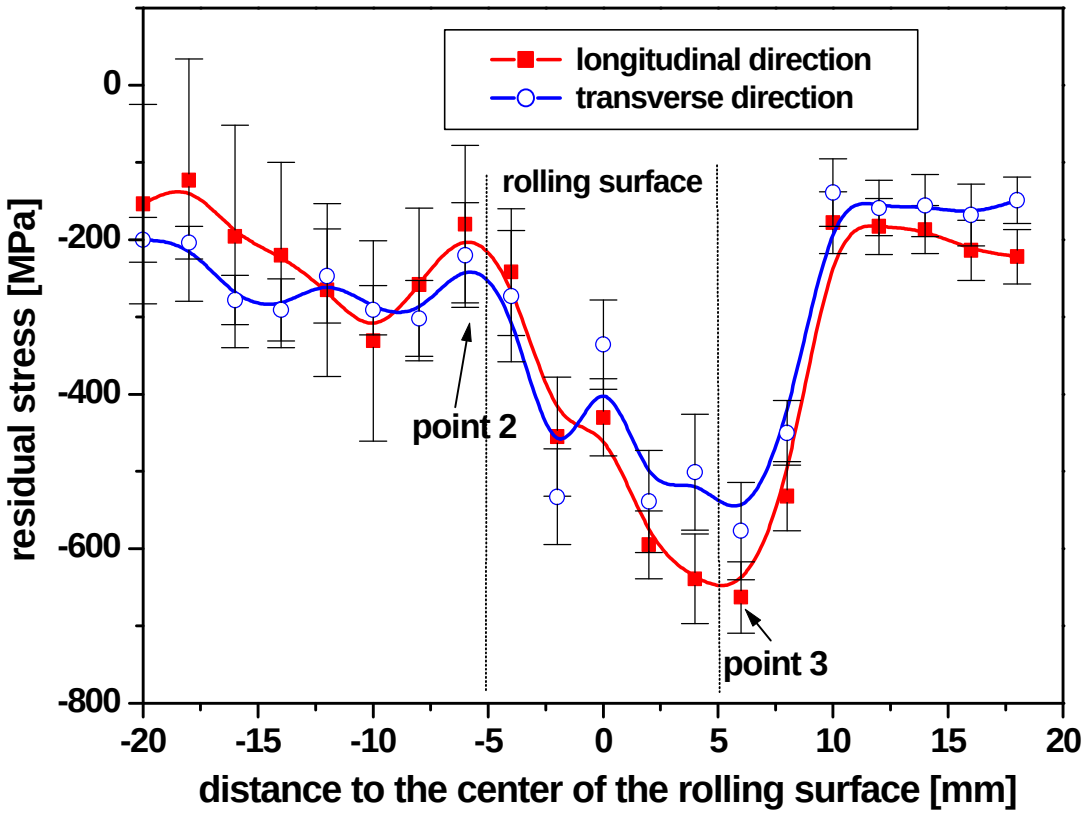

Fig. 5.3.1 Residual stresses distribution along line 1 on rail DB AG

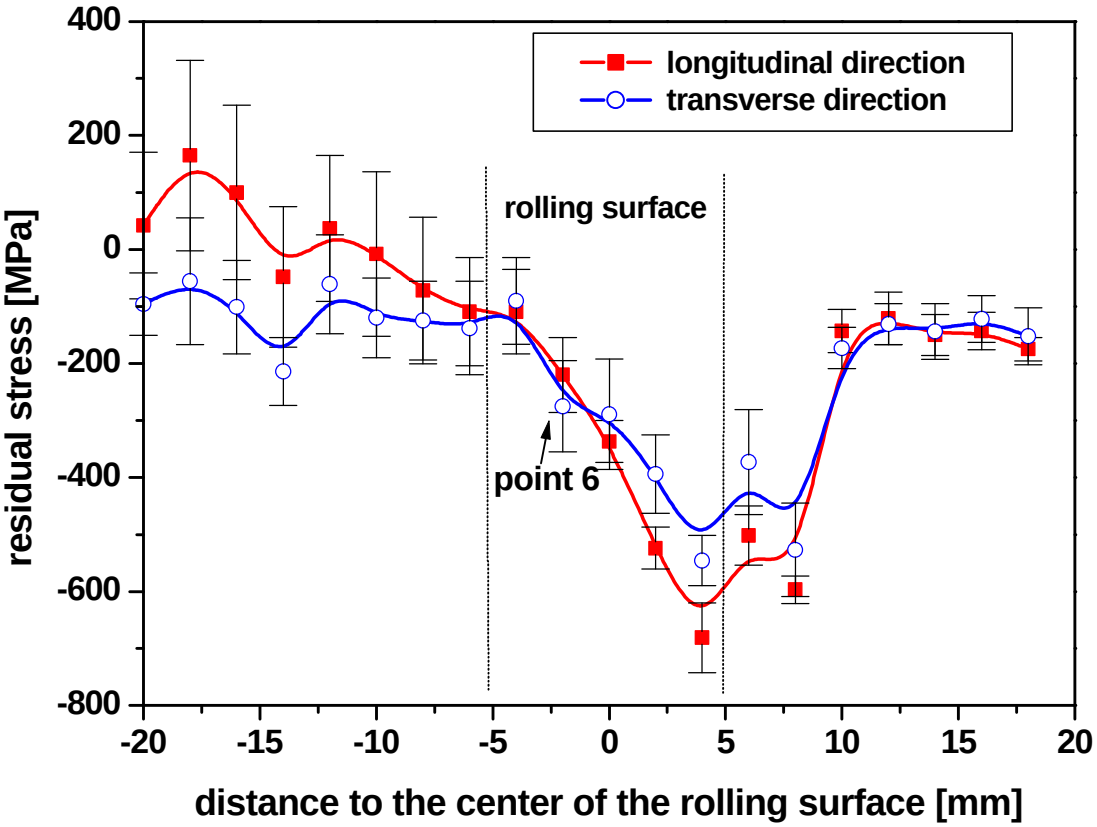

Fig. 5.3.2 Residual stresses distribution along line 6 on rail DB AG

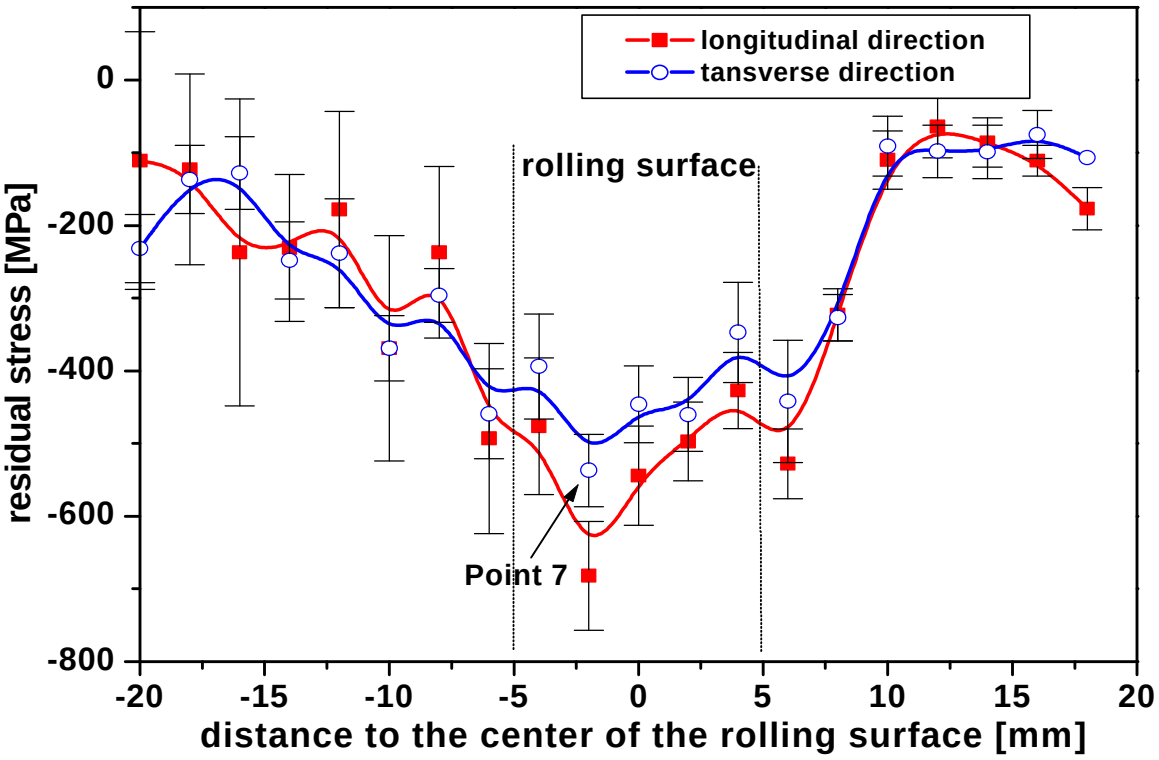

Fig. 5.3.3 Residual stresses distribution along line 7 on rail DB AG

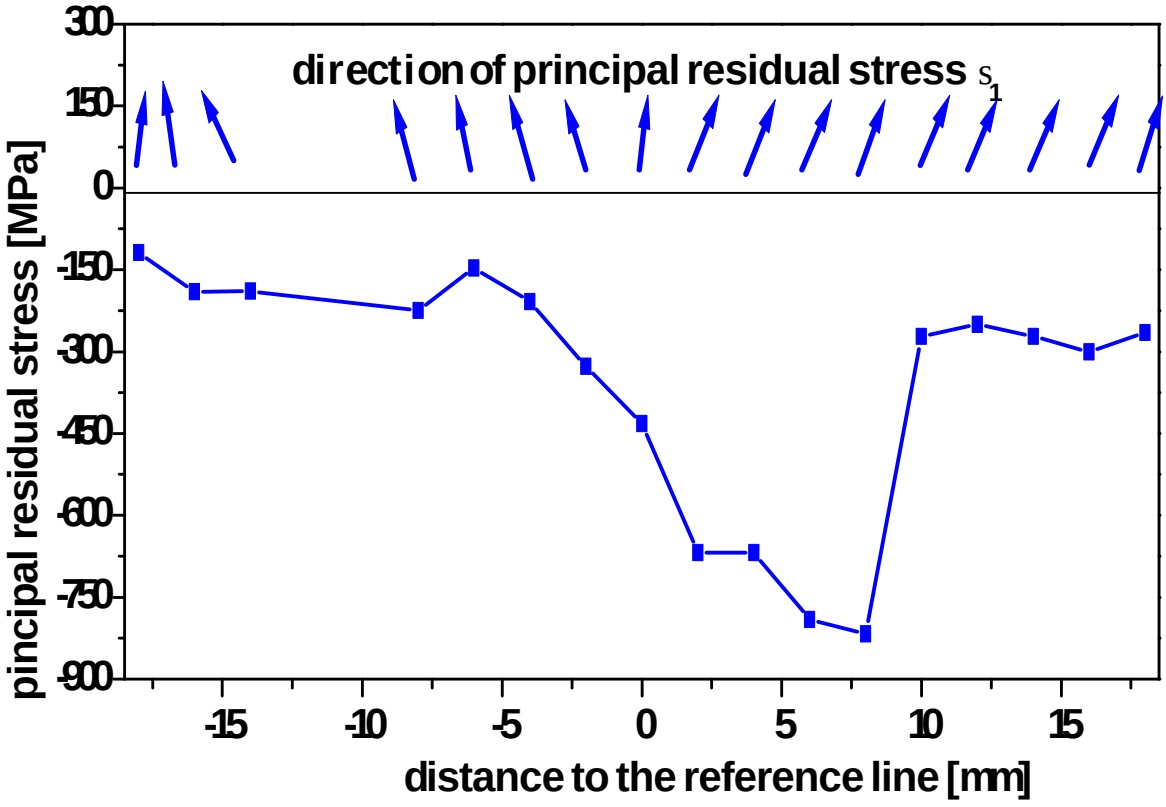

Fig. 5.3.4 Principal residual stress σ_1 along line 1 on rail DB AG

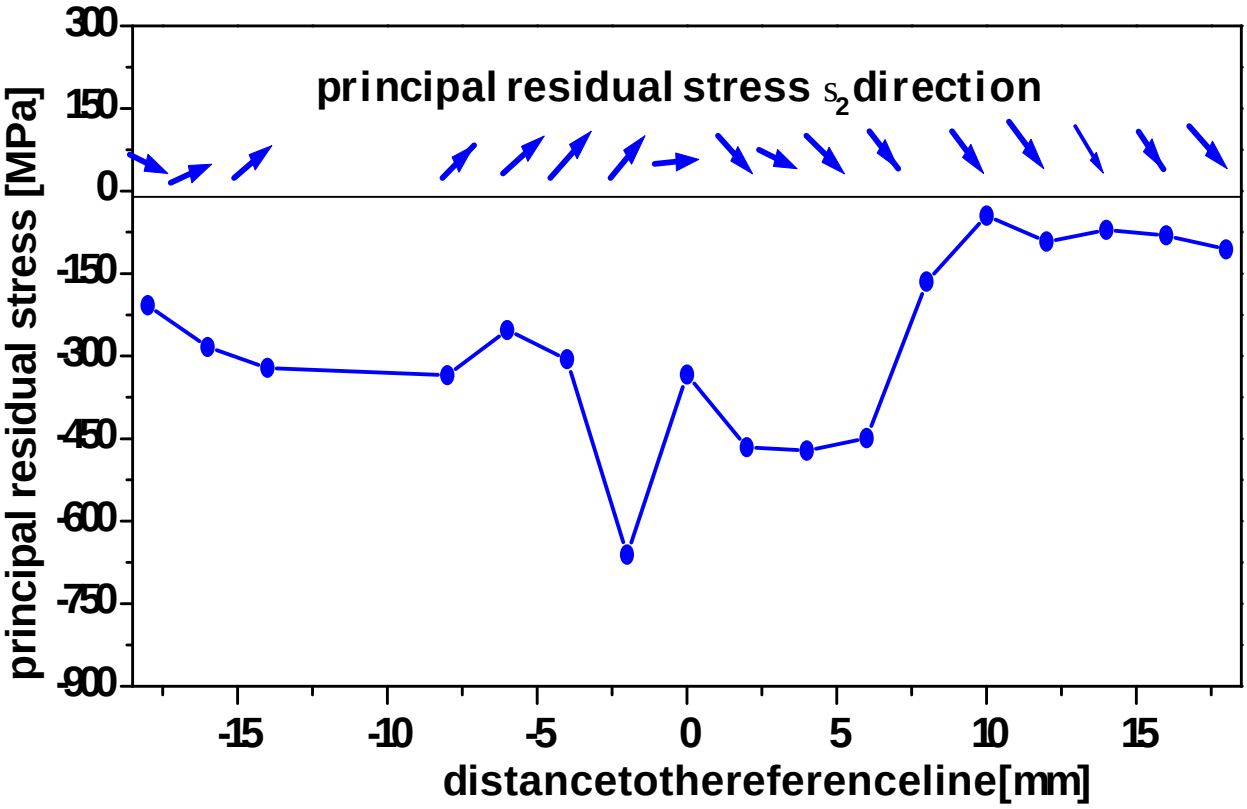

Fig. 5.3.5 Principal residual stress σ_2 along line 1 on rail DB AG

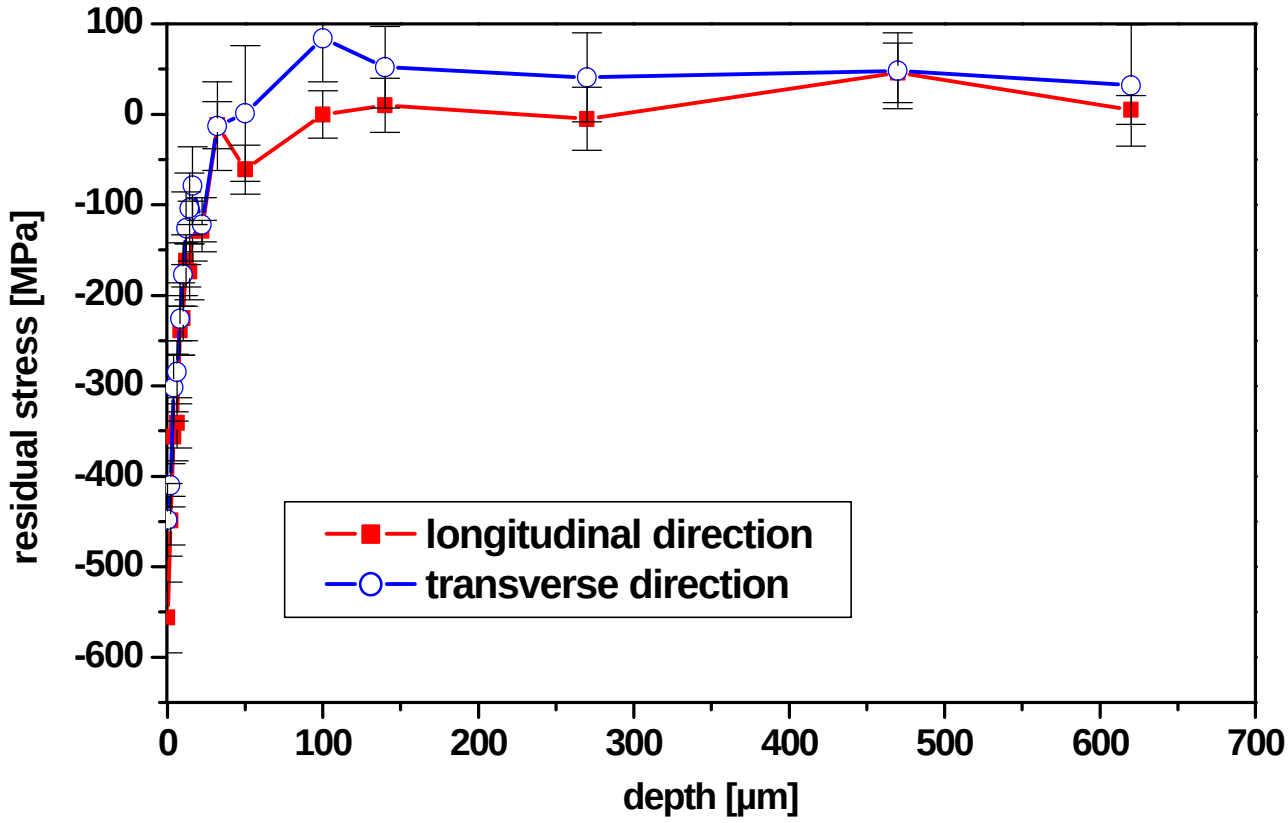

Fig. 5.3.6 Residual stress distribution in the subsurface region of rail DB AG

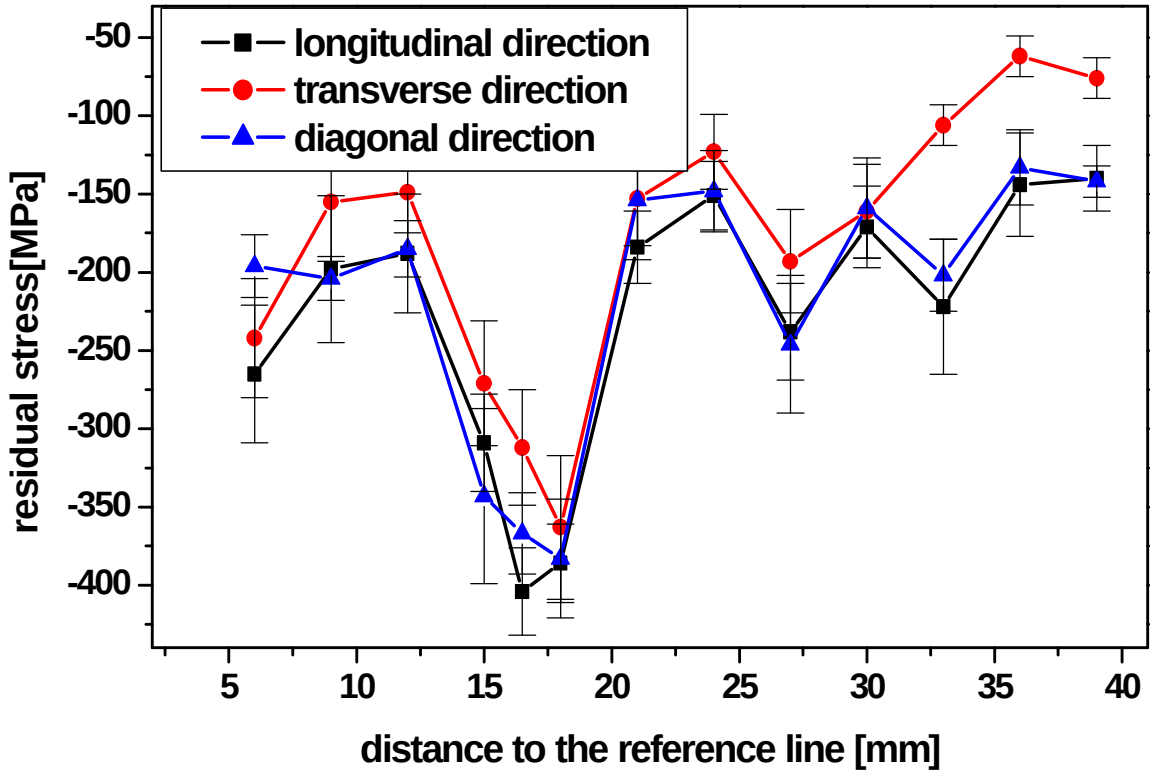

Fig. 5.3.7 Residual stress distribution along line 1 on rail Baumann

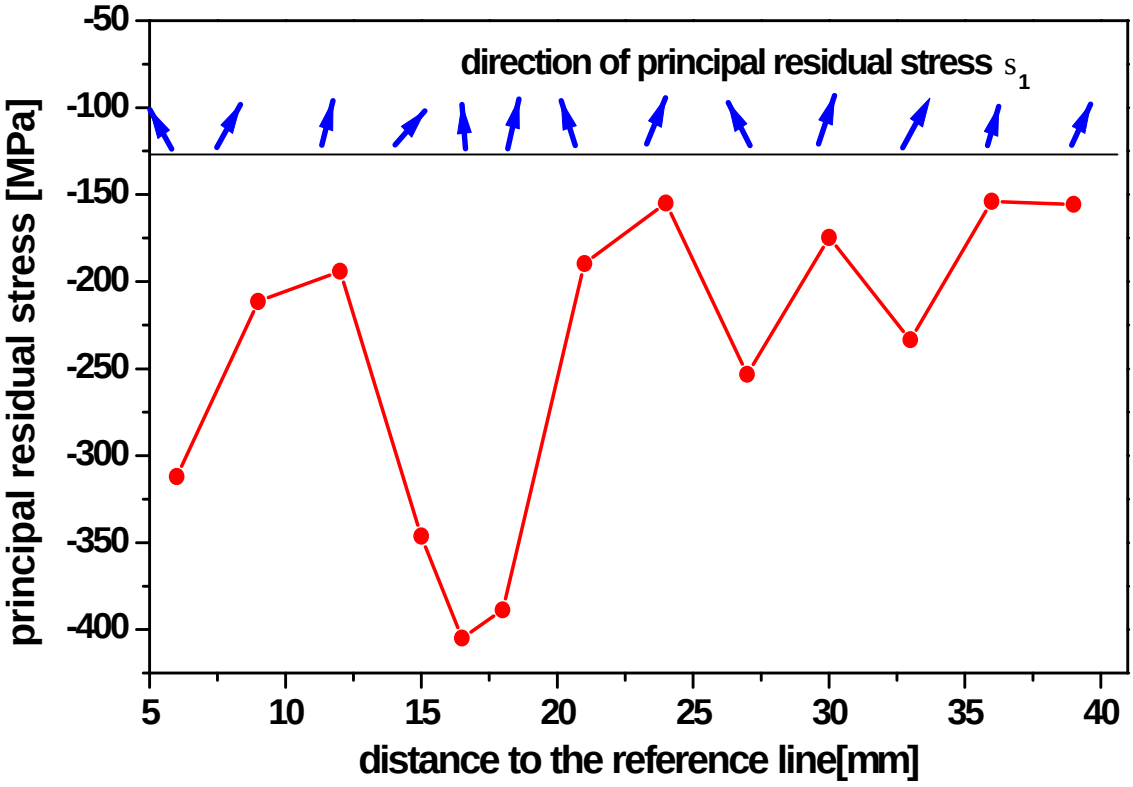

Fig. 5.3.8 Principal residual stress σ_1 along line 1 on rail Baumann

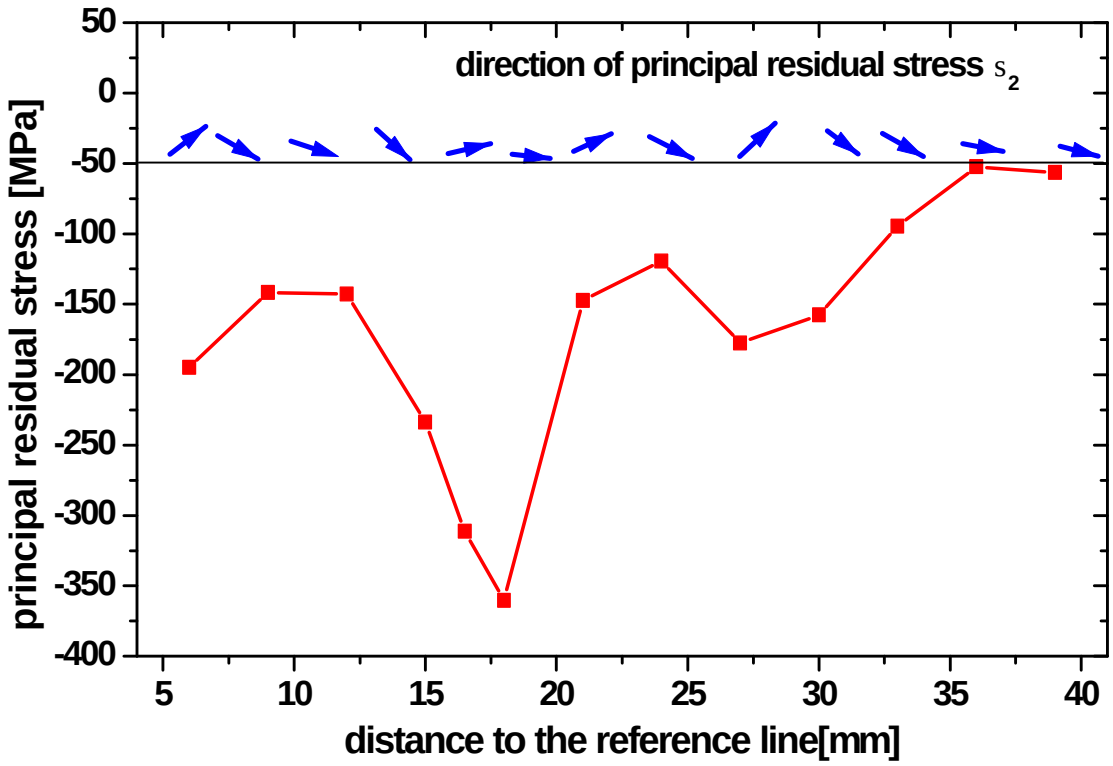

Fig. 5.3.9 Principal residual stress σ_2 along line 1 on rail Baumann

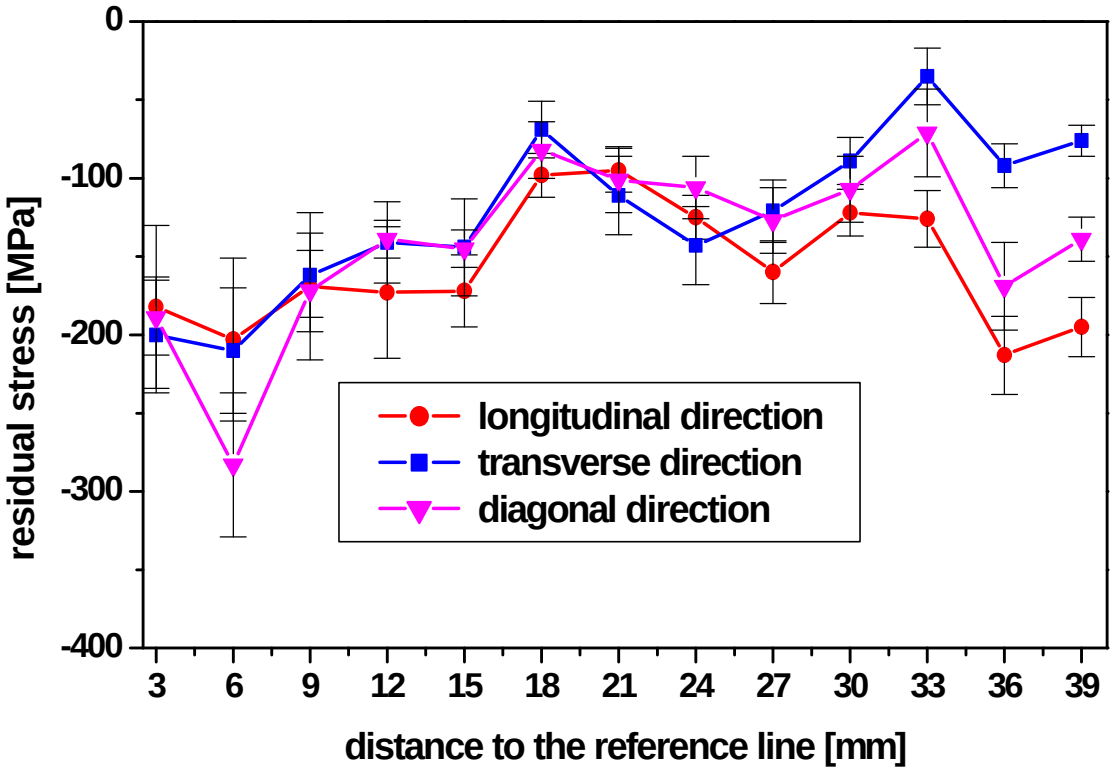

Fig. 5.3.10 Residual stresses distribution along line 2 on rail Baumann

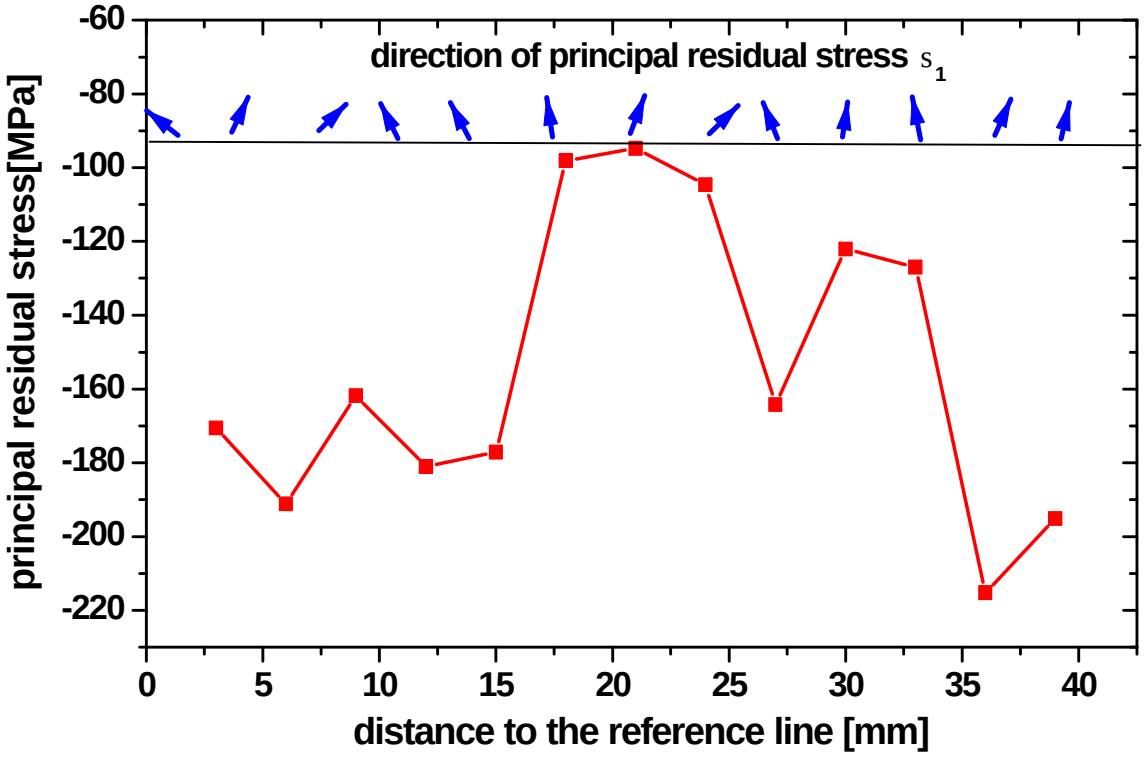

Fig. 5.3.11 Principal residual stress σ_1 along line 2 on rail Baumann

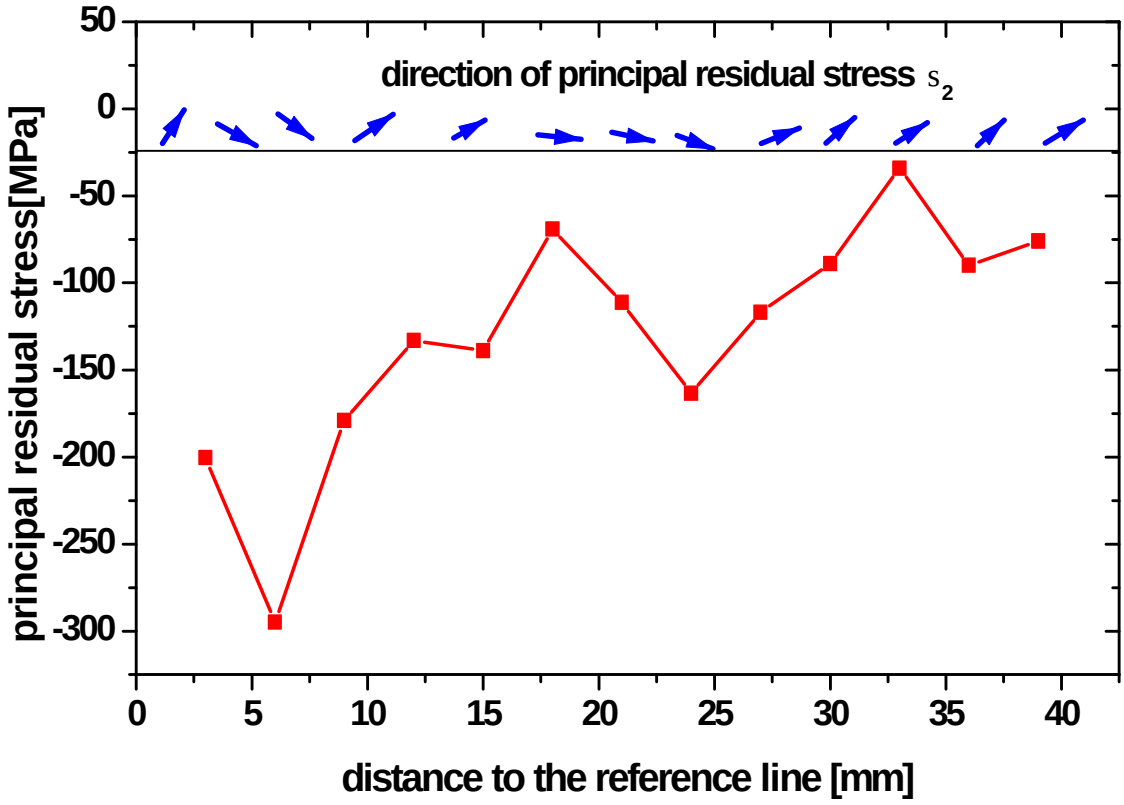

Fig. 5.3.12 Principal residual stress σ_2 along line 2 on rail Baumann

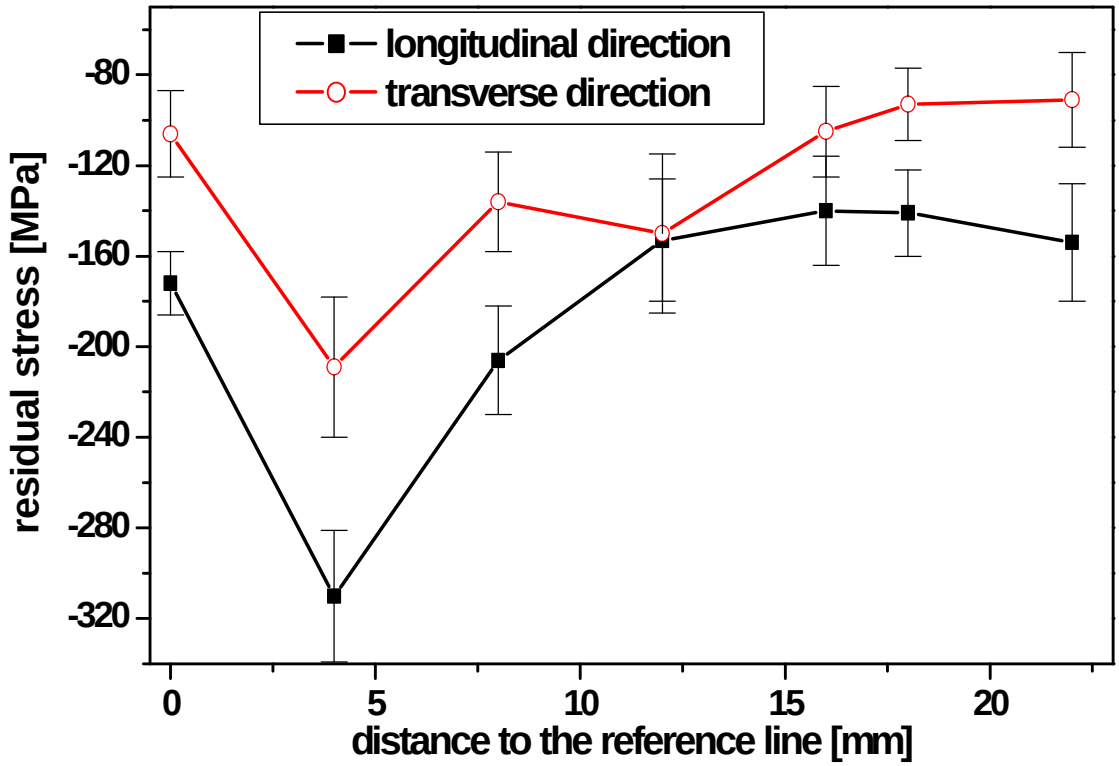

Fig. 5.3.13 Residual stress distribution from X = 0mm to X = 24mm on rail Baumann

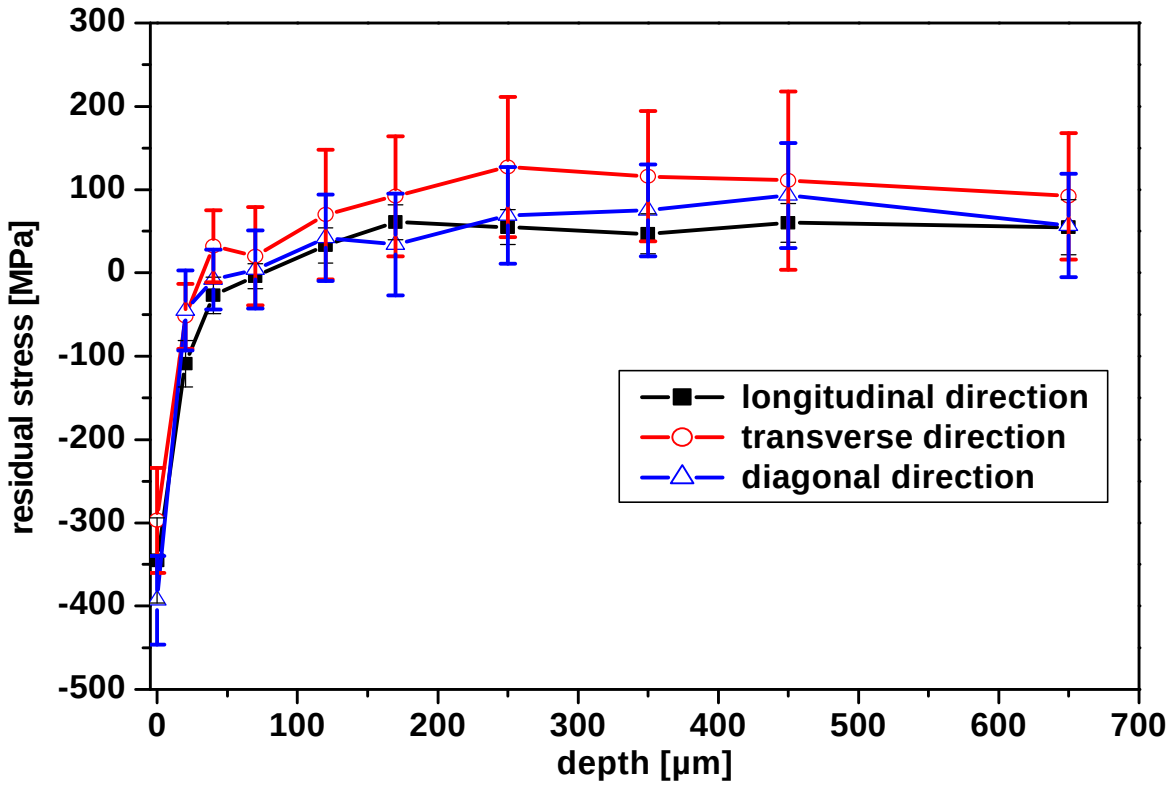

Fig. 5.3.14 Residual stresses distribution below the “riffle hill” of rail Baumann

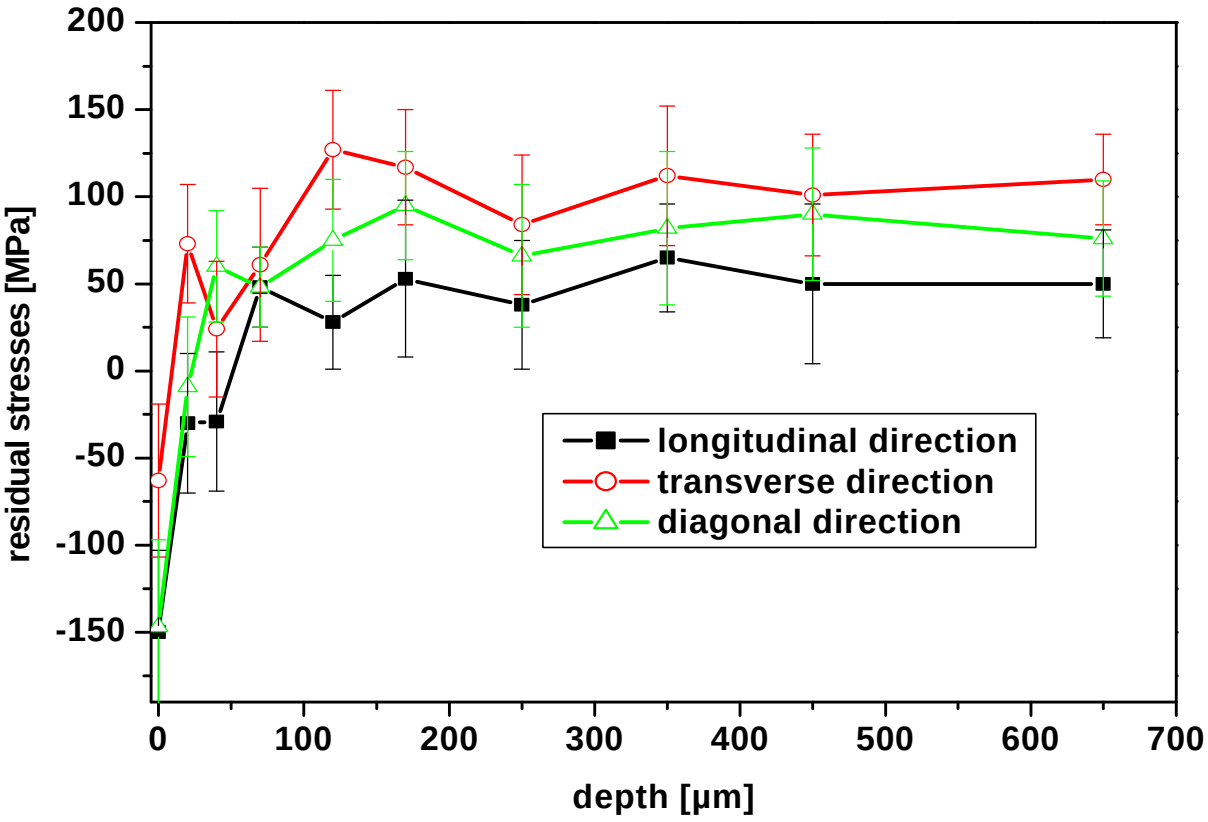

Fig. 5.3.15 Residual stress distribution below the “riffle valley” of rail Baumann

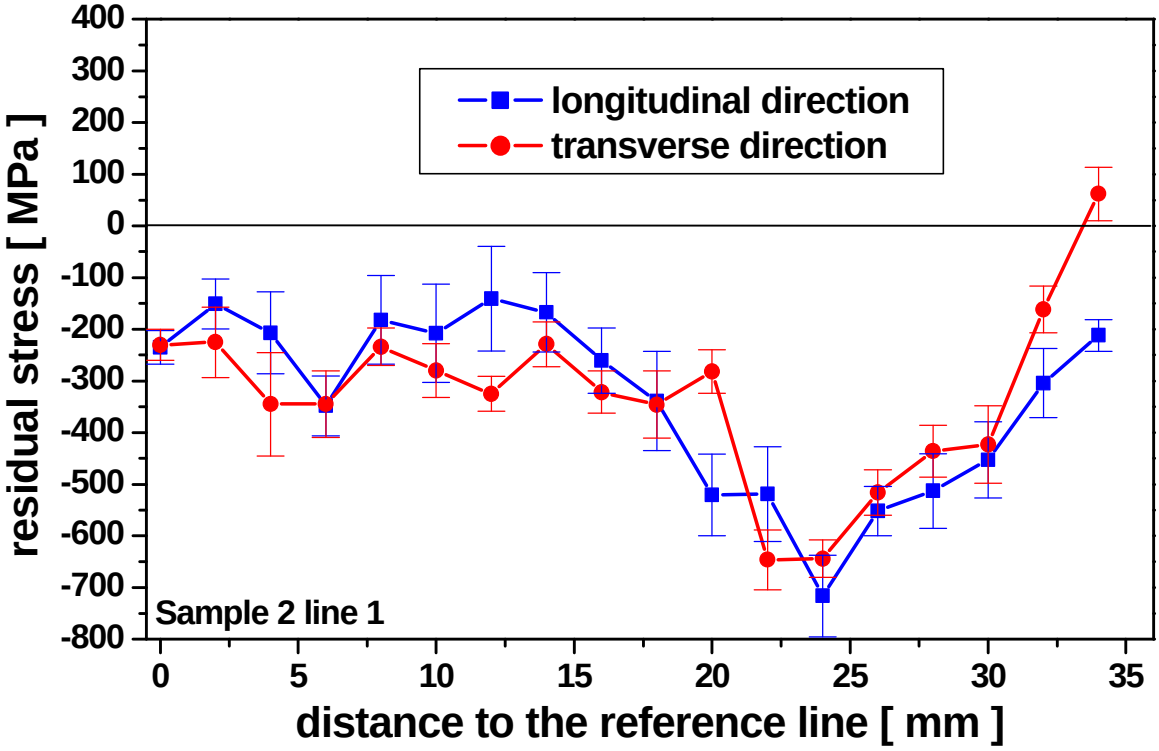

Fig. 5.3.16 Residual stresses distribution of martensite/ferrite along line 1 on rail sample 2

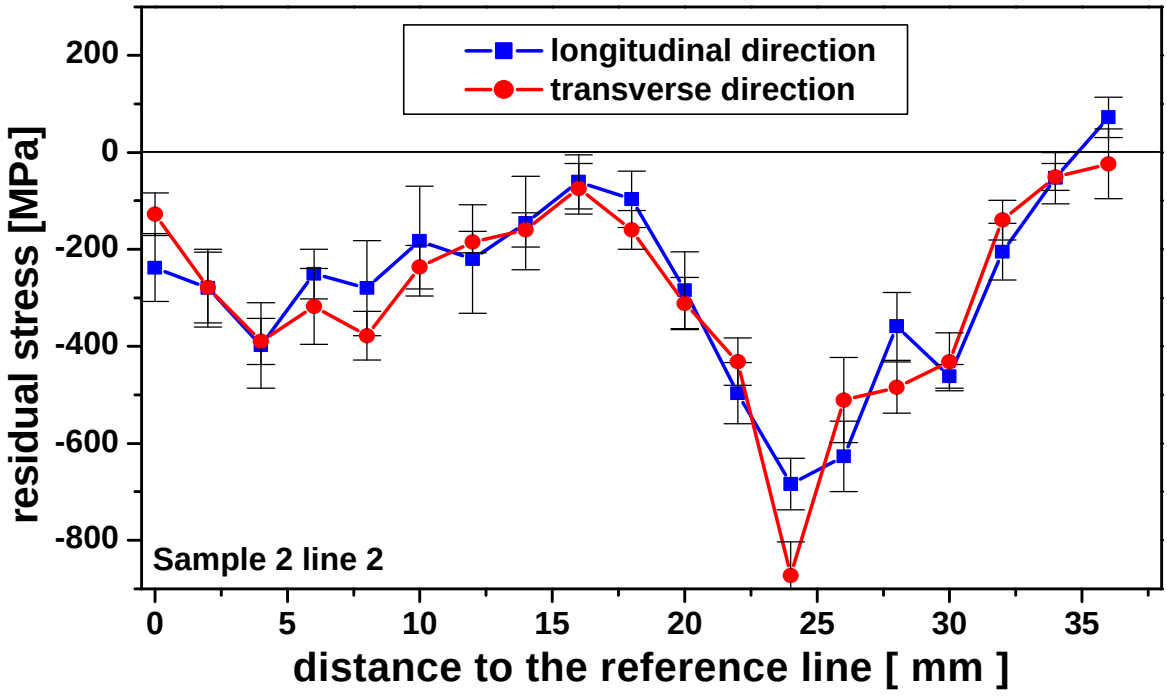

Fig. 5.3.17 Residual stresses distribution of martenisite/ferrite along line 2 on rail sample 2

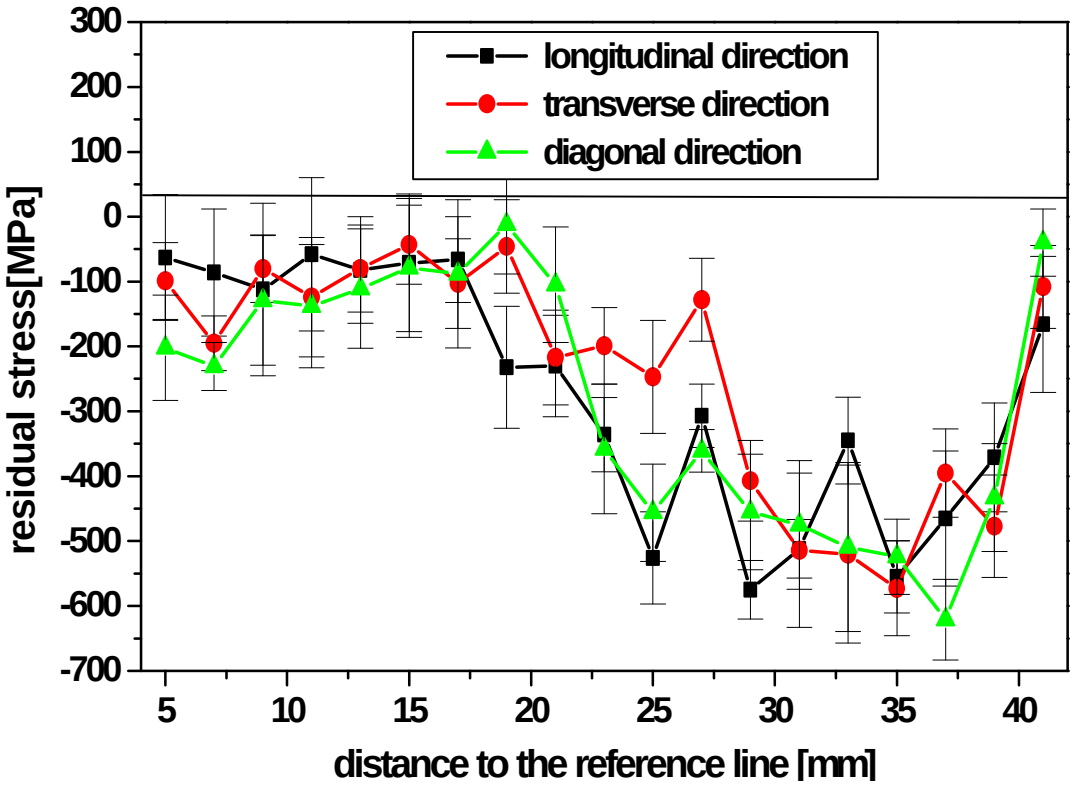

Fig. 5.3.18 Residual stress distribution of martensite/ferrite across the surface of rail sample 3

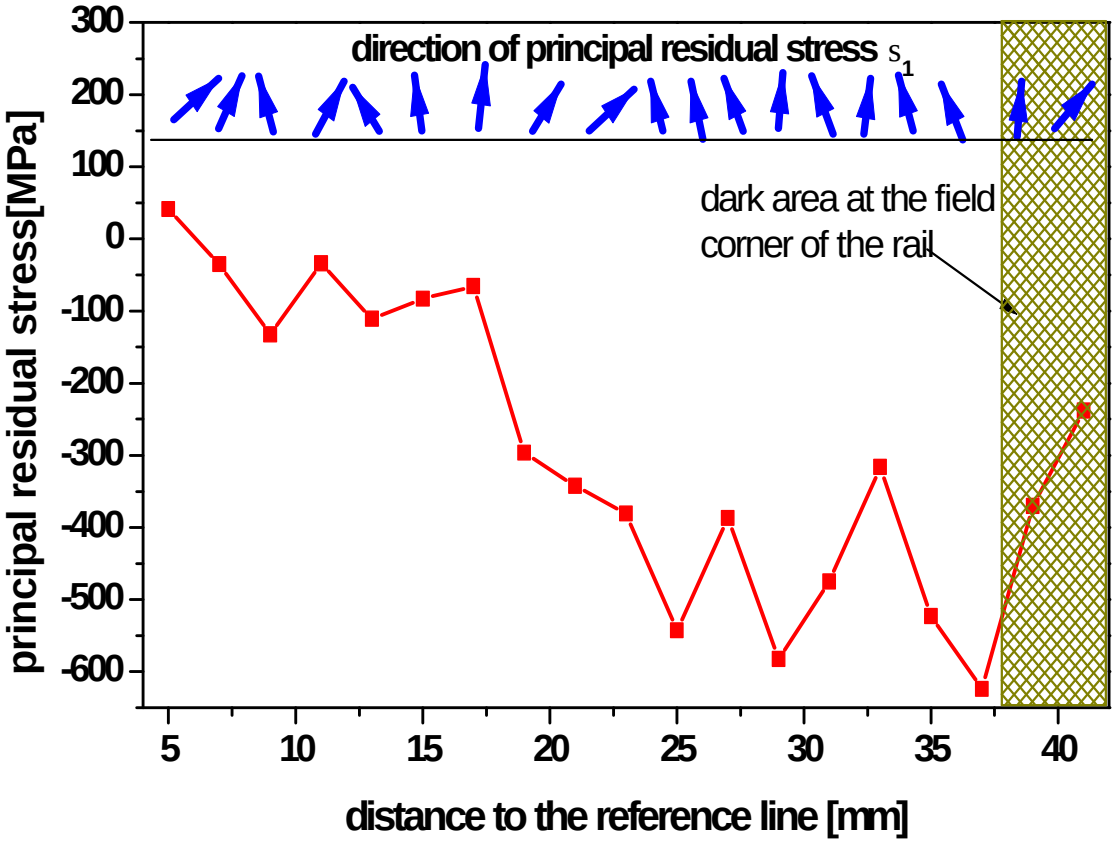

Fig. 5.3.19 Principal residual stress σ_1 on rail sample 3

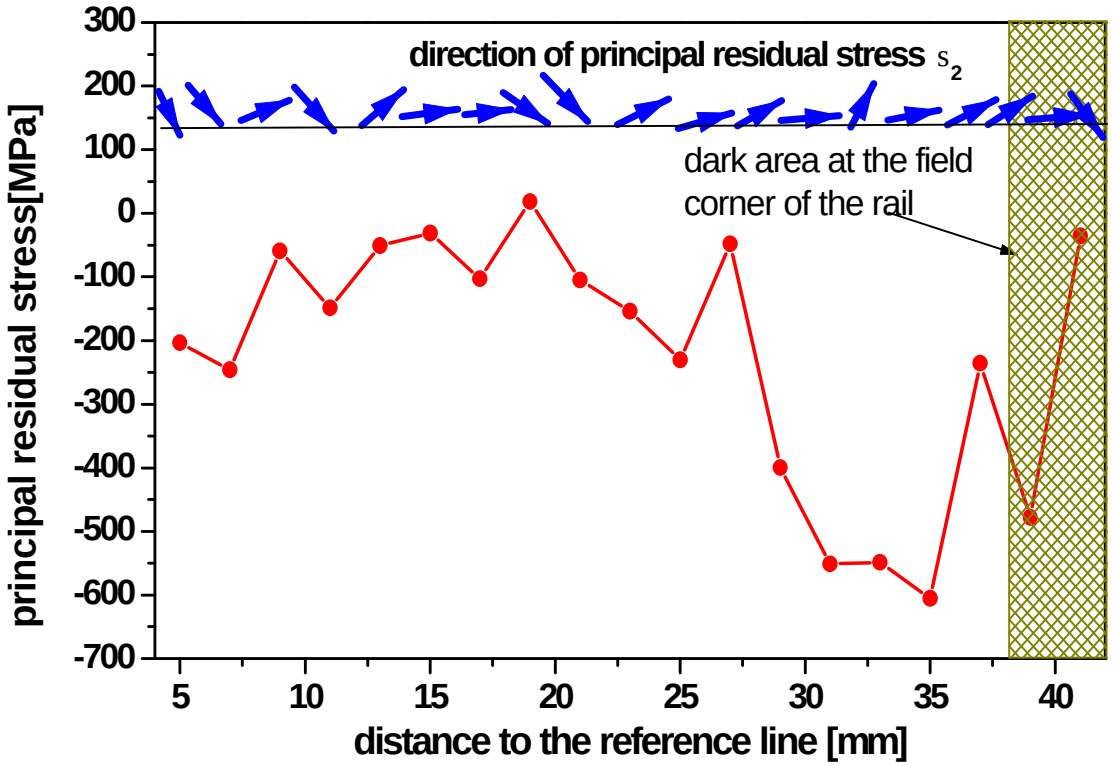

Fig. 5.3.20 Principal residual stress σ_2 on rail sample 3

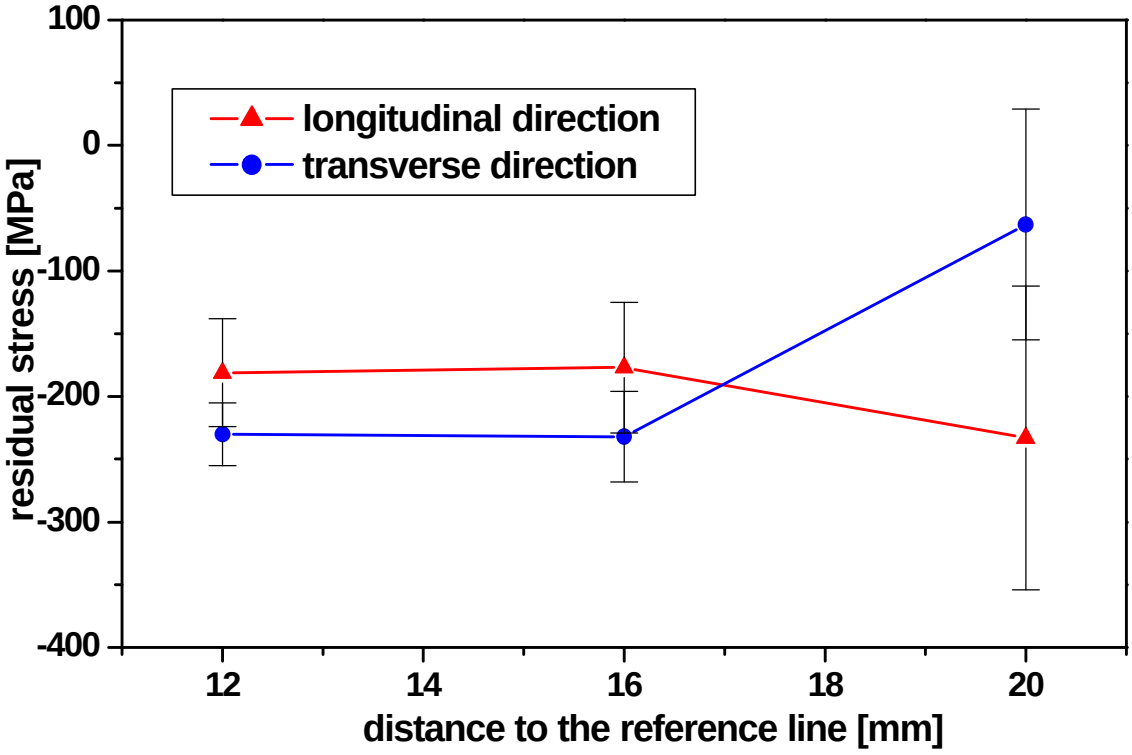

Fig. 5.3.21 Residual stress of austenite on rail sample 2

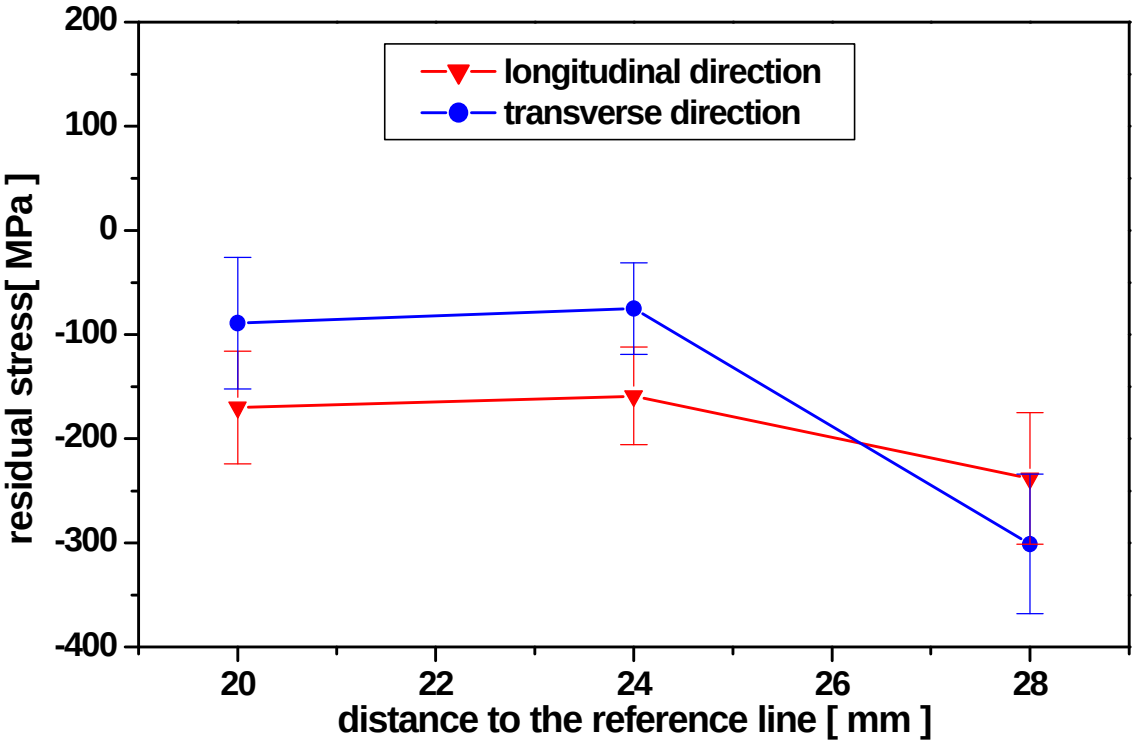

Fig. 5.3.22 Residual stress of austenite on rail sample 3

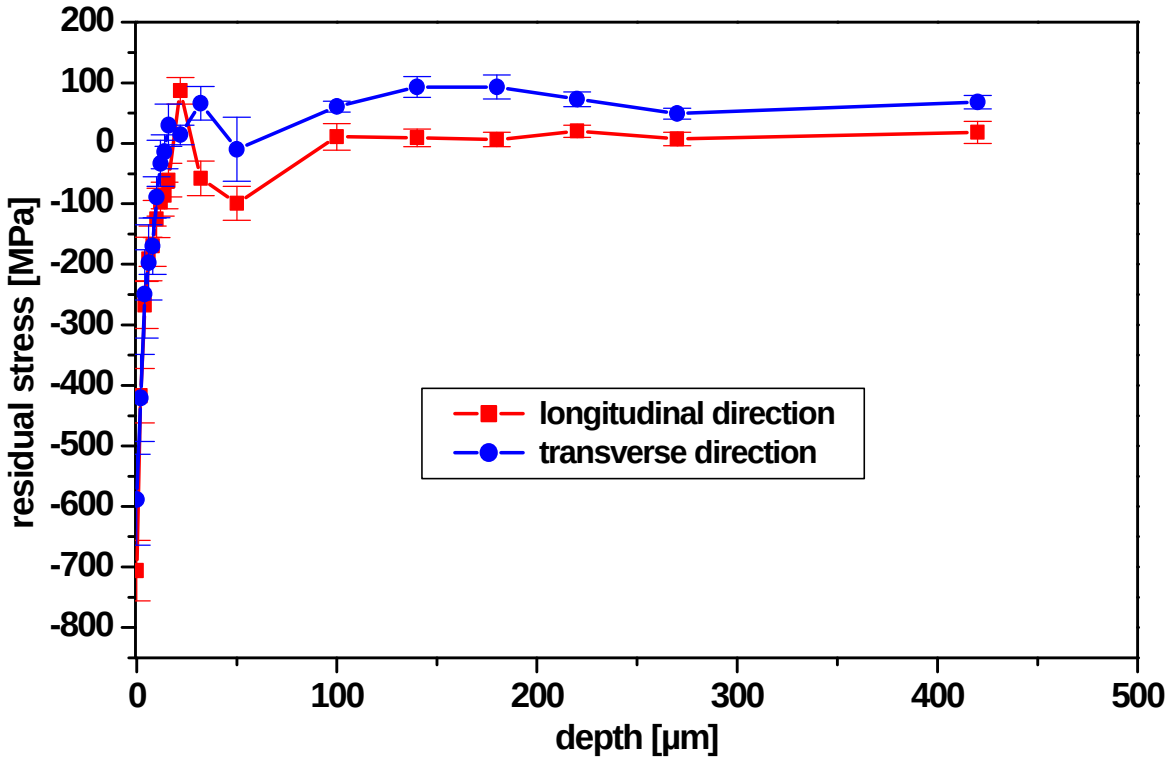

Fig. 5.3.23 Residual stress distribution below the surface of rail sample 3

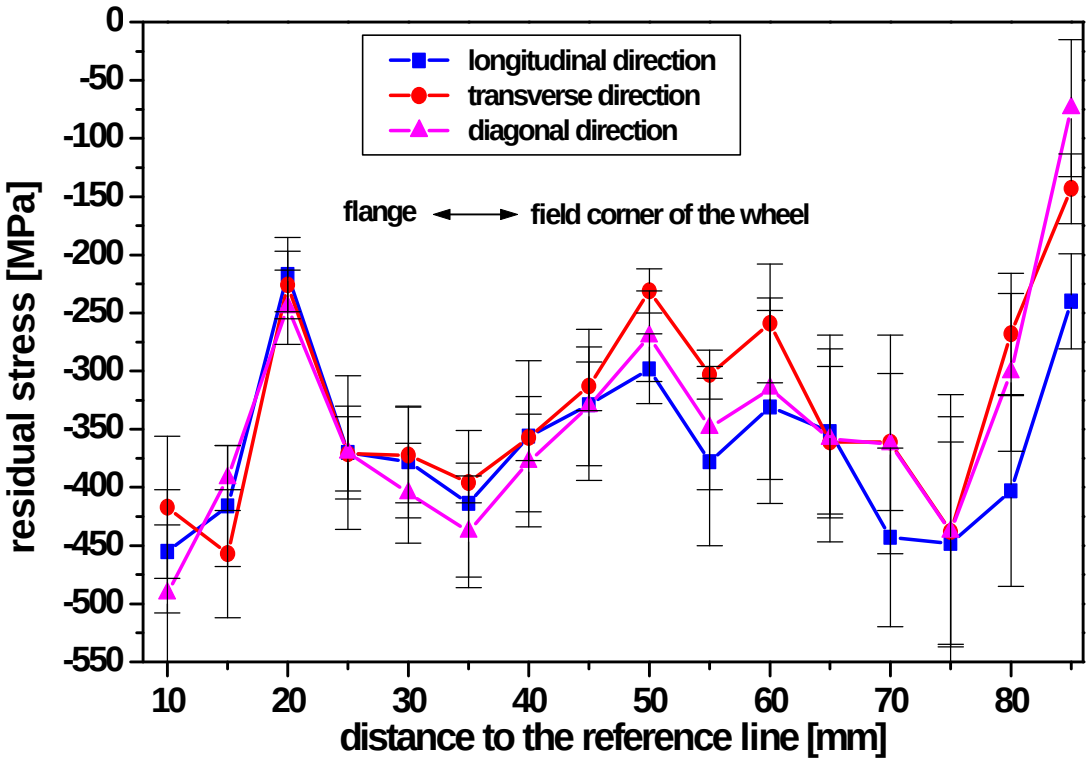

Fig. 5.3.24 Residual stress distribution along line 1 on wheel sample

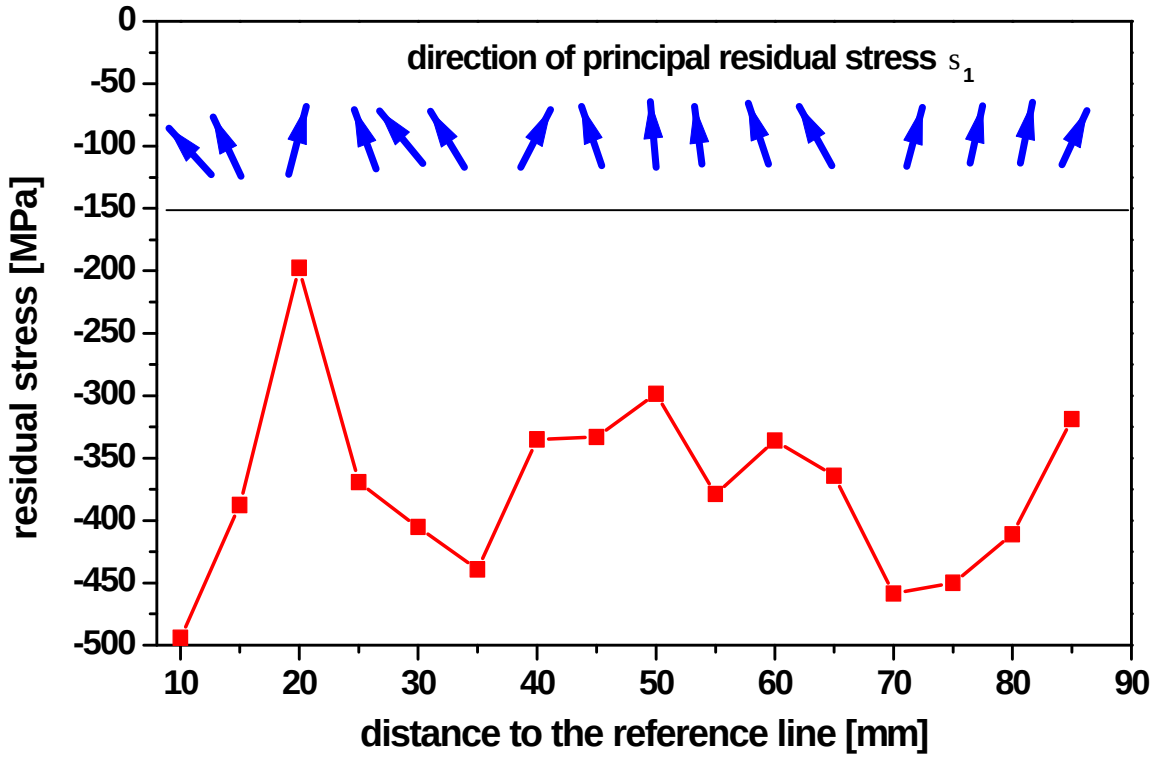

Fig. 5.3.25 Principal residual stress σ_1 distribution on wheel sample

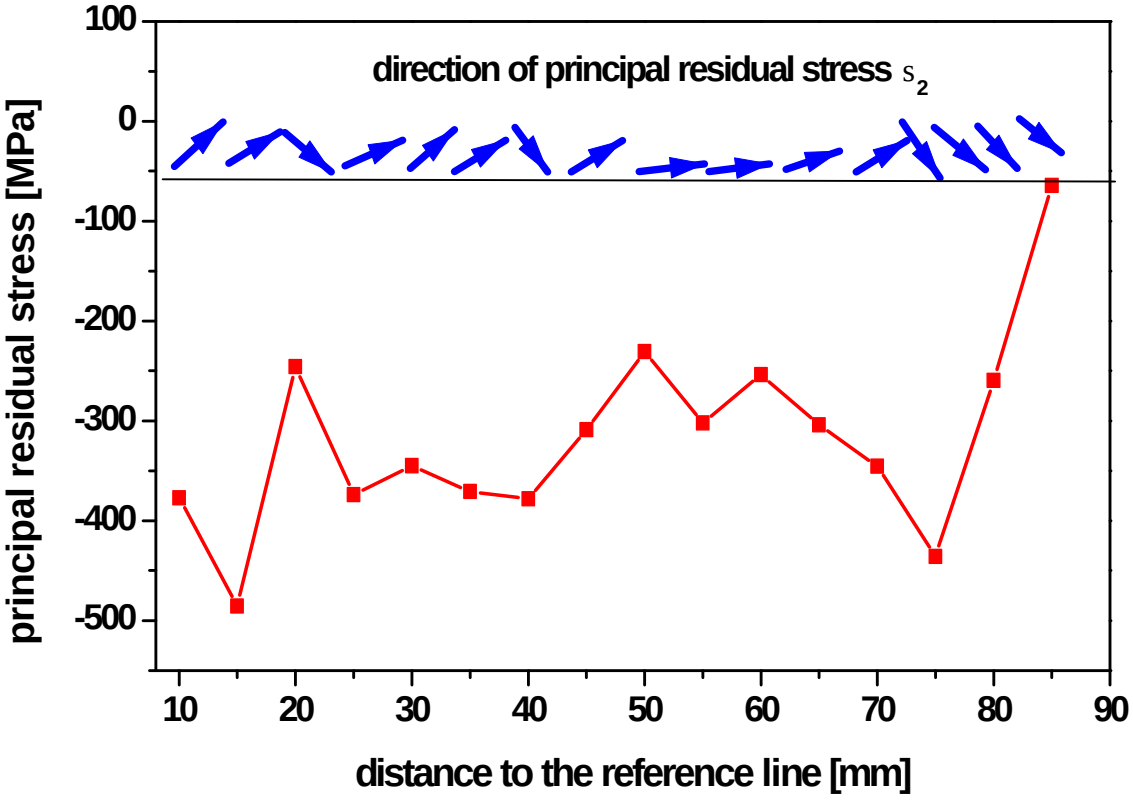

Fig. 5.3.26 Principal residual stress σ_2 distribution on wheel sample

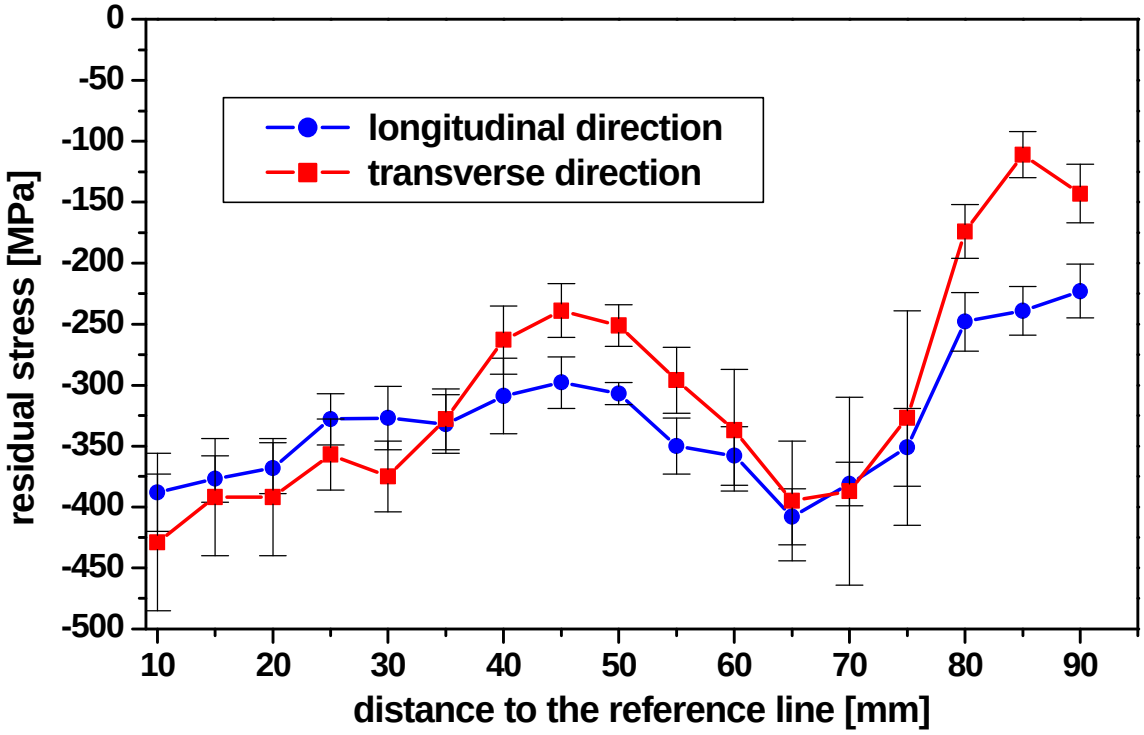

Fig. 5.3.27 Residual stresses distribution along line 2 on the surface of wheel sample

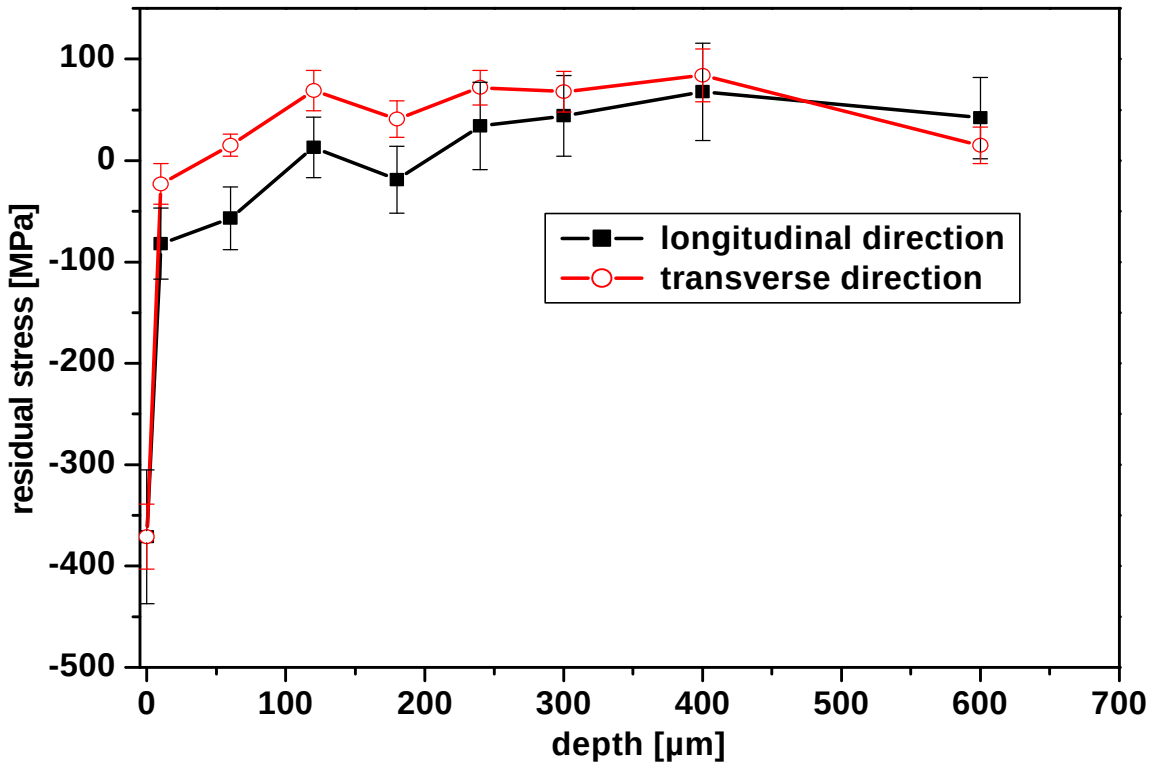

Fig. 5.3.28 Residual stress distribution in the in - depth direction of wheel sample

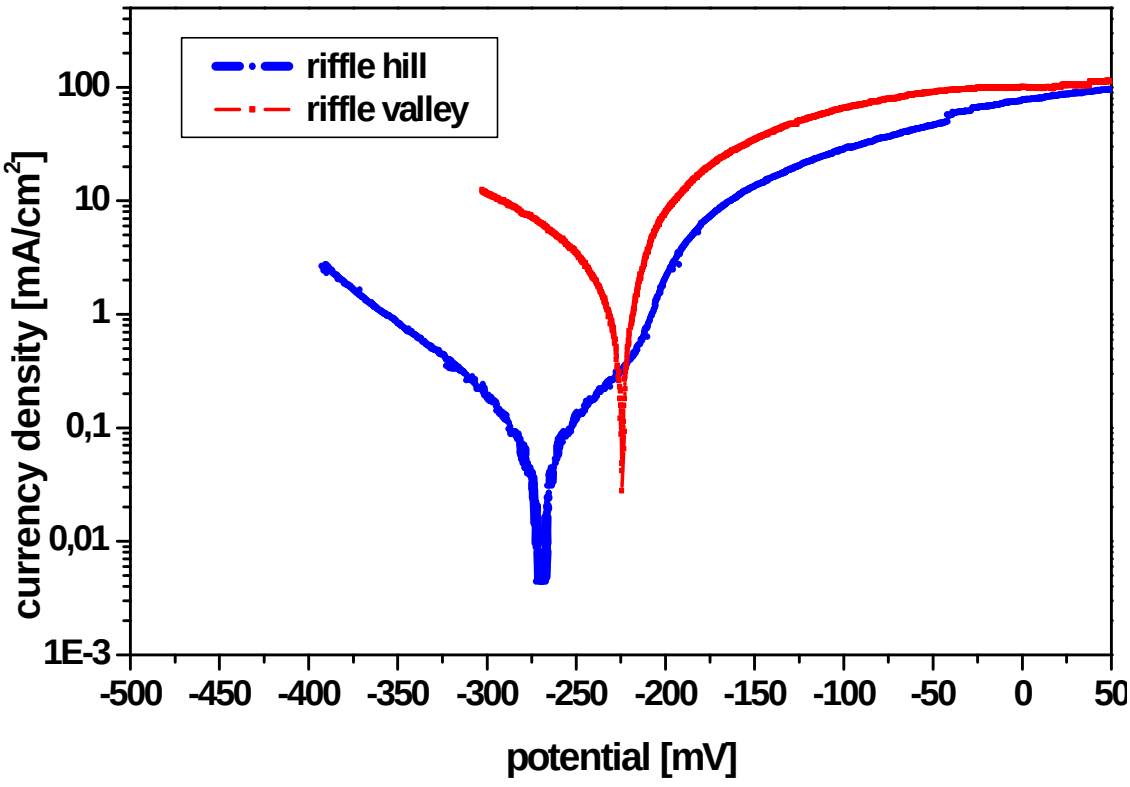

Fig. 5.4.1 Potential curves for WEL area and non - WEL on rail Baumann

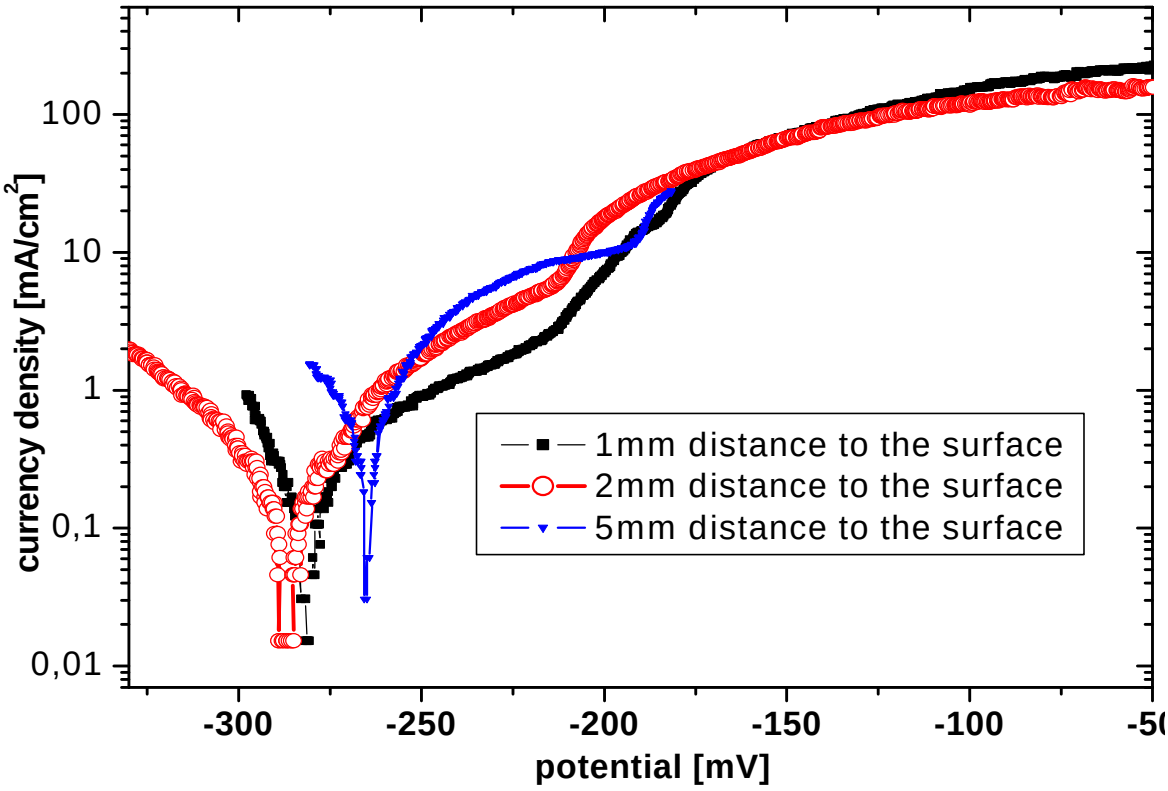

Fig. 5.4.2 Potential curves in different depths below the surface of rail Baumann

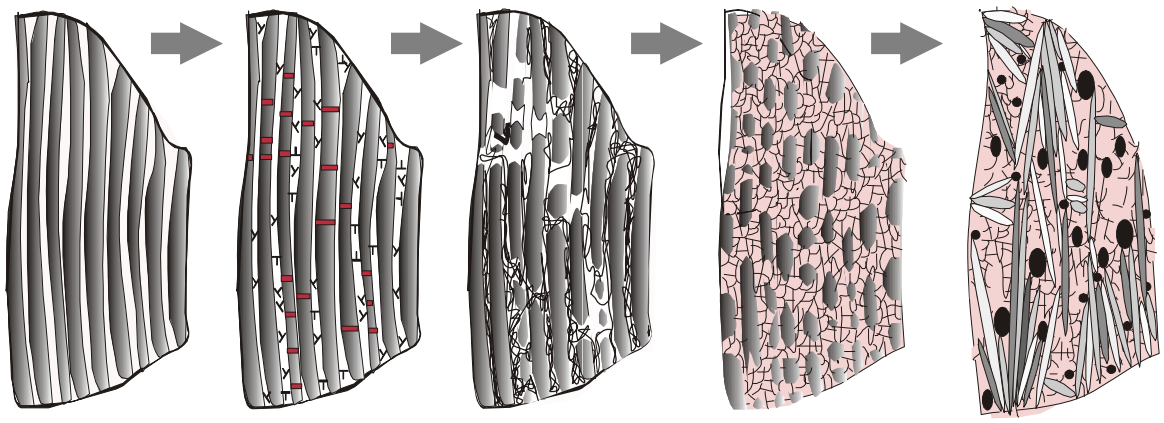

Fig. 6.1 Sketch picture of WEL formation under loading